Measurements of Atmospheric OH and HO_2 Radicals by Laser-Induced Fluorescence on the HALO Aircraft during the OMO-ASIA 2015 Campaign

Inaugural-Dissertation

zur

Erlangung des Doktorsgrades

der Mathematisch-Naturwissenschaftlichen Fakultät

der Universität zu Köln

vorgelegt von

Christopher Künstler

aus Coesfeld

Berichterstatter (Gutachter):

Prof. Dr. Astrid Kiendler-Scharr

PD Dr. Andreas Hofzumahaus

Tag der mündlichen Prüfung: 18.05.2020

Kurzzusammenfassung

Ziel dieser Arbeit ist die Chemie atmosphärischer OH und HO_2 Radikale in der oberen Troposphäre im Rahmen der Oxidation Mechanism Observation (OMO) Kampagne während des Asiatischen Sommer Monsuns 2015 zu untersuchen. OH und HO_2 Konzentrationen wurden auf Basis eines Laser induzierten Fluoreszenz Instrumentes (AirLIF) auf dem deutschen Forschungsflugzeug HALO vom Mittelmeer bis zu den Malediven gemessen. Die gemessenen Daten werden mit theoretischen Modelvorhersagen verglichen um das Verständnis atmosphärischer Oxidationsprozesse zu verbessern. Zu diesem Zweck wurde das zuvor am Forschungszentrum Jülich entwickelte AirLIF Instrument vollständig im Labor charakterisiert und verschiedene Kalibrierkonzepte angewendet und verglichen. Die OMO Radikalmessungen wurden anschließend ausgewertet und den berechneten OH und HO_2 Radikalkonzentrationen eines null-dimensionalen chemischen Box-Models gegenüber gestellt.

Um Verluste wegen der hohen OH Radikalreaktivität zu minimieren, wird die gesammelte Luft mit Hilfe eines in die Außenhaut von HALO installierten Inlet Shrouds zunächst um einen Faktor 10 verlangsamt und erst dann von einer Düse in eine Niederdruckzelle im Flugzeug gesaugt. Die Detektion von OH findet dort dann mittels Laser angeregter Fluoreszenz statt. HO_2 wird innerhalb der Zelle zuvor durch Reaktion mit NO teilweise in OH konvertiert. Zur Auswertung der gemessenen Signale benötigten sowohl der OH als auch der HO_2 Kanal von AirLIF umfassende Charakterisierungen um sämtliche Flugbedingungen während OMO Asien zu erfassen. Dazu wurden unter anderem verschiedene Kalibrierkonzepte angewendet und kombiniert um die OH und HO_2 Empfindlichkeiten als Funktion der Flughöhe, Umgebungsdruck und Temperatur zu bestimmen. Diese beinhalteten die bereits etablierten bodengebundenen Kalibrationen auf dem Flugfeld um absolute Änderungen in der Empfindlichkeit festzustellen. Die relative Abhängigkeit mit der Flughöhe wurde separat im Labor mit einer für diese Zwecke neu entwickelten photochemischen Radikalquelle gemessen, die es gestattet Kalibrationen bei Unterdruck durchzuführen um die Außendrücke während des Fluges zu simulieren. Für den OH Kanal gibt es die zusätzliche Option einer in-flight Kalibration im Innern des Inlet Shrouds. Diese ist jedoch auf Flughöhen unterhalb 10 km beschränkt, da die Radikalerzeugung durch künstliche Wasserdampfphotolyse zu klein wird.

Zur Simulation der Flugbedingungen verwendeten andere Forschungseinrichtungen bisher verschiedene Düsendurchmesser um den Massenfluss durch die Zelle zu ändern, statt den Vordruck zu variieren. Im Rahmen eines Konsistenzchecks wurden beide Methoden verglichen und deren Äquivalenz bestätigt. Unstetigkeiten in der Druckabhängigkeit der OH Kalibrationskurve hängen jedoch vermutlich mit Änderungen in den Gasexpansionsbedingungen zusammen und sind daher düsenspezifisch nur mit der neu entwickelten Radikalquelle detektierbar. Während der Laborcharakterisierungen des HO_2 Kanals wurde festgestellt, dass der ursprünglich angenommene statische Umgebungsdruck auf Grund der hohen Strömungsgeschwindigkeit über der HO_2 Düse tatsächlich zu einem verringerten effektiven HO_2 Einlassdruck führt. Mit Hilfe der Software ANSYS Fluent konnte dieser zu einem real geringeren Massenfluss führende Effekt herausgerechnet werden.

Die OMO Kampagne erstreckte sich zeitlich vom 21. Juli bis zum 27. August 2015 und war in drei Phasen eingeteilt. Bis zum 01. August 2015 war HALO auf dem Flughafen von Paphos (Zypern) stationiert und beschränkte sich zunächst auf Flugrouten über Zypern und dem Mittelmeer. Während der zweiten Phase lag der Ausgangsflughafen auf Gan (Malediven). Dadurch boten sich zugleich Flugziele wie Bahrain westlich, aber auch Sri Lanka östlich von Indien an. Ab dem 10. August bis zum Ende der Kampagne befand sich HALO wieder auf Zypern, von wo aus dann die Arabische Halbinsel, Ägypten und Griechenland als Primärziele gewählt wurden. Gegen Ende der Kampagne stattete HALO auch dem Vulkan Mount Enta einen Besuch ab. Im Ganzen beinhaltete die OMO Asien Kampagne 17 Flüge, die mit bis zu 15 km Höhe zum Teil die Tropopause erreichten. Das AirLIF Instrument lief zu 2/3 der Zeit problemlos. Andere Institute die an OMO teilgenommen haben waren das Karlsruher Institut für Technologie (KIT), das Deutsche Zentrum für Luft- und Raumfahrt (DLR), das Max-Planck Institut für Chemie (MPIC Mainz) und die Universitäten Bremen, Wuppertal, Heidelberg und Leipzig. Das MPIC Mainz betrieb zur Messung von OH und HO_2 Radikalen ein zweites LIF Instrument, so dass mit OMO Asien erstmalig zeitgleiche HO_x Flugzeugradikalmessungen verglichen werden können.

Der Vergleich der Ergebnisse beider - AirLIF und HORUS - in-flight OH und HO_2 Radikalmessungen als Teil dieser Arbeit zeigt sowohl flugweise als auch im Allgemeinen eine gute Übereinstimmung der von beiden Grup-

pen durchgeführten Kalibrationen. Es wird das OH und HO_2 Vertikalprofil bis zu 15 km anhand der wesentlichen atmosphärischen Parameter wie CO und NO die Einfluss auf das HO_x Budget nehmen diskutiert. Mit Hilfe eines einfachen analytischen Ansatzes wird das HO_2/OH Verhältnis untersucht. Dieses zeigt gute Übereinstimmung mit den Messungen oberhalb 7 km Flughöhe, jedoch darunter Abweichungen bis zu einem Faktor 3. Ferner werden die Vertikalprofile im Rahmen eines null-dimensionalen chemischen Box-Models berechnet, in dem wichtige Spurengase durch die Flugzeugmessungen anderer Instrumente während OMO vorgegeben werden. Hier zeigt sich gute Übereinstimmung innerhalb der Fehlertoleranzen zwischen 7 km und 11.5 km, wobei unterhalb 7 km OH um bis zu einen Faktor 2.5 überschätzt und HO_2 korrekt vorhergesagt wird. Dies deckt sich mit der Unterschätzung des HO_2/OH Verhältnisses bis zu einem Faktor von 3 welcher durch das analytische Model vorhergesagt wurde. Oberhalb 11.5 km werden sowohl OH als auch HO_2 jeweils um einen Faktor 2.5 zu hoch prognostiziert. Diese Diskrepanz kürzt sich allerdings im HO_2/OH Verhältnis heraus und deutet somit entweder auf fehlende HO_x Senken oder überschätzte HO_x Quellen hin. Die beobachteten Abweichungen werden zum Schluss durch eine Empfindlichkeitsstudie zu erklären versucht. In der unteren Troposphäre ist die naheliegendste Erklärung wohl auf fehlende VOC Reaktivität zurückzuführen, die hauptsächlich für OH eine Senke darstellt. Durch leichte Erhöhung der OH Reaktivität ($0.1\,{}^{1}/_{s}$) wegen fehlender VOC Messungen während der OMO Asien Kampagne, konnte die Diskrepanz für OH bei zeitgleicher Aufrechterhaltung der Übereinstimmung für HO_2 weitestgehend geschlossen werden. Lediglich unterhalb von 2 km verblieb eine Abweichung um bis zu einen Faktor 2.5. Umgekehrt gab es in der oberen Troposphäre Hinweise auf eine Überschätzung des durch das von EMAC MPIC vorhergesagten Formaldehyd, welches zu einer gleichzeitigen Erhöhung von OH und HO_2 führt.

Diese Arbeit liefert Hinweise für technische Verbesserungen zukünftiger LIF-Flugzeuganwendungen.

Abstract

The goal of this work was to investigate the chemistry of atmospheric OH and HO_2 radicals in the upper troposphere during the Asian summer monsoon period 2015 within the Oxidation Mechanism Observation (OMO) campaign. Concentrations of OH and HO_2 were measured by a laser-induced fluorescence instrument (AirLIF) on the German research aircraft HALO between the Mediterranean Sea and the Maldives in the Indian Ocean. The measured data are compared to theoretical model predictions in order to test the understanding of atmospheric oxidation processes. For this purpose the precedingly developed AirLIF instrument at Forschungszentrum Jülich was thoroughly characterized in the laboratory and different calibration concepts applied and compared. The radical measurements during OMO were then evaluated and a zero-dimensional chemical box-model calculation for the expected OH and HO_2 radical concentrations was tested against the measurement results.

For the radical measurements using the AirLIF instrument on HALO, the ambient air is first sampled and decelerated by a factor of 10 inside a shrouded inlet. The air is then expanded into a measurement cell at low pressure inside the aircraft, where OH is detected by laser excited fluorescence. The OH and HO_2 channel of AirLIF needed to be characterized for the flight conditions during OMO. Different calibration concepts have been applied and combined to determine the OH and HO_2 detection sensitivities as a function of flight altitude, ambient pressure and temperature. These include the well-established ground-based calibrations between flights to track the absolute sensitivities. The relative dependence with altitude was measured in the laboratory using a newly designed photochemical radical source which allows calibration at reduced pressure to simulate ambient air pressure at flight conditions. For the OH-channel as an additional option an in-flight calibration unit inside the shrouded inlet was used. It is however limited to below 10 km, because the radical production by the artificial photolysis of ambient water vapour becomes too small.

To simulate the in-flight conditions, other research groups have confided in using different nozzle sizes to change the mass-flow through the system instead of varying ambient pressure. As part of a consistency check, both methods have been compared in detail and it is confirmed that they essentially agree. However, discontinuities in the pressure dependence of the OH cali-

bration curve are presumably related to a change in conditions of the gas expansion and are thereby unique to a specific nozzle. The correct detection of this jump in sensitivity is therefore limited to the newly developed radical source. During the laboratory characterization of the HO_2 channel a fluid dynamical effect on the HO_2 nozzle was discovered which is due to the lacking shrouded inlet and led to an overestimated HO_2 inlet pressure, originally assumed to be static ambient pressure. It was possible to correct this by calculating the true mass flow through the nozzle using the computational fluid dynamics (CFD) software ANSYS Fluent.

The OMO campaign took place from 21 July until 27 August 2015 and was divided in three phases. Till 01 August 2015 HALO was stationed on the airport of Paphos (Cyprus) and mainly flew over Cyprus and the Mediterranean Sea. During the second phase HALO was stationed on Gan (Maldives) aiming for the flight targets Bahrain and Sri Lanka, west and east of India respectively. From 10 August till the end of the campaign, HALO was again stationed on Cyprus and covered the Arabian Peninsula, Egypt and Greece as primary flight targets. At the end of the campaign for two flights Mount Etna was visited. In total OMO Asia comprised 17 flights up to 15 km of which AirLIF measured 2/3 of the time. Other institutes involved in OMO were the Karlsruhe Institute of Technology (KIT), the German Aerospace Center (DLR), the Max-Planck Institute for Chemistry (MPIC Mainz) and the universities Bremen, Wuppertal, Heidelberg and Leipzig. The MPIC Mainz provided a second LIF instrument measuring OH and HO_2 radicals contemporaneously for the first time.

Both, AirLIF and HORUS OH and HO_2 in-flight measurements are intercompared flight-wise showing a general good agreement of their calibrations. The vertical profile of OH and HO_2 up to 15 km is discussed in particular with respect to important atmospheric controlling parameters such as CO and NO. The HO_2/OH ratio is then analyzed by a simple analytic approach. It is found that the latter is well explained above 7 km, while below a gap of a factor up to 3 remains. The altitude profiles and oxidation processes are further studied by using a zero-dimensional chemical box-model which is constrained by parameters measured by other instruments during the OMO campaign. Good agreement of OH and HO_2 is found between 7 km and 11.5 km, while below 7 km OH is overestimated by a factor of 2.5 and HO_2 is predicted correctly within the combined model-measurement uncertainty.

This result is consistent with the underestimation of the HO_2/OH ratio by up to a factor of 3 which is in agreement by the analytical model. Above 11.5 km both, OH and HO_2, are overestimated by a factor up to 2.5. In the HO_2/OH ratio however, this overestimation cancels out which indicates that there is either a missing HO_x termination reaction or an overestimated HO_x primary source in the model. The discrepancies observed in the upper and lower troposphere are finally addressed by sensitivity studies. In the lower troposphere these are most likely due to missing VOC reactivity, which primarily acts as an OH sink. The addition of a small amount of OH reactivity ($0.1\,{}^{1}/_{s}$) due to unmeasured VOCs during the OMO Asia campaign, closed the gap for OH, while HO_2 stayed in agreement. Only below 2 km a discrepancy of the HO_2/OH ratio by a factor up to 2.5 remained. In the upper troposphere there are indications, that formaldehyde from the EMAC MPIC model is overestimated, which results in a contemporaneous increase in OH and HO_2.

This work, in particular the correction necessary to the HO_2 channel, hints to further technical improvements for prospective LIF-aircraft applications.

Contents

Chapter 1

Introduction

The main constituents of the earth's atmosphere are nitrogen, oxygen and argon. They together make up over 99.9 % by volume (here and from now on mixing ratios are always with respect to volume) of dry air. Beside these permanent gases, which are homogeneously mixed in the lowest 100 km, the atmosphere contains a variable amount of water vapour that is mainly present in the lower troposphere. The other part of atmospheric air essentially consists of CO_2 (407 ppm) with minor additions of methane (1.8 ppm), molecular hydrogen and noble gases such as helium, neon and krypton whose mixing ratios are in the same range (Finlayson-Pitts and Jr., 2000). Reactive traces gases are present only in orders of magnitude smaller mixing ratios (ppb, ppt). While the bulk species oxygen and nitrogen can be photolized in the upper atmosphere by solar radiation and thereby engage in photochemistry, the influence of atmospheric traces gases on the living conditions on Earth is much broader. Greenhouse gases not only interact with solar, but also with terrestrial radiation and thereby affecting Earth's climate twofold. They either arise due to natural or anthropogenic emissions (e.g. CO_2, CH_4, N_2O, Chlorofluorocarbons) or by photochemical processes (e.g. ozone, organic aerosols, nitrate- and sulphate-aerosols). The strongest greenhouse gas is water vapour, which is affected implicitly via temperature variations and therefore promotes a self-enhancing feedback mechanism. Trace gases such as NO_x, CO, O_3, SO_2, HNO_3 and H_2SO_4 are toxic pollutants which deteriorate air quality (Finlayson-Pitts and Jr., 2000).

Since the industrial revolution started in 1750, many different trace gases have increased in atmospheric concentrations by a substantial amount due to increasing anthropogenic emissions. CO_2 levels have increased by 48 % up to today (2019) while they have been below 300 ppm for the last 3 million years prior. Similarly methane levels have been varying between 350 and 700 ppb in the past million years, but have risen to 1800 ppb up to today only since 1750 (Stocker and Qin, 2013). Today anthropogenic vs. natural methane sources are in ratio roughly 2:1. Natural emissions mainly stem from wetlands, termites and oceans while human sources are due to livestock, landfills, rice cultivation - in particular from the strongly growing Asian agricultural regions -, coal mining and biomass burning (Saunois et al., 2016). Both CO_2 and methane are major greenhouse gases that are drivers of climate change (Stocker and Qin, 2013). Apart from the impact on global climate, trace gases from industry and traffic – e.g. CO, NO_x, SO_2, ammonia and VOCs – lead to poor

air quality within cities, in particular also because it is coupled to photochemical ozone generation and thus smog events (Finlayson-Pitts and Jr., 2000). In addition, noxious trace gases can also originate from biomass burning and intense farming. Many of the emitted trace gases are not water soluble and have to undergo oxidation processes before they are eventually removed from the atmosphere (cf. Chapter 2). These oxidation processes are initiated by radicals which are highly reactive. The most prominent of all is the OH radical which together with the HO_2 radical builds the HO_x radical group. In this way for example CO is oxidized to CO_2 which is then washed out. Another example is the removal of NO_x: NO can react with O_3 to form NO_2. NO_2 then reacts with OH to form HNO_3, which will eventually deposit at ground.

Most radical measurements are ground based, but few measurements on aircraft have been around since 20 years, which however were mainly initiated by American groups (cf. Section 2.4.1). These campaigns prevalently concentrated on the Pacific, North-Atlantic and North-America whilst only very little took place in Europe, Middle East and the Asian Region. One reason has been the lack of an adequate research aircraft in Europe and Asia with intercontinental cruising range that could reach altitudes up to 15 km while still maintaining a decent payload to carry enough instruments for a sufficient coverage of atmospheric trace gases and radical measurements. With the introduction of the new German High Altitude and LOng range research aircraft (HALO) in 2009, a suitable measurement platform has become available to the German science community. HALO is run by the DLR and stationed in Oberpfaffenhofen (http://www.halo.dlr.de/).

During July/August 2015 HALO's first mission to study tropospheric photochemistry was the Oxidation Mechanism Observation (OMO) campaign over the Mediterranean Sea, the Arabian Peninsula, the Arabian Sea and the Indian Ocean, which set three major goals to understand the

1. Oxidation processes and the free radical chemistry of HO_x in the upper troposphere

2. Influence of the Asian Summer Monsoon on atmospheric chemistry

3. Long-distance transport of air pollution.

The first topic is subject of the present work. The chemistry of HO_x radicals in the upper troposphere during the Asian Summer Monsoon is investigated using corresponding measurements on board of HALO and a state-of-the-art chemical box model for interpretation. The radical measurements were performed by two laser-induced fluorescence (LIF) instruments - AirLIF (Forschungszentrum Jülich) and HORUS (Max-Planck Institute for Chemistry Mainz) -, which for the first time measured OH and HO_2 radicals contemporaneously at the Middle East and over the Indian Ocean west and east of India till the Maldives. The AirLIF instrument was developed at Forschungszentrum Jülich (institute IEK-8) with technical support from the Central Institute of Engineering, Electronics and Analytics (ZEA). The new instrument was tested in the laboratory for ground-based conditions by

Broch (2011), before the instrument was deployed on HALO for the first time during the OMO-EU test campaign in January 2015.

In the present work the OH and HO_2 measurement channels of the instrument have been characterized for the flight conditions during OMO. Different calibration concepts have been applied and combined to determine the OH and HO_2 detection sensitivities as a function of flight altitude, ambient pressure and temperature (cf. Chapter 4). These include ground-based calibrations between flights to track the absolute sensitivities. The relative dependence with altitude is measured in the laboratory using a newly designed photochemical radical source which allows calibration at reduced pressures to simulate ambient air pressure at flight conditions. Part of the calibration procedure includes the proper characterization of the calibration source itself. For the OH-channel there is the additional option to use an in-flight calibration unit inside the shrouded inlet. It is however limited in use to below 10 km, because it relies on ambient water vapour. To simulate the in-flight conditions, many groups have relied on using different nozzle sizes to change the mass-flow through the system instead of varying ambient pressure. As part of a consistency check, both methods will be compared in detail. For the proper application of the entire calibration procedure, possible interferences will be discussed and parametrized corrections will be applied if necessary.

Chapter 5 will give a brief introduction to the aims and the course of the campaign with participants and time schedule. This is followed by a description of the AirLIF radical measurements and - for the first time - an in-flight inter-comparison with flight-wise time series and a full campaign correlation. The vertical profile of OH and HO_2 up to 15 km will be discussed in particular also with respect to important atmospheric controlling parameters such as CO and NO. The HO_2/OH ratio will be analysed by a simple analytic approach. In the last part a zero dimensional chemical box model is advised with the attempt to predict OH, HO_2 and HO_2/OH, which are then compared to the in-flight measurements. After the discussion of the vertical model profiles, the most important radical sources and sinks are analysed in order to explain possible model gaps i.e. overestimation of radicals in the upper troposphere and near ground. Finally the measurement-model discrepancies are addressed via sensitivity runs.

Chapter 6 summarizes all the important results. Additional information to individual flight tracks and measurements during OMO, as well as model input and results can be found in the Appendix.

Chapter 2

Fundamentals of Tropospheric Chemistry

2.1 Atmospheric chemical composition

Dry atmospheric air consists mainly of nitrogen (78.1 %), oxygen (20.95 %) and argon (0.93 %). In addition the atmosphere contains a variable amount of water vapour (0–4 %). Even though these gases make up over 99.9 % of atmospheric air by volume, only the last per-mille of trace gases is responsible for air quality and climate change. These remaining trace gasses essentially consist of CO_2 (407 ppm) with minor additions of methane (1.8 ppm), molecular hydrogen (550 ppb) and noble gases such as helium (5.24 ppm), neon (18.18 ppm) and krypton (1.14 ppm) (Finlayson-Pitts and Jr., 2000). Reactive trace gasses such as CO, NO_x, ozone, VOCs and others are present only in even lower mixing ratios (ppb, ppt).

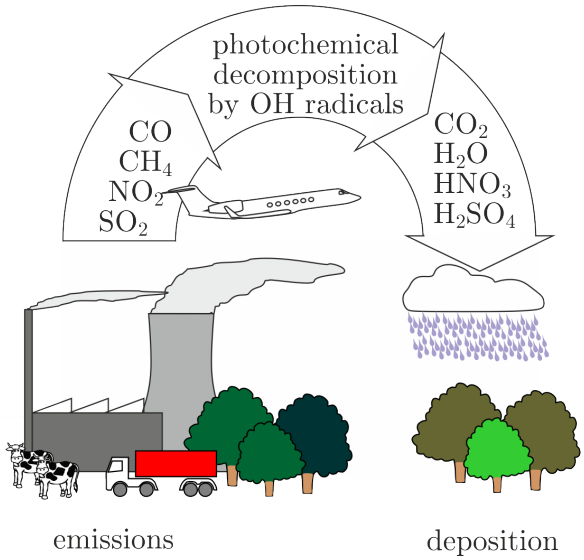

Figure 2.1: Hardly soluble substances are emitted by natural (lightning, volcanism), biogenic (land use) and anthropogenic (industry, traffic, energy production) activities. Initiation of oxidation due to reactions with OH radicals lead to better soluble substances which can then be washed out by rain. (Broch, 2011)

Most of the trace gases are emitted into the atmosphere and undergo chemical reactions including direct photolysis by solar radiation and reactions with photochemically formed oxidants like OH (hydroxyl radicals) and ozone. The reaction with OH controls in most cases the rate of atmospheric trace gas removal (Levy, 1972). This is of importance, because temperatures are typically too low for direct oxidation by oxygen to take place. Compounds which are destroyed photo-chemically are for example O_3 and NO_2, however in most cases solar photons carry too little energy, because short wavelengths below 300 nm are absorbed by ozone in the stratosphere.

Trace gases like CO, SO_2, NO_x (NO + NO_2) and VOCs are emitted by anthropogenic activities (traffic, industrial activities, energy production, biomass burning etc.) and natural processes (e.g. lightning, volcanism, cf. Figure 2.1). Furthermore, VOCs and methane are produced by the biosphere i.e. landfills, livestock farming and use of fossil fuel as well as naturally from wetlands, termites and oceans.

These trace gases are then attacked by OH which initiates oxidation chain-reactions whose stable products can be deposited dry or wet (Ehhalt, 1999). Photochemical oxidation involves the formation of OH primarily by the photolysis of ozone and reaction of $O(^1D)$ with water vapour (cf. Reaction R2 and R3). The oxidation of trace gases leads to secondary pollutants like HCHO, H_2O_2, HNO_3, H_2SO_4 and eventually particles by condensation of highly oxidized molecules which are transported and finally either dissolved in rain and washed out or taken up by plants (cf. Section 2.3).

On the one side OH radicals are relevant for the self-cleaning capacity of the atmosphere to remove primary pollutants, while on the other side the formation of these secondary pollutants can lead to significant air-quality issues particularly in densely populated areas with high emissions of contaminants like CO and NO_2. This can be seen in major cities like Beijing where large amounts of VOCs, NO_2 and sunlight lead to strong smog-events due to ozone (Chan and Yao, 2008).

Among others, H_2O, CO_2, CH_4, O_3 and N_2O are the major so called greenhouse gases ordered with respect to their significance as the drivers of the prevalent climate change (Stocker and Qin, 2013). Although water vapour is not primarily emitted in the conventional sense, warming due to CO_2 results in higher water vapour concentrations by increased saturation vapour pressure which leads to an amplifying feed back mechanism. Since methane is a greenhouse gas which is only degraded by OH, this indicates to the importance of OH. Its lifetime of roughly eight years, results in the relatively large methane levels of 1.8 ppm. Tropospheric Ozone - as a toxic greenhouse gas - is essentially created due to photo-chemical oxidation of CO and VOCs by OH (cf. Section 2.3.2).

2.2 Vertical structure of the atmosphere

The atmosphere has a layered structure which is depicted in Figure 2.2 (left panel) with dependencies of pressure and temperature on altitude. In general, the pressure decreases exponentially with height (barometric formula). The lower atmosphere is called the troposphere and is characterized by a linear temperature profile with a

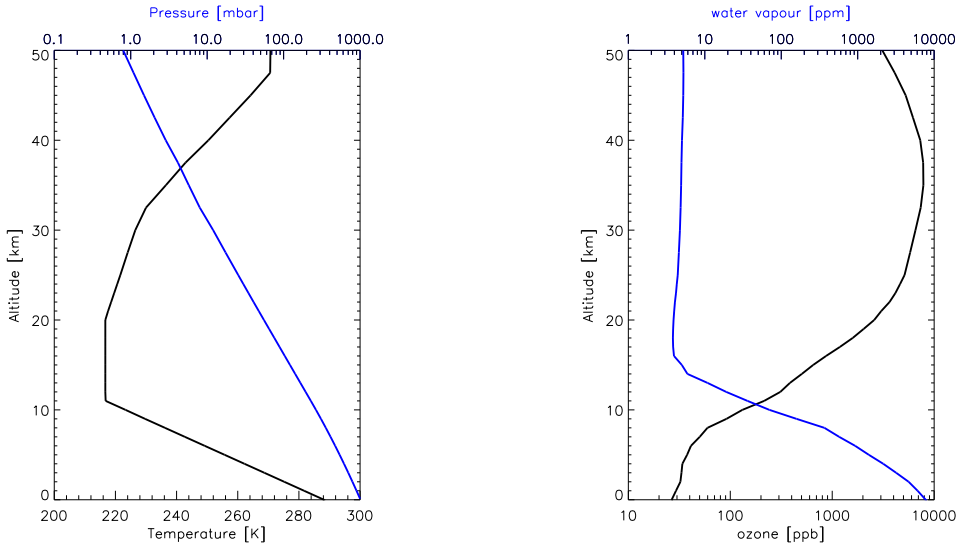

Figure 2.2: Left: Vertical profiles of temperature and pressure in the atmosphere between sea level (0 km) and 50 km altitude. The vertical course of the temperature gives rise to different atmospheric layers (troposphere, stratosphere, mesophere, ...) which are separated by reversal of the temperature gradient (Finlayson-Pitts and Jr., 2000). **Right:** Vertical profiles of water vapour and ozone in the atmosphere between ground (0 km) and 50 km altitude. Values are annual means for mid-latitudes (AFGL, 1986).

negative gradient called the *lapse rate* typically in the range of 5–10 $^{\circ}$C/km (the lower value applies to humid air, the higher value to dry air).

As the saturation vapour pressure of water follows Clausius-Clapeyron's equation, its mixing ratio will decrease nearly exponentially with altitude being ≈1 % near ground and ≈10 ppm at 13 km (cf. Figure 2.2, right panel). In contrast ozone mixing ratios are relatively low near ground (≈50 ppb) and increase slowly until 10 km. Above they quickly rise up to 10 ppm in the stratosphere where ozone is formed from O_2 photolysis. Global lower tropospheric ozone is strongly influenced by transport from higher altitudes for example during atmospheric inversion. Minor contributions also stem from the photo-chemical oxidation of CO and VOCs.

As solar radiation is driving the entire tropospheric chemistry (cf. Chapter 2.3), its vertical distribution must be known. Figure 2.3 shows an example of the vertical distribution of solar UV measured under cloud free conditions between 0 and 12 km height above the Aegean Sea. The shown wavelengths cover the range 298–420 nm where the most important photolysis reactions take place. As can be seen there is no strong dependence on altitude under cloud-free conditions in particular for the higher wavelength range.

Above the troposphere the temperature lapse rate gradually changes sign. This region called the tropopause is characterized in the *International Meteorological Vocabulary* of the *World Meteorological Organization* as the lowest level at which the lapse rate decreases to 2 $^{\circ}$C/km or less, provided that the average lapse rate between this level and all higher levels within 2 km does not exceed 2 $^{\circ}$C/km (Secretariat of the

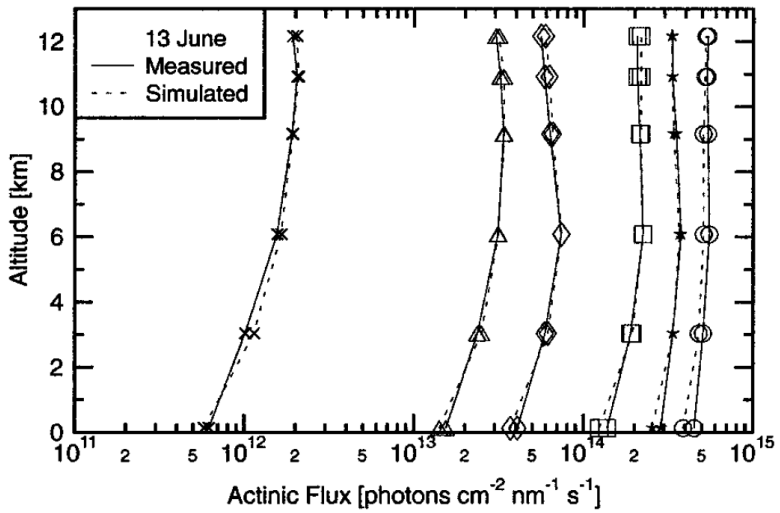

Figure 2.3: Actinic flux profile over the Aegean Sea under cloud-free conditions measured and simulated for different wavelengths. **crosses:** 298 nm, **triangles:** 305 nm, **diamonds:** 310 nm, **squares:** 325 nm, **stars:** 380 nm, **circles:** 420 nm (Hofzumahaus et al., 2002)

World Meteorological Organization, 1992). The focus of this subsequent work is mainly limited to the troposphere.

2.3 Tropospheric HO_x radical chemistry

2.3.1 OH sources

The OH radical plays an essential role in the degradation of various atmospheric trace gases. Its high reactivity results in very low concentrations of the order of $10^6/\mathrm{cm}^3$ (Finlayson-Pitts and Jr., 2000) though it is still capable to turn over large amounts of trace gases into their soluble products. The major global source of OH is the photolysis of ozone (O_3). The photo-dissociation of O_3 by solar radiation yields $O(^3P)$ atoms at wavelengths below 1180 nm and electronically excited $O(^1D)$ atoms at wavelengths below 340 nm (Takahashi et al., 2002)

$$\mathrm{O_3} + h\nu \longrightarrow \mathrm{O}(^3\mathrm{P}) + \mathrm{O_2}\left(X^3\Sigma_g^-\right) \qquad \lambda < 1180\,\mathrm{nm} \qquad \text{(R1)}$$

$$\mathrm{O_3} + h\nu \longrightarrow \mathrm{O}(^1\mathrm{D}) + \mathrm{O_2}\left(a^1\Delta_g\right) \qquad \lambda < 340\,\mathrm{nm}\,. \qquad \text{(R2)}$$

The reaction of $O(^1D)$ atoms with water vapour yields OH

$$\mathrm{O}(^1\mathrm{D}) + \mathrm{H_2O} \longrightarrow 2\,\mathrm{OH}\,. \qquad \text{(R3)}$$

Besides Reaction R3 $O(^1D)$ can also lose its energy via collisions with ambient molecules (N_2, O_2) which is referred to as quenching. $O(^3P)$ then reacts back to ozone

$$\mathrm{O}(^1\mathrm{D}) + \mathrm{M} \longrightarrow \mathrm{O}(^3\mathrm{P}) + \mathrm{M} \qquad \text{(R4)}$$

$$\mathrm{O}(^3\mathrm{P}) + \mathrm{O_2} + \mathrm{M} \longrightarrow \mathrm{O_3} + \mathrm{M}\,. \qquad \text{(R5)}$$

For Reactions R2 - R5, the rate equations for $O(^1D)$ and OH can be written as

$$\frac{\mathrm{d}\,[\mathrm{O}(^1\mathrm{D})]}{\mathrm{d}t} = \underbrace{j(\mathrm{O}^1\mathrm{D})\,[\mathrm{O}_3]}_{\text{production}} \underbrace{- \left(k_{\mathrm{O}(^1\mathrm{D})+\mathrm{N}_2}\,[\mathrm{N}_2] + k_{\mathrm{O}(^1\mathrm{D})+\mathrm{O}_2}\,[\mathrm{O}_2] + k_{\mathrm{O}(^1\mathrm{D})+\mathrm{H}_2\mathrm{O}}\,[\mathrm{H}_2\mathrm{O}]\right)\left[\mathrm{O}(^1\mathrm{D})\right]}_{\text{destruction}} \quad (2.1)$$

$$\frac{\mathrm{d}\,[\mathrm{OH}]}{\mathrm{d}t} = 2\,k_{\mathrm{O}(^1\mathrm{D})+\mathrm{H}_2\mathrm{O}}\,[\mathrm{H}_2\mathrm{O}]\left[\mathrm{O}(^1\mathrm{D})\right] \equiv P_{\mathrm{OH},\mathrm{O}_3} \quad (2.2)$$

where $P_{\mathrm{OH},\mathrm{O}_3}$ is the production rate of OH and $j(\mathrm{O}^1\mathrm{D})$ is called the photolysis frequency for $O(^1D)$ and can be calculated from the photon-flux F_λ (also called actinic radiation [$^{\text{photons}}/_{\text{cm}^2\,\text{s}\,\text{nm}}$]), the absorption cross-section σ ([cm^2]) and the quantum yield Φ of O^1D (Matsumi et al., 2002)

$$j(\mathrm{O}^1\mathrm{D}) = \int_\lambda \Phi_{\mathrm{O}^1\mathrm{D}}(\lambda, T)\,\sigma_{\mathrm{O}_3}(\lambda, T)\,I_\lambda(\lambda)\,\mathrm{d}\lambda\,. \quad (2.3)$$

The rate constants k_i for Reactions R3 and R4 are given in Table 2.1. For typical

Table 2.1: Rate constants for the reaction of major air constituents (N_2, O_2, H_2O) with $O(^1D)$.

R#	reaction i	k_i [$^{\text{cm}^3}/_{\text{s}}$]	source
R4	$O^1D + N_2$	$2.15 \cdot 10^{-11}\ \exp\left(\frac{110\,\text{K}}{T}\right)$	JPL (2015)
R4	$O^1D + O_2$	$3.95 \cdot 10^{-11}\ \exp\left(\frac{55\,\text{K}}{T}\right)$	JPL (2015)
R3	$O^1D + H_2O$	$1.63 \cdot 10^{-10}\ \exp\left(\frac{60\,\text{K}}{T}\right)$	JPL (2015)

pressures in the troposphere between 200 and 1000 hPa the $O(^1D)$ lifetime is of the order of nano-seconds (given by the part in the round bracket of the destruction term). Therefore it is sufficient to approximate Equation 2.1 by its steady state value $\frac{\mathrm{d}[\mathrm{O}(^1\mathrm{D})]}{\mathrm{d}t} \approx 0$. Plugging this into Equation 2.2 gives a production rate of OH due to the photolysis of ozone given by

$$P_{\mathrm{OH},\mathrm{O}_3} = 2\,j(\mathrm{O}^1\mathrm{D})\,[\mathrm{O}_3]\;\Phi_{\mathrm{OH}} \quad (2.4)$$

with the branching ratio

$$\Phi_{\mathrm{OH}} = \frac{k_{\mathrm{O}(^1\mathrm{D})+\mathrm{H}_2\mathrm{O}}\,[\mathrm{H}_2\mathrm{O}]}{k_{\mathrm{O}(^1\mathrm{D})+\mathrm{N}_2}\,[\mathrm{N}_2] + k_{\mathrm{O}(^1\mathrm{D})+\mathrm{O}_2}\,[\mathrm{O}_2] + k_{\mathrm{O}(^1\mathrm{D})+\mathrm{H}_2\mathrm{O}}\,[\mathrm{H}_2\mathrm{O}]}\,. \quad (2.5)$$

Obviously this quantity is independent of the number density of ambient air and can as well be written solely in terms of mixing ratios. For 1 % of water vapour, for example, it gives a yield of 7 %. As water vapour decreases exponentially with altitude, also the yield follows accordingly, being only 0.01 % at 13 km.

In the polluted atmosphere, photolysis of nitrous acid (HONO) is another important source of OH. This process takes place at wavelengths below 390 nm.

$$\mathrm{HONO} + h\nu \quad \longrightarrow \quad \mathrm{OH} + \mathrm{NO} \qquad\qquad \lambda < 390\,\text{nm}. \quad (\mathrm{R6})$$

Significant concentrations however have been only observed in the planetary boundary layer (PBL), with highest values near the ground (Li et al., 2014). Small amounts are produced by the pressure dependent reaction

$$\mathrm{OH + NO + M \quad \longrightarrow \quad HONO + M\,,} \tag{R7}$$

while most is produced heterogeneously at the Earth's surface. Due to the relatively short lifetime with respect to photolysis, HONO produced in the PBL does not reach the free troposphere, because transport times are usually of the order of a week.

Another significant contribution to OH production can be the ozonolysis of alkenes. Ozone adds to the alkene double bond to create an intermediate ozonide which is unstable and subsequently breaks into a carbonyl oxide (Criegee) and a carbonyl-compound. The OH molecule is eventually attained by further re-arrangements involving H-shifts on the Criegee, followed by a final decomposition. The production depends on the alkene and typically larger alkenes produce more OH. On the other hand most of these alkenes react strongly with OH itself which limits the importance of this pathway to night-times where the other sources do not play a role (Bey et al., 2001). Since most alkenes are short-lived they as well seldomly arrive at the free troposphere.

2.3.2 Degradation of trace gases by OH

Most reactive trace gases in the atmosphere are degraded by OH. In case of CO and VOC oxidation, peroxy-radicals are formed which can regenerate OH by reaction with NO. One of the most important reaction is the degradation of CO

$$\mathrm{CO + OH \quad \xrightarrow{O_2} \quad CO_2 + HO_2\,,} \tag{R8}$$

producing a hydro-peroxy radical HO_2. OH also attacks methane forming an organic peroxy radical CH_3O_2 which by reaction with NO eventually forms HO_2 and formaldehyde

$$\begin{aligned}
\mathrm{CH_4 + OH} &\xrightarrow{\mathrm{O_2,M}} \mathrm{CH_3O_2 + H_2O} && \text{(R9)}\\
\mathrm{CH_3O_2 + NO} &\longrightarrow \mathrm{CH_3O + NO_2} && \text{(R10)}\\
\mathrm{CH_3O + O_2} &\longrightarrow \mathrm{HCHO + HO_2\,.} && \text{(R11)}
\end{aligned}$$

In a similar way this is true for a general class of volatile organic compounds (VOC)

$$\begin{aligned}
\mathrm{RH + OH} &\xrightarrow{\mathrm{O_2}} \mathrm{RO_2 + H_2O} && \text{(R12)}\\
\mathrm{RO_2 + NO} &\longrightarrow \mathrm{RO + NO_2} && \text{(R13)}\\
\mathrm{RO + O_2} &\longrightarrow \mathrm{R'CHO + HO_2} && \text{(R14)}
\end{aligned}$$

eventually producing HO_2 and an aldehyde (or ketone). The rate determining step in the degradation of trace gases is the reaction with OH. In Reactions R9 - R11 for example, the reaction of methane with OH proceeds over the order of 8 years while the subsequent reactions are very fast compared to the former.

As do the peroxy radicals above, also HO_2 will react with NO which finally regenerates OH and at the same time forms NO_2

$$NO + HO_2 \longrightarrow NO_2 + OH\,. \tag{R15}$$

The OH-recycling has a stabilizing effect on the OH-concentration and leads to an efficient trace gas removal mechanism. As a result of the interconversion between OH and HO_2, both radicals are collectively referred to as HO_x (= OH + HO_2).
Since the OH radical is highly reactive with a lifetime of only a second at ground conditions, its concentration is small and of the order $10^6/cm^3$. Since transport processes are on the scale of a few metres per second the concentration is only dependent on the local concentrations of the reactive species.
In competition to NO, HO_2 also reacts with ozone

$$HO_2 + O_3 \longrightarrow OH + 2O_2 \tag{R16}$$

but for typical ambient ozone and NO mixing ratios over continental Europe of 40 ppb and $\gg$ 10 ppt respectively, Reaction R15 is faster than Reaction R16 by a factor of more than 4000 (Atkinson et al., 2004). In clean air with NO concentrations <10 ppt Reaction R16 starts to dominate though.

The degradation of NO by HO_2 is not the only pathway, in fact it can also react with ozone

$$NO + O_3 \longrightarrow NO_2 + O_2\,. \tag{R17}$$

During daytime NO_2 can photolyse back to NO to produce ozone which is indeed the major production process within the lower troposphere

$$NO_2 + h\nu \longrightarrow O(^3P) + NO \qquad \lambda < 420\,\text{nm} \tag{R18}$$

$$O(^3P) + O_2 + M \longrightarrow O_3 + M \qquad M = N_2, O_2\,. \tag{R19}$$

If Reaction R17 would be the only NO_2 production process, every O_3 produced by R18 and R19 would have been consumed in Reaction R17 and the combined process would be neutral with respect to ozone. However Reaction R15 and R13 and likewise anthropogenic and biogenic emissions act as a source to NO_2 and give rise to a net ozone formation (Ehhalt, 1999). On the contrary there is loss in ozone with a lack of NO_x, because then HO_2 mainly destroys ozone by Reaction R16 without producing NO_2. A simple expression can be given for the number of ozone molecules produced per turned over HO_2 molecule involved

$$\frac{\Delta O_3}{\Delta HO_2} \approx \frac{k_{R15}\,[NO] - k_{R16}\,[O_3]}{k_{R15}\,[NO] + k_{R16}\,[O_3]}\,. \tag{2.6}$$

From this result the 10 ppt threshold for NO can be approximated (Carpenter et al., 1997).
Oxidation products in the VOC degradation process like formaldehyde (HCHO) in Reaction R11 can again contribute to the HO_x concentration

$$HCHO + OH \xrightarrow{O_2} HO_2 + CO + H_2O \tag{R20}$$

$$HCHO + h\nu \longrightarrow H_2 + CO \qquad \lambda < 360\,\text{nm} \tag{R21}$$

$$HCHO + h\nu \xrightarrow{O_2} 2\,HO_2 + CO \qquad \lambda < 335\,\text{nm}\,. \tag{R22}$$

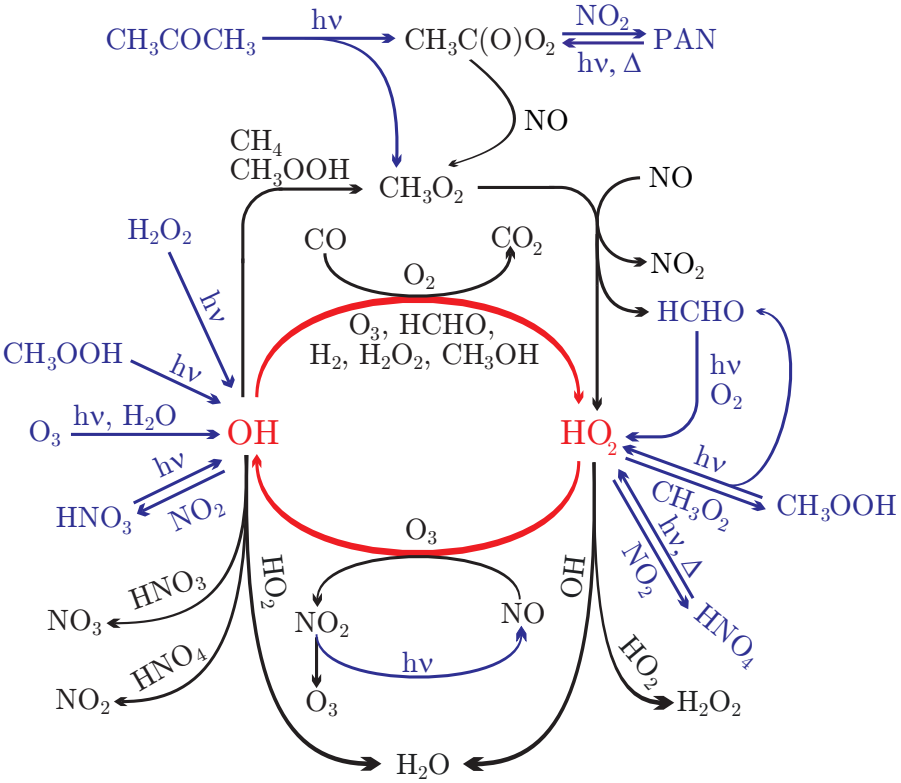

Figure 2.4: Simplified scheme of the HO_x cycle (red) relevant for upper tropospheric conditions. The blue arrows show the sources contributing by photolysis.

The first and second reaction are neutral with respect to the HO_x concentration while the last one contributes with 2 HO_2 radicals. Effectively about 0.3 HO_x radicals are formed per degraded methane molecule (Ehhalt, 1999).

2.3.3 Radical sinks

The above mentioned reactions of OH with CO, CH_4, RH and HCHO produce peroxy radicals (HO_2, RO_2) which regenerate OH by reaction with NO. This radical cycle can be terminated by radical-radical reactions, which eliminate HO_x radicals from the atmosphere.

$$\begin{aligned}
OH + OH &\longrightarrow H_2O + O && \text{(R23)}\\
OH + HO_2 &\longrightarrow H_2O + O_2 && \text{(R24)}\\
HO_2 + HO_2 \quad (+H_2O) &\longrightarrow H_2O_2 + O_2 \quad (+H_2O) && \text{(R25)}\\
RO_2 + HO_2 &\longrightarrow ROOH + O_2 && \text{(R26)}\\
RO_2 + RO_2 &\longrightarrow \text{products}\,. && \text{(R27)}
\end{aligned}$$

Because of the small OH concentration, Reaction R23 and R24 play a negligible role, whereas Reaction R25 and R26 can be of significant magnitude. Another important radical loss process is

$$OH + NO_2 + M \longrightarrow HNO_3 + M \qquad M = N_2, O_2\,. \qquad \text{(R28)}$$

In a similar manner, HO_2 reacts with NO_2 forming HNO_4

$$HO_2 + NO_2 + M \longrightarrow HNO_4 + M\,. \tag{R29}$$

Nevertheless in warm air (298 K), it is thermally unstable and decomposes back within seconds

$$HNO_4 + M \xrightarrow{\Delta} HO_2 + NO_2 + M\,. \tag{R30}$$

In the lower troposphere, the products of Reactions R25 - R28 are generally lost by deposition. In the upper troposphere, loss by deposition is generally slow and some components like HNO_4 are thermally stable at low temperatures. Due to the extended lifetime, the product species can be considered as reservoir species of radicals and NO_x in the free troposphere.

2.3.4 HO_x chemistry in the upper troposphere

In the previous chapters the main focus applied to atmospheric chemistry in the lower troposphere. In the upper troposphere however, there are several obvious differences.

1. Physical conditions

   - **Pressure:** With increasing altitude the pressure drops exponentially according to the barometric formula. Since lower pressure means a decreased collision rate, this slows down the overall chemistry quadratically. While the lifetime of OH is roughly 1 s near ground, it will increase to about 1 min at 13 km altitude. There are also pressure dependent rate-constants for some reactions (e.g. OH + CO, OH + NO_2).
   - **Temperature:** In the adiabatic atmosphere approximation, the temperature decreases linearly with altitude which in most cases reduces the rate-constants additionally. A prominent example for such a change due to temperature is the NO_2 to NO ratio following from Equation R17 - R18

     $$\frac{[NO_2]}{[NO]} \approx \frac{k_{R17}\,[O_3]}{j_{R18}} \tag{2.7}$$

     which at ground has approximately a value of 3 to 5. As the ozone concentration increases by roughly a factor of 2 from ground to 13 km and additionally the rate constant reduces about a factor of 10 due to temperature, the ratio reverses its behaviour at higher altitudes and consequently also HO_2 is progressively suppressed.
   - **Humidity:** The saturation vapour pressure follows Clausius-Clapeyron's equation. Thus water vapour mixing-ratios will decrease nearly exponentially which affects the primary HO_x production by over three orders of magnitude (cf. Reaction R3).

2. Photochemical products like H_2O_2, CH_3OOH, HNO_3 or HNO_4 are only slowly removed by transport and represent reservoir species. The deposition proceeds by slow downward movement of air-masses on bigger scales and typically takes several days. If available, uptake in cloud droplets can be fast however, while in the presence of sunlight radicals and NO_x are reactivated

$$\begin{aligned}
HNO_3 + h\nu &\longrightarrow OH + NO_2 \qquad \lambda < 350\,\text{nm} && \text{(R31)}\\
H_2O_2 + h\nu &\longrightarrow OH + OH \qquad \lambda < 557\,\text{nm} && \text{(R32)}\\
ROOH + h\nu &\xrightarrow{O_2} R'CHO + OH + HO_2 && \text{(R33)}\\
&\xrightarrow{O_2} RO_2 + HO_2 && \text{(R34)}\\
HNO_4 + h\nu &\longrightarrow HO_2 + NO_2 \qquad \lambda < 325\,\text{nm}\,. && \text{(R35)}
\end{aligned}$$

   All of these compounds constitute an additional OH sink viz

$$\begin{aligned}
H_2O_2 + OH &\longrightarrow HO_2 + H_2O && \text{(R36)}\\
CH_3OOH + OH &\longrightarrow CH_3O_2 + H_2O && \text{(R37)}\\
HNO_3 + OH &\longrightarrow NO_3 + H_2O && \text{(R38)}\\
HNO_4 + OH &\longrightarrow NO_2 + O_2 + H_2O\,. && \text{(R39)}
\end{aligned}$$

3. Most of the short lived pollutants emitted at ground do not reach the upper troposphere, as the transport time to the latter is of the order 10 days (Jacob et al., 1997). From this it is expected, that the general chemistry will be more simple compared to ground, where lots of different VOCs and other biogenic compounds make the chemistry rather complex. Nevertheless, deep convection plays a significant role in the tropics, where convective injections of peroxides (H_2O_2, CH_3OOH) perturb the typically simple chemistry (Jaegle et al., 1997). Similarly fast vertical transport of acetone can play an important role, as photo-chemically excited acetone can decompose prior to quenching at higher altitudes (Wennberg et al., 1998).

   Deep convection also plays a role in the Asian Monsoon with transport times less than one hour. The impact of such events on the global atmospheric composition and climate is still an unsolved problem and currently investigated (Lelieveld et al., 2018; Gottschaldt et al., 2018; Vogel et al., 2016).

Due to the low pressure, acetone can become an important source of HO_x contrary to ground chemistry where photolised acetone typically quenches prior to fragmentation

$$\begin{aligned}
CH_3COCH_3 + h\nu &\xrightarrow{2O_2} CH_3C(O)O_2 + CH_3O_2 && \text{(R40)}\\
CH_3C(O)O_2 + NO &\xrightarrow{O_2} CH_3O_2 + CO_2 + NO_2\,. && \text{(R41)}
\end{aligned}$$

The acetyl-peroxy radical can be converted to a methyl-peroxy-radical in the presence of NO which subsequently contributes to HO_x via Reaction R10 and R11. Under cold conditions in the upper troposphere, more likely though is the addition of NO_2 to form PAN

$$CH_3C(O)O_2 + NO_2 \xrightarrow{M} CH_3C(O)O_2NO_2\,. \qquad \text{(R42)}$$

It is another reservoir species, which can be photolysed back or decompose thermally in the lower troposphere in warmer air

$$\mathrm{PAN} \quad \xrightarrow{h\nu,\Delta} \quad \mathrm{CH_3C(O)O_2} + \mathrm{NO_2}\,. \tag{R43}$$

2.4 HO_x chemistry studies on aircraft

2.4.1 Aircraft campaigns

There are significantly fewer studies on the chemistry of the free troposphere compared to investigations on the ground. First highly sensitive and reliable measurements of tropospheric OH and HO_2 radical concentrations were reported from ground-based field campaigns in the early 1990's using LIF at 308 nm excitation wavelength, CIMS and DOAS techniques (Heard and Pilling, 2003).

First airborne measurements were achieved in the upper troposphere and lower stratosphere (6-21 km) in the STRAT campaign 1995/96 by LIF using 282 nm excitation wavelengths on board of the NASA aircraft ER-2 (Jaegle et al., 1997). The application of 282 nm was not an issue as discussed earlier, because almost no water vapour is present at these altitudes to interfere.

In 1995 first ventures were done by F. Eisele (Mauldin III et al., 1998) during the ACE-1 campaign on board the NCAR C-130 to address the lower troposphere (0-6 km) measuring HO_x radicals with the CIMS (*chemical ionization mass-spectrometer*). Other measurements using CIMS were done by Cantrell et al. during the TRACE-P campaign on a P-3B (Cantrell et al., 2003a). Brune et al. (Brune et al., 1998) measured HO_x radicals using LIF (called ATHOS, 308 nm) during the SUCCESS campaign which eventually covered the troposphere up to 12 km on-board the NASA DC-8 aircraft. Their second campaign (SONEX) using LIF (308 nm) dates back to 2000, again on the NASA DC-8 (Faloona et al., 2000).

Tropospheric US research air-crafts (DC-8, P-3B, C-130) have been used since then for many more airborne missions that took place mainly over North America, the North Atlantic Ocean, the Arctic and the Pacific Ocean e.g. (Olson et al., 2006), (Jaegle et al., 2001). The US aircraft have generally high scientific payloads (6-15 tons) that allow to carry a large suite of instruments for the measurement of HO_x and other trace gases. Nevertheless they lack the capacity to reach altitudes above 12 km. First airborne radical measurements of OH and HO_2 by European research groups were performed by the Max-Planck Institute Mainz (MPIC) measuring HO_x with LIF (called HORUS, 308 nm) on a Learjet 35A (< 10 km) in the GABRIEL campaign over the Amazonian rainforest in Suriname 2005 (Martinez et al., 2010) and in the HOOVER campaign over Europe 2007 (Regelin et al., 2013). Around the same time, the university of Leeds measured HO_x with LIF (308 nm) on a BAe 146-300 aircraft (< 10 km) in the AMMA campaign 2006 above West Africa (Stone et al., 2010).

In Germany and Europe, there was for a long time a general lack for a large tropospheric research aircraft. Since 2009 the German research aircraft HALO - a modified Gulfstream G550 - is available for global atmospheric research that allows to perform flights over large, intercontinental distances and that can reach high altitudes (up to 15 km). It has enabled to perform first HO_x measurements in the troposphere up to 15 km altitude by two LIF (308 nm) instruments (FZJ, MPIC) during the OMO mission 2015 between the Eastern Mediterranean and the Indian Ocean (this work).

2.4.2 HALO

The general need for a high-flying long-range tropospheric aircraft gave rise to the HALO consortium which consists of the DFG (*Deutsche Forschungsgemeinschaft*) representing the German universities and the six German research centres which comprise the research centres in the Helmholtz Association (Helmholtz-Gemeinschaft; HGF) and the institutes of the Max Planck Society (Max-Planck-Gesellschaft; MPG) as the main users besides the DLR. The aim was to modify a Gulfstream G550 business jet for use as a research aircraft.

Table 2.2: Technical details for the research aircraft HALO. (DLR, 2009)

dimensions airplane	
length	29.4 m
height	7.9 m
wing-span	28.5 m
# inlets	23
# viewports	6
dimensions cabine	
length	15.3 m
height	1.88 m
width	2.24 m
volume	47.3 m^3
flight characteristics	
max. cruising altitude	15 545 m
mean cruising altitude	13 100 m
max. aircraft speed	0.885 Ma
cruising range at 0.8 Ma	12 500 km
max. payload	3000 kg
elect. power supply for scientific instruments	55 kW

HALO is run by the DLR and stationed in Oberpfaffenhofen near Munich since 24th of January 2009. It is deployed to study various atmospheric and meteorological phenomena from local to global scales such as atmospheric self cleaning, chemistry

Figure 2.5: Research aircraft HALO during landing at DLR Oberpfaffenhofen. (DLR, 2009)

and dynamics of the upper troposphere and lower stratosphere, but also general weather and climate change. As the name stands, HALO is capable to fly over 15 km reaching the tropopause at the equator and even surpassing it at mid-latitudes. Some technical details of the airplane are given in Table 2.2. During August/September 2015 it was deployed on Cyprus and Gan (Maldives) for the purpose of the OMO campaign (*Oxidation Mechanism Observation*). The instrumental set-up for the application of the AirLIF on HALO had to be modified compared to the well-established ground based instruments (cf. Chapter 3).

Chapter 3

HO_X Measurement Instrument

3.1 OH detection by laser induced fluorescence

The laser induced fluorescence technique (LIF) was first reported by the Zare group as a selective method for spectroscopic detection of molecules by narrow-bandwidth lasers (Tango et al., 1968). First LIF studies on OH radicals were performed in the early 1970s in the laboratory (Hogan and Davis, 1974; Becker et al., 1974) using tunable dye lasers which had been invented 1967 (Sorokin et al., 1967; Schaefer and Schmidt, 1967). First attempts to measure OH radicals by LIF in the atmosphere were performed at the Ford Motor Company in Michigan, USA (Baardsen and Terhune, 1972; Wang and Davis, 1974) using pulsed laser radiation for excitation at a characteristic absorption line at 282 nm. The excited molecules radiate by spontaneous emission called fluorescence whose photons are detected by a photomultiplier. Since ambient air is composited of various substances, it is important not to choose a wavelength which would in addition excite another molecule as well leading to unwanted cross-interference. Figure 3.1 shows a scheme of a variety of transitions of the OH radical from the electronic ground state $X^2\Pi$ to the first excited state $A^2\Sigma^+$. Each electronic state has several vibrational states with different mode numbers $v = 0, 1, 2, ...$ with energy-differences being small compared to the electronic ground and first exited state. Likewise a rotational quantum number N splits each vibrational state into sub-states whose energy-differences again are in magnitude much smaller than those of the different vibrational states. The notation using a double prime next to a quantum number refers to the electronic ground state, while one prime corresponds to the excited state. The electronic A-X transition of OH has two strong vibrational bands, the 1-0 and 0-0 bands, which can be used for highly sensitive OH detection (Figure 3.1). The 1-0 band is located at 282 nm, the 0-0 band at 308 nm. When a selected rotational state in OH $(A, v' = 1)$ is excited, the populated rotational state redistributes over the different rotational states of the $v' = 1$ vibrational band due to collisions with the ambient molecules within a few nano-seconds at atmospheric pressure. This is called rotational relaxation (RR). The rate constants for rotational relaxation are faster than for electronic quenching, in case of nitrogen as collision partner by a factor of 10 (Lengel and Crosley, 1977). Similarly vibrational relaxation (VR) redistributes into the $v' = 0$ band towards thermal equilibrium before going back into the electronic ground state via emission of a photon. The rate constant for vibrational relaxation ($v' = 1 \rightarrow 0$) is 3 times

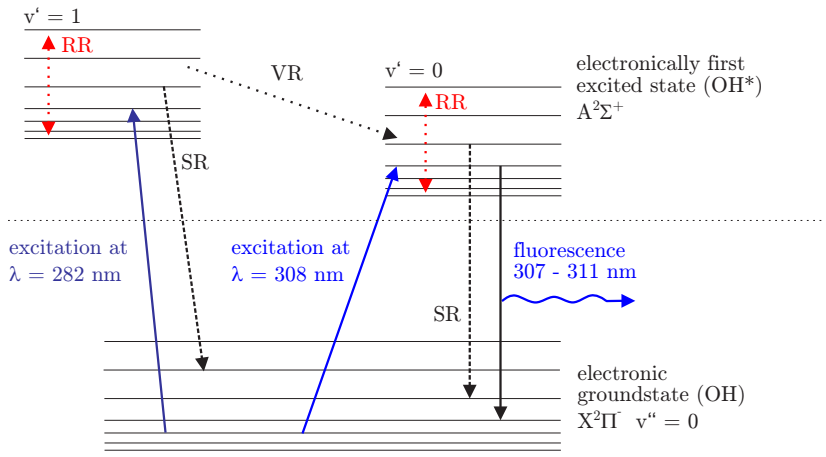

Figure 3.1: Simplified scheme with various absorption lines from the electronic ground state (underneath the dashed line) to the first excited state (above). The shown electronic ground state has vibrational quantum number $v'' = 0$. In the first electronically excited state the vibrational ground state $v' = 0$ is at the right side with excitation wavelength of 308 nm whereas the vibrationally first excited state $v' = 1$ is seen at the left with excitation wavelength 282 nm. (Broch, 2011)

faster than for electronic quenching (Lengel and Crosley, 1978) and roughly 30 % of the molecules in the $v' = 1$ band choose this path. The other 70 % return to the electronic ground state either by fluorescence (282 nm) or collisional quenching. Therefore when OH is excited at 282 nm, fluorescence can be observed at 282 nm and 308 nm. For OH detection, this excitation scheme has the advantage that fluorescence at 308 nm can be easily separated by an optical interference filter from scattered laser light at 282 nm. Such a simple optical discrimination between laser and fluorescence wavelengths is not possible, when 308 nm is used for excitation. For these reasons, first measurements of atmospheric OH used the 282 nm excitation scheme (Wang and Davis, 1974; Davis et al., 1976). However, soon it was discovered that OH measurements at ambient pressure and 282 nm excitation artificially produce OH by laser photolysis of ozone (cf. Reaction R2, R3) in higher than ambient concentrations (Wang et al., 1976; Davis et al., 1981).

In 1984 Hard and O'Brien (Hard et al., 1984) presented a modified version of the LIF OH detection system which they termed FAGE (Fluorescence Assay by Gas Expansion). In this set-up the air is sampled through a critical orifice into a low pressure region - called detection cell - where OH is eventually detected by LIF. FAGE has a few systematic advantages over the conventional LIF at that time. The decreased pressure in the cell (typically a factor 100) reduces the amount of ozone generated interference drastically, which however as it turned out was still enough of a problem when 282 nm was used (Crosley and Smith, 1990). Only the introduction of 308 nm LIF FAGE would finally lead to the long sought after breakthrough that managed to measure lower tropospheric OH to a large extent without the problematic interferences (Stevens et al., 1994; Holland et al., 1995). At the same time interference-free measurements have succeeded in the stratosphere using 282 nm, since the very low water vapour concentration works in favour in diminishing artificial OH generation (Wennberg et al., 1994).

Using 308 nm over 282 nm has the additional advantage, that the ozone absorption cross-section is greatly reduced by a factor of 30, while the OH absorption cross-section is increased by a factor of 4. Obviously the reduced pressure also lowers the amount of OH radicals that are quenched to the ground state instead of fluorescing.

3.2 OH measurement principle

The excitation spectrum of the OH radical schemed in Figure 3.1 has strong absorption lines within the $A^2\Sigma$-$X^2\Pi(0,0)$-band at 308 nm. The de-excitation can take place via emission of a photon or by collisional deactivation. The corresponding lifetime τ is calculated from

$$\frac{1}{\tau} = \frac{1}{\tau_{\mathrm{rad}}} + \sum_i k_i^{\mathrm{cd}} \, [\mathrm{M}_i] \tag{3.1}$$

where

- τ_{rad}: natural radiative lifetime of the OH radical (688 ns, (German, 1975)) often expressed by the Einstein coefficient $A = \tau_{\mathrm{rad}}^{-1}$ of spontaneous emission.
- k_i^{cd}: rate constant for collisional deactivation by air molecules $[^{\mathrm{cm}^3}/_{\mathrm{s}}]$ ($i = \mathrm{N}_2, \mathrm{O}_2, \mathrm{H}_2\mathrm{O}$)
- $[\mathrm{M}_i]$: number density of air constituent i $[^{\mathrm{molec}}/_{\mathrm{cm}^3}]$.

The radiative lifetime and the quenching constants of excited OH ($A, v' = 0$) depend on the rotational quantum state (McDermid and Laudenslager, 1982). The effective lifetime of excited OH therefore depends on the rotational distribution in $v' = 0$, which undergoes rotational relaxation after laser excitation. In practice (see further below), the OH fluorescence is collected with some time delay which is usually sufficient for relaxation to a thermal rotational distribution in $v' = 0$. This redistribution pattern will however be the same for all measurements as long as the air temperature is constant and it is thus reasonable to use such measured effective values instead. For the major constituents of air - N_2, O_2 and $\mathrm{H}_2\mathrm{O}$ - the effective rate constants for quenching under thermalized conditions are given in Table 3.1.

The rate equation for the excited radicals OH^* reads

$$\frac{\mathrm{d}}{\mathrm{d}t} [\mathrm{OH}^*] = -\left(A + k_q \, [\mathrm{M}]\right) [\mathrm{OH}^*] \, , \tag{3.2}$$

with the solution $[\mathrm{OH}^*] = [\mathrm{OH}^*]_0 \exp\left[-\left(A + k_q \, [\mathrm{M}]\right) t\right]$. Here k_q is short-hand for the mean quenching rate constant $\sum_i x_i \, k_i^{\mathrm{cd}}$ where x_i is the mixing ratio of the i-th gas constituent. The rate equation expresses the change of the number of excited OH radicals per volume and time with contribution due to quenching and by natural emission. The time-dependent fluorescence intensity after excitation can be expressed as the number of photons (γ) per volume and time emitted isotropically in any direction

$$\frac{\mathrm{d}}{\mathrm{d}t} [\gamma] = +A \, [\mathrm{OH}^*] \, . \tag{3.3}$$

Table 3.1: Effective rate constants for collisional deactivation of excited rotationally thermalized OH radicals in the state $A^2\Sigma^+(0)$ at 293 K for the major components of air. (Heard and Henderson, 2000)

Gas i	Quenching Constant $[1 \times 10^{-11}\,\mathrm{cm^3/s}]$
N_2	3.14 ± 0.1
O_2	14.1 ± 0.4
H_2O	66.7 ± 0.5

Counting the photons within a time-interval $[\Delta T_C, \Delta T_C + T_C]$ using the solution above, it follows

$$[\gamma] = [\mathrm{OH}^*]_0 \underbrace{\frac{A}{A + k_q\,[\mathrm{M}]} \left\{\exp\left[-\left(A + k_q\,[\mathrm{M}]\right)\Delta T_C\right] - \exp\left[-\left(A + k_q\,[\mathrm{M}]\right)\left(\Delta T_C + T_C\right)\right]\right\}}_{\eta(\Delta T_C)} . \tag{3.4}$$

This quantity is directly proportional to the measured signal if the detection volume, the solid angle of the detection volume seen by the detector and the efficiency of the photon detection system is known (Broch, 2011). The last two factors in Equation 3.4 are called the fluorescence yield η. The first factor $\frac{A}{A+k_q[\mathrm{M}]}$ is the fraction of excited OH radicals which emit a fluorescence photon. The second factor represents the proportion of fluorescence photons recorded within a given time window (counting gate). The process of gated fluorescence counting is depicted in Figure 3.2 schematically. Within this picture the maximum of the laser pulse is assumed

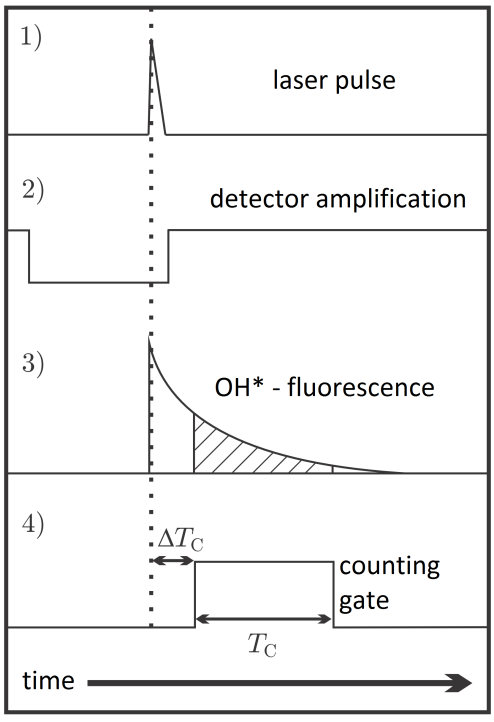

Figure 3.2: Scheme of the gated photon counting during an OH-fluorescence measurement. (Broch, 2011)

1. Laser pulse
2. During the laser pulse the detector amplification is switched off to prevent the detector from being damaged by scattered laser light
3. Time-dependence of OH-fluorescence. The shaded area represents the time-window in which the photons are counted
4. The counting gate starts at time ΔT_C after the laser pulse and has a width of T_C

to be at $t = 0$. During this time the detector is switched off in order to prevent damage by scattered laser light. After some time when the intensity of the laser pulse has sufficiently dropped the detector is switched back on again. At time ΔT_C the detection system starts counting the fluorescence photons for the time-span of T_C. This process repeats with the frequency of the laser repetition rate. For the AirLIF system the length of the counting gate T_C is 496 ns, while the delay of photon counting ΔT_C is 112 ns and 80 ns for OH and HO_2 respectively. Detector amplification is turned on roughly a few nano-seconds before the counting starts. A typical half-width of the laser pulse is 35 ns.

The OH fluorescence is superimposed by non-resonant background which is partly laser generated and partly laser independent (dark signal of detector and ambient light). The number of counted photons (N_{on}) per laser pulse is then given by

$$N_{\mathrm{on}} = N_{\mathrm{OH}} + N_{\mathrm{L}} + N_{\mathrm{S}} + N_{\mathrm{D}} \,. \tag{3.5}$$

N_{OH}: OH fluorescence photons
N_{L}: laser dependent non-resonant background
N_{S}: ambient light, solar radiation
N_{D}: dark signal of photon detector

The dark signal of the photon detector is much smaller than the other signals. The total number of counted photons N_{on} lies typically in the range of only 0.01 counts per laser pulse. In order to achieve a good signal-to-noise ratio, the signal is accumulated over an integration time of 5 seconds at a laser repetition rate of 3 kHz. The background contributions are handled in separate ways since the laser generated background is proportional to laser-power while the sun-background is not. The laser-independent background ($N_{\mathrm{S}} + N_{\mathrm{D}}$) is measured in a second time window ($T_{\mathrm{sun}} = 20\,000$ ns) with a long delay (24 800 ns) after laser dependent signals have decayed to zero. The signal is scaled to the length of the first time window (counting gate) by a factor T_C/T_{sun} and subtracted from the total counts N_{on} of the first time window. This procedure yields the signal $N_{\mathrm{OH}} + N_{\mathrm{L}}$, which is proportional to the laser power P_{on}. When the laser wavelength is tuned off-resonance such that no OH is excited ($= N_{\mathrm{off}}$), the same procedure yields N_{L} only, also proportional to the laser power P_{off}. Thus, tuning the laser between on- and off-resonance positions allows to distinguish between N_{OH} and N_{L} (Broch, 2011). This procedure repeats with each laser shot (laser repetition rate: ν_{rr}) and integrating over several shots normalized to 1 s integration time gives the signal S_{OH} in units $\left[{}^{\mathrm{cts}}/_{\mathrm{mW\,s}}\right]$

$$S_{\mathrm{OH}} = \frac{\left(N_{\mathrm{on}} - \frac{T_C}{T_{\mathrm{sun}}} N_{\mathrm{sun}}\right) \nu_{\mathrm{rr}}}{P_{\mathrm{on}}} - \frac{\left(N_{\mathrm{off}} - \frac{T_C}{T_{\mathrm{sun}}} N_{\mathrm{sun}}\right) \nu_{\mathrm{rr}}}{P_{\mathrm{off}}} \,. \tag{3.6}$$

3.3 HO_2 measurement principle

It is also possible to detect HO_2 radicals with the instrumental set-up for the detection of OH-radicals described above. This indirect method uses chemical conversion (Reaction R15) within the measurement cell by addition of a well-defined flow of

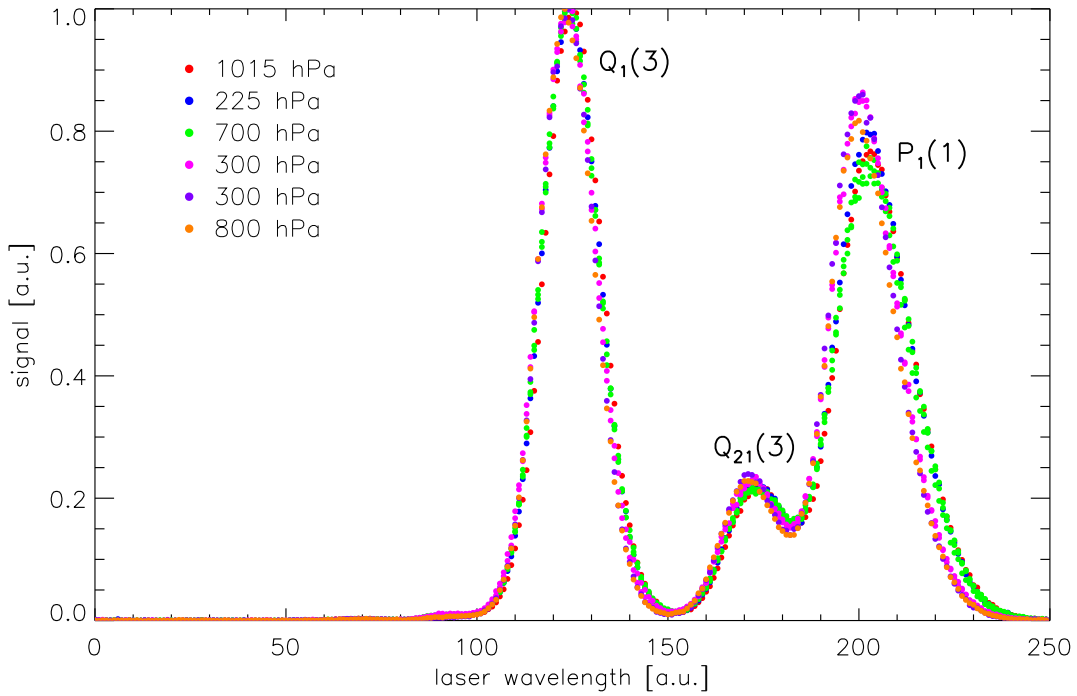

Figure 3.3: Section of the OH spectrum around 308 nm for various inlet pressures representing altitudes between 0 and 15 km. AirLIF uses the $Q_1(3)$-line for excitation at 308.1548 nm while the $P_1(1)$-line is at 308.1671 nm.

NO at the entrance of the detection cell (Holland et al., 2003; Fuchs et al., 2011). Depending on the amount of NO added the ambient HO_2 is converted to OH with efficiency κ_{NO} which is then detected by laser induced fluorescence. In an analogous way to Equation 3.5 the signal is constituted by various contributions

$$N_{on} = N_{HO_2} + N_{OH} + N_L + N_S + N_{NO} + N_D \,. \tag{3.7}$$

Apart from the already known quantities, N_{HO_2} is the number of counts due to converted HO_2. This adds to the counts induced by OH already present in ambient air. The addition of NO gives rise to background N_{NO} whose precise origin is not quite clear (Li et al., 2014). It can nevertheless be characterized by an additional NO background measurement and is a laser-power dependent quantity which means NO contributes to the OH concentration by some unknown reaction. The magnitude is small compared to ambient signals.

By removing the background contributions like in the previous section and then normalizing with respect to laser-power and integration time finally gives the dimensional signal

$$S = S_{OH} + S_{HO_2} = S_{HO_x}. \tag{3.8}$$

To extract information about the HO_2 concentration it is therefore necessary to know the contribution of the signal due ambient OH. In the present work two separate measurement cells are used for OH and HO_x to address this.

3.4 AirLIF instrument

A detailed description of the entire instrument can be found in Broch (2011). Broch discusses the AirLIF measurement system for OH and HO_2 as designed for the deployment on HALO (complete set-up, individual measurement racks, mounting on aircraft, dimensions, weight and power consumption; lasersystem, vacuum pumps, LIF data acquisition), but also a test version of the OH measurement cell and its characterization in the laboratory for ambient pressures at 1 atm. Broch also investigates the application of AirLIF at flight conditions theoretically. In this section the focus lies on the set-up and measurement conditions of the OH- and HO_2-channel as it was deployed during OMO. A complete characterization of the instrument at flight conditions up to 15 km altitude is given in the subsequent chapter.

3.4.1 OH channel

OH inlet system

The application of AirLIF (FZJ) on HALO required some changes in the layout compared to previous instrument versions for ground based measurements (Holland et al., 2003; Lu et al., 2012; Fuchs et al., 2016). In the latter the detection volume was close to the orifice as depicted in Figure 3.4. Cell pressure is typically around 5 hPa with a pinhole diameter of 0.4 mm for the nozzle. Since OH detection takes place close behind the orifice, the detection volume is only the small overlap of the laser beam (308 nm) and the narrow gas jet of the critical expansion behind the pinhole. The photo multiplier collects the fluorescence perpendicular to the plane spanned by the gas jet and the laser beam. It is a characteristic property of a critical

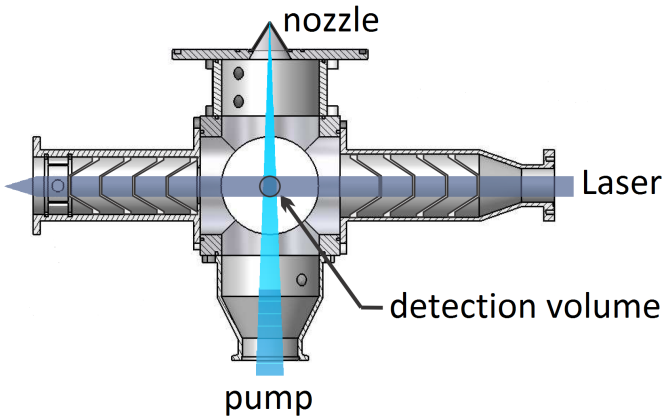

Figure 3.4: Scheme of the detection cell used for ground based applications. The distance of the nozzle to the detection volume is close with only 5 to 10 cm and the cell pressure is in the order of 5 hPa. The sampled air crosses the detection cell as a free jet without wall contact. (Broch, 2011)

nozzle, that the velocity of the expanding air reaches Mach 1 at the bottleneck of the orifice. For short distances (5 to 10 cm) the air flow will stay confined in a narrow jet with velocities of about 200 $^{m}/_{s}$ when it crosses the laser beam. For this reason, OH in the gas expansion does not get into contact to the chamber walls, where it would

be destroyed by wall reaction. In the AirLIF instrument, however, an additional inlet tube with a length of 220 mm is required to transfer air from outside the airplane into the OH detection cell inside the aircraft cabin (Figure 3.5). The nozzle (pinhole diameter: 1 mm) is located at the entrance of the inlet tube which has the same internal pressure as the detection cell. Due to the length of the inlet tube and the reduced pressure, some OH is lost by diffusion to the reactive wall in the tube (cf. Chapter 4). The inlet tube is sticking in a shrouded inlet which decelerates the incoming air flow during flight. The reduction of the air flow velocity reduces OH losses in the inlet tube (cf. Section 3.4.2) and enables in-flight calibration of OH (cf. Section 4.2.1). The OH inlet for HALO was developed in cooperation between the

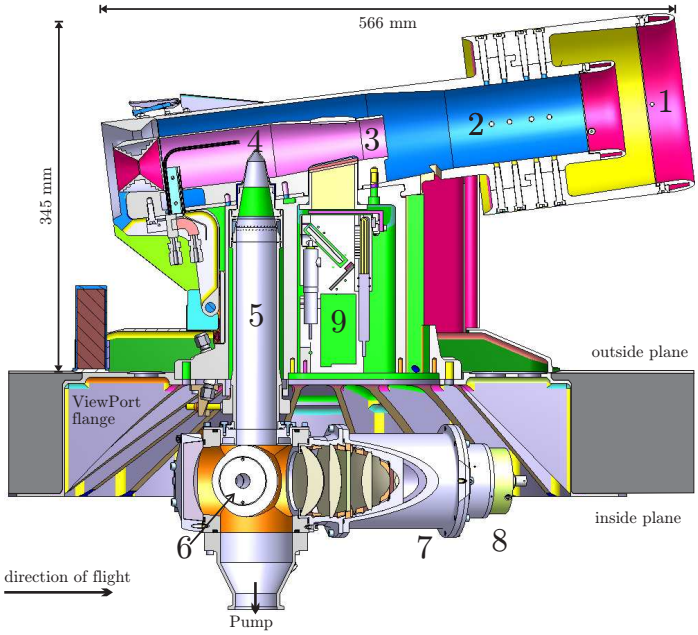

Figure 3.5: Cross section drawing of the OH cell installed on HALO with the shrouded inlet outside the air plane guiding air to the nozzle. (Broch, 2011)

1. Shroud
2. Outer deceleration tube
3. Inner deceleration tube
4. OH nozzle
5. OH inlet tube
6. OH measuring cell
7. Detection optics
8. Detector
9. UV unit (cf. Figure 4.3)

Institute for Energy and Climate - Troposphere (IEK-8) and the Central Institute of Engineering, Electronics and Analytics (ZEA) at Forschungszentrum Jülich. The design is a modification of the shrouded inlet originally devised by Eisele et al. (1997) for application on a C-130 aircraft. The HALO inlet is optimized for the much higher flight altitudes (< 15 km) and higher velocity of HALO (200-250 $^{m}/_{s}$) compared to the C-130 (8 km, 140-150 $^{m}/_{s}$). It is a 3-stage system in which the velocity is decelerated successively without generating any turbulence in front of the nozzle (cf. 1,2,3 in Figure 3.5). The computational fluid dynamics (CFD) simulations done at ZEA showed a decrease in velocity in the inner deceleration tube by a factor of 10 going from 250 $^{m}/_{s}$ to 25 $^{m}/_{s}$. This has been confirmed during OMO which is shown in Figure 3.6 (top panel). The correlation is linear with a ratio outside vs. inside of roughly 11.3. These velocities of 20 $^{m}/_{s}$ are in fact crucial in order to be able to detect OH at all (cf. Section 3.4.2). They are calculated by means of a Pitot-tube which measures the differential $\Delta p_{\mathrm{inlet}}$ and total inlet pressure p_{inlet}. The temperature in the inner deceleration tube can be calculated by Bernoulli's principle (Landau and Lifshitz, 1987)

$$T_{\mathrm{inlet}} = T_{\mathrm{amb}} \frac{1 + \frac{\kappa-1}{2}\,\mathrm{Ma}^2}{1 + \frac{\kappa-1}{\kappa}\,\frac{\Delta p_{\mathrm{inlet}}}{p_{\mathrm{inlet}}}} \tag{3.9}$$

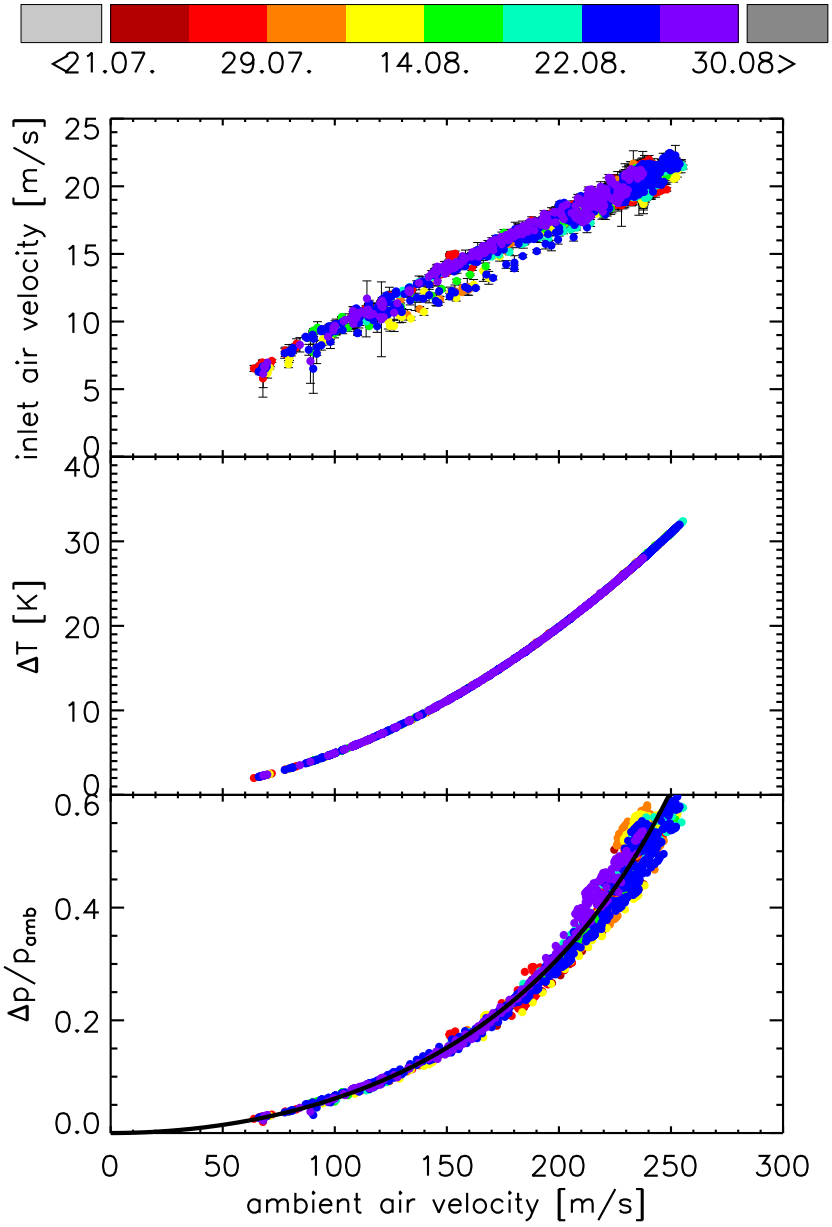

Figure 3.6: Correlation between true ambient airspeed v_{amb} vs. inlet air speed v_{inlet}, temperature rise $\Delta T = T_{\text{inlet}} - T_{\text{amb}}$ and relative ram pressure $\Delta p/p_{\text{amb}} = (p_{\text{inlet}} - p_{\text{amb}})/p_{\text{amb}}$ in the inner deceleration tube. Since the air velocity inside the inlet can be neglected in the kinetic energy term, temperature rise does only depend on the ambient air velocity v_{amb}, while the relative ram pressure depends on v_{amb} and T_{amb}. The temperature rise has a simple quadratic relationship to the ambient velocity i.e. $\Delta T \sim v_{\text{amb}}^2$. Relative ram pressure rise on the other hand can be simply expressed in terms of the Mach number (Ma) only, that is $\Delta p/p_{\text{amb}} \approx \left(1 + \frac{\kappa-1}{2}\,\text{Ma}^2\right)^{\frac{\kappa}{\kappa-1}} - 1$. The solid black line in the bottom panel represents this theoretical curve where the static ambient temperature dependence of the Mach number is fitted against true ambient airspeed from the in-flight data. Even though the dependence of the inlet air velocity appears linear with respect to the ambient air velocity, no exact relationship can be given, as it would be the result of a solution to the Navier-Stokes equations with complex boundary conditions. For important parameters altitude dependencies can be found in the Appendix B.3. Colour code date in 2015.

where Ma is the Mach-number given by the on-board BAHAMAS system and $\kappa = 1.4$ is the adiabatic exponent for air. p_i, T_i, v_i are the pressure, temperature and velocity respectively of (static) ambient air ($i = \text{amb}$) or inside the inlet ($i = \text{inlet}$, cf. Table B.1). Note that the denominator is essentially 1, because $\Delta p/p \ll 1$, so that the static inlet temperature can be identified with the total inlet temperature. Equivalently the temperature rise can be calculated by the formula $\Delta T = T_{\text{inlet}} - T_{\text{amb}} = \frac{v_{\text{amb}}^2(\kappa-1)}{2\kappa R}$ when the inlet air velocity is neglected (specific gas constant R). With this good approximation also the (total) inlet pressure can be calculated by using the adiabatic equation

$$p_{\text{inlet}} = p_{\text{amb}} \left(\frac{T_{\text{inlet}}}{T_{\text{amb}}} \right)^{\frac{\kappa}{\kappa-1}} \tag{3.10}$$

instead of measuring it. Finally the inlet velocity is extracted by the formula again associated to Bernoulli

$$v_{\text{inlet}} \approx \sqrt{\frac{2\Delta p_{\text{inlet}}}{\rho_{\text{inlet}}}} \tag{3.11}$$

which was used in the denominator of Equation 3.9. The Pitot-tube is placed directly behind the nozzle within the deceleration tube as seen in Figure 3.5 (behind 4. seen from direction of flight).

OH measuring cell

As shown in Figure 3.5 the OH cell sits directly underneath the inlet-system. It is pushed against the upper flange by a bayonette-closure. A long tube guides the air

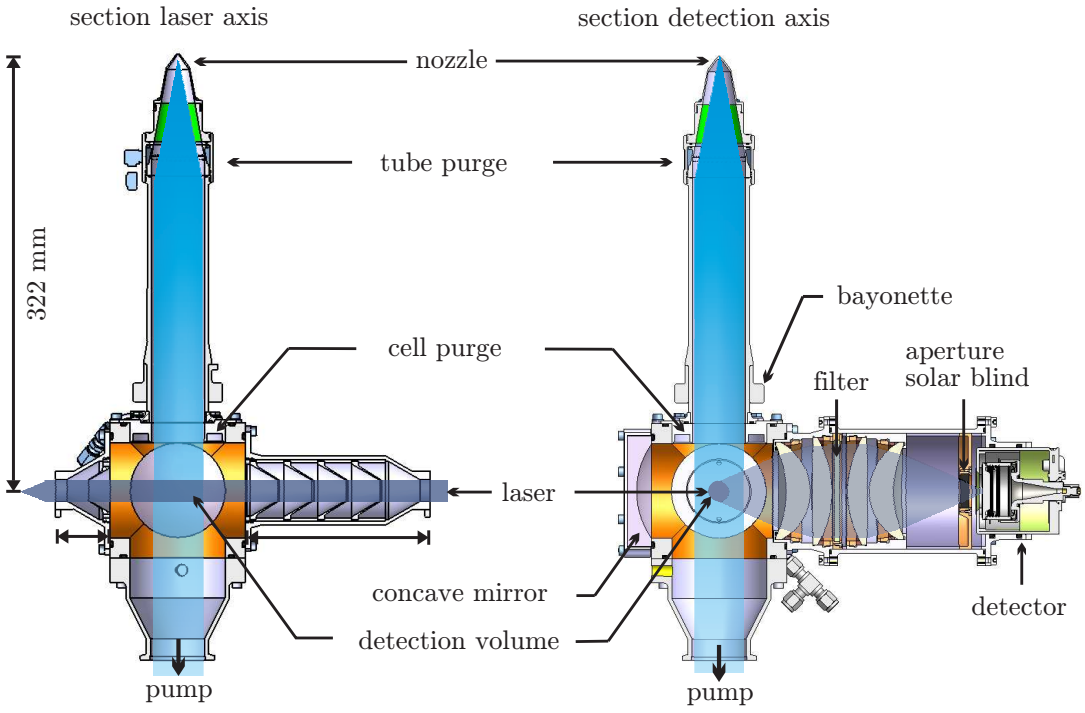

Figure 3.7: Left: Section of the OH cell seen from the axis of the detector **Right:** Section seen from the axis of the laser (Broch, 2011)

Table 3.2: Important parameters for the OH cell.

Laser	
repetition rate	3000 Hz
UV-power	≈20 mW
beam diameter	8 mm
pulse duration (FWHM)	35 ns
spectral bandwidth (FWHM)	2.5 pm
excited OH-line	$Q_1(3)$ (308.1541 nm)
Photon counter	
Delay in photon counting (ΔT_C)	112 ns
length of counting gate (T_C)	496 ns
OH cell	
tube length	220 mm
tube diameter	39 mm
distance nozzle - detection volume	322 mm
nozzle diameter	1 mm
inlet tube heating (set)	293 K
inlet tube temperature (measured)	285 K-295 K
pumping speed accredited to OH cell	≈ 54-72 $^{m^3}/_{h}$
cell purge flow	0 $^{std\,l}/_{min}{}^{*}$
baffle purge flow	0.2 $^{std\,l}/_{min}{}^{*}$
tube purge flow	0.8 $^{std\,l}/_{min}{}^{*}$
transmission of optical filter	72 %
focal length/lens diameter	75 mm/75 mm
quantum yield of photomultiplier	11 %

* std = 273.15 K, 1013.25 hPa

into the cell. Directly behind the nozzle a tube purge is installed which has tangential pinholes. The idea is to create a rotating sheath flow of nitrogen (N_2) which helps to confine the sampled air in the centre of the inlet tube. The distance between nozzle and detection volume is 322 mm. As seen in Figure 3.7 the laser and detection optics are aligned orthogonal to the symmetry axis of the tube. The laser passes multiple baffles to suppress stray-light before it enters the detection volume. These apertures can be flushed with nitrogen as well. The detection optics are aligned perpendicular to the laser with a mirror installed opposite to it to collect additional light. In front of the detector a narrowband filter (Filtrop AG 447026, 309.5 ± 2 nm, FWHM = 8 ± 2 nm, T_{max} = 72 %) only allows light of the correct wavelength to bypass. The distance of the detection cathode itself to the centre of the detection volume is 200 mm. Because of its small aperture a system of lenses collects photons emitted in a larger solid angle and focusses them onto the cathode. Several other system parameters for the OH cell are summarized in Table 3.2.

3.4.2 HO_2 Channel

HO_2 Inlet

In contrast to the OH cell, the HO_2 cell does not have a shrouded inlet system. For OH the shrouded inlet is necessary in order to prevent major losses of OH at the walls of the inlet tube when the aircraft travels with high speed. It is well known that the expansion jet at the orifice of the nozzle is of the order of Mach 1 whereas the speed of ambient air perpendicular to the sampling axis is of similar order at higher flight altitudes (cf. Figure B.1). In a simplified picture the vectorial addition

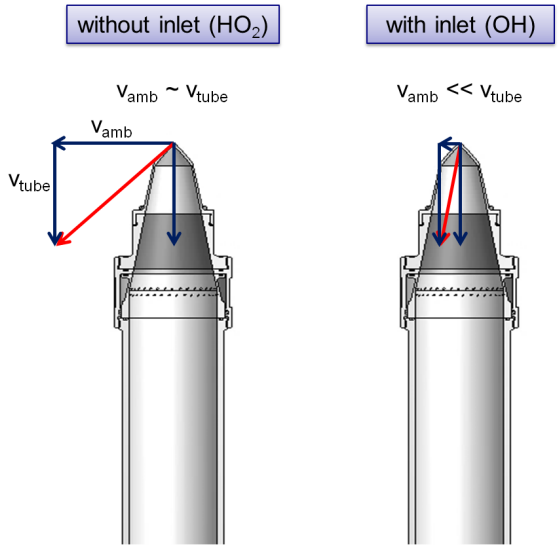

Figure 3.8: Left: The velocity of ambient air without a shrouded inlet is of the same order as the sampling velocity through a critical nozzle (Mach 1) $v_{\mathrm{amb}} \sim v_{\mathrm{tube}}$. OH losses at the walls are inevitable due to its high reactivity. **Right:** The shrouded inlet decelerates ambient air flow by a factor of 10. Air is therefore sampled almost perpendicular to the cross-section of the inlet tube making diffusion-driven losses the predominant factor. (Figure kindly provided by S. Broch)

of the velocities seen in Figure 3.8 on the left will lead to a resulting vector (red) which indicates that sampled air will hit the wall close behind the nozzle, giving rise to major losses due to the high reactivity of OH. The HO_2 detection cell did not have such an inlet-system since HO_2 is much less reactive compared to OH.

During OMO EU in the beginning of 2015, both measurement channels of the AirLIF instrument were tested in-flight for OH measurements. In the HO_2 channel, a flow of nitrogen replaced the NO flow, which is normally used for HO_2 conversion. This set-up allowed to test the influence of the different inlets on the detection of OH radicals, which are very sensitive to wall losses. At high altitudes ($> 5\,\mathrm{km}$) and correspondingly high flight velocities, large OH signals were measured in the OH channel, but no OH signal was detectable in the HO_2 channel. At low altitudes and low velocities, both channels recorded OH signals of similar magnitude (cf. Figure 3.9). This test demonstrates the importance of the shrouded inlet for the measurement of highly reactive species such as OH.

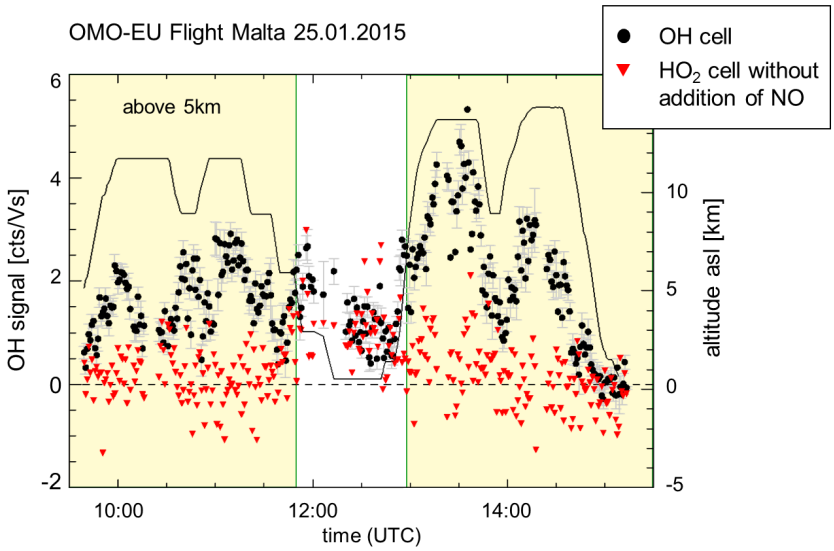

Figure 3.9: During OMO-EU (January 2015) OH was measured simultaneously on the OH- and HO_2 cell without NO-addition. While the OH cell sampled through the shrouded inlet, the HO_2 nozzle sampled directly from not decelerated ambient air. For altitudes above 5 km OH on the HO_2 cell broadly scatters around zero, while OH on the OH cell shows distinct signals greater zero. This confirms the assumption, that OH is essentially lost in the inlet tube of the HO_2 cell before it can be detected in the measurement cell.

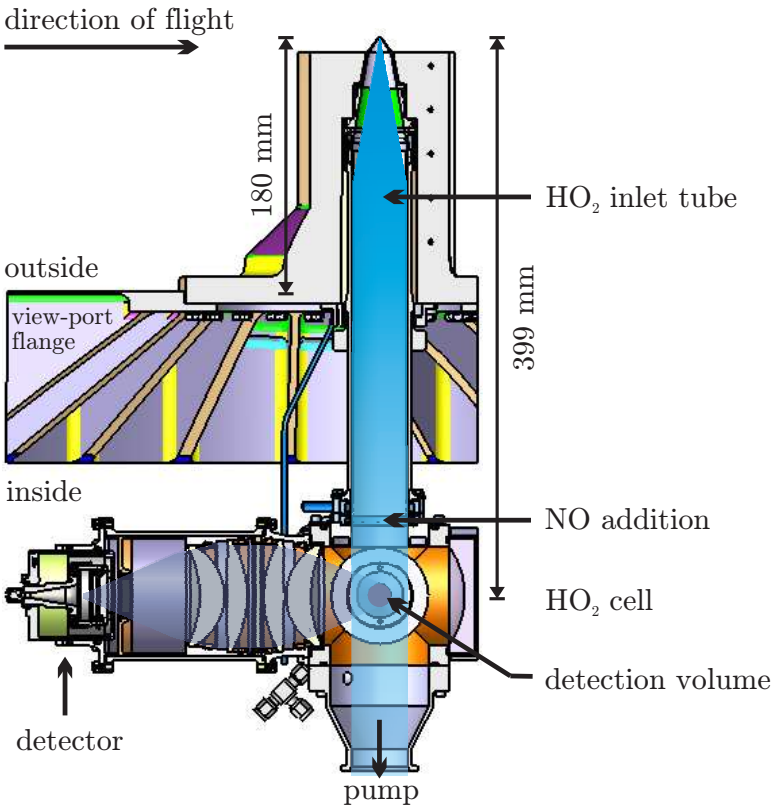

Figure 3.10: Section of the HO_2 inlet with cell. In contrast to the OH channel the HO_2 cell does not have a shrouded inlet system. The NO addition is done right before the entrance into the detection volume, approximately 50 mm before its centre which is 399 mm behind the nozzle. (Broch, 2011)

It also shows that OH was completely lost in the HO_2 channel as it was used during OMO. The in-flight calibration system, which is part of the shrouded inlet of the OH channel (cf. Figure 3.5), is not available for the HO_2 inlet. If applied, the in-flight calibration system would not produce sufficient HO_2 to be distinguishable from the relative large ambient HO_2 background. This is another reason why the HO_2 channel has a relatively simple inlet system (cf. Figure 3.10).

HO_2 measuring cell

The HO_2 cell is in principle constructed identical to the OH cell (Figure 3.10). The inlet tube however is 80 mm longer than that of OH because there is not enough space within the view-port flange of HALO where the entire inlet system is build in to align them next to each other. Like the OH cell the HO_2 cell has purge pinholes directly behind the nozzle. These are not used in the same way though as they point perpendicular to the wall. This design originally served the purpose to add NO in the tube for additional RO_2 detection (Fuchs et al., 2008) which however was not successful. Every three scan cycles the mode would switch between RO_x and HO_x. Since the RO_x mode was not used in the end, the NO-addition was replaced

Table 3.3: Important parameters for the HO_2 cell that can differ from those for the OH cell.

Laser	
UV-power	≈10 mW
beam diameter	8 mm
Photon counter	
Delay in photon counting (ΔT_C)	80 ns
length of counting gate (T_C)	496 ns
HO_2 cell	
tube length	300 mm
tube diameter	39 mm
distance nozzle - detection volume	399 mm
nozzle diameter	1 mm
inlet tube heating (set)	293 K
inlet tube temperature (measured)	288 K-295 K
pumping speed accredited to HO_2 cell	≈ 15-50 $^{m^3}/_{h}$
cell purge flow	0.8 $^{std\,l}/_{min}{}^{*}$
baffle purge flow	0.2 $^{std\,l}/_{min}{}^{*}$
tube purge flow	0.015 $^{std\,l}/_{min}{}^{*}$ CO^{**} + 0.020 $^{std\,l}/_{min}{}^{*}$ N_2
NO flow	0.002 $^{std\,l}/_{min}{}^{*}$ NO^{**}
conversion efficiency at ground	10 %

* std = 273.15 K, 1013.25 hPa
** 10 % in N_2

by a small nitrogen flow 0.020 $^{\mathrm{std\,l}}/_{\mathrm{min}}$ and the CO-flow was reduced to a minimal value (0.015 $^{\mathrm{std\,l}}/_{\mathrm{min}}$, 10 % CO in N_2). Due to technical reasons these flows could not be switched off, but had no effect otherwise on the detection of OH and HO_2 in the HO_2-channel. The HO_2 cell is flushed directly at the detection volume with 0.8 $^{\mathrm{std\,l}}/_{\mathrm{min}}$ in order to ensure a steady exchange of sampled air, that could otherwise recirculate within the side volumes and accumulate trace gases that lead to a possible interference by the reaction with NO. The baffle purges remain the same as in the OH case. Right before the air enters the detection volume, 0.002 $^{\mathrm{std\,l}}/_{\mathrm{min}}$ of 10 % NO in N_2 are added to convert HO_2 to OH (cf. Figure 3.10). At ground conditions typical reactions times Δt until detection of OH are 4 ms. Assuming perfect mixing, one can estimate a conversion efficiency of $k_{\mathrm{HO_2+NO}}\,[\mathrm{NO}]\,\Delta t \approx 0.2$ (see also the discussion following after Equation 4.48). The relatively small value helps to suppress unwanted RO_2 interference (Fuchs et al., 2011). Additional information are summarized in Table 3.3.

3.4.3 Gas flows and pressures

Important meteorological parameters which are necessary to evaluate the OH and HO_2 signals during the later characterization are provided by the on-board BAHAMAS system (cf. Table B.2). As the HO_2 cell was collecting ambient air directly while the OH cell sampled from inside the shrouded inlet, these conditions are significantly different. Air in the shrouded inlet is compressed adiabatically and thus always warmer than ambient air. Likewise static pressure inside the inlet is much

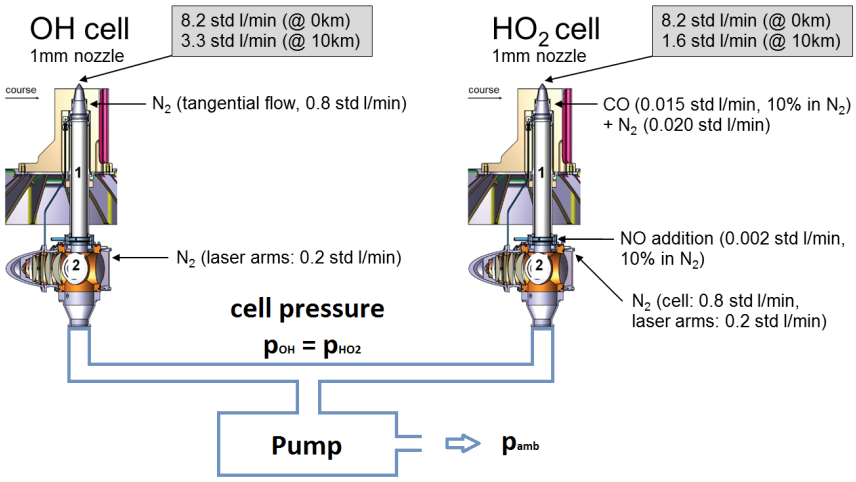

Figure 3.11: Schematic of the gas flow through the OH and HO_2 cell. Since both cells are on the same pump, they must have the same pressure. Volume flow rate is then essentially a function of mass flow through each nozzle, since this changes the pump load which needs to be accredited to each cell. At ground, the mass flows through both nozzles are similar, but start to differ with increasing altitude, because of the different inlet pressures. To a lesser degree volume flow rate is also affected by the resistance of the pump exhaust, which is determined by static ambient pressure. Relevant for radical losses or conversion from HO_2 to OH however is merely the tube flow rate which includes tube purges, but excludes baffle or cell purges. The above Figure also shows the positions where purge flows and reactive gases (NO, CO) are added. 1: inlet tube, 2: detection cell.

higher than static ambient pressure (cf. Figure B.3). For example, at 14 km altitude inlet pressure is 250 hPa while static ambient pressure is only 150 hPa. From mass conservation two different volume flow rates through the cell can be determined that are of importance

$$n_{\text{cell}} q_{\text{cell}} = n_{\text{amb}} q_{\text{noz}} + n_0 q_{\text{purge}} \tag{3.12}$$

$$n_{\text{cell}} q_{\text{tube}} = n_{\text{amb}} q_{\text{noz}} + n_0 q_{\text{purge-tube}} \tag{3.13}$$

where

- n_i is the number density of gas in the cell (i = cell), in ambient air i.e. in front of the nozzle (i = amb) and for the standard conditions ($i = 0$, 1013.25 hPa and 273.15 K) for which the purge flow controllers were calibrated. i = inlet is later specifically used for the nozzle inlet conditions, in particular for OH inside the inner deceleration tube.
- q_i is the volume flow rate through the entire cell (i = cell, pumping speed on cell) that considers all purge flows (i = purge, at standard conditions), through the inlet tube (i = tube) where only tube purge flows are accounted for (i = purge-tube, at standard conditions) and through the entrance of the nozzle (i = noz).

q_{noz} is only a function of the nozzle cross-section σ, static ambient temperature T_{amb} and a nozzle specific parameter $\mu < 1$, which for the case of a simple de Laval nozzle takes the form (Landau and Lifshitz, 1987)

$$q_{\text{noz}} = \mu\sigma \left(\frac{2}{\kappa+1}\right)^{\frac{1}{\kappa-1}} \sqrt{\frac{\kappa}{\kappa+1}} \sqrt{2RT_{\text{amb}}} \qquad \text{if} \qquad \frac{p_{\text{cell}}}{p_{\text{amb}}} \leq \left(\frac{2}{\kappa+1}\right)^{\frac{\kappa}{\kappa-1}} \tag{3.14}$$

with specific gas constant R and adiabatic exponent $\kappa \approx 1.4$. The nozzle factors μ were determined by measuring the mass flow through the nozzle and comparing it with the theoretically calculated mass flow using the above formula without nozzle factor. For the OH nozzle it is found $\mu \approx 0.9$ and for the HO_2 nozzle $\mu \approx 0.95$.

While this shows that the mass flow through the nozzle depends on the pressure in front of the nozzle p_{amb} and since both cells are on the same pump leading to the same cell pressure p_{cell} (cf. Figure B.4), at ground the pumping load on each cell is therefore roughly the same as the purge flows are similar on each cell ($q_{\text{purge}} \approx 1\,\text{std}\,\text{l}/\text{min}$). At higher altitudes however this leads to a different mass flow through each nozzle and therefore to a differing volume flow rate of the sampled air through each cell (cf. Figure B.5, B.7, B.8). Contrary to the original assumption however, HO_2 inlet pressure is not static ambient pressure, but a much reduced effective inlet pressure - and thus reduced mass flow through the nozzle - due to the streamline curvature of air passing over the nozzle which depends on the aircraft velocity (cf. Chapter 4). This effect even exacerbates the just discussed discrepancy in the unequal pumping load on each cell. Apart from direct influence due to the mass flow shift with altitude between the two nozzles, the volume flow rate through each cell to a lesser degree is also impacted by variations in the total pumping power, that depends on the exhaust pressure of the pump and which happens to

be static ambient pressure. Effectively the cell pressures therefore not only depend on altitude, but also on ambient air velocity (cf. Appendix B.3). The volume flow rate has direct implications for the conversion efficiency in the HO_2 cell and when estimating possible effects due to OH wall losses in the tube by a simple model (cf. Equation 4.16) in order to explain the OH sensitivity, which makes the correct knowledge of the corresponding pressures and temperatures a crucial ingredient for the evaluation of the altitude dependent sensitivities (cf. Chapter 4).

Chapter 4

Calibration

4.1 LIF detection sensitivity

LIF is a very sensitive optical detection technique that yields a fluorescence signal S_{OH} for a given ambient OH concentration $[\mathrm{OH}]_{\mathrm{amb}}$ in a linear relationship

$$S_{\mathrm{OH}} \propto [\mathrm{OH}]_{\mathrm{amb}} \ , \tag{4.1}$$

where the proportionality factor is a complex function which depends on ambient conditions (T_{amb}, p_{amb}, air composition) and on various instrumental parameters. In order to determine OH concentrations from measured signals accurately, the most convenient approach is to perform an instrumental calibration with known OH concentrations under ambient conditions (cf. Section 4.2.3ff). Nevertheless, a theoretical understanding of the LIF detection sensitivity is essential to understand the dependence on parameters such as laser power, cell pressure, temperatures, which may change during measurement flights (see below). As is seen in equation (3.4) the measured signal is directly proportional to the excited OH radical number density in the detection cell. In the same way it can be derived from the rate equation for absorption (Demtroeder, 2011)

$$\frac{\mathrm{d}}{\mathrm{d}t}\, n_2 = \int\int B_{12} L_{\mathrm{np}} \left(\nu_0 - \nu', \Delta\nu_{\mathrm{np}}\right)\, n_1 G_{\mathrm{D}} \left(\nu' - \nu, \Delta\nu_{\mathrm{D}}\right)\, u\, G_{\mathrm{l}} \left(\nu - \nu_{\mathrm{l}}, \Delta\nu_{\mathrm{l}}\right)\, \mathrm{d}\nu \mathrm{d}\nu' \tag{4.2}$$

that the population of the excited state n_2 is proportional to the number of OH radicals in the ground state n_1. The constant pre-factors in Equation 4.2 are the Einstein coefficient for absorption B_{12} in units $[B_{12}] = {}^{\mathrm{cm}^3}/_{\mathrm{J\,s}^2}$ and the radiant energy density u in units $[u] = {}^{\mathrm{J}}/_{\mathrm{cm}^3}$. In the case of a collimated laser-beam it is directly proportional to the radiant energy flux density $j = uc$ where c is the speed of light. ν_0 and ν_l are the central OH resonance transition- and laser-frequency respectively and the summation over ν, ν' then takes into account for all these transition possibilities. Here $L(\nu, \Delta\nu) = \frac{1}{\pi} \frac{\Delta\nu}{\nu^2 + \Delta\nu^2}$ stands for a Lorentz profile of the natural line width (n) and the pressure broadening (p) with $\Delta\nu_{\mathrm{np}} = \Delta\nu_{\mathrm{n}} + \Delta\nu_{\mathrm{p}}$ and $G(\nu, \Delta\nu) = \sqrt{\frac{4\ln 2}{\pi}} \frac{1}{\Delta\nu} \exp\left(-\frac{4\ln 2}{\Delta\nu^2}\, \nu^2\right)$ is a Gaussian profile for the Maxwell-Boltzmann distribution (D: Doppler) and the spectral laser pulse width (l), respectively. The convolution of a Lorentz profile with a Gaussian is a Voigt profile

(Demtroeder, 2011).

If cell pressure p_{cell} is only a few hecto-pascal, the line width $\Delta\nu_{\text{np}}$ is much smaller ($\Delta\nu_{\text{n}} \approx 0.25\,\text{MHz} \mathrel{\widehat{=}} 0.1\,\text{fm}$, $\Delta\nu_{\text{p}} \approx 6\,\text{GHz}\,\frac{p_{\text{cell}}}{1013.25\,\text{hPa}} \mathrel{\widehat{=}} 2\,\text{pm}\,\frac{p_{\text{cell}}}{1013.25\,\text{hPa}}$) than the broadening due to the thermal motion of the molecules ($\Delta\nu_{\text{D}} \approx 3\,\text{GHz} \mathrel{\widehat{=}} 1\,\text{pm}$)(Dorn et al., 1995) or the laser line width ($\Delta\nu_{\text{l}} \approx 8.5\,\text{GHz} \mathrel{\widehat{=}} 2.7\,\text{pm}$, cf. Figure 3.3), and the Lorentz profile can thus be viewed as a Dirac delta function. The convolution of the remaining Gaussian profiles are again Gaussian with modified line width $G\left(\nu_0 - \nu_{\text{l}}, \sqrt{\Delta\nu_{\text{D}}^2 + \Delta\nu_{\text{l}}^2}\right)$.

If the central frequency of the laser ν_{l} matches precisely the central excitation frequency ν_0 for the transition, Equation 4.2 becomes

$$\frac{\mathrm{d}}{\mathrm{d}t}\, n_2 = B_{12}\sqrt{\frac{4\ln 2}{\pi}}\frac{1}{\sqrt{\Delta\nu_{\text{D}}^2 + \Delta\nu_{\text{l}}^2}}\,\frac{j}{c}\,n_1\,. \tag{4.3}$$

In thermal equilibrium, the ground state population n_1 for a rotational level from which the transition occurs will be populated according to the Boltzmann distribution i.e.

$$n_1 = \underbrace{\frac{g_{J''}}{Q_{\text{Rot}}(T)}\,\exp\left(-\frac{E_{J''}}{k_B T}\right)}_{P_{J''}}\,[\text{OH}]_{\text{cell}} \tag{4.4}$$

with the

- degeneracy of the energy level corresponding to the total rotational quantum number $J'' = N'' \pm \frac{1}{2}$: $g_{J''} = 2J''+1$. N'' and N' are the total angular momenta without spin for the electronic ground- and first excited state, respectively. For the transition $Q_1(3)$ these take the value $N'' = N' = 3$ and $J'' = J' = 3.5$.
- energy $E_{J''}$ corresponding to the total rotational quantum number J''.
- rotational partition function $Q_{\text{Rot}}(T)$.
- Boltzmann constant k_B.
- absolute temperature of the gas inside the detection volume T.
- OH concentration $[\text{OH}]_{\text{cell}}$ within detection volume.

Dorn et al. (1995) gave a parametrization for the partition function

$$Q_{\text{Rot}} = 1.42 \cdot 10^{-6} \cdot T^2 + 0.1485 \cdot T - 4.1\,. \tag{4.5}$$

With the identification $n_2 = [\text{OH}^*]_0$ and the definition

$$\alpha = \frac{B_{12}}{c}\sqrt{\frac{4\ln 2}{\pi}}\frac{P_{J''}}{\sqrt{\Delta\nu_{\text{D}}^2 + \Delta\nu_{\text{l}}^2}} \tag{4.6}$$

which has units [cm²/J], Equation 4.3 can be written as

$$\mathrm{d}\,[\mathrm{OH}^*]_0 = \alpha\, j\, [\mathrm{OH}]_{\mathrm{cell}}\, \mathrm{d}t\,. \tag{4.7}$$

If the total energy of each laser pulse is small enough to be far away from saturation, the only time-dependent quantity on the right hand side of Equation 4.7 is the energy flux density $j(t)$, since the laser has finite width (FWHM: 35 ns) with some normalized distribution $f(t)$ having a maximum at $t = 0$ (cf. Figure 4.1). By factorizing $j(t) = \frac{P}{\nu_{\mathrm{rr}} \pi r_{\mathrm{l}}^2}\, f(t)$ where the pre-factor is the areal energy density per laser pulse, P the mean laser power averaged over successive laser pulses which arrive with a repetition rate ν_{rr} and r_{l} the radius of the laser beam through the cell, an estimate for the ratio $\frac{[\mathrm{OH}^*]_0}{[\mathrm{OH}]_{\mathrm{cell}}}$ can be found after integrating the equation over the laser pulse duration

$$\frac{[\mathrm{OH}^*]_0}{[\mathrm{OH}]_{\mathrm{cell}}} = \frac{\alpha P}{\nu_{\mathrm{rr}} \pi r_{\mathrm{l}}^2}\,. \tag{4.8}$$

When using the parameters from Table 4.1 for the OH cell, this ratio takes the value 0.0035 i.e. only 0.35 % of all the OH radicals in the detection volume are eventually excited.

Table 4.1: Important instrumental and physical parameters for the excitation of OH at conditions inside the measurement cell.

Parameter	Value	Error [%]	Source
temperature T	293 K	3	measured
excited OH-line	$Q_1(3)$ (308.1541 nm)	$5 \cdot 10^{-4}$	(Dorn et al., 1995)
B_{12}	1.01×10^{24} cm³ Hz/J s	5	(Dimpfl and Kinsey, 1979)
$P_{J''}$	0.075	<1	(Dorn et al., 1995)
$\Delta\nu_{\mathrm{D}}$	2.9 GHz	3	(Dorn et al., 1995)
$\Delta\nu_{\mathrm{l}}$	8.5 GHz	10	cf. Figure 3.3
$\Delta\nu_{\mathrm{rr}}$	3 kHz	-	manufacturer
laser power P	20 mW	10	measured
laser beam radius r_{l}	4 mm	10	measured

Going back to Equation 4.7 it allows the following interpretation: At each instant t in time, the amount of OH radicals excited $\mathrm{d}\,[\mathrm{OH}^*]_0$ within the interval $\mathrm{d}t$ obeys Equation 3.4 with time-dependent $\eta(\Delta T_C - t) = \eta(\Delta T_C)\, \exp\left[(A + k_q\,[\mathrm{M}])\, t\right]$ where ΔT_C is the start of photon counting. Combining with Equation 3.4 and integrating over the laser pulse duration yields the number of photons per volume emitted in all directions within the counting time window Δt, i.e.

$$[\gamma] = \alpha \underbrace{\eta(\Delta T_C)}_{\equiv\eta} \frac{P}{\nu_{\mathrm{rr}} \pi r_{\mathrm{l}}^2}\, [\mathrm{OH}]_{\mathrm{cell}} \int_{\mathrm{pulse}} f(t) \exp\left[(A + k_q\,[\mathrm{M}])\, t\right] \mathrm{d}t\,. \tag{4.9}$$

The integral over the laser pulse duration is a correction factor to the fluorescence yield η and typically close to 1 contributing a correction up to 5 % and will be neglected in the following. When Equation 4.9 is multiplied with the laser repetition rate ν_{rr} and divided by 4π steradian (isotropy), the left hand side becomes $[^{\mathrm{photons}}/_{\mathrm{cm}^3\,\mathrm{s\,sr}}]$

$$[\dot{\gamma}] = \frac{\alpha\eta}{4\pi}\,\frac{P}{\pi r_{\mathrm{l}}^2}\,[\mathrm{OH}]_{\mathrm{cell}}\ . \tag{4.10}$$

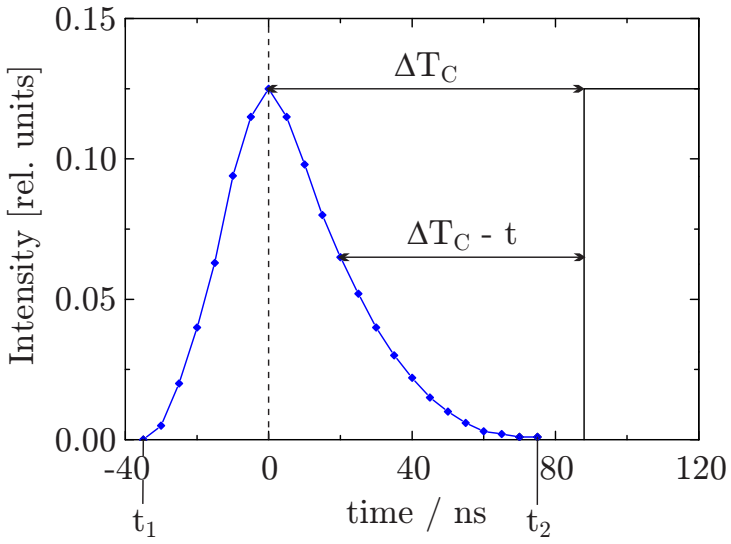

Figure 4.1: The distribution function $f(t)$ for a real laser pulse of width Δt_{FWHM} leads to an increase in the fluorescence yield compared to the ideal in which the pulse has width $\Delta t_{\mathrm{FWHM}} = 0$ because contributions closer to the measurement have a higher impact than those further away. (Broch, 2011)

To obtain the total amount of counts given the rate in Equation 4.10, it is necessary to know the detection volume, the solid angle of the optics collecting the fluorescence as seen from the centre of the detection volume, the transmission efficiency of the optics T_{opt} (i.e. optical interference filter and lenses) and the quantum efficiency of the photomultiplier ϵ registering a photon. The effective volume with excited OH radicals seen by the detector is given by some effective length l_{eff} and the cross-section πr_{l}^2 of the laser beam inside the gas flow (cf. Figure 4.2). The fluorescence within this volume happens to be independent of direction. Therefore only those photons emitted in the direction of the detector are registered which is the solid angle Ω of the detection optics from the view point of the centre of the detection volume. This angle is doubled by installing a mirror opposite of the detector. Multiplying all these fractions with the rate 4.10 and dividing by laser power, gives the signal S_{OH} in units $[^{\mathrm{cts}}/_{\mathrm{mW\,s}}]$ (cf. Equation 3.6):

$$\begin{aligned} S_{\mathrm{OH}} &= [\dot{\gamma}] \cdot \frac{\pi r_{\mathrm{l}}^2\, l_{\mathrm{eff}} \cdot \Omega \cdot T_{\mathrm{opt}} \cdot \epsilon}{P} \\ &= \epsilon T_{\mathrm{opt}} G \eta \alpha\, [\mathrm{OH}]_{\mathrm{cell}} \end{aligned} \tag{4.11}$$

with the geometric factor $G = \frac{\Omega\, l_{\mathrm{eff}}}{4\pi}$.

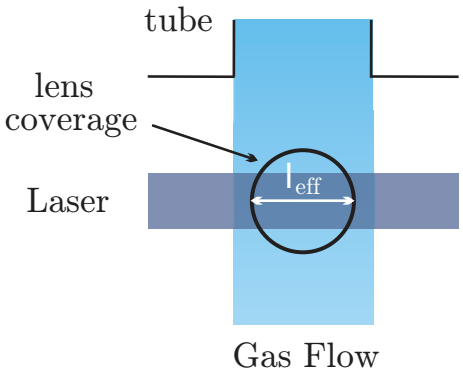

Figure 4.2: Scheme of the detection volume seen by the photomultiplier. It is given by the overlap of the laser beam and the cylindrical plug flow which then defines an effective length l_{eff}. The photons within this volume are emitted isotropically and only those emitted in the direction of the optics contribute to the signal. To double the effect a mirror is installed opposite of the detector. (Broch, 2011)

In order to relate the OH concentration in the cell to the ambient OH concentration, it should be remembered that the gas in the cell consists of ambient air flowing through the nozzle and purge gas with constant mass-flow of N_2 regulated by mass-flow controllers (cf. Section 3.4.3 and Equation 3.12). Then the OH concentration in the cell is given by

$$\begin{aligned}
[\text{OH}]_{\text{cell}} &= x_{\text{OH}_{\text{cell}}} \cdot n_{\text{cell}} \\
&= x_{\text{OH}_{\text{amb}}} \cdot x_{\text{amb/cell}} \cdot n_{\text{cell}} \\
&= x_{\text{OH}_{\text{amb}}} \cdot \frac{n_{\text{amb}} q_{\text{noz}}}{n_{\text{cell}} q_{\text{tube}}} \cdot n_{\text{cell}} \\
&= \underbrace{\frac{q_{\text{noz}}}{q_{\text{tube}}}}_{\omega} [\text{OH}]_{\text{amb}}
\end{aligned} \tag{4.12}$$

with

- $x_{\text{OH}_{\text{amb}}}$, $x_{\text{OH}_{\text{cell}}}$: volume mixing ratio of ambient OH and cell OH, respectively.
- $x_{\text{amb/cell}}$: volume fraction of ambient air in the cell gas which is composed of ambient air and purge gas (N_2).
- n_{amb}, n_{cell}: gas number density $[^{\text{molec}}/_{\text{cm}^3}]$ at static pressure and temperature at ambient conditions and inside the cell, respectively.
- q_{noz}, q_{tube}: volume flow rate through the entrance of the nozzle at given static ambient temperature and volume flow rate through the inlet tube, respectively $[^{\text{cm}^3}/_{\text{s}}]$.
- $n \cdot q$: mass flow $[^{\text{molec}}/_{\text{s}}]$.

The fraction $x_{\text{amb/cell}}$ is 1 if no tube purges are used on the cell. With purges however $x_{\text{amb/cell}} < 1$ since $n_{\text{cell}} q_{\text{tube}} = n_{\text{amb}} q_{\text{noz}} + n_0 q_{\text{purge-tube}}$ by mass conservation. ω is called expansion ratio and measures the dilution effect by going from ambient to low pressure. Equation 4.12 is again simply a statement of mass conservation for

OH: The OH mass flow through the nozzle is the same as the OH mass flow through the cell.

Since OH is highly reactive this conservation is obviously not fulfilled in practise. For that purpose a transmission factor $\beta < 1$ is introduced, which incorporates the losses directly at the nozzle as well as losses due to surface reactions in the tube. Broch (2011) estimated these losses by a simple model

$$\beta = \beta_0 \exp\left(-k_w \, t_{\text{res}}\right) \tag{4.13}$$

where β_0 is the transmission of the nozzle, k_w a first order rate coefficient ($^1/_\text{s}$) for wall loss in the inlet tube and t_{res} the residence time of air in the inlet tube (s). The latter is given by the tube volume $\pi r^2 \cdot l_{\text{tube}}$ and the volume flow rate q_{tube} through the tube

$$t_{\text{res}} = \frac{\pi r^2 \cdot l_{\text{tube}}}{q_{\text{tube}}} \tag{4.14}$$

with the radius of the inlet tube r and the tube length l_{tube}. As discussed by Broch (2011) the nozzle transmission is close to 1 for a large nozzle orifice (here 1 mm). Broch (2011) concluded that k_w is diffusion controlled for cell pressures between 2 and 11 hPa. As a further simplification, k_w can be approximated using the mean squared displacement relationship for 2-dimensional diffusion (*root-t-law*)

$$r^2 = 4D(p)\, t_{\text{diff}} \qquad \Rightarrow \qquad k_w \approx \frac{1}{t_{\text{diff}}} = \frac{4D(p)}{r^2} \tag{4.15}$$

with the pressure dependent diffusion constant $D(p) = D_0 \cdot \frac{p_0}{p}$, where $D_0 = 0.22\,\text{cm}^2/\text{s}$ is given at $p_0 = 1013.25\,\text{hPa}$ and 296 K (Ivanov et al., 2007). Combining the last two equations, it readily follows

$$\beta = \beta_0 \exp\left(-\frac{4\pi D_0 p_0 \, l_{\text{tube}}}{p_{\text{cell}} \, q_{\text{tube}}}\right) . \tag{4.16}$$

This shows, that the transmission is essentially an exponential function of the mass flow $p_{\text{cell}}\, q_{\text{tube}}$ through the inlet tube. In the vicinity of a discontinuity that is found for the pressure dependent sensitivity, it however appears to have a significantly more complex dependence which will be discussed in Section 4.3.1 and 4.3.2.

Replacing $[\text{OH}]_{\text{cell}}$ in Equation 4.11 by the just found relation to $[\text{OH}]_{\text{amb}}$ finalizes the deduction of the relationship between ambient OH and measured signal

$$S_{\text{OH}} = \underbrace{\epsilon T_{\text{opt}} G \eta \alpha \beta \omega}_{C_{\text{OH}}} [\text{OH}]_{\text{amb}} . \tag{4.17}$$

C_{OH} has units $^{\text{cts}}/_{\text{mW s } 10^6/\text{cm}^3}$ and is called detection *sensitivity*.

4.1.1 Dependence on operating conditions

The LIF detection sensitivity depends on a number of parameters that may change during measurement flights:

- **inlet pressure and temperature**
  With altitude and aircraft velocity the nozzle inlet pressures and temperatures show significant changes. This has implications on the mass flow through the nozzle, the expansion ratio ω, the cell pressure, the pump load distribution on both cells and the total pumping speed.

- **cell pressure**
  Cell pressure affects the fluorescence yield and the diffusion driven tube losses. In principle cell pressure can also influence the OH line-profile, but this effect appears to be negligible (cf. Figure 3.3).

- **cell temperature**
  Since cell temperature influences a lot of important parameters e.g. the cell gas density, the distribution of the OH rotational state population, OH-Doppler broadening and the quantum yield of the photomultiplier, the cell inlet tube is heated to keep the temperature almost constant at all flight levels (cf. Table 3.2 + 3.3). The possible influence of cell temperature variations was therefore not considered in the following.

- **cell gas composition**
  The cell gas composition (N_2, O_2, H_2O) depends on the mixing of the sampled ambient air and the added purge flow (dry nitrogen). The mass flow through the nozzle changes with altitude whereas the purge mass flow remains constant (cf. Section 3.4.3). The gas composition and the water vapour contents influence the fluorescence yield η by electronic quenching of the excited OH.

Under the assumption that the temperature of the inlet tube and cell are essentially constant during flights, the parameters $\epsilon, T_{\text{opt}}, G$ and α in Equation 4.17 can be considered as constant. There remain three parameters that exhibit major variations with flight altitude

$$C_{\text{OH}} \propto \eta\left(p_{\text{cell}}, x_{\text{H}_2\text{O}}, x_{\text{N}_2}, x_{\text{O}_2}\right) \cdot \beta\left(p_{\text{cell}}, q_{\text{tube}}\right) \cdot \omega\left(T_{\text{inlet}}, q_{\text{tube}}\right) \tag{4.18}$$

The fluorescence yield η depends on the cell pressure and the gas composition as mentioned above, the transmission factor β depends on the cell pressure which influences diffusion-controlled radical losses and the residence time in the tube which is inversely proportional to the volume flow rate, and the expansion ratio ω depends on the ambient temperature at the entrance of the inlet nozzle and the volume flow through the inlet tube (q_{tube}). The fluorescence yield η and the expansion ratio ω can be calculated using measured values that are obtained during the flights for ambient pressure and temperature, cell pressure and temperature, and ambient water vapour concentrations via Equations 3.4 and 4.12+3.13+3.14, respectively.

During the OMO flights, typical values for the expansion ratio vary between 0.007 and 0.01 for the OH cell (cf. Figure C.1) and between 0.01 and 0.015 for the HO_2 cell (cf. Figure C.2). The fluorescence yield on the other hand is strongly dependent on altitude being 0.011 at ground (cell pressure: 11 hPa) and 0.135 at 15 km (cell pressure: 2.5 hPa) (cf. Figure C.3, OH cell).

Other quantities from Equation 4.17 ($\epsilon, T_{\text{opt}}, G, \beta$) on the other hand are practically difficult to access and their calculation will contain large uncertainties. In practise it is therefore sensible to determine C_{OH} via measurement, which is done by sending known amounts of OH through the system. This procedure is called calibration and an evident requirement is a stable source providing OH. Similar arguments which lead to Equation 4.17 can as well be made for HO_2 where an additional step introduces a conversion efficiency factor κ_{NO} due to reaction with NO and the same result of proportionality with C_{HO_2} remains.

4.2 Calibrations during OMO

During the OMO-campaign two calibration procedures were applied:

- In-flight calibrations provide an altitude dependent relative sensitivity measure. Due to the lack of water vapour used for artificial OH generation this method is however limited to below 10 km.
- Ground based calibrations between flights yield absolute sensitivities for the duration of the campaign, but only for ground conditions.

By combining both methods, an absolute and altitude dependent sensitivity is obtained up to 10 km altitude.

4.2.1 In-flight calibration

The shrouded inlet system was devised to sample ambient air with reduced speed in order to alleviate OH losses on the walls of the inlet tube (cf. Section 3.4). In addition, the reduced air speed enables in-flight calibrations for OH to keep track of changes in the sensitivity due to ambient pressure and temperature variations. The in-flight calibration is achieved by a UV unit which is incorporated in the pylon of the shrouded inlet system (cf. Figure 3.5) as described in Broch (2011). OH is artificially produced by photolysis of ambient water vapour using the 185 nm emission line from a low-pressure discharge mercury lamp (pen-ray lamp) while ambient air is passing through the inner deceleration tube of the shrouded inlet system (cf. Figure 4.3)

$$\mathrm{H_2O} + h\nu \longrightarrow \mathrm{OH} + \mathrm{H} \qquad \lambda = 185\,\mathrm{nm} \qquad \text{(R44)}$$

$$\mathrm{H} + \mathrm{O_2} + \mathrm{M} \longrightarrow \mathrm{HO_2} + \mathrm{M} \qquad \mathrm{M} = \mathrm{N_2}, \mathrm{O_2}\,. \qquad \text{(R45)}$$

The OH enriched air is then sampled through the nozzle of the inlet tube to be detected by LIF. It is possible to calculate the amounts of OH produced by the lamp. For that purpose consider the rate equation for the centre of the inner deceleration tube

$$\frac{\mathrm{d}}{\mathrm{d}t}\,[\mathrm{OH}] = j_{\text{OH}}\,[\mathrm{H_2O}] \tag{4.19}$$

with the photolysis frequency $j_{\text{OH}} = \int \sigma_{\mathrm{H_2O}} \Phi_{\text{OH}} I_\lambda \,\mathrm{d}\lambda$. Since the irradiation time t_{rad} is short such that water can be viewed as constant the direct integration gives

$$[\mathrm{OH}] = [\mathrm{H_2O}]\ \sigma_{\mathrm{H_2O}} \Phi_{\text{OH}}\, t_{\text{rad}} \underbrace{\int_{\text{Hg-185 nm}} I_\lambda \,\mathrm{d}\lambda}_{\equiv I_{185}}\,. \tag{4.20}$$

The H_2O absorption cross-section ($[\sigma_{H_2O}] = cm^2$) and OH quantum yield ($[\Phi_{OH}] = 1$) were pulled in front of the integral since they are constant over the range of integration. The integral over the spectral light intensity I_λ ($[I_\lambda] = {}^{photons}/_{cm^2\,s\,nm}$) gives the lamp intensity I_{185} ($[I_{185}] = {}^{photons}/_{cm^2\,s}$) of the Hg-185 nm emission line.

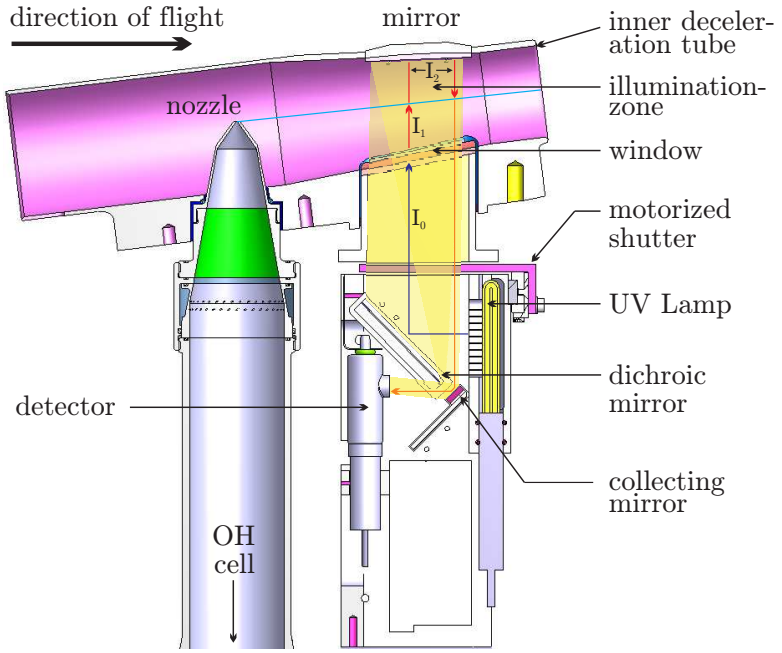

Figure 4.3: UV-unit of the in-flight calibration system. When the shutter is open the 185 nm radiation of the pen-ray lamp is deflected by the dichroic mirror into the inner deceleration tube and is reflected back at the top of the tube by a concave mirror and focused onto a collecting mirror in the UV-unit which guides the radiation to the detector. (Broch, 2011)

Experimental values have been published for the absorption cross-section and quantum yield and absolute water-vapour concentration measurements can be obtained from the BAHAMAS system of HALO (cf. Appendix B.3). However, values of the photon flux density and irradiation time in Equation 4.20 are difficult to measure in absolute terms and are determined indirectly as relative quantities (see below). Accordingly, the in-flight calibration can track only relative changes of the OH detection sensitivity. As will be shown in Section 4.2.3, the relative in-flight calibrations can be linked to absolute calibrations performed at ground.

The irradiation time in Equation 4.20 is proportional to the inverse velocity of the air which is tracked by a Pitot tube in the back of the inner deceleration tube. The inverse flow velocity is therefore used as a relative measure of the irradiation time.

The 185 nm intensity (I_{185}) of the UV-lamp is monitored by a solar-blind photomultiplier, which has a Cesium Iodide cathode (Hamamatsu R10825) that is sensitive to vacuum UV radiation (< 200 nm). In front of the entrance window of the photomultiplier, an optical interference filter (Acton Research 185HR) is installed which has a transmission maximum at 185 nm with a bandwidth of 27.5 nm (FWHM). In the UV unit, the light of the UV-lamp is deflected by the dichroic mirror and passes through

a fused silica window separating the UV-unit and the inner deceleration tube. On top of the tube is a concave mirror redirecting the light back into the UV-unit onto the collecting mirror which then guides the radiation to the detector (cf. Figure 4.3). The inner space of the UV-unit is sealed and permanently purged with dry nitrogen gas, in order to avoid absorption of the 185 nm radiation by water vapour or oxygen.

Besides the 185 nm emission line, the pen-ray lamp emits other atomic lines at longer wavelengths, which do not photolise water vapour, but could contribute to the photomultiplier signal. The most relevant line which could interfere is located at 254 nm and is about 10 times more intense than the one at 185 nm. The detection of 254 nm radiation is essentially eliminated in the UV-unit due to the spectral sensitivity of the solar-blind photomultiplier and the transmission filter. Furthermore, spectral selection is achieved by the dichroic mirror, which has a reflectivity of 95 % for 185 nm, but only 3 % for 254 nm (Broch, 2011). The radiation detected by the photomultiplier contains 80 % radiation that passes the inner deceleration tube along the light path shown in Figure 4.3, while 20 % came from scattered radiation inside the UV-unit. These numbers were determined by blocking the light path in the inner deceleration tube by a black cardboard. The background due to scattered radiation was corrected in the evaluation of the in-flight calibrations. In order to determine whether 254 nm radiation that passes the inner deceleration tube contributes to the 185 nm radiation signal, the inner deceleration tube was filled with N_2O gas, which absorbs 185 nm, but is transparent to the 254 nm radiation. The contribution of 254 nm to the photomultiplier signal compared to the black cardboard blockage was less than 0.5 %. The dark signal of the detector was completely negligible. For the purpose of stability the lamp was always switched on during the flights and a shutter between the UV lamp and the window was closed during normal measurement times. In addition the lamp, detector and amplifier were temperature controlled to counteract possible electronic drifts, when the pylon of the inlet system cooled down during flight at high altitudes. Going back to Equation 4.20, it can be written as

$$[\mathrm{OH}] \propto \frac{[\mathrm{H_2O}]\,\sigma_{\mathrm{H_2O}}\Phi_{\mathrm{OH}}\,f\!f\,I_{185}^{\mathrm{meas}}}{v_{\mathrm{inlet}}} \tag{4.21}$$

where $I_{185} = I_{185}^{\mathrm{meas}} \cdot f\!f$. The first quantity is the measured light intensity and $f\!f$ is the so called flight factor. It considers the fact that the radiation intensity in the centre of the deceleration tube, which is responsible for the artificial production of the measured OH, is not scaling linearly with the intensity received by the photomultiplier. The two intensities are differently affected by optical absorption due to ambient O_2 and H_2O in the deceleration tube, when the air pressure is changing with altitude. Water vapour in the above equation is taken from the BAHAMAS system of HALO, v_{inlet} is the air velocity inside the deceleration tube (cf. Equation 3.11), $\Phi_{\mathrm{OH}} = 1$ the OH quantum yield (cf. Table 4.2) and $\sigma_{\mathrm{H_2O}}$ the absorption cross-section of water vapour at 185 nm (cf. Table 4.2). This quantity has a slight positive temperature dependence which was measured by Cantrell et al. (1997) between 0 and 80 degree Celsius. For the evaluation of this work it was extrapolated linearly to negative temperatures with a variability up to 5 % over all altitudes. The calibration procedure by the photolysis of H_2O is only sensible if sufficient water vapour is present to produce OH concentrations much higher than background OH

which implies $[OH]_{cal} > 1 \times 10^{7\ molec/cm^3}$. At altitudes higher than 10 km this is not the case, limiting this method to below 10 km. The upper limit of concentrations created by this method with water mixing ratios of 2 to 3 % found close to ground is roughly $1 \times 10^{10\ molec/cm^3}$.

A quantitative expression for the flight factor can be derived from Figure 4.3. It shows the light path from the pen-ray lamp inside the UV unit through the inner deceleration tube and back onto the detector. The unit itself is flushed with nitrogen which does not absorb 185 nm. At the top of the inner deceleration tube is a mirror which doubles the light path in the inner deceleration tube and thereby enhances the OH production. The attenuation of the 185 nm radiation by oxygen and water vapour along the light path of length l through the tube can be described by Beer-Lambert's law

$$I_{185}(l) = I^0_{185} \exp\left[-l\left(\sigma_{H_2O}\,[H_2O] + \sigma^{app}_{O_2}(x)\,[O_2]\right)\right] \tag{4.22}$$

where I^0_{185} is the light intensity if no absorber is present and $x = [O_2]\,l$ is the column density of oxygen. σ_{H_2O} is constant over the spectral width of the Hg-emission line

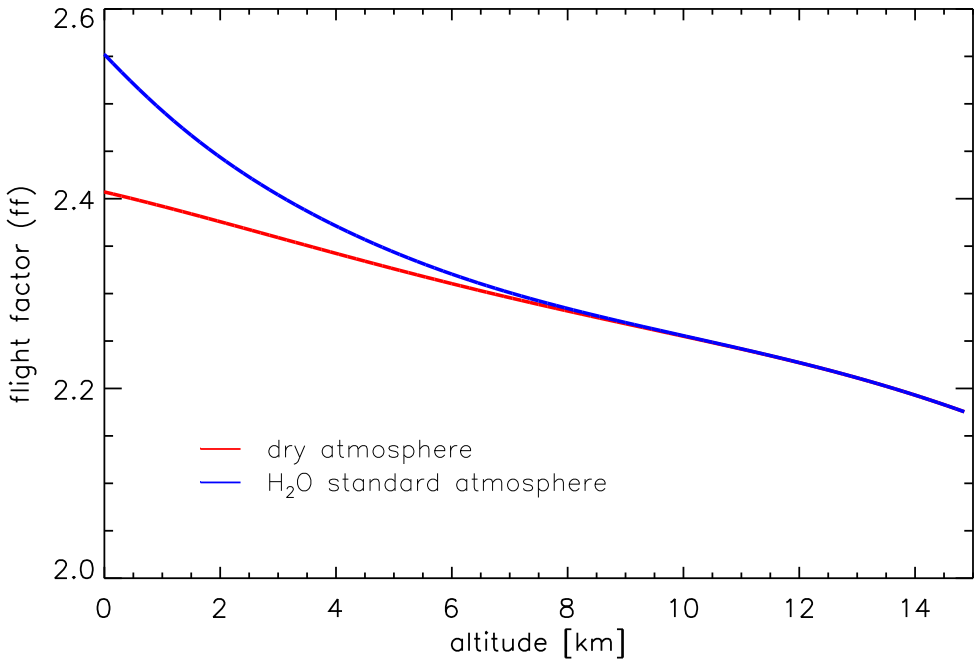

Figure 4.4: Flight factor $f\!f$ and its dependence on altitude for conditions during OMO inside the shrouded inlet shown for a dry atmosphere (red) and a H_2O standard atmosphere (blue).

and therefore independent of the column density x the light traverses. The absorption spectrum of oxygen on the other hand shows a distinct fine structure called Schumann-Runge bands, which leads to an apparent cross-section that depends on column density

$$\sigma^{app}_{O_2}(x) \equiv -\frac{1}{x}\,\ln\frac{I_{185}(x)}{I^0_{185}}\,. \tag{4.23}$$

It was measured for the inner deceleration tube in the laboratory within an independent experiment (cf. Appendix C.2). Finally, using Equation 4.22 an expression for the flight factor follows

$$\begin{aligned} I_{185}^{\text{centre}} &= \frac{I_{185}^{\text{centre}}}{I_{185}^{\text{meas}}} I_{185}^{\text{meas}} \\ &= \underbrace{\frac{I_{185}(l_1) + I_{185}(l_1 + l_2)}{I_{185}(l_1 + l_2 + l_1)}}_{\equiv \ell\ell} I_{185}^{\text{meas}} . \end{aligned} \tag{4.24}$$

The arguments $l_1 \approx 2.15\,\text{cm}$ and $l_2 \approx 3.85\,\text{cm}$ refer to the light path lengths, when the light has travelled from the fused window to the centre (l_1), and from the centre to the concave mirror back to the centre (l_2). This is depicted in Figure 4.3 where $I_1 = I_{185}(l_1)$ and $I_2 = I_{185}(l_1 + l_2)$. Figure 4.4 shows the calculated flight factor and its dependence on altitude for different water vapour mixing ratios. Note that both, the water vapour and the oxygen cross-section which go into $\ell\ell$ depend on temperature which is neglected here, since it is a secondary correction for $\ell\ell$ whose impact itself is relatively small (up to 10 %) with only a weak water vapour dependence in the upper troposphere.

4.2.2 Ground based calibrations

For ground based calibrations, a radical source is used that is typically deployed during ground based LIF measurements at 1 atm (Holland et al., 2003; Fuchs et al., 2011; Broch, 2011). Its basic principle also relies on the photolysis of water vapour (cf. Reaction R44 and R45). Synthetic air is humidified by sending it through a bubbler with Milli-Q water and then enters a quartz flow tube (cf. Figure 4.5), where water vapour is photolised by a pen-ray lamp at its end using collimated 185 nm radiation producing OH and HO_2 in equal amounts (Fuchs et al., 2011). For HO_2 calibrations, 250 ppm of CO (10 % in N_2) was added in order to convert all of the OH into HO_2

$$\text{OH} + \text{CO} \quad \xrightarrow{\text{O}_2} \quad \text{HO}_2 + \text{CO}_2 . \tag{R46}$$

The flow tube has an internal diameter of 18.7 mm and a frit at the top with the purpose to create a plug-flow behind it. The air will then develop a velocity profile over the length of the tube of 600 mm. With a flow of $20\,^{\text{std l}}/_{\text{min}}$ these values give a Reynolds number of $Re \approx 1600$ at 1 atm, which suggests a laminar flow by the time the air reaches the photolysis region. At these conditions, diffusion driven radical wall losses are negligible within the transit time from the photolysis region to the nozzle. The calculation of the OH concentration relies on the knowledge of the product $I_{185}t_{\text{rad}}$ in the centre of the flow tube (cf. Equation 4.20). This can be circumvented by expressing it in terms of the amount of ozone created, since the photolysis of oxygen takes place at the same wavelength (185 nm)

$$\text{O}_2 + h\nu \quad \longrightarrow \quad \text{O} + \text{O} \qquad \lambda = 185\,\text{nm} \tag{R47}$$

$$\text{O} + \text{O}_2 + \text{M} \quad \longrightarrow \quad \text{O}_3 + \text{M} \qquad \text{M} = \text{N}_2, \text{O}_2 . \tag{R48}$$

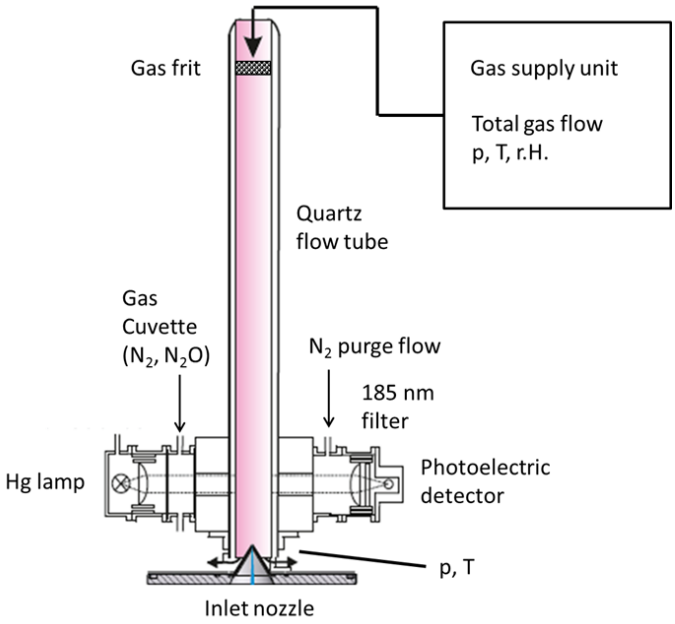

Figure 4.5: Scheme of a radical source used for ground-based calibration. A gas supply sends humidified air through a flow tube. Water is then photolised by a pen-ray lamp ($\lambda = 185\,\mathrm{nm}$) to produce OH and HO_2. The intensity of the light is measured by a photo-diode.

From this it follows

$$[O_3] = [O_2]\ \Phi_{O_3}\, t_{\mathrm{rad}} \int_{\text{Hg-185 nm}} \sigma_{O_2} I_\lambda \,\mathrm{d}\lambda\,, \tag{4.25}$$

but now the cross-section of oxygen can not be pulled in front of the integral, because it has fine structures in the Schumann-Runge band spectrum over the spectral width of the Hg-emission line (Sedlacek, 2001). It is therefore advisable to define an effective cross-section

$$\sigma_{O_2}^{\mathrm{eff}} = \frac{\int_{\text{Hg-185 nm}} \sigma_{O_2} I_\lambda \,\mathrm{d}\lambda}{\int_{\text{Hg-185 nm}} I_\lambda \,\mathrm{d}\lambda} \tag{4.26}$$

such that Equation 4.25 can be written as

$$[O_3] = [O_2]\ \sigma_{O_2}^{\mathrm{eff}} \Phi_{O_3}\, t_{\mathrm{rad}} I_{185}\,. \tag{4.27}$$

At constant radius and fixed velocity profile, the radiation time t_{rad} is inversely proportional to the volume flow rate through the tube and this equation can be simplified to

$$x_{O_3} = \frac{a\, I_{185}^{\mathrm{meas}}}{q_{\mathrm{v}}} \tag{4.28}$$

with a constant of proportionality a at fixed conditions. It can be determined experimentally by measuring the amount of ozone formed for a given volume flow q_{v} of synthetic air and measured intensity I_{185}^{meas}. The factor a is constant as long as the flow profile in the tube and the cross-section at the centre from which the nozzle

samples remain unchanged. This is a reasonable approximation, if the volume flow stays constant within 10 %. By combining Equation 4.20, 4.27 and 4.28 an expression for the OH mixing ratio is obtained

$$x_{\mathrm{OH}} = \frac{a\, I_{185}^{\mathrm{meas}}}{q_{\mathrm{v}}} \frac{[\mathrm{H_2O}]\ \sigma_{\mathrm{H_2O}} \Phi_{\mathrm{OH}}}{[\mathrm{O_2}]\ \sigma_{\mathrm{O_2}}^{\mathrm{eff}} \Phi_{\mathrm{O_3}}} \,. \tag{4.29}$$

All the quantities in 4.29 are either already known or can be measured. The volume flow q_{v} can be calculated from the mass flow which is regulated by a MFC (*mass flow controller*) if the pressure and temperature in the flow tube are known. The light intensity I_{185}^{meas} in units [V] is tracked by a photo detector as seen in Figure 4.5. A Vaisala HUMICAP sensor measures the relative humidity of the synthetic air which can then be converted into mixing ratios by measuring the pressure and temperature in the glass bulb of the HUMICAP. The effective cross-section $\sigma_{\mathrm{O_2}}^{\mathrm{eff}}$ is also measurable (Hofzumahaus et al., 1997; Sedlacek, 2001), but the absolute value depends on the spectral lamp profile and pre-absorption by O_2, and varies within ±15 % for different calibration sources used at FZJ. During OMO the calibration source KQ4 was used on the HO_2 channel. For it an effective oxygen cross-section of $1.28 \times 10^{-20}\,\mathrm{cm}^2$ was adopted from previous measurements with KQ2 (cf. Table 4.2). The method for measuring the ozone production factor a is described in Appendix C.4. For KQ4, a value of 73 ± 2 $^{\mathrm{ppb\,cm^3}}/_{\mathrm{V\,s}}$ at 1 atm was determined. The yields and the water vapour absorption cross-section are literature values and given in Table 4.2. The total uncertainty of a calibration with KQ4 will then be dominated by the measurement error of the effective oxygen cross-section and is roughly 15 %.

During the OMO campaign, the radical source KQ4 was directly mounted on top of the HO_2 inlet for calibration. KQ4 is however not suitable for use on the OH inlet, which is enclosed by the shrouded inlet system. For ground-based OH calibrations, a quartz tube (18.7 mm internal diameter) which is solidly mounted in a round aluminium frame, was coaxially inserted into the inner deceleration tube (cf. Figure 4.6).

Table 4.2: Cross-sections and quantum yields needed for the calculation of the OH concentration in the radical source (cf. Equation 4.29). The cross-sections shown are for 1 atm and 20 °C. The temperature dependent absorption cross-section measured by Cantrell et al. (1997) agrees at room temperature within a few percent with the value obtained by Hofzumahaus et al. (1997).

Parameter	Value	Error [%] (1σ)	Source
$\sigma_{\mathrm{H_2O}}$	$7.1 \times 10^{-20}\,\mathrm{cm}^2$	3	Cantrell et al. (1997)
$\sigma_{\mathrm{O_2}}^{\mathrm{eff}}$	$1.28 \times 10^{-20}\,\mathrm{cm}^2$	15	Sedlacek (2001)
Φ_{OH}	1.0	$<$ 0.5	Engel et al. (1992)
$\Phi_{\mathrm{O_3}}$	2.0	$<$ 0.5	by stoichiometry

A flow of 20 $^{\mathrm{std\,l}}/_{\mathrm{min}}$ of humidified air enters the quartz tube at the front and overflows the OH inlet nozzle after leaving the tube. OH radicals are produced inside the quartz tube by water vapour photolysis using the 185 nm radiation from the pen-ray lamp of the UV unit. This set-up was used as a secondary calibration standard

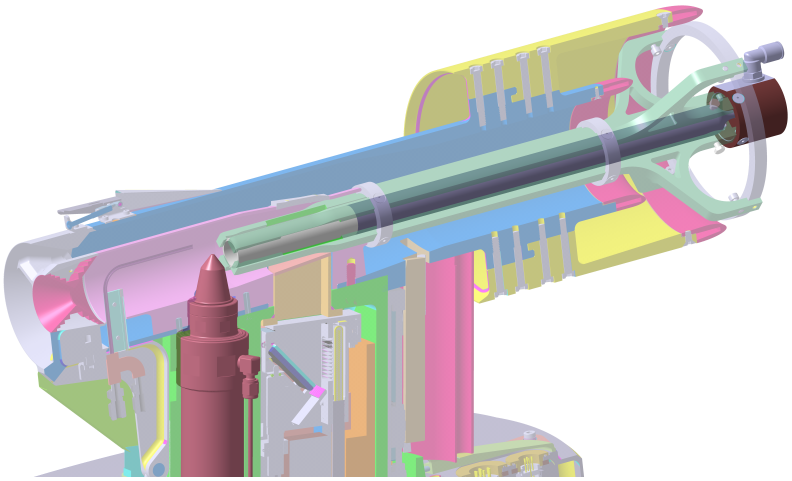

Figure 4.6: Since the use of KQ4 required access to the OH nozzle blocked by the inlet system, a secondary calibration standard was used during OMO.

which was inter-calibrated against KQ4 in the laboratory at the beginning of the OMO campaign. The dependence of the produced OH concentration on the water vapour concentration, the volume flow through the quartz tube and the pen-ray lamp intensity were taken into account according to Equation 4.29. The inter-calibration adds an additional uncertainty to the 15 % coming from KQ4, and the total error for a calibration with the secondary standard becomes 20 %.

4.2.3 Field calibration results

During OMO, calibrations were done between flights and when HALO was stationed on Cyprus. This was roughly every second day. Since the inlet system was on top of the air plane, it had to be accessed by a platform as can be seen in Figure 4.7. A close up of the set-up is depicted in Figure 4.8. In-flight calibrations were done when HALO was on a constant flight level.

OH channel

The ground calibrations of the OH channel over the period of OMO are shown in Figure 4.9. The calibrations were performed at Oberpfaffenhofen and on Cyprus at slightly different altitudes above sea level. At Oberpfaffenhofen (in the week before 20 July 2015) the ambient pressure was 951 ± 5 hPa and the ambient temperature was 297 ± 1 K. On Cyprus, pressure and temperature at ground were 1005 ± 1 hPa and 303 ± 1 K, respectively. In order to compare the calibrations, the influence of ambient pressure and temperature variations at the two different locations has been removed by normalization to standard conditions using Equation 4.30

$$C_{\mathrm{OH},0} = \frac{\omega_0 \eta_0}{\omega \eta} C_{\mathrm{OH}} \,. \tag{4.30}$$

The not indexed quantities are the individual results from each calibration and those with subscript 0 refer to a reference state. This state was arbitrarily chosen to be the mean static temperature (303 K) and static pressure (1005 hPa) on Cyprus during

Figure 4.7: The OH and HO_2 inlets were on top of HALO and had to be accessed by a platform.

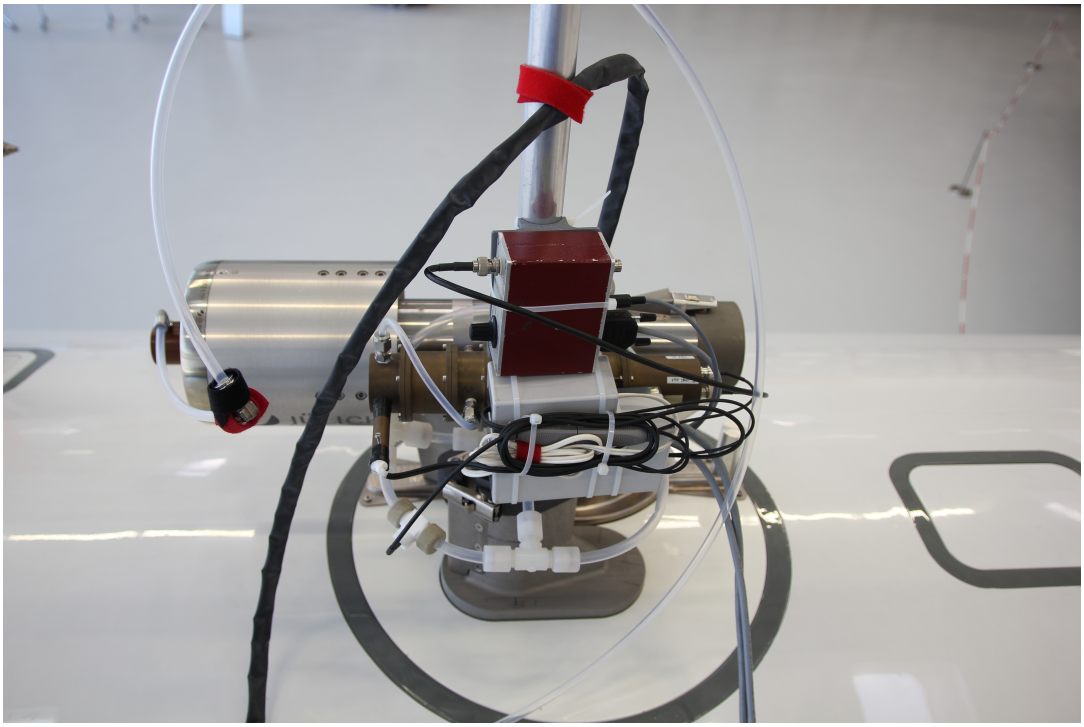

Figure 4.8: Calibration of the OH and HO_2 channel while HALO is in the flight hangar.

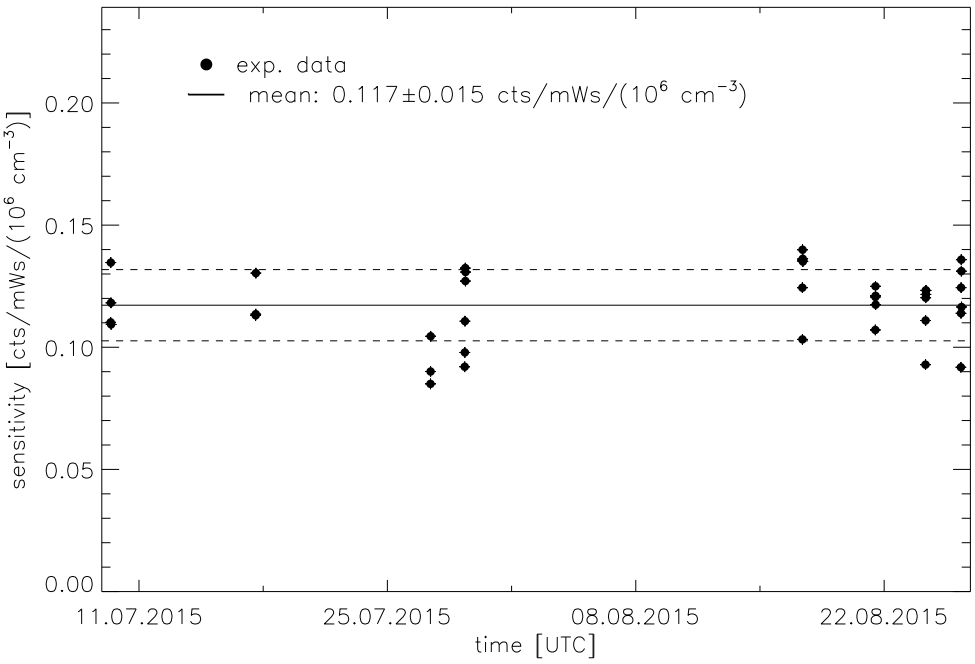

Figure 4.9: Ground based sensitivity of the OH channel during OMO normalized to standard conditions. Dashed lines show the 1σ uncertainty and error bars are covered by the individual data points.

ground calibrations with a mean cell pressure of 11 hPa. In addition, as calibrations were done at different water vapour concentrations, the influence of fluorescence quenching by water vapour η (cf. Equation 3.4) has been normalized to an H_2O mixing ratio of 1 %. This assumes complete mixing of the sampled calibration and purge gas (N_2). The normalized sensitivities where checked for potential laser power dependence and none was found.

The mean normalized sensitivity over the entire campaign is 0.117 ± 0.015 $^{\mathrm{cts}}/_{\mathrm{mW\,s\,10^6/cm^3}}$ with no noticeable trend over time.

HO_2 channel

The HO_2 calibrations were done using the KQ4 radical source. The entire procedure is more comprehensive, because different modes have to be measured. Since the radical source provides OH and HO_2 in equal amounts, the sensitivity with respect to HO_2 can be immediately acquired by converting all OH to HO_2 via the addition of CO to the synthetic air

$$S_{\mathrm{HO_2}} = 2\, C_{\mathrm{HO_2}}\, [\mathrm{HO_2}] \ . \tag{4.31}$$

The OH sensitivity on the HO_2 channel is then obtained without the addition of CO, for then the quantity

$$S_{\mathrm{HO_x}} = C_{\mathrm{OH}}\, [\mathrm{OH}] + C_{\mathrm{HO_2}}\, [\mathrm{HO_2}] \tag{4.32}$$

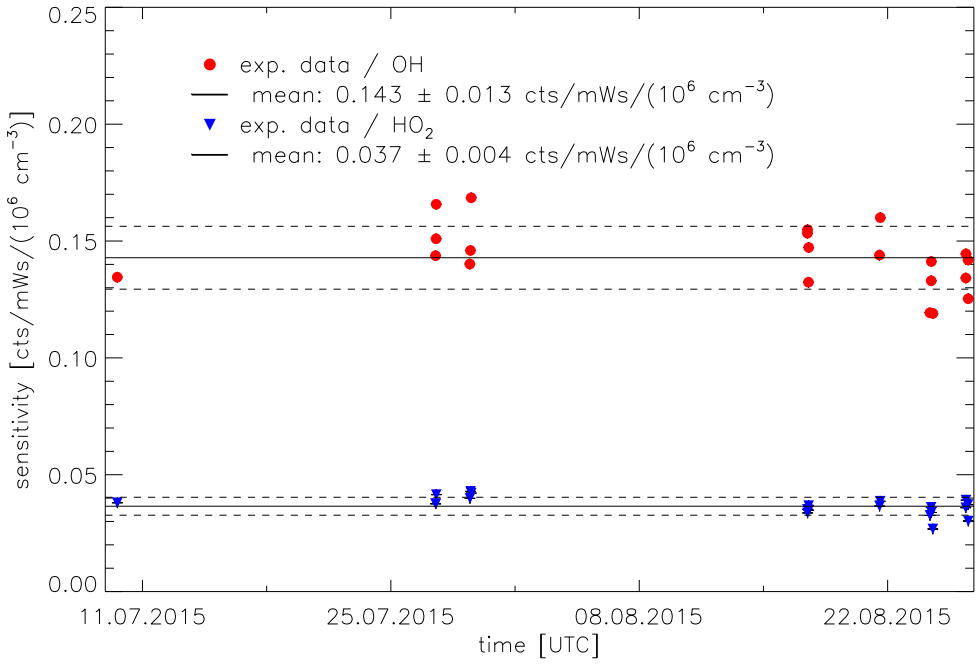

Figure 4.10: Ground-based sensitivities for OH and HO_2 in the HO_2 channel during OMO. Calibrations were done at different water vapour concentrations. The varying influence of the fluorescence quenching by H_2O was removed by normalisation to a water vapour mixing ratio of 1 %. Dashed lines show the 1σ uncertainty and error bars are covered by the individual data points.

is measured while noting $[OH] = [HO_2]$. The result is shown in Figure 4.10 where a campaign mean of 0.037 ± 0.004 $^{cts}/_{mW\,s\,10^6/cm^3}$ for the normalized (cf. Equation 4.30) HO_2 sensitivity was found. It is almost a factor of 4 smaller than the OH sensitivity on the HO_2 cell, because only a fraction of the HO_2 is converted to OH in order to suppress unwanted RO_2 interferences (cf. Section 4.6). The OH sensitivity is not needed, because the OH is lost in the inlet tube of the HO_2 cell at high air speeds during flights (cf. Section 3.4.2). A third mode was frequently run by adding methane to the synthetic air. This converts all the OH to CH_3O_2 to track the sensitivity with respect the methyl-peroxy radicals, which by design (low NO addition in the cell) was supposed to be negligible.

Connecting OH ground- to in-flight calibrations

Ground based calibrations were typically done at 11 hPa cell pressure. In-flight calibrations were evaluated for all altitudes up to 10 km, but the lowest altitude in-flight calibration was done at 10.5 hPa during OMO-EU over the Mediterranean sea. As with the calibrations in Oberpfaffenhofen, this already had a slight impact on the sensitivity. In this regime the main influence on the sensitivity is the fluorescence yield η and the expansion ratio ω, which can be calculated by instrumental and meteorological data. By labelling the normalized quantities at ground calibration conditions with a 0 (cf. Equation 4.30) and with a 1 for the lowest flight altitude

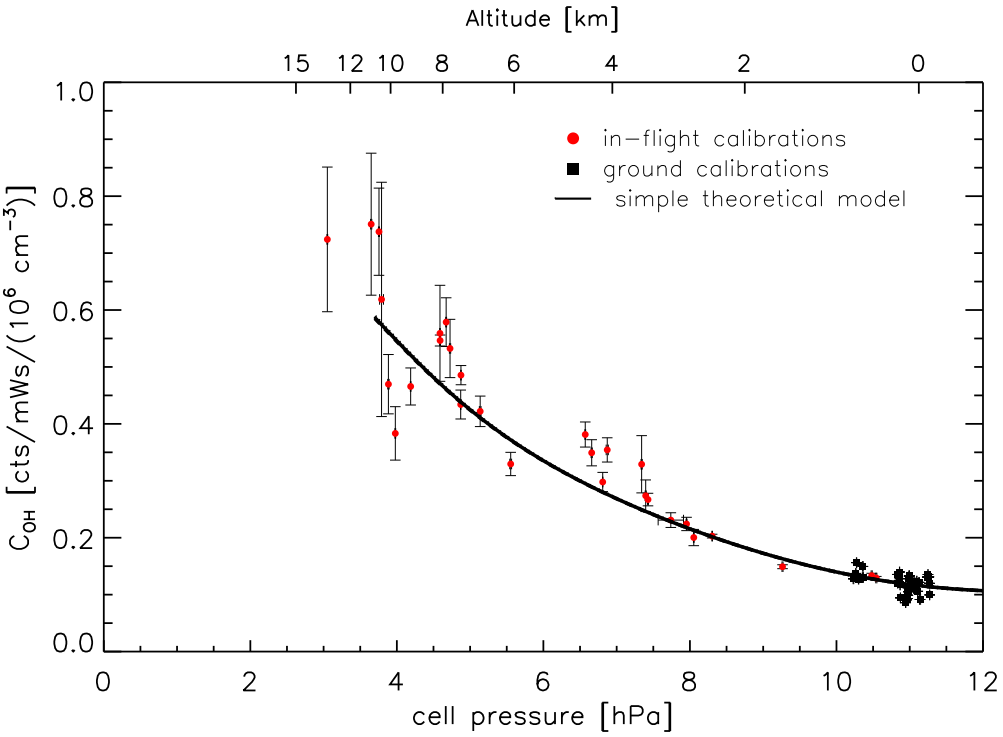

Figure 4.11: The calculated in-flight sensitivity (red circles) is normalized to the sensitivity $C_{\mathrm{OH},1}$ obtained from the ground calibrations (black squares).

with an in-flight calibration, the latter can therefore be written as

$$C_{\mathrm{OH},1} = \frac{\omega_1 \eta_1}{\omega_0 \eta_0} C_{\mathrm{OH},0} \,. \tag{4.33}$$

The calculated relative in-flight sensitivity (cf. Equation 4.21, ambient OH is interpolated and subtracted from the signal) is then normalized to $C_{\mathrm{OH},1}$ at its cell pressure of 10.5 hPa and the associated static inlet pressure and temperature. Besides the result shown in Figure 4.11, it also shows the ground calibrations (black squares) done on Cyprus (11 hPa) and in Oberpfaffenhofen (10.3 hPa). These are uncorrected and as pointed out above the sensitivities obtained from Oberpfaffenhofen are slightly increased, which however is in accordance with the in-flight calibration result and the simple model used as a parametrization. This model is only based on ω, η and β (cf. Equation 4.16).

4.3 Laboratory OH calibration

The procedure described in the previous section gives altitude-dependent calibration factors only for the OH cell up to 10 km. For higher altitudes and for the HO_2 cell, additional laboratory calibrations were performed. The increase of the OH sensitivity with altitude (cf. Figure 4.11) is essentially due to the reduced cell pressure at higher altitudes, that is caused by a decreasing mass flow through the inlet nozzle as a result of the lower static ambient pressure. On the highest flight level at 15 km altitude, the static ambient pressure was roughly 130 hPa which corresponds to a static inlet pressure (OH inlet) of 200 hPa while the HO_2 inlet pressure was only

80 hPa (cf. Figure B.3). At the same time cell pressure was approximately 2.7 hPa (cf. Figure B.4). After the OMO campaign two additional complementary calibration methods were deployed in the laboratory to further characterize the altitude dependence of the sensitivities, which differ in the way the mass flow through the nozzle is varied:

- Calibration by a newly developed radical source KQ5, which supplies known OH and HO_2 concentrations in synthetic air between 50 and 1000 hPa pressure and therefore simulates inlet pressures up to 15 km.
- Calibration by a radical source at 1000 hPa inlet pressure while the reduced mass flow through the inlet nozzle is achieved with different nozzle orifice diameters.

4.3.1 Variation of inlet pressure

A new radical source (KQ5) was devised and built by ZEA at Forschungszentrum Jülich which can be vacuumed to simulate ambient pressures up to 15 km altitude (cf. Figure 4.12). The dimensions of the source (inner tube diameter: 18.7 mm, tube length: 600 mm) and the functional principle are the same to that of the radical source (cf. Figure 4.5) described in Section 4.2.2 which was used for ground based calibrations. However, the new source allows to control the pressure in the flow tube by means of a vacuum pump at the exhaust of the source. This source is also operated at 20 $^{\mathrm{std\,l}}/_{\mathrm{min}}$ of humidified synthetic air. The mode of operation is the same as for the radical source KQ4. The applicability of Equation 4.29 for the calculation of absolute radical concentrations at reduced pressures requires that the various experimental parameters in the equation are known as a function of pressure and that radical losses remain negligible over the whole range of applied pressures (50 to 1000 hPa).

The quantities $[O_2]$, $[H_2O]$, $[M]$, I_{185}^{meas} and q_v are either directly measured or can be deduced from measurements. While σ_{H_2O} is pressure independent, the effective oxygen cross-section $\sigma_{O_2}^{\mathrm{eff}}$ has to be measured in dependence of pressure (cf. Appendix C.3). The ozone production factor a also has to be known as a function of pressure (cf. Appendix C.4). The OH quantum yield ($\Phi_{OH} = 1$) is independent of pressure, because the dissociation of electronically excited water molecules is much faster than collisional deactivation (Engel et al., 1992). The situation is more complicated for the quantum yield of ozone, because the time needed for conversion of $O(^3P)$ atoms to O_3 is strongly pressure dependent. As discussed in Appendix C.4, even at reduced pressures the transport time from the photolysis region to the inlet nozzle is sufficiently long to convert all $O(^3P)$ to O_3, resulting in a quantum yield of 2. Similar considerations are done for the conversion of H-atoms from water photolysis to HO_2 where transport times are order of magnitude larger than the H-lifetime. Since the application of Equation 4.29 assumes that no radical losses occur from the photolysis region to the inlet nozzle, some theoretical investigations were undertaken to estimate if the assumption of laminarity remains fulfilled. This included a complete CFD modelling of the source, but simple criteria can already be drawn from two aspects:

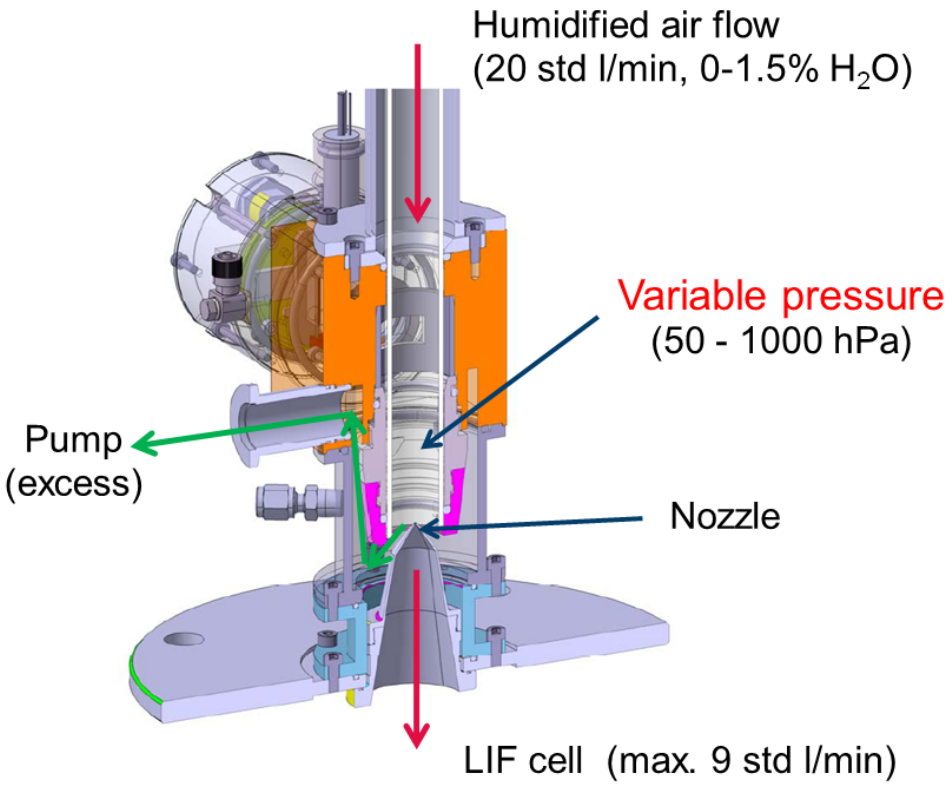

Figure 4.12: Section of the new radical source KQ5 showing pressure and flow conditions (technical drawing by P. Jansen, ZEA-1, Forschungszentrum Jülich).

- Laminarity applies if the dimensionless Reynolds number $Re = \frac{\rho v d}{\eta}$ has a value of less than 2300 (Rotta, 1956). Here ρ is the density of air, v the mean air velocity, d the tube diameter and η the dynamic viscosity. While the latter two quantities are independent of pressure in the regime the source is run, the product ρv (mass flux density) is associated to the total mass flow which is constant ($20\,^{\mathrm{std\,l}}/_{\mathrm{min}}$). This implies that the Reynolds number does not change i.e. $Re \approx 1600$ and laminarity should be present over the relevant pressure range.

- Laminar conditions imply that wall losses of the radicals occur only by molecular diffusion to the tube wall. At atmospheric pressure, this process is much slower than the transport of OH to the nozzle and can be neglected. The rate at which the circular cross-section of the diffusion front increases is $4\pi D$, where $D = D(p)$ is the diffusion coefficient which is inversely proportional to the pressure p. Since at constant mass flow through the tube the transition time t of air from the photolysis region to the nozzle is proportional to the pressure, the product $D \cdot t$ as a measure of the degree by which the front propagates is independent of the pressure, thereby implying that to a first approximation the OH concentration is not affected by wall loss when the source is run at lower pressure, if it is already well behaved at ground conditions.

The CFD model is based on the commercial software ANSYS Fluent, which uses a 3D-CAD model of the radical source shown in Figure 4.12 to initialize the flow

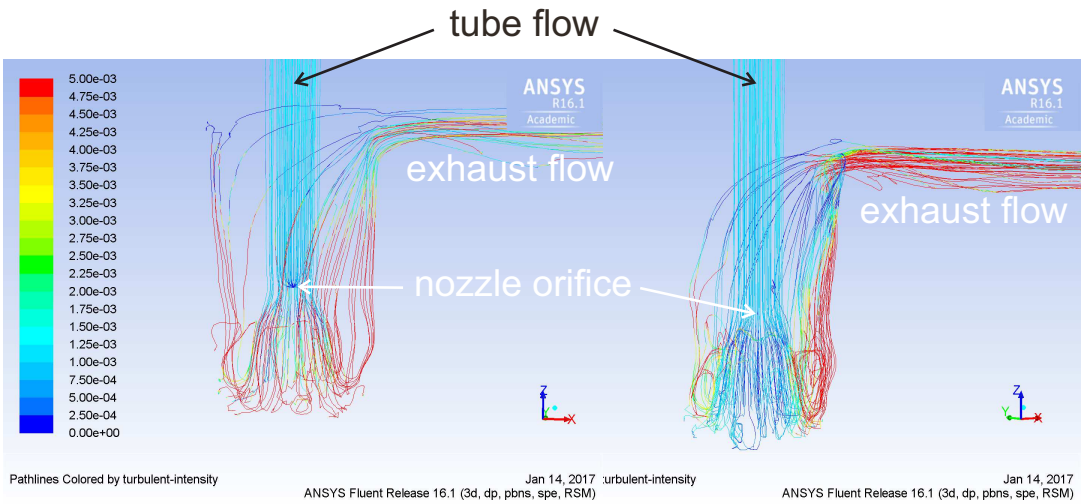

Figure 4.13: CFD model calculation with ANSYS Fluent at room temperature and $20\,\mathrm{std\,l/min}$. The colour code shows the dimensionless quantity turbulent intensity v'/v. **Left:** Calculation done at 1000 hPa. **Right:** Calculation done at 100 hPa.

regime and runs a complete steady Reynold-Stress Omega turbulence model. To quantify turbulence, an important quantity is one third of the trace of the Reynold-Stress tensor $v'^2 = \frac{1}{3}\left(\overline{v'^2_x} + \overline{v'^2_y} + \overline{v'^2_z}\right)$, which gives the mean fluctuation velocity magnitude v'. The ratio with respect to the velocity magnitude v of the fluid then defines the turbulent intensity $I = \frac{v'}{v}$. If $I < 1\,\%$, turbulence is generally considered low (ANS, 2018). Figure 4.13 shows the pathlines of a test particle colour coded by turbulent intensity. As can be seen, turbulent intensity is roughly 0.1 % up until the point where the test particle reaches the nozzle inlet, giving a good proxy for laminarity. In particular turbulence compares well to the calculation at 1000 hPa (cf. Figure 4.13, left panel), for which wall losses by diffusion are known to be negligible. Turbulence only starts to occur after the nozzle has been passed and excess air is guided into the exhaust line (colour code for turbulent intensity is limited to below 0.5 %, implying that red pathlines can have much higher turbulence).

For the practical application of the pressure dependent laboratory calibration which aims to simulate the boundary conditions during flight, there are several other aspect that have to be considered. As the inlet tube was heated close to 20 °C during flight (cf. Table 3.2), the application of the new radical source under laboratory conditions should generally be admissible. In order to simulate the pressure pairs $(p_{\mathrm{cell}}, p_{\mathrm{inlet}})$ for various altitudes, it is not enough to start with the corresponding pair at ground conditions and consecutively vary the pressure in the source. This is because the pumping speed in the laboratory is almost constant, while during flight both cells were pumped parallel and the load on each cell changed due to the different mass flows through each nozzle. Additionally the overall total pumping speed changes with altitude as cell and exhaust pressure changes. Therefore both pressures were regulated using MKS pressure regulators according to the $(p_{\mathrm{cell}}, p_{\mathrm{inlet}})$ in-flight pressure curve (cf. Figure B.3 and B.4). As the purge mass flow (N_2) adds to the cell pressure, it was kept the same during calibrations as during the flights. According to Equation 3.12 the mass-flow through the nozzle is determined

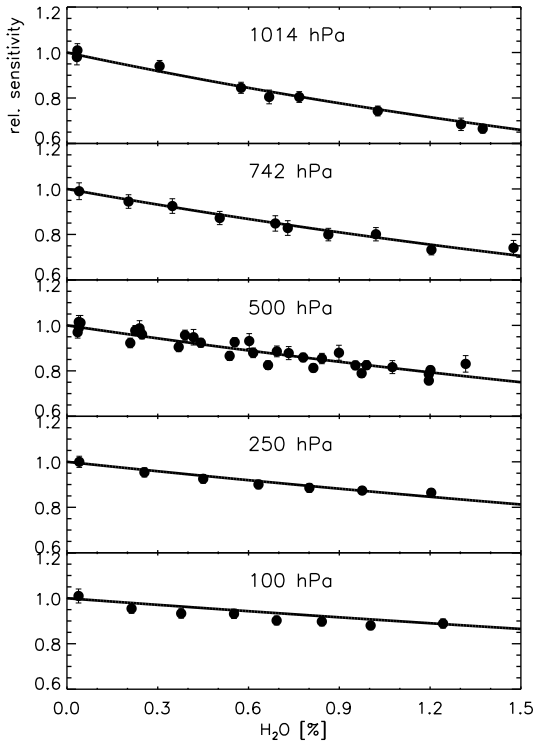

Figure 4.14: Relative water-vapour dependence of the OH detection sensitivity at different inlet pressures. Solid lines represent the theoretical dependence of the fluorescence yield (cf. Equation 3.4). Circles are experimental data scaled to 1 at $H_2O = 0$ by a linear least square fit.

by $n_{\text{inlet}}\, q_{\text{noz}}$. During the laboratory calibrations, the temperature of the calibration gas was approximately 296 K, whereas the inlet temperatures during the flights were in the range between 210 K and 300 K (cf. Figure B.6). As the mass flow through the inlet nozzle depends inversely on the square root of the inlet temperature, the reduced temperatures during the flights were compensated by an increase in the inlet pressure for laboratory calibrations ($n_{\text{inlet}}\, q_{\text{noz}} \sim \frac{p_{\text{inlet}}}{T_{\text{inlet}}} \cdot \sqrt{T_{\text{inlet}}} = \frac{p_{\text{inlet}}}{\sqrt{T_{\text{inlet}}}}$) i.e.

$$\frac{p_{\text{fl}}}{\sqrt{T_{\text{fl}}}} = \frac{p_{\text{lab}}}{\sqrt{T_{\text{lab}}}} \qquad \Longleftrightarrow \qquad p_{\text{lab}} = p_{\text{fl}} \sqrt{\frac{T_{\text{lab}}}{T_{\text{fl}}}}\,, \tag{4.34}$$

where the subscript fl stands for in-flight and lab for laboratory. For the lowest temperature (210 K at 15 km altitude), the required pressure increase is 19 %.

Calibrations were performed for the OH and HO_2 cell at various pressures. At each pressure, the water-vapour mixing ratio in the calibration gas was varied from 0.1 % to 1.2 % to study the influence of H_2O on the radical detection (cf. Figure 4.14). This water-vapour dependence obtained from the laboratory OH and HO_2 calibrations is described very well by theory (cf. Equation 3.4). Figure 4.14 shows the relative OH detection sensitivity as a function of the water-vapour mixing ratio at different inlet pressures. At 1 atm, the reduction for 1 % of water vapour is largest (23 %). The effect becomes smaller at lower pressures, because the air number density decreases.

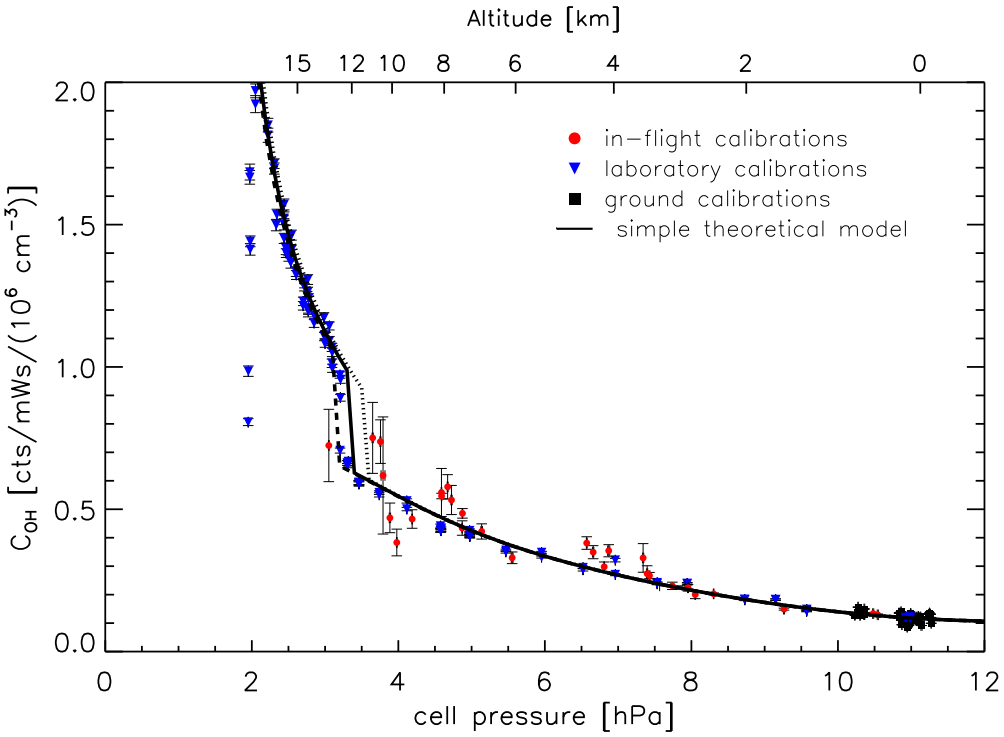

Figure 4.15: Pressure dependent OH sensitivity. Red data show in-flight calibrations while blue dots show the pressure dependent sensitivity obtained with the new pressure adjustable radical source. All values were normalized to 1 % water using η from Equation 3.4. Errors in the in-flight calibrations increased rapidly with decreasing cell pressure, since ambient water vapour became rather scarce as altitude increased.

At low pressures (100 to 250 hPa) the sensitivity reduction for 1 % of water vapour is between 7 and 13 %. However, due to the very small mixing ratios (< 0.01 %) in the cold upper troposphere, the relative effect of H_2O on the OH detection sensitivity becomes smaller than 1 % above an altitude of 10 km. During OMO, a slightly larger dependence on H_2O was observed than predicted by theory, which accounts for part of the scatter of the normalized sensitivity data (cf. Figure 4.9). The reason was the use of a different photomultiplier with a slower rise time of the PMT gate when it was turned on after the laser pulse. This behaviour had a small influence on the effective dependence of the measured OH signal on water vapour, but played no role for respective sensitivity variations in the upper troposphere where the quenching by water vapour is negligible. For the HO_2 cell, the dependence of the detection sensitivity on water vapour followed the theoretical prediction during OMO ground-based calibrations and laboratory calibrations as well.

Figure 4.15 shows the pressure and altitude dependence of the OH detection sensitivity obtained from laboratory experiments using calibration source KQ5 (blue triangles). At each pressure, several data points were recorded at different water-vapour mixing ratios and normalized to 1 % water concentration. Because the PMT used during OMO had a different photon detection sensitivity (roughly factor 1.6), the pressure-dependent laboratory calibration curve has been normalized to 1 at the mean reference cell pressure during the ground-based calibrations on Cyprus

and subsequently multiplied by the campaign mean OH ground sensitivity (cf. Figure 4.9) to match the field calibrations which are also shown in Figure 4.15. The curves shown in this Figure are for a constant ambient temperature of 20 °C, as the expansion ratio introduces a slight T-dependence. Apparently, the laboratory results have a higher precision than the field calibration data. When the cell pressure decreases from 11 hPa (0 km altitude) to 3.3 hPa (12 km altitude), both data sets show a consistent steady increase of the OH detection sensitivity by a factor of 6. Below 3.3 hPa, the laboratory calibration shows a sudden discontinuous increase of the sensitivity by a factor of 1.5, which could not be tracked by in-flight calibrations due to decreasingly small water vapour concentrations. At even lower cell pressures, the OH detection sensitivity continues to increase strongly down to 2 hPa cell pressure. However, for the evaluation of the flight data only altitudes less than 15 km are relevant, which corresponds to 2.7 hPa cell pressure. During flights, the cell pressure showed some variability at a given pressure altitude, because the pumping speed of the instrument was not entirely constant and the inlet pressures of the detection cells were dynamically influenced by the flight velocity of the aircraft (cf. Appendix B.3). For that reason, the cell pressure shows an uncertainty of ± 0.17 hPa (1σ) which propagates to the uncertainty of the position of the jump in OH sensitivity. This uncertainty is indicated by the vertical dashed lines in Figure 4.15 and is further discussed in Section 4.7. Beside experimental calibration data, Figure 4.15 also shows the result of a simple theoretical model which represents well the calibrations between 2 hPa and 11.5 hPa. An in-depth analysis of its pressure dependence can be found in Section 4.5.1.

4.3.2 Variation of inlet nozzle diameter

A different calibration concept for airborne OH instruments using gas expansion and LIF detection has been applied for the ATHOS instrument on the NASA-DC8 (Faloona et al., 2004), the HORUS instrument on a Lear-jet (Martinez et al., 2010) and the FAGE instrument on the British BAe-146 (Commane et al., 2010). In all cases, the variation of the cell pressure at different flight altitudes was simulated at ground by varying the orifice diameter of the inlet nozzle at constant atmospheric pressure (1 atm). This concept is assumed to yield the same OH detection sensitivity $\tilde{C}_{\mathrm{OH}}$ as that during flight at the same cell pressure, when the detection sensitivity refers to OH mixing ratios x_{OH} (Faloona et al., 2004),

$$S_{\mathrm{OH}} = \tilde{C}_{\mathrm{OH}}\, x_{\mathrm{OH}} \tag{4.35}$$

where $\tilde{C}_{\mathrm{OH}} = C_{\mathrm{OH}} \cdot n_{\mathrm{amb}}$. With η, β, ω from Equation 3.4, 4.16, 4.12, it follows by Equation 4.18

$$\begin{aligned} \tilde{C}_{\mathrm{OH}} &= \text{const.} \cdot \eta\left(p_{\mathrm{cell}}\right) \cdot \beta\left(p_{\mathrm{cell}} \cdot q_{\mathrm{tube}}\right) \cdot \omega\left(T_{\mathrm{inlet}}, q_{\mathrm{tube}}\right) \cdot n_{\mathrm{amb}} \\ &= \text{const.} \cdot \eta\left(p_{\mathrm{cell}}\right) \cdot \beta\left(p_{\mathrm{cell}} \cdot q_{\mathrm{tube}}\right) \cdot \frac{q_{\mathrm{noz}} n_{\mathrm{amb}}}{q_{\mathrm{tube}}}\,. \end{aligned} \tag{4.36}$$

The mass flow $q_{\mathrm{noz}} n_{\mathrm{amb}}$ through the nozzle can be varied by adjusting the pressure in-front of the nozzle or by changing the volume flow rate through the nozzle. The latter is achieved with different nozzle orifice diameters (cf. Equation 3.14). In any case, at given purge flows and fixed pump speed on the cell, the same cell pressure

p_{cell} will set in (cf. Equation 3.12) as long as the mass flow through the nozzle is unchanged. This obviously implies the same volume flow rate q_{tube} through the tube (cf. Equation 3.13). Hence, the product $\omega \cdot n_{\text{amb}}$ is invariant and therefore also $\tilde{C}_{\text{OH}}$ should not change.

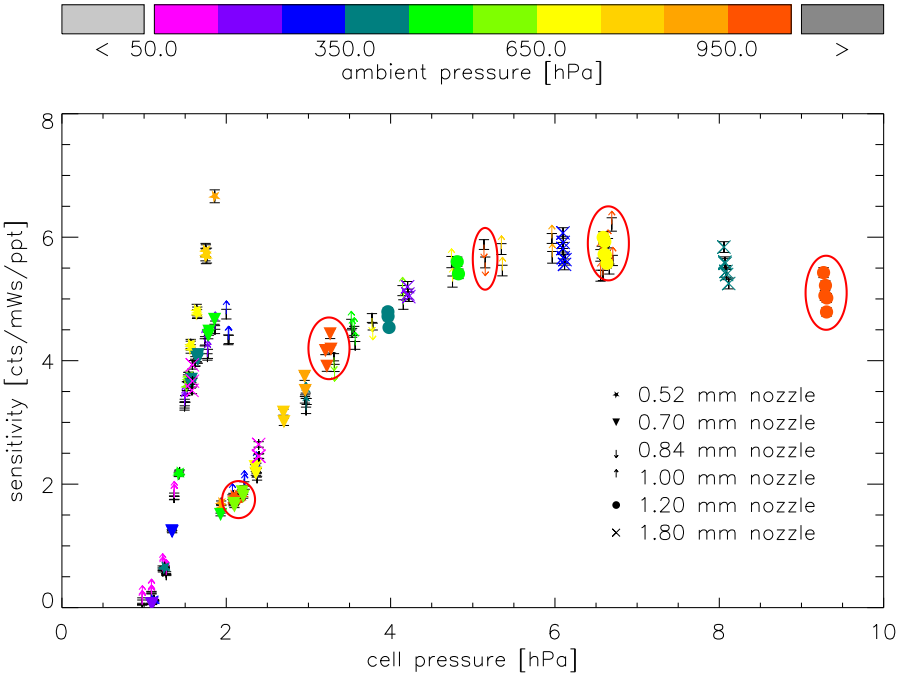

Figure 4.16: Sensitivity in units $^{\text{cts}}/_{\text{mW s ppt}}$ against the cell pressure. Varying the pressure in the radical source at constant nozzle orifice diameter is essentially equivalent to changing the nozzle orifice diameter in order to obtain the same cell pressure. The red circles distinguish the traditional calibrations done at atmospheric pressure (orange data) from the rest.

The theoretical expectation was tested in the laboratory. Different inlet nozzles with diameters between 0.52 mm and 1.80 mm were mounted on the OH detection cell and pressure dependent calibration curves were measured for each nozzle as described in the previous section 4.3.1. For the measurements, the pump was directly connected to the cell with no valves in between and the pump speed was assumed to be constant or at least changed in a reproducible way as various mass flows were set. This implies that mass flow and cell pressure can be used simultaneously, that is a specific nozzle size or a corresponding ambient pressure with a different nozzle size leading to the same mass flow, give the same cell pressure. No tube or cell purge N_2 gas flows were used; only a baffle purge flow of $0.2\,^{\text{std l}}/_{\text{min}}$ N_2 gas to prevent dead volumes at the baffle arms. This however does not affect the tube gas flow relevant for the detection volume, and hence the mass flow through the nozzle is equal to the mass flow through the tube. Since the nozzle factor μ in Equation 3.14 was determined explicitly only for the 1 mm nozzle, these factors for the other nozzles were calibrated such that all mass flow cell pressure curves - which at constant pumping speed are linearly related by Equation 3.12 - for the various nozzles lie on top of

each other (cf. Figure C.9). The μ-values are summarized in Table C.1.

The evaluation was done with the same pressure dependent ozone production factor which was determined for the 1 mm nozzle (cf. Appendix C.4), while each nozzle should - in principle - have its own a-factor. The a-factor is proportional to the effective oxygen cross-section $\sigma_{O_2}^{eff}$ which changes with pressure in the calibration tube. This effect can be corrected by means of the measured data shown in Figure C.7. Furthermore, the a-factor depends on the flow velocity profile and the mass flow fraction that is sampled by the nozzle. As the geometry and mass flow of the flow tube are fixed, the Reynold number is constant (cf. Section 4.3.1). For this boundary condition, the development of a laminar flow profile in a cylindrical tube is invariant and independent of total pressure in the tube (Sparrow et al., 1964). Also the sampled mass flow fraction is constant, because the mass flow through the tube as well as through the nozzle were kept constant at given cell pressure. As a result the ozone production factor $a_d(p)$ for the nozzle with diameter d and at radical source tube pressure p can be expressed as

$$a_d(p) = a_{d_0}(p_0)\,\frac{\sigma_{O_2}^{eff}(p)}{\sigma_{O_2}^{eff}(p_0)} \tag{4.37}$$

where $d_0 = 1\,\text{mm}$ and p_0 is the radical source tube pressure for which the 1 mm nozzle yields the same cell pressure as the set-up with nozzle diameter d and radical source tube pressure p. The net effect is small though, since the total variability of the ozone production factor is limited by 6 % (cf. Figure C.8) and also the effective oxygen cross-section is only weakly dependent on the number density inside the tube (cf. Figure C.7). In particular the effects of both factors partially cancel, limiting the overall influence to less than 3 %.

Figure 4.16 shows the OH detection sensitivity $\tilde{C}_{OH}$ measured for different nozzle diameters as a function of cell pressure. The variation of the nozzle orifice between 0.52 mm and 1.8 mm corresponds to an inlet pressure variation at fixed nozzle size by a factor of up to 12. Between 2 hPa and 10 hPa the cell-pressure dependence of $\tilde{C}_{OH}$ is found to be the same for all tested nozzles. The agreement of the single curves confirms, that the factors β and $\omega \cdot n_{amb}$ really only depend on the mass-flow through the nozzle, but not on the dimension of the nozzle orifice which insinuates $\beta_0 \approx 1$ (cf. Equation 4.16) for all these nozzles. By that, Figure 4.16 confirms the calibration concept via nozzle orifice diameter variation, which is applied by other research groups at atmospheric pressure.

The consistency of both methods also implies, that calibrations with the OMO relevant 1 mm nozzle at 250 hPa ambient pressure coincide with a calibration at 1 atm, but 0.5 mm nozzle orifice diameter for which the calibration concept has been already proved valid (Schlosser et al., 2009). This therefore shows, that the pressure variable radical source reliably supplies radical concentrations calculated by Equation 4.29 over the applied pressure range, and confirms the calibration concept via pressure variation used in this work (cf. Section 4.3.1).

Remarkably, all curves show a sensitivity jump upwards when the cell pressure falls

below 2 hPa and the mass flow rate drops below 2 $^{\mathrm{std\,l}}/_{\mathrm{min}}$. However, the amplitude of the curves measured for different nozzles between 1.5 hPa and 2 hPa is not the same. The jump in sensitivity for the 0.52 mm nozzle is a factor of 1.4 higher than for the 0.7 mm and 1 mm nozzle. Thus, the two calibration methods (nozzle variation versus inlet pressure variation) are not equivalent under these conditions. However, below 1.5 hPa, all curves are again in agreement. It becomes clear, that slow variations in the sensitivity with cell pressure can be resolved with the deployment of a few nozzles, but this method will be practically blind to sudden sensitivity jumps. The continuous pressure variation should in respect thereof be the method of choice.

4.4 Laboratory HO_2 calibration

The HO_2 cell was calibrated in the laboratory for different inlet pressures using the procedure outlined in Section 4.3.1. Notwithstanding, there remains a practical complication that arises due to the technically limited CO flow to convert all OH to HO_2 if pressure inside the radical source becomes too low. This needs to be corrected as follows. If κ_{CO} is the conversion efficiency for Reaction R46, then Equation 4.31 is modified to

$$S_{\mathrm{HO_2}} = (1 - \kappa_{\mathrm{CO}})\, C_{\mathrm{OH}}\, [\mathrm{OH}] + (1 + \kappa_{\mathrm{CO}})\, C_{\mathrm{HO_2}}\, [\mathrm{HO_2}] \ . \tag{4.38}$$

Combined with equation 4.32, this system gives the sensitivities if the conversion efficiency is known. It is determined in two separate measurements - without cell NO - in which the ratio of the OH signals with and without CO gives the quantity $1 - \kappa_{\mathrm{CO}}$. The pressure dependence was then investigated only for HO_2, since the system without shrouded inlet was not sensitive to OH during the flights (cf. Section 3.4.2). For the calibration, it was assumed that the HO_2 inlet pressure during the flight was equal to the static ambient pressure outside the aircraft, ranging from 1 atm at 0 km to 130 hPa at the highest flight level of 15 km (cf. Figure B.3). The corresponding cell pressure changed from 11.5 hPa to 2.7 hPa (cf. Figure B.4). The resulting HO_2 sensitivity is shown in Figure 4.17 on a logarithmic scale as a function of cell pressure. A more than exponential increase of the sensitivity by two orders of magnitude is observed when the cell pressure drops from 11.5 hPa (0 km) to 3 hPa (14 km). At even lower pressure the detection sensitivity has a discontinuity. In contrast to the OH cell, the sensitivity decreases at the jump by roughly a factor of 2.4, whereafter it increases back to its peak value by that amount at 2.5 hPa. Relevant cell pressures during OMO range between 2.7 hPa and 11 hPa. As in the case of the pressure-dependent OH sensitivity (cf. Figure 4.15), the laboratory calibration curve has been scaled to match the ground-based field calibrations during OMO. Furthermore, the data shown in Figure 4.17 have been corrected for a gas-dynamic effect that does not occur in the laboratory. During flights, the top of the HO_2 inlet is overflowed by ambient air with high speed leading to a reduction of the true inlet pressure by up to 40 % at the highest flight altitude (cf. Figure B.3). The required correction factors range from a value of 1 at 0 km to 2.8 at 15 km. Further details are given in Section 4.6.1.

As already discussed for the OH cell, the cell pressure at a given altitude has an uncertainty caused by the variability of the pumping speed and the influence of

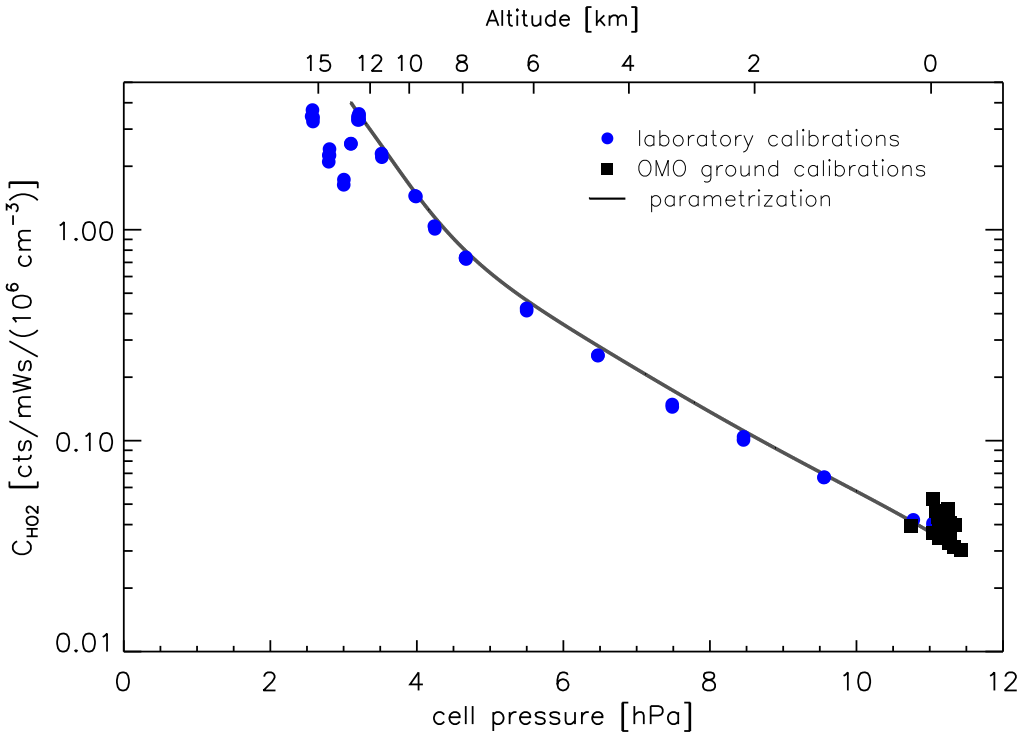

Figure 4.17: Cell pressure dependence of the HO_2 sensitivity. The strong increase with decreasing pressure is a combination of two additional effects besides the fluorescence yield. 1. At ground the pump speed is nearly equally distributed over the OH and HO_2 cell as the pressure in both cells have to be the same (same exhaust) and the mass flow is similar. With higher altitudes the mass flow through the HO_2 tube progressively differs from that of the OH tube, since there are no tube purges for the HO_2 cell and static ambient pressure is systematically lower than the pressure inside the inner deceleration tube of the shrouded inlet system. Due to the same pressures on both cells, this decreased mass flow through the tube of the HO_2 cell implies an increased residence time which increases the conversion efficiency from HO_2 to OH. 2. The decreased volume flow rate increases the NO concentration, since the standard flow of NO added is fixed. The parametrization follows from Figure 4.23.

the flight velocity on the inlet pressures of both measurement cells. As a result, the position of the discontinuity of the HO_2 detection sensitivity is uncertain by ± 0.15 hPa (1σ) during flight, which increases the calibration error at altitudes above 13.5 km (cf. Section 4.7).

4.5 OH channel

4.5.1 Detection sensitivity

Starting with the simple model Equation 4.36, the pressure dependence of the water vapour normalized OH detection sensitivity (cf. Figure 4.16) is expected to be caused by the parameters η, ω and β according to Equation 3.4, 4.12 and 4.16, respectively. The variation of quenching and expansion ratio can be accurately calculated from measured pressures and flow rates (cf. Section 4.1). The expression $\tilde{C}_{\mathrm{OH}}/(\eta\omega n_{\mathrm{amb}})$

should therefore represent the transmission factor

$$\beta = \text{const.} \times \frac{\tilde{C}_{\mathrm{OH}}}{\eta\omega n_{\mathrm{amb}}} \quad \text{with} \quad \text{const.} = (\epsilon T_{\mathrm{opt}} G \alpha)^{-1} \ . \tag{4.39}$$

This expression is shown in Figure 4.18 calculated from the data taken from Figure 4.16. The transmission factor is plotted as a function of the mass flow ($p_{\mathrm{cell}} q_{\mathrm{tube}}$) through the inlet tube, because it is the controlling parameter in the diffusion-limited transmission model (cf. Equation 4.16). The figure shows a considerable variability

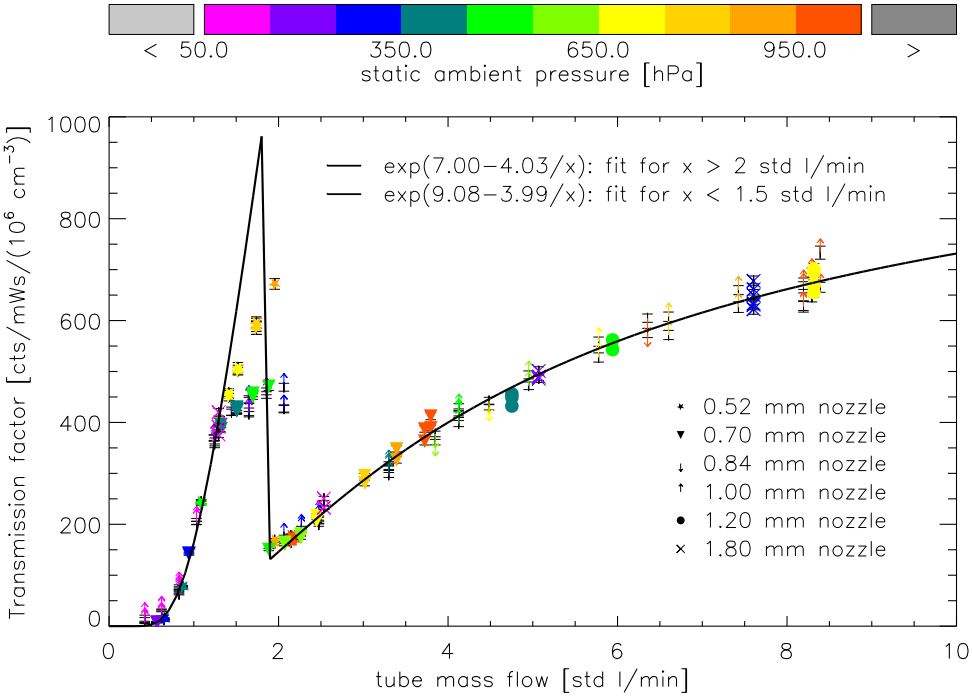

Figure 4.18: Transmission factor β/const. (cf. Equation 4.39) against the mass flow rate through the nozzle orifice. It is obtained from Figure 4.16 by removing the expansion ratio $\omega \cdot n_{\mathrm{amb}}$ and the fluorescence yield η. The discontinuity divides the transmission factor into two separate regimes and for each a fit function based on Equation 4.16 is used.

of the transmission factor, of which large parts can be described excellently by a parametrization based on the diffusion model (solid line). Reducing the tube mass flow from $10\,^{\mathrm{std\,l}}/_{\mathrm{min}}$ ($p_{\mathrm{cell}} = 8\,\mathrm{hPa}$) to $2\,^{\mathrm{std\,l}}/_{\mathrm{min}}$ ($p_{\mathrm{cell}} = 2\,\mathrm{hPa}$), apparently causes a continuous decrease of the transmission by a factor of 5. This behaviour is identical for all applied inlet nozzle diameters. Slightly below $2\,^{\mathrm{std\,l}}/_{\mathrm{min}}$ (2 hPa), the transmission rises in a jump by a nozzle-dependent factor 3 - 4.5. At even lower mass flows, the transmission continuously decreases again and becomes zero at $0.5\,^{\mathrm{std\,l}}/_{\mathrm{min}}$. Below $1.25\,^{\mathrm{std\,l}}/_{\mathrm{min}}$, the transmission curves for the different nozzles become identical again. According to the diffusion model, the logarithmic transmission factor should vary linearly with the inverse mass flow. Indeed, the logarithmic functionality is linear right of the discontinuity with a slope of $4\,^{\mathrm{std\,l}}/_{\mathrm{min}}$ which corresponds to an effective inlet length of 26 cm for an assumed OH diffusion coefficient $D_0 = 0.22\,^{\mathrm{cm}^2}/_{\mathrm{s}}$ at 1 atm and 296 K (Ivanov et al., 2007). The calculated effective length is smaller

than the geometrical length of the tube (30 cm). A possible explanation is the strong cooling of the gas when it is expanded in the nozzle from ambient pressure to cell pressure. For the expansion ratios in this work, the gas forms initially a supersonic Mach disk of a few millimetre lengths which then changes to a subsonic collimated gas jet which eventually fills the whole tube diameter. Depending on the expansion ratio, nozzle shape and orifice diameter, the subsonic gas jet can have initial temperatures as low as 150 K and gradually warms up to room temperature over a distance of 10 cm or more (Holland et al., 1995; Creasey et al., 1997; Kanaya et al., 2001). In general, gas diffusion coefficients are strongly temperature dependent, being proportional to $T^{7/4}$ (Fuller et al., 1966). Therefore, the mass flow dependence of the measured transmission factor could also be explained by the tube lengths of 30 cm and a slightly reduced effective diffusion coefficient of $0.19\,{}^{\mathrm{cm}^2}/_{\mathrm{s}}$. The decrease of D_0 would correspond to a temperature reduction by almost 50 K, which appears plausible for the given gas expansion.

For very small mass flows the logarithmic dependence with respect to the inverse mass flow is again linear with a slope of $4\,{}^{\mathrm{std\,l}}/_{\mathrm{min}}$. This implies that these two regimes are reasonably approximated by the diffusion limited model of transmission. In the intermediate range left of the jump some discrepancies were already discussed in Section 4.3.2. The ratio of both fits gives a theoretical jump size by the factor $\exp(2.08) \approx 8$, which is higher than the observation (0.52 mm nozzle: factor 4.5, other nozzles: factor 3). An unknown effect though flattens out the steep dependence which is also seen even more distinct for the OMO relevant laboratory pressure dependent calibrations (cf. Figure 4.19). A full explanation about the origin of the discontinuity however remains. It is possible that a sudden change of the flow pattern and physical conditions occur which could be linked to the transition from the supersonic gas expansion to normal tube flow.

The parametrization shown in Figure 4.18 directly gives the transmission factor through the inlet tube for a given mass flow. For example at $8.3\,{}^{\mathrm{std\,l}}/_{\mathrm{min}}$ (mass flow through the HO_2 inlet tube at conditions during the OMO ground based calibrations, cf. Figure 4.10) this yields $\beta/\beta_0 = \exp(-4/8.3) \approx 0.62$. This value can be compared to another approximation for β also obtained from Figure 4.18 where the data points represent $\beta/\mathrm{const.} = \epsilon T_{\mathrm{opt}} G \alpha \beta$ (cf. Equation 4.39). For all of these quantities except β, an estimate under ideal conditions is known: $\epsilon = 0.08$, $T_{\mathrm{opt}} = 0.72$ (cf. Table 3.2, ϵ includes the discriminator efficiency), $G = 0.15$ cm (Broch, 2011) and $\alpha = 264\,{}^{\mathrm{cm}^2}/_{\mathrm{J}}$ (cf. Equation 4.6 with Table 4.1). At $8.3\,{}^{\mathrm{std\,l}}/_{\mathrm{min}}$ Figure 4.18 reads $680\,{}^{\mathrm{cts}}/_{\mathrm{mW\,s\,10^6/cm^3}} = 0.68\,{}^{\mathrm{cm}^3}/_{\mathrm{J}}$. This laboratory value is in complete agreement with $0.68\,{}^{\mathrm{cm}^3}/_{\mathrm{J}}$ which can be derived from the mean OH sensitivity on the HO_2 cell ($0.143\,{}^{\mathrm{cts}}/_{\mathrm{mW\,s\,10^6/cm^3}}$) during ground-based field calibrations (cf. Figure 4.10) by removing $\eta = 0.019$ and $\omega = 0.011$ (from Figure C.3 and C.2 at 11.2 hPa, respectively). Finally dividing out the estimated parameters ϵ, T_{opt}, G and α, the transmission factor is estimated to be $\beta \approx 0.3$ which is off by a factor of 2 compared to 0.62 calculated within the first method. While this seems large, it can be already explained by moderate deviations for ϵ, T_{opt} and G which are optimal under ideal conditions and are likely to be lower in practise. α on the other hand should be reasonably accurate within 10 %. Hence a reduction by only 20 %

for these 3 quantities ϵ, T_{opt} and G already gives $0.3/0.8^3 = 0.59$, much closer to 0.62. It should be noted that the first method essentially gives β/β_0, while the latter yields β only. The nozzle transmission factor β_0 is however expected to be close to 1, for if it would be significantly lower 1, it would likely depend on the nozzle diameter which is not observed as of Figure 4.18.

The pressure dependent OH detection sensitivities measured for the OMO configuration (cf. Figure 4.15) can be treated in a similar way as in Figure 4.18 in order to obtain the OH transmission for the OH cell. Normalising the data from Figure 4.15 with respect to η and ω (taken from Figures C.3 and C.1, respectively) yields the mass flow dependence shown in Figure 4.19. Compared to Figure 4.18, the data shown here apply to a 1 mm nozzle mounted on a shorter inlet tube which is operated with $0.8\,^{\mathrm{std\,l}}/_{\mathrm{min}}$ tangential purge flow and pumping speed as used during the OMO flights. For low mass flow rates, there is a sharp ascent in the trans-

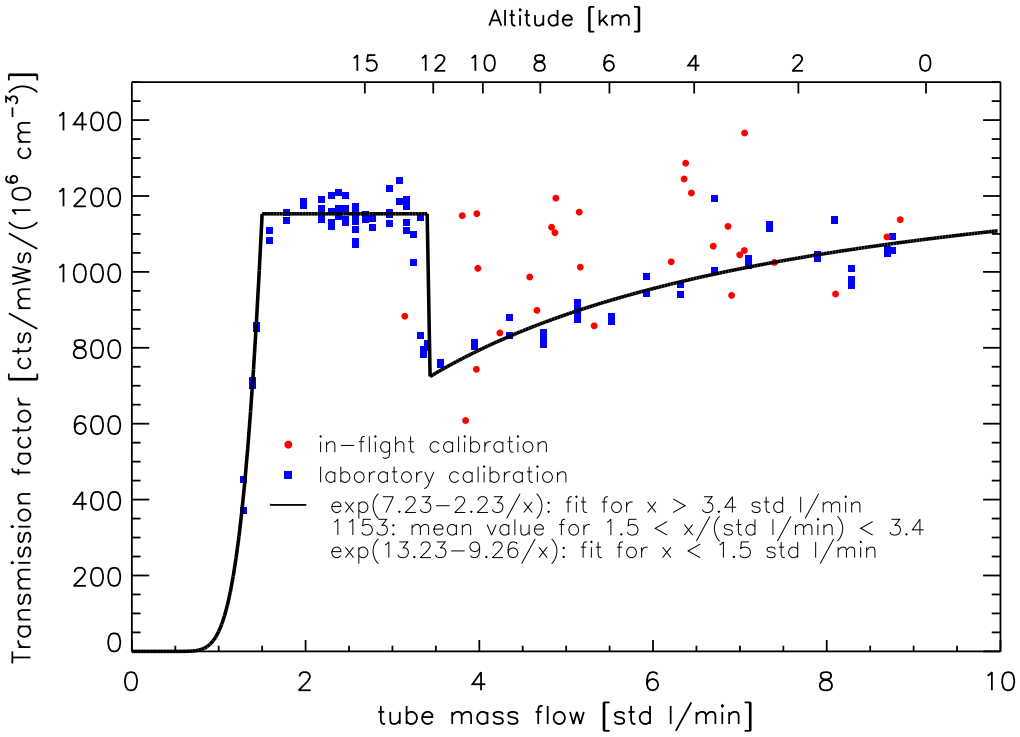

Figure 4.19: Sensitivity in arbitrary units where fluorescence quenching (η) and the expansion ratio (ω) have been removed. According to Equation 4.18 the remaining quantity should be proportional to the transmission factor (β). The solid line is a fit based on the diffusion limited wall loss model (cf. Equation 4.16) for the measurement data right of the discontinuity.

mission by a factor of 3 at $1.5\,^{\mathrm{std\,l}}/_{\mathrm{min}}$. From 1.5 to 3.2 $^{\mathrm{std\,l}}/_{\mathrm{min}}$ there is a plateau of constant transmission, after which it suddenly declines by a factor of 1.5. For larger mass flow rates (cell pressures) there is a slow and non-linear increase by a factor of 1.4 till 11 hPa. For OMO, the relevant mass flow range is above $2.7\,^{\mathrm{std\,l}}/_{\mathrm{min}}$ which corresponds to flight altitudes below 15 km. For mass flow rates right of the jump the functional dependence for β from Equation 4.16 can be used to fit the exponent of the exponential function. This gives the solid line in Figure 4.19 right

of the discontinuity, where the slope of the exponent is given by 2.23 $^{\mathrm{std\,l}}/_{\mathrm{min}}$. This value corresponds to an effective tube length of 15 cm with an assumed tube temperature of 293 K. The physical length of the tube is 22 cm. As in the case for the OH calibration on the HO_2 cell above, the more likely explanation is a decreased diffusion coefficient corresponding to a lower effective gas temperature than 293 K within the inlet tube. From Equation 4.16 with a temperature dependent diffusion coefficient $D_0 \propto T^{7/4}$, given the fitted slope of 2.23 $^{\mathrm{std\,l}}/_{\mathrm{min}}$ and using the physical tube length of 22 cm (cf. Table 3.2) yields an effective tube temperature of 171 K. This is about 70 K lower than what was found for the HO_2 cell. From a qualitative perspective this is plausible, because a smaller tube length increases the portion of the tube where the air is cold. Nevertheless, this picture does not incorporate the effect of the tube purge which acts as a sheath flow and would effectively decrease the first order rate constant and as such the determined slope. Additionally the N_2 purge flow (0.8 $^{\mathrm{std\,l}}/_{\mathrm{min}}$, $> 10\,\%$ mixing ratio of the tube gas) has a partial temperature of about 293 K and would increase the effective temperature within the tube. As a result, the most probable reason for the decreased slope of 2.23 $^{\mathrm{std\,l}}/_{\mathrm{min}}$ on the OH cell compared to 4 $^{\mathrm{std\,l}}/_{\mathrm{min}}$ on the HO_2 cell is a combination of both effects.

Another major difference is the distinct plateau in Figure 4.19 compared to 4.18. It extents over a range of 1.7 $^{\mathrm{std\,l}}/_{\mathrm{min}}$ vs. 0.5 $^{\mathrm{std\,l}}/_{\mathrm{min}}$. At low altitudes the mass flow through the nozzle dominates the momentum flux density through the inlet tube and the purge gas has a negligible effect on the flow. For low mass flow rates - left of the jump - the purge gas mass flow is of the same magnitude as the flow through the nozzle orifice. In this regime the sheath flow can develop undisturbed and meets its design principle to temporarily prevent OH losses, before the exponential suppression by too large residence times prevails.

For the evaluation of the OMO OH concentrations, the parametrization for β is given by the fitted theoretical model right of the discontinuity with slope parameter 2.23 $^{\mathrm{std\,l}}/_{\mathrm{min}}$ as of Figure 4.19 and a constant value of 1153 $^{\mathrm{cts}}/_{\mathrm{mW\,s\,10^6/cm^3}}$ left of the jump in sensitivity for mass flow rates down to 2.7 $^{\mathrm{std\,l}}/_{\mathrm{min}}$, relevant for OMO. An absolute scaling factor is used to connect the sensitivity to ground calibrations as was described at the end of Section 4.2.3. This parametrization was the basis for Figure 4.15. According to the parametrization, the transmission factor β/β_0 for OH at ground conditions (inlet tube mass flow with N_2 tube purge: 9 $^{\mathrm{std\,l}}/_{\mathrm{min}}$) in the OH cell has a value of about 0.78, which is slightly higher than in the case of the HO_2 cell which has a longer inlet tube and no inlet purge flow.

4.5.2 OH interferences

During a pulse of the 308 nm laser, not only is OH excited, but also ozone is photolised and produces $O(^1D)$, which subsequently reacts with water vapour to OH (cf. Reaction R3). The lifetime of $O(^1D)$ atoms at 1 hPa is roughly 1 µs; short enough to immediately form OH till the next laser shot after 0.3 ms. Within that time, an air parcel travelled only the distance of roughly half the diameter of the laser beam (cf. Table 4.1), and laser generated OH will interfere with ambient OH at the next laser shot to some extent. The amount of OH generated is proportional to the OH

production rate in Equation 2.4, where the photolysis frequency is proportional to the measured 308 nm laser power P (cf. Equation 4.8)

$$[\mathrm{OH}]_{\mathrm{int}} \propto P\,[\mathrm{O_3}]_{\mathrm{cell}}\,\Phi_{\mathrm{OH}}\,. \tag{4.40}$$

In terms of the OH signal S_{OH}, this quantity must be complemented by the fluorescence yield η (cf. Equation 3.4) and the expansion ratio ω (cf. Equation 4.12) when referenced to ambient ozone concentrations. As Broch (2011) has shown, the interference signal depends on a variety of other parameters, such as the nozzle orifice, the volume flow rate through the cell and the cell pressure. This dependence is combined in a pressure dependent proportionality constant ξ

$$S_{\mathrm{OH\ int}} = \xi\,\eta\omega\,[\mathrm{O_3}]_{\mathrm{amb}}\,\Phi_{\mathrm{OH}}\,P\,. \tag{4.41}$$

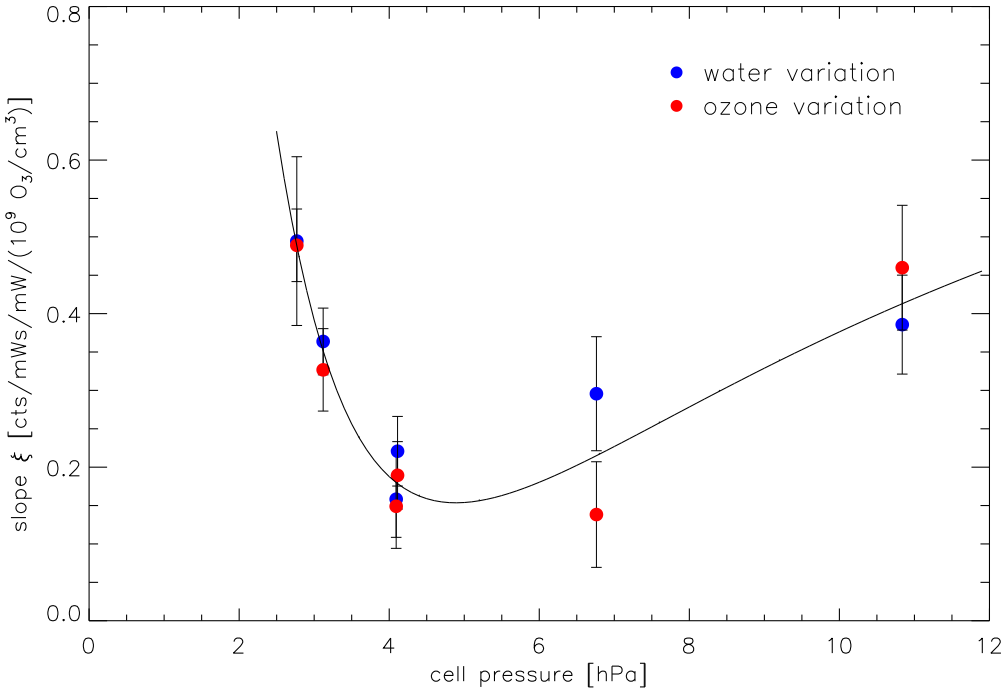

Figure 4.20: Ozone water interference on the OH cell. As ozone is photolised by the laser beam, O(^{1}D) will react with water to form interference OH. For fixed cell pressure the dependence is linear in the cell ozone concentration, the laser power, the fluorescence yield and the OH branching ratio for the reaction of the O(^{1}D). The blue points are obtained by measurements where water vapour is varied while ozone is constant. Likewise the red points have constant water and varying ozone. The solid line is the parametrization using a fit function $-25.8\,x^{-3} + 33.5\,x^{-2} - 10.5\,x^{-1} + 1.12$. Error bars are obtained from the linear regression for each slope parameter ξ by gaussian error propagation.

In order to characterize the OMO campaign relevant ozone-water interference, the radical source KQ5 was deployed as a flow tube with the UV lamp switched off. As test gas, synthetic air with varying ozone- and water vapour concentrations was used. The measurement was done for different cell pressures, which followed the

ambient conditions in the shroud during OMO flights, equivalently to the pressure dependent calibrations. The experiment was conducted in two different ways. In a first series of measurements ozone was kept constant at roughly 200 ppb and water vapour mixing ratios were varied between 0 and 1 % at fixed pressure. The quantities η, P, $\omega\,[O_3]_{amb}$ in Equation 4.41 are divided out of the measured signal and the result should be a linear dependence in Φ_{OH}. The slope is determined by a linear regression and is shown as a function of the cell pressure in Figure 4.20 (blue dots). The second series of measurements is essentially the same, but the role of water and ozone is interchanged i.e. water vapour mixing ratio is kept constant at 1 % and ozone is varied between 0 and 200 ppb (red points in Figure 4.20). This was done as a consistency check, as the slopes ξ determined by either method should give the same result. Laser power during the experiment varied between 10 and 15 mW, and the theoretically justified linearity was shown to be experimentally valid by Broch (2011). Both measurement data were used to parametrize the relative interference by using a fit function $-25.8\,x^{-3} + 33.5\,x^{-2} - 10.5\,x^{-1} + 1.12$ (solid line in Figure 4.20). In using Equation 4.41 for the ozone-water interference signal, a final constant scaling by the factor 1.6 was added, because the OH detection sensitivity determined during the OMO ground based calibrations was higher by that factor than later in the laboratory when this test was done (change of photomultiplier).

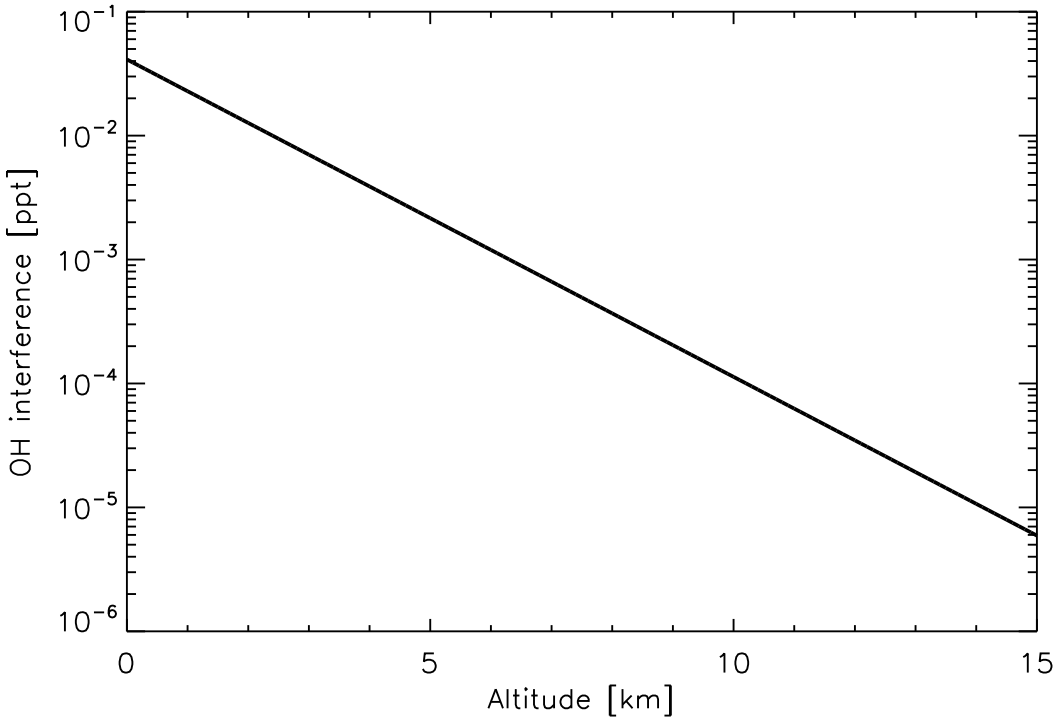

Figure 4.21: OH interference in equivalent OH mixing ratios. The exponential decrease is mainly because of the strongly decreasing water vapour mixing ratio with altitude.

The overall influence of the ozone-water interference in evaluating the OMO OH concentrations is only of relevant magnitude at ground. Figure 4.21 shows the interference parametrization in equivalent OH mixing ratios using the OH measurement

sensitivity ($S_{\text{OH int}}/\tilde{C}_{\text{OH}}$). The altitude dependence is evaluated with a mean ozone and water vapour mixing ratio profile from the OMO data (cf. Figure B.9 and B.10). With an OH mixing ratio of 0.18 ppt at ground (cf. Figure 5.8), this is 20 % of the total OH mixing ratio. However, the interference drops exponentially because of the decreasing water vapour, and for altitudes above 3 km the impact is less than 3 %.

Broch (2011) analysed various dependencies of the ozone-water OH interference, in particular with respect to the laser pulse repetition rate ν_{rr}. For a laser pulse energy of 3 µJ at 3 kHz repetition rate, ozone and water vapour mixing ratios of 155 ppb and 1.5 % respectively, and a cell pressure of 3.6 hPa, Broch (2011) found an interference signal of about 0.25 $^{\text{cts}}/_{\text{mW s}}$. For these values inside the cell - $\eta = 0.09$, $P = 9$ mW, $\Phi_{\text{OH}} = 0.092$ - Figure 4.20 with Equation 4.41 gives 0.26 $^{\text{cts}}/_{\text{mW s}}$.

4.5.3 OH limit of detection

The lower limit of detectivity - also called the limit of detection (LOD) - is defined as the concentration whose equivalent signal is equal to a constant multiple (signal to noise ratio: snr) of the photon counting statistical uncertainty due to background shot-noise and the ozone-water interference signal (Holland et al., 1995). The background shot-noise is mainly due to laser stray-light and sunlight, while the ozone-water interference is calculated by Equation 4.41 using Figure 4.20. During an on-resonant measurement the background shot-noise is not directly available and is therefore estimated from the accumulated counts while the laser is measuring off-resonant.

It is assumed that the total accumulated counts over a given integration time are subject to Poisson statistics. The uncertainty of an average number of counts N calculated from n data points is therefore given by $\sqrt{N/n}$. Here and in the sequel the following notation is used.

$N_{\text{OH int}}$:	Accumulated counts ([cts]) over a given integration time due to the ozone-water interference ($= S_{\text{OH int}} \cdot t_{\text{int}} \cdot P$)
$N_{\text{off/on}}$:	Accumulated counts ([cts]) during an off/on-resonant measurement over a given integration time due to (laser) stray light
$n_{\text{off/on}}$:	Number of off/on-resonant measurements over a given integration time
t_{int}:	Integration time ([s])
σ_{bkg}:	Propagated total statistical uncertainty ([cts]) of all relevant background noises

The on-resonant contribution to the background statistical uncertainty is therefore given by $\sqrt{\frac{N_{\text{off}}}{n_{\text{on}}} + \frac{N_{\text{OH int}}}{n_{\text{on}}}}$. However, the subtraction of the n_{off}-point off-resonant measurement - which carries a significant statistical uncertainty - from the full on-resonant signal in order to obtain the signal without instrumental background, propagates to the full statistical uncertainty of the OH signal, giving

$$\sigma_{\text{bkg}} = \sqrt{\frac{N_{\text{off}}}{n_{\text{off}}} + \frac{N_{\text{off}}}{n_{\text{on}}} + \frac{N_{\text{OH int}}}{n_{\text{on}}}}\,. \tag{4.42}$$

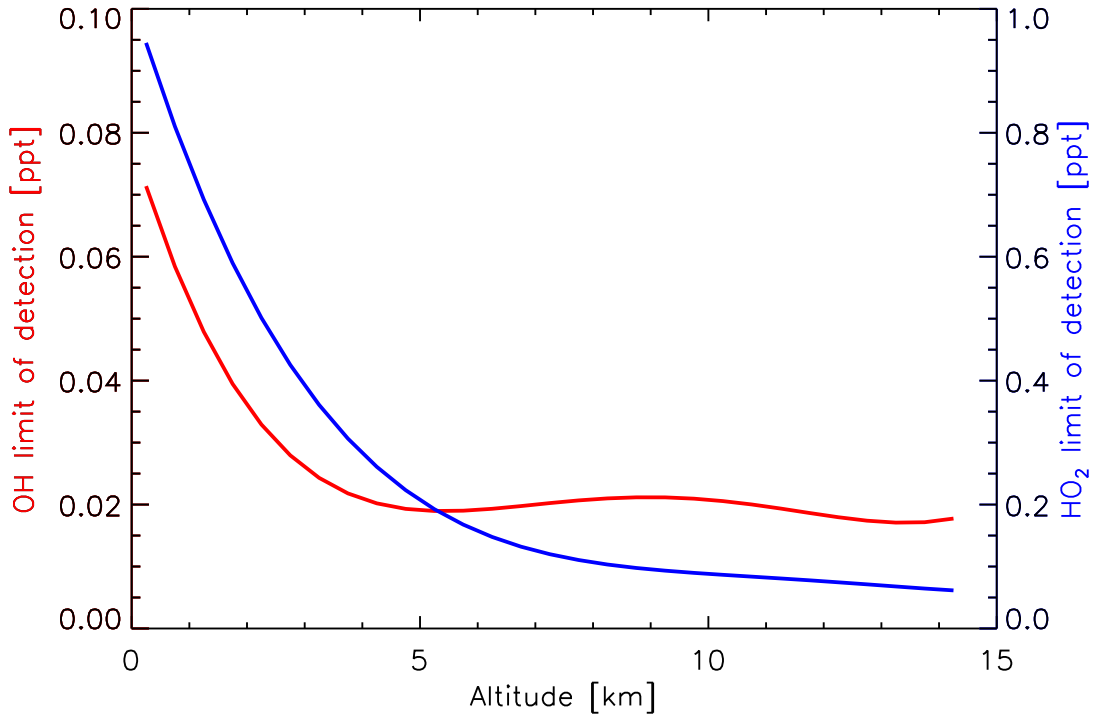

Figure 4.22: OH (red) and HO_2 (blue) limit of detection during OMO with signal to noise ratio of two.

It should be noted, that the statistical error due to the ozone-water interference, that propagates into the full statistical uncertainty when the latter is subtracted from the on-resonant signal, is negligible because of the long measurement times needed for its determination. The statement at the beginning then formulates as

$$C_{\mathrm{OH}} P\, t_{\mathrm{int}}\, LOD = snr\, \sigma_{\mathrm{bkg}} \tag{4.43}$$

with the laser power P. A reasonable value for the signal to noise ratio is $snr = 2$. During OMO two off- and five on-points with an integration-time of $t_{\mathrm{int}} \approx 4\,\mathrm{s}$ was used and the noise $N_{\mathrm{off}} \approx 25$ was mainly due to laser background, since the shrouded inlet system shielded the pinhole from the sun. With 20 mW laser power, 1 % water vapour mixing ratio, 100 ppb ozone mixing ratio and a branching ratio of 7 %, using Figure 4.20 the number of counts for the ozone-water interference becomes $N_{\mathrm{OH\ int}} \approx 15\mathrm{cts}$. With altitude however the water vapour mixing ratio decreases significantly and therefore this contribution can be neglected.

Figure 4.22 shows the limit of detection (LOD) in equivalent OH mixing ratios (red curve). Above 3 km altitude the limit of detection is small compared to measurements ($< 5\,\%$, cf. Figure 5.8), while in the very lower troposphere it can be as high as 40 %. However, most measurements were done at altitudes above 3 km, implying that the limit of detection was not an issue.

4.6 HO_2 channel

4.6.1 Detection sensitivity

The HO_2 sensitivity model is analogous to the model discussed for the OH sensitivity. Sampled air with HO_2 radicals traverses the HO_2 inlet tube and heats up to cell temperature (T_{cell}). Due to its much lower reactivity compared to OH, it is assumed that HO_2 radicals do not get lost. Right before the entrance of the detection cell, NO is added over a short distance of only 5 cm until detection. This allows for Reaction R15 and R7 and gives rise to a conversion efficiency $\kappa_{\text{NO}} = [\text{OH}]_{\text{cell}} / [\text{HO}_2]_{\text{cell}}$ by which the simple model equation 4.18 has to be complemented, so that it can be written as

$$C_{\text{HO}_2} = \text{const.} \cdot \eta \cdot \beta \cdot \omega \cdot \kappa_{\text{NO}} \,. \tag{4.44}$$

In contrast to the OH cell the HO_2 cell sees static ambient pressure at the nozzle entrance which is different from the OH inlet pressure (cf. Figure B.3). The purges in the tube of the HO_2 cell are negligible compared to the OH cell while also the mass flow through the nozzle is much lower with higher altitude and thence the residence time of the sampled air in the tube is larger. Since HO_2 is a lot less reactive than OH, the increased residence time affects the transmission factor β only slightly. A bigger impact should be noticed for the conversion efficiency (κ_{NO}) of HO_2 to OH, because for the current set-up the conversion of HO_2 to OH is in the linear regime. This can be seen from the System R15 and R7 which can be solved explicitly and results in a theoretical conversion efficiency

$$\kappa_{\text{theo}} = \frac{k_1}{k_2 - k_1} \left(\mathrm{e}^{-k_1 \Delta t} - \mathrm{e}^{-k_2 \Delta t} \right) \tag{4.45}$$

where $k_1 = k_{\text{HO}_2+\text{NO}} [\text{NO}]$ and $k_2 = k_{\text{OH+NO+M}} [\text{NO}]$. The rate constant $k_{\text{HO}_2+\text{NO}}$ is pressure independent and NASA/JPL (Burkholder et al., 2015) recommends $8.1 \times 10^{-12}\,\text{cm}^3/\text{s}$ (298 K). The rate constant $k_{\text{OH+NO+M}}$ for the ternary reaction decreases with cell pressure and NASA/JPL gives the two limits $1.9 \times 10^{-13}\,\text{cm}^3/\text{s}$ (298 K, $p_{\text{cell}} = 11$ hPa, 0 km altitude) and $0.5 \times 10^{-13}\,\text{cm}^3/\text{s}$ (298 K, $p_{\text{cell}} = 3$ hPa, 14 km altitude). The NO concentration in the cell can be calculated from

$$[\text{NO}]_{\text{cell}} = \frac{n_0 q_{\text{NO}}}{q_{\text{tube}}} \tag{4.46}$$

where the notation from Equation 3.13 was adopted and $q_{\text{NO}} = 2 \times 10^{-4}\,\text{std l/min}$ is the standard flow of pure NO added at the entrance of the HO_2 detection cell. Lastly the reaction time Δt can be estimated from the geometry and the volume flow rate. The former is given by the reaction length of $\Delta z \approx 5$ cm given above and the tube cross-section $A_{\text{tube}} \approx 12\,\text{cm}^2$ (cf. Table 3.3). The volume flow rate at ground is taken from Figure B.8 and gives $q_{\text{tube}} \approx 820\,\text{l/min}$. Putting everything together yields $\Delta t \approx \Delta z\, A_{\text{tube}} / q_{\text{tube}} \approx 4$ ms. Since $k_1 \Delta t \ll 1$ and $k_2 \Delta t \ll 1$, Equation 4.45 can be approximated by

$$\kappa_{\text{theo}} \approx k_1 \Delta t \tag{4.47}$$

which gives a conversion efficiency of about 20 % when assuming perfect mixing.

It is possible to experimentally estimate the conversion efficiency from Figure 4.10. The ratio of the HO_2 to OH ground sensitivity can be expressed in terms of the quantities in Equation 4.17 by

$$\frac{C_{HO_2}}{C_{OH}} = \frac{\beta_{HO_2}\kappa_{NO}}{\beta_{OH}} \approx 0.25 \tag{4.48}$$

from which κ_{NO} can be calculated: While in the previous section an estimate for the OH transmission efficiency on the HO_2 cell of $\beta_{OH} \approx 0.62$ was found, it is safe to assume that HO_2 does not get lost in the tube ($\beta_{HO_2} \approx 1$, see above). Solving for κ_{NO} in the above Equation 4.48 yields $\kappa_{NO} \approx 0.15$, which is a bit lower than the theoretical value found. This is either due to the uncertainty in the estimate for β_{OH}, or more likely due to imperfect mixing leading to segregated NO patches which effectively decrease the mean NO concentration.

There are a couple of effects that lead to an increase in sensitivity by two orders of magnitude when cell pressure is lowered to 3 hPa as shown in Figure 4.17:

- The fluorescence yield η increases by a factor of 7.5 (Figure C.3)
- The expansion ratio ω increases by a factor of 1.5 (Figure C.2)
- The mass-flow correction factor increases by a factor of 2.8 (Figure 4.24)

When the first two of these effects are removed from Figure 4.17, an increase by a factor of 10 remains (cf. Figure 4.23).
From the simple model above, the only remaining two possibly dependent quantities on cell pressure (or volume flow rate) are the transmission factor β and the conversion efficiency κ_{NO}. However, as mentioned above the HO_2 transmission factor can be estimated close to 1 over all cell pressures, since HO_2 is much less reactive than OH. Figure 4.23 therefore essentially shows the conversion efficiency κ_{NO}, which is the fraction of HO_2 radicals in the cell being converted to OH by the reaction with NO and to which the mass-flow correction factor is related to (see below). As the cell is run in the low NO regime, this conversion factor is proportional to the product of NO concentration and residence (reaction) time

$$\begin{aligned}\kappa_{theo} \approx k_1 \Delta t &= \frac{k_{HO_2+NO} n_0 q_{NO} \Delta z A_{tube}}{q_{tube}^2} \\ &= \frac{\text{const.}}{q_{tube}^2}\,.\end{aligned} \tag{4.49}$$

This functional dependence can be seen in Figure 4.23 where the two regimes left and right of the discontinuity have to be considered separately. For high volume flow rates (high cell pressures/low altitudes) it indeed shows a linear behaviour with respect to q_{tube}^{-2}. For low volume flow rates (low cell pressures/high altitudes) left of the jump, the functional dependence appears to flatten out. This is reasonable as for large reaction times the conversion is not linear any more. Conversely to the OH case, the jump is in the other direction.

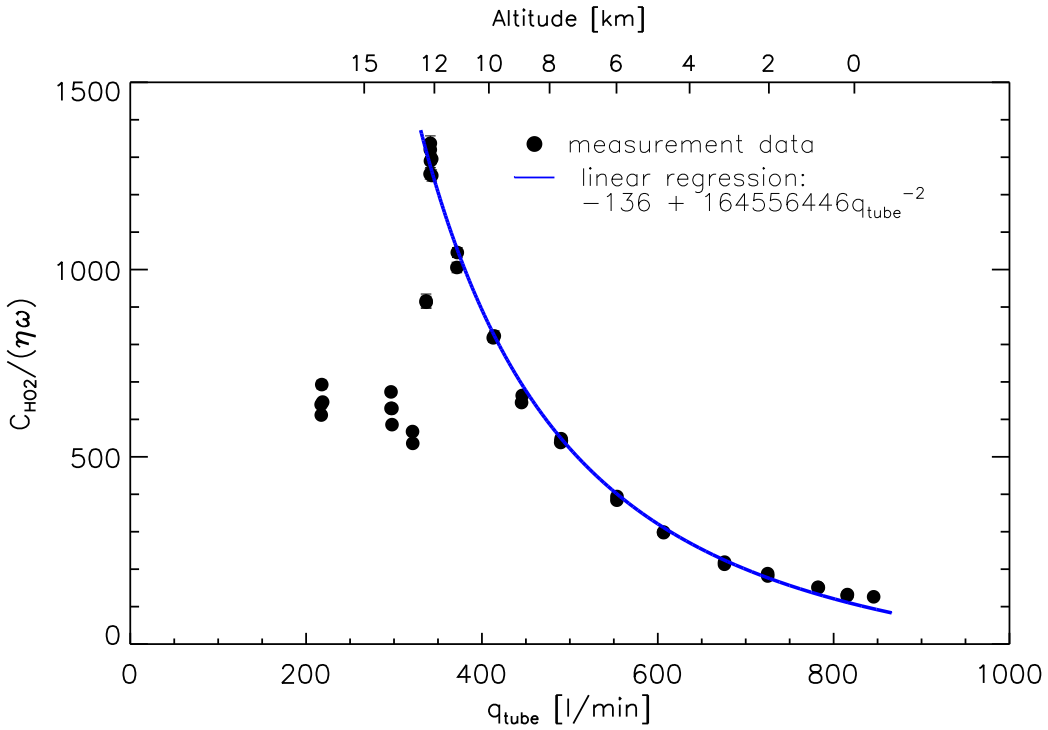

Figure 4.23: HO_2 measurement sensitivity where the fluorescence yield η and the expansion ratio ω have been divided out of the data points from Figure 4.17. Since the transmission factor β should be close to 1, the remaining dependence is essentially due to the conversion efficiency κ_{NO}. The blue line shows the linear regression for the measurement data right of the discontinuity ($340\,^{\mathrm{std\,l}}/_{\mathrm{min}} < q_{\mathrm{tube}} < 850\,^{\mathrm{std\,l}}/_{\mathrm{min}}$).

HO_2 mass-flow dependent correction factor

On HALO, ambient air on the HO_2 channel was sampled without an inlet-system. For the pressure-dependent calibration in the laboratory (Section 4.4) it was assumed that the inlet pressure at a given cell pressure is equal to the static ambient pressure. Later, it was recognized that during flights the inlet pressure will be smaller than the static ambient pressure when the air is flowing at high speed across the nozzle, which is the case at high altitudes (cf. Figure B.1). This problem is addressed using computational flow dynamics calculations (see below). The basic principle is that the presence of the nozzle with air of a speed up to $250\,^{\mathrm{m}}/_{\mathrm{s}}$ passing over it, results in a depression at the orifice due to streamline curvature that requires a pressure gradient, similar to the depression at the topside of a wing which gives lift to the airplane. The lower pressure compared to static ambient leads to a lower mass-flow through the nozzle. The HO_2 detection sensitivity depends on four parameters (η, β, ω, κ_{NO}) which change with flight altitude. Only the conversion efficiency κ_{NO} is affected by the mass flow change, if the cell pressure is prescribed. The fluorescence yield η depends only on the cell pressure, but not on the flow rate and is therefore constant. Since a reduction of the mass flow causes a lower volume flow rate at a given pressure in the detection system and κ_{NO} varies with the inverse of the square of q_{tube} (cf. Equation 4.49), an increase of the HO_2 detection sensitivity is expected at high flight velocities compared to the case when the air is at rest. In case of the

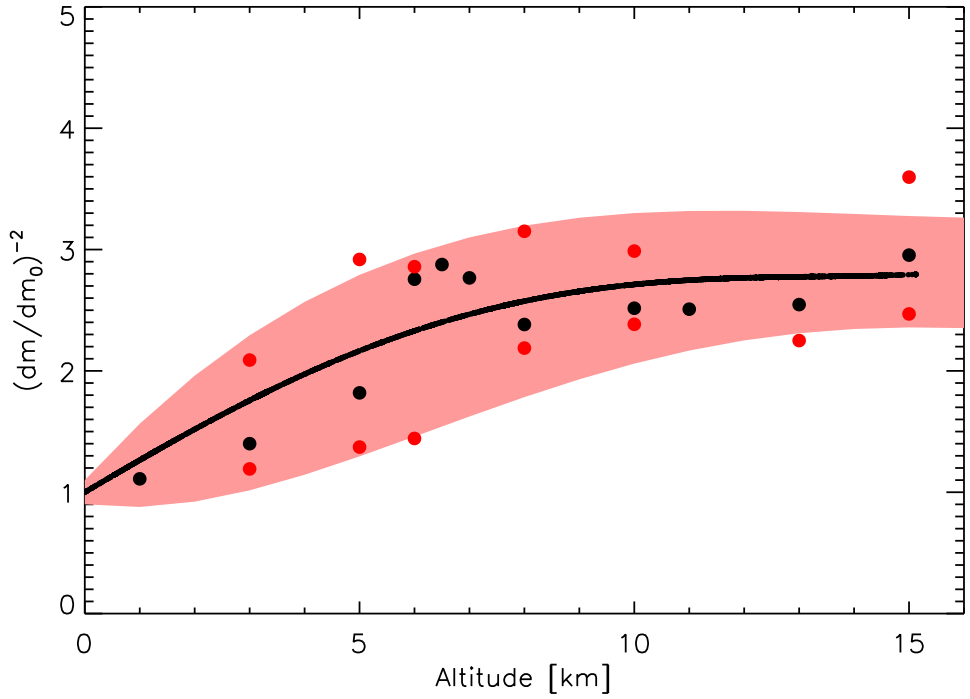

Figure 4.24: The correction factor has to be multiplied with the laboratory determined sensitivity (included in Figure 4.17). Red data points show upper and lower bounds corresponding to upper and lower limits of velocity at a specific altitude. The red band can be interpreted as the 2σ uncertainty of the correction.

tube transmission β, no influence of the flow rate is expected, because HO_2 wall loss is considered to be unimportant (see previous section). The relevant expansion ratio ω - which refers to unperturbed ambient air (with p_{amb}, T_{amb}, $[HO_2]_{amb}$) - is also not affected. Under the assumption that there is no chemical loss and no dilution of the sampled air (the tube purge flow is almost zero), the mixing ratio of HO_2 in the cell will be the same as in ambient air. Therefore, at a given cell pressure, the concentration $[HO_2]_{cell}$ is independent of aerodynamic changes in the inlet pressure and inlet temperature; only the residence time of the HO_2 in the inlet tube and cell will change. Accordingly, also $\omega = [HO_2]_{cell} / [HO_2]_{amb}$ will remain unaffected.

The variation of the mass flow through the inlet nozzle of the HO_2 cell was simulated for the flight conditions at different altitudes using a Reynold-Stress-Omega model in the software ANSYS Fluent (Figure 4.25). The HALO HO_2 pylon CAD model was put in the middle of a 1 m×1 m×1 m box and dry air (T_{amb}) comes from the right with the given flight velocity using a velocity inlet (constant normal velocity over the box inlet surface) and exits at an ambient pressure outlet (constant outlet surface pressure p_{amb}) to the left. The pylon was designed high enough to be outside the boundary layer close to the wall. The nozzle orifice of 1 mm diameter in the middle of the box was also set as a pressure outlet with a low enough pressure (e.g. 2 hPa as in the cell) in order for the flow to become supersonic at the entrance. This changes the boundary value problem to an initial value problem (mathematically speaking the equations change from elliptic to hyperbolic) and the precise boundary outlet

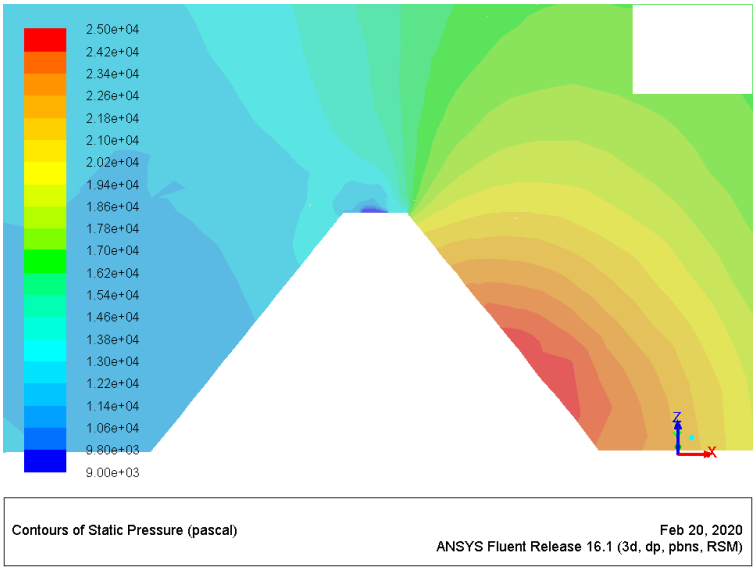

Figure 4.25: Colour coded contour plot of the static pressure distribution around the inlet nozzle (white contour). Air comes from the right and flows in negative x-direction. This CFD simulation was done at 180 hPa static ambient pressure, 220 K static ambient temperature (13 km altitude) and an aircraft velocity of 235 $^{m}/_{s}$.

pressure does not matter and is determined by the calculation. All walls (box, pylon, nozzle) obey the no-slip condition and are adiabatic type allowing zero heat flux.

Figure 4.25 shows the effect size in terms of static pressure for a selected example at 13 km altitude. The simulation was run with a static ambient pressure of 180 hPa and a static ambient temperature of 220 K. Dry air comes from the right with a velocity of 235 $^{m}/_{s}$. The nozzle obstacle leads to the streamline curvature that requires a pressure gradient normal to the streamlines. In the vicinity of the nozzle orifice from where the air is sampled, the static pressure is decreased to about 110 hPa on average, which is 40 % less compared to static ambient pressure. The discrepancy of ambient pressure and actual inlet pressure increases with flight altitude, as the aircraft velocity increases with height (cf. Figure B.3).

The model is run for the ambient airspeed, pressure and temperature at a specific altitude and as reference for an airspeed set to a low value of 10 $^{m}/_{s}$. The squared ratio of the simulated mass-flows through the inlet orifice at a given altitude from both runs is used as a correction factor for the HO_2 detection sensitivity, which was determined under laboratory conditions. The correction factor is shown in Figure 4.24 and has been included in the calibration curve shown in Figure 4.17. The correction factor is 1 at ground and approaches a value of about 3 in the upper troposphere. It might be important to note, that the CFD calculations assume stationarity. This does however not mean that the result is essentially stationary. In fact a common phenomenon named vortex shedding can arise due to the non-linearity of the equations when passing an obstacle resulting in a chaotic-like behaviour. The associated eddies and vortices are actually seen in the model output within the plane downstream of the orifice and accompanied with this is an oscillation in the mass-flow through the nozzle of about 10 % to 15 %. For the sake of this analysis a mean

value is evidently the choice to take. The biggest error nevertheless comes from the variability in the aircraft velocity at a certain altitude as seen in Figure B.1. For this reason upper and lower bounds corresponding to the upper and lower limits of the velocity at a specific altitude shown as red data points in Figure 4.24 were considered. The red band shown can be interpreted as the uncertainty of the correction.

4.6.2 HO_2 interferences

Like in the section for OH the ozone-water interference is determined by Equation 4.41. Since the variation with respect to water did not give as concise results as on the OH cell, a water averaged value was used. However, this is not of significance since the ozone water interference for HO_2 is negligible (cf. Figure 4.26). It decreases exponentially with altitude and is less than 0.1 ppt at ground. A larger interference for HO_2 is due to NO.

To convert HO_2 to OH, NO is added at the entrance of the detection cell. If however synthetic air is sampled from the radical source without producing HO_2, a small background signal remains. A possible explanation is the heterogeneous production of HONO on wall surfaces due to present humidity, that is then photolised to OH. This interference will be pressure dependent (cf. Figure 4.27).

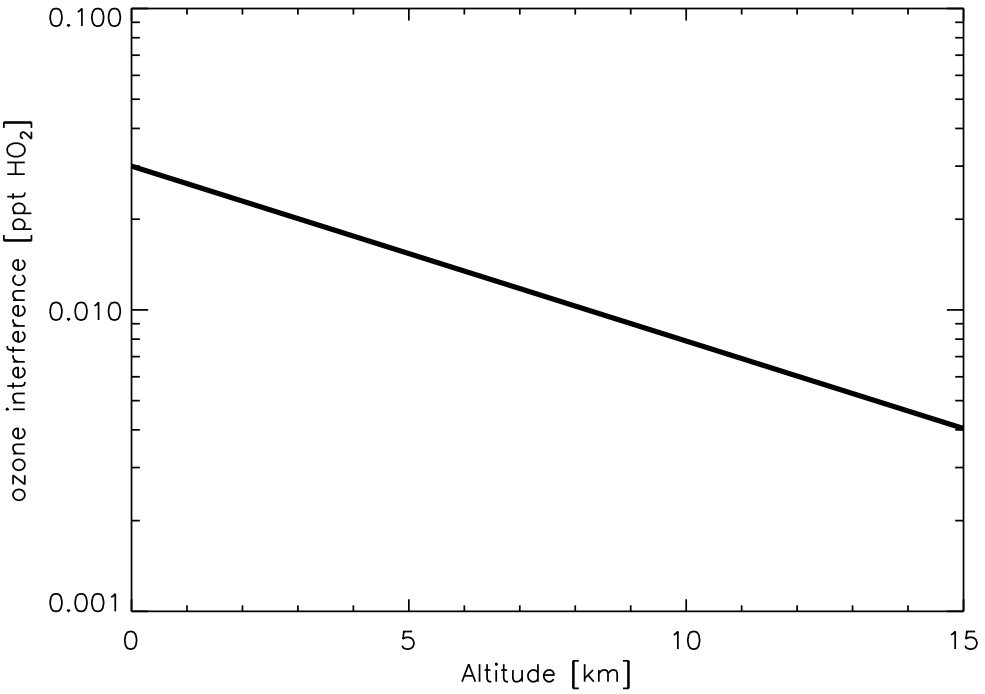

Figure 4.26: Ozone-water interference on the HO_2 cell in equivalent HO_2 mixing ratios. With 0.03 ppt at ground and a steady reduction with altitude being only 0.004 ppt at 15 km, it is negligible compared to the HO_2 mixing ratios.

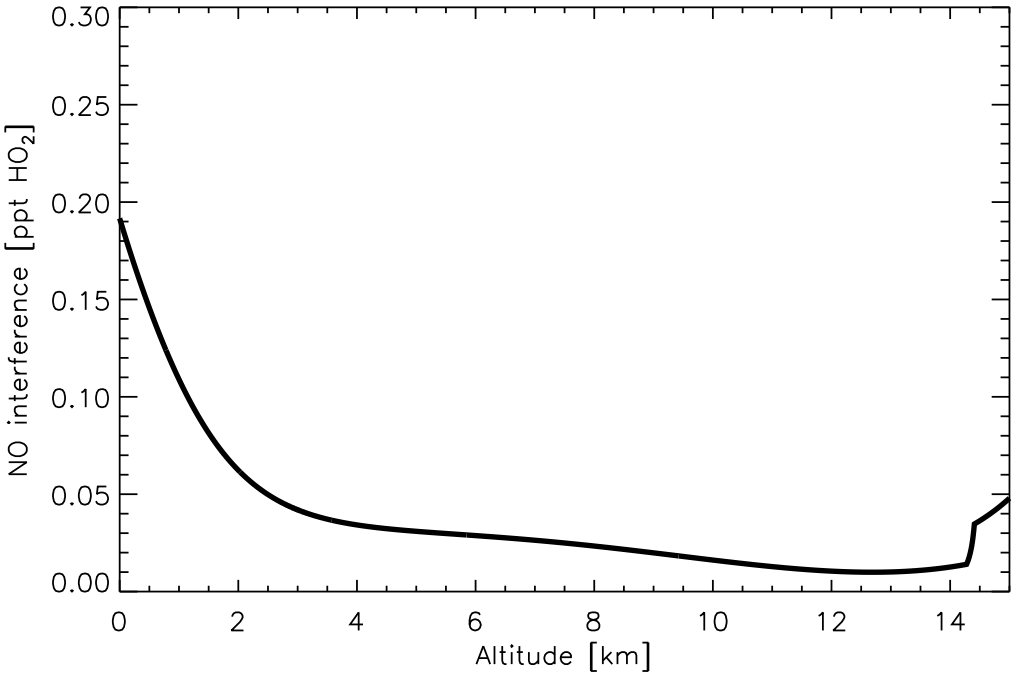

Figure 4.27: Cell pressure dependence of the NO background. While a little larger than the ozone-water interference, it can also be neglected compared to the measured HO_2 mixing ratios.

4.6.3 HO_2 limit of detection

The HO_2 limit of detection can be defined along the lines of Equation 4.43. In this case the signal due to ambient OH poses a Poisson noise for the signal solely due to HO_2 and therefore in principle has to be accounted for in the uncertainty σ_{bkg}. The defining equation similarly reads

$$C_{\mathrm{HO_2}} P\, t_{\mathrm{int}}\, LOD = snr\, \sigma_{\mathrm{bkg}} \tag{4.50}$$

with $\sigma_{\mathrm{bkg}} = \sqrt{\frac{N_{\mathrm{off}}}{n_{\mathrm{off}}} + \frac{N_{\mathrm{off}}}{n_{\mathrm{on}}} + \frac{N_{\mathrm{OH}}}{n_{\mathrm{on}}} + \frac{N_{\mathrm{int}}}{n_{\mathrm{on}}}}$. The off-signal on the HO_2 cell is much higher, because of the sunlight: $N_{\mathrm{off}} \approx 200$. It is much higher than on the OH cell, since there is no shrouded inlet that shields the nozzle pinhole from the sun. The interference counts N_{int} will result from the parametrizations above (cf. Figure 4.26 and 4.27) which give the normalized signals and subsequently thus have to be multiplied with the integration time of 4 s and the laser power P. In this particular case, there is no ambient OH signal on the HO_2 cell (cf. Section 3.4.2) and thus N_{OH} can be neglected. The HO_2 limit of detection is shown in Figure 4.22. It decreases strongly with altitude; however at ground it is about 10 times worse than the limit of detection for OH on the OH cell. This is due to the laser power on the HO_2 cell being about a factor of 2 smaller than on the OH cell and the decreased sensitivity by a factor of 3 compared to the OH sensitivity. Additionally the high sun background contributes significantly to σ_{bkg}.

4.7 Error analysis

Accuracy and precision are kept separated, where the latter is determined by the instrumental statistical Poisson noise and is given in the data files for each measurement point. Here the focus lies only on the accuracy and systematic biases.

The calibration errors for OH and HO_2 depend on the uncertainties associated with the parameters in Equation 4.29 which are needed to calculate the radical concentrations in the calibration source. These parameters are the ozone production factor a, the absorption cross-sections for O_2 ($\sigma^{\text{eff}}_{O_2}$) and H_2O (σ_{H_2O}), the quantum yields for OH, HO_2 and ozone, the volume flow q_v in the calibration tube and the intensity I^{meas}_{185} of the photolysis radiation. Furthermore, as the radical measurements are normalized to the power of the excitation laser, the stability of the detection sensitivity of the laser photo diode has to be controlled regularly. It depends, for example, on the laser beam alignment through the LIF detection cells. All these contributions are discussed in Broch (2011) and cause a total 1σ error of 15 %. When the calibrations are performed over the pressure range from 150 to 1000 hPa, there is no reason why specific uncertainties should differ vastly and the given uncertainty should hold for this pressure range as well, as long as the HO_x production by photolysis is not too small. This is because at lower pressures the water vapour partial pressure decreases as well as the photolysis time, resulting in a quadratically decreasing fluorescence signal with pressure. The reduced precision was no major issue for OH, but for HO_2 not all of OH could be converted to HO_2 with the given CO flow. It was however possible to correct for it (cf. Section 4.4).

Table 4.3: OH and HO_2 error contributions (1σ) to the sensitivity.

	OH [%]		HO_2 [%]	
calibration source	15		15	
pressure uncertainty	8 30 8	$(0-10.5\,\text{km})$ $(10.5-13\,\text{km})$ $(13-15\,\text{km})$	$8-16$ 30	$(0-13.5\,\text{km})$ $(13.5-15\,\text{km})$
mass-flow correction factor	-		15	
total accuracy	17 34 17	$(0-10.5\,\text{km})$ $(10.5-13\,\text{km})$ $(13-15\,\text{km})$	$18-26$ 35	$(0-13.5\,\text{km})$ $(13.5-15\,\text{km})$

The main controlling variables, which cause the altitude dependent change of the calibrations in Figure 4.15 and 4.17, are the cell pressures, and the temperatures and pressures at the radical inlets. Together with the vacuum pump speed and the constant purge flows, these parameters control the mass flow and volume flow of air through the measurement system. The influence of all these parameters on the detection sensitivity of OH and HO_2 is explained in Section 4.5.1 and 4.6.1. As shown in Figures B.3, B.4 and B.6, the conditions for the measurements showed

some variability at a given flight altitude during the campaign. Since it is practically not possible to reproduce all flight conditions during laboratory calibrations, the curves shown in Figure 4.15 and 4.17 were determined for mean conditions at a given altitude. However, from flight to flight, the cell pressure at a given pressure altitude was slightly variable by about 0.17 hPa (1σ), depending on altitude. The resulting calibration error due to this uncertainty can be estimated by shifting the pressure dependent calibration curves to the left and right by the statistical uncertainty of the cell pressure measurements at a given altitude and then normalizing it to the unshifted version. This gives another 8 % error for the OH sensitivity over almost the entire pressure range. Around the sensitivity jump itself the error is 30 %.

A similar analysis leads to an uncertainty for the HO_2 calibrations of 8 to 16 % above the sensitivity jump. At the discontinuity and below an estimate of 30 % is given. As was discussed in the previous part, the HO_2 sensitivity needed to be corrected for the mass-flow reduction due to the pressure gradient which constitutes the stream-line curvature over the HO_2 nozzle at high air velocities. The numerical calculation of this correction is subject to the knowledge of the precise air velocity and Figure 4.24 implies to add another 15 to 30 % uncertainty (2σ) only for HO_2. All errors are summarized in Table 4.3. The resulting total accuracy of the OH and HO_2 calibrations are shown in Figure 4.28 as a function of altitude.

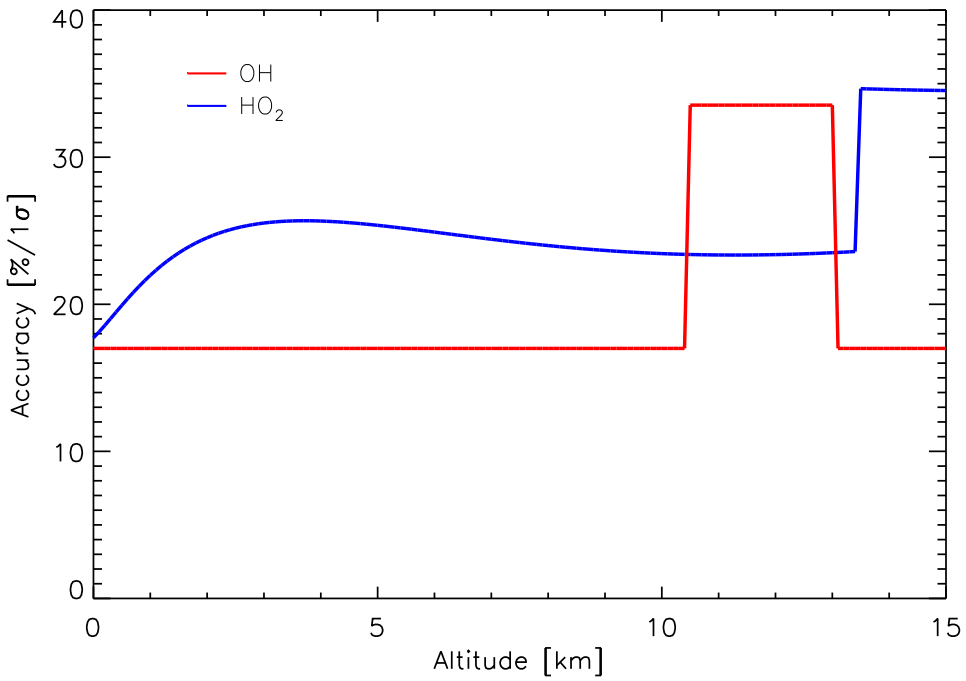

Figure 4.28: Total accuracy of OH and HO_2 respectively. Two contributions contribute to OH and three to HO_2 (cf. Table 4.3) which are added up Gaussian.

Preliminary HO_x data were uploaded into the HALO data base (https://halo-db.pa.op.dlr.de/) in December 2016. The final version (this thesis) was uploaded in November 2018 and contains two major changes. The mass-flow correction from

Figure 4.24 was applied to the previous HO_2 data. In case of OH, the position of the discontinuity (jump) in the OH cell pressure dependent calibration curve (cf. Figure 4.15) was shifted from 3.25 hPa to 3.6 hPa, while the rest of the calibration curve remained unchanged. The shift lies within the uncertainty of the position of the jump under flight conditions (cf. Section 4.3.1). The correction improves the agreement between AirLIF and HORUS data at altitudes between 11.5 km and 12.5 km, where the sensitivity jump in the AirLIF instrument is relevant (cf. Section 5.2.2). AirLIF data at other altitudes (80 % of all AirLIF data) are not affected by the correction.

Chapter 5

OH- and HO_2 measurements during OMO

5.1 OMO-campaign

5.1.1 Scientific goals

The OMO campaign was the first HALO mission studying the tropospheric photochemistry. Test flights were performed over Europe in January 2015 (OMO-EU) and the main mission was carried out over the Mediterranean Sea, the Arabian Peninsula, the Arabian Sea and the Indian Ocean during July/August 2015 (OMO-ASIA). The major goal of OMO comprises three aspects:

1. Oxidation processes and free radical chemistry of HO_x
   OMO-Asia was designated to study the chemical composition and chemistry in the outflow of the summer monsoon in particular downwind of South Asia. It primarily focused on oxidation processes, free radical chemistry (OH, HO_2) in the free and upper troposphere and air pollution chemistry above the Middle East and South Asia during the Asian Summer Monsoon (ASM) period. The mission helps to understand the influence of natural and human-made pollutants on the atmospheric *self-cleaning capacity* and how pollutants are converted into more soluble products that are eventually removed by rain. It goes without saying that this mechanism is crucial for air quality considering the ever growing pollution emissions especially in Asia. In the present work radical concentrations and their spatial (horizontal and vertical) distribution during OMO flights is studied. Tropospheric chemical mechanisms and models are tested against measurements and radical budgets (sources and sinks) are discussed.

2. Influence of ASM clouds on atmospheric chemistry
   The ASM is one of the largest atmospheric weather systems on Earth which transports large amounts of trace gases from the lower into the upper troposphere by deep convection within hours. Since the lifetime of trace gases in the upper troposphere is much longer under low temperature and pressure conditions, pollutants can be distributed globally and affect climate. Aircraft measurements during the HALO missions TACTS/ESMval (Vogel et al., 2016)

and OMO (Lelieveld et al., 2018) have shown enhanced tropospheric concentrations, for example, of CO, CH_4 or H_2O due to vertical convection over South East Asia between mid-June and late October. Increased lightning activity in deep convective clouds can additionally affect the radical chemistry as large amounts of NO_x are formed (Lelieveld et al., 2018).

3. Long-distance transport of air pollution
   The climatological conditions of the ASM drive an anticyclone in the upper troposphere which extends from eastern Europe to East Asia and distributes pollutants globally (Vogel et al., 2016; Lelieveld et al., 2018; Rauthe-Schoech et al., 2016).

5.1.2 Asian Summer Monsoon

During summer the Inter-Tropical Convergence Zone (ITCZ) crosses the Indian continent, resulting in low pressure regions and consequently an in-draft of humid air from the sea. During the ASM the air is extraordinary hot and humid which leads to the formation of cumulonimbus clouds while the air rises. These strong convective clouds are capable to transfer air from the surface to the upper troposphere within less than an hour which is usually a process over the time-scale of 1-2 weeks. In fact, the up-draft can be so strong, that air reaches the tropopause and enters into the lower stratosphere. This effect is known as *overshooting* (Park et al., 2009).

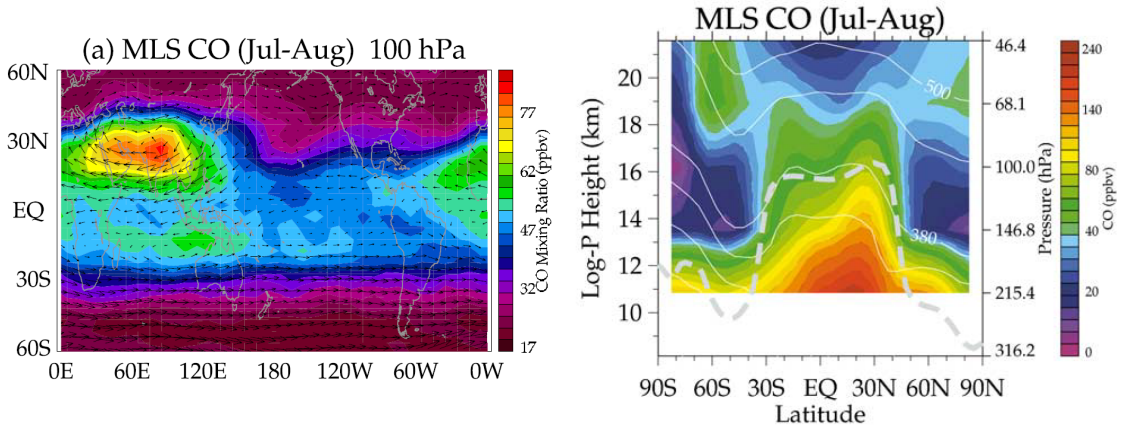

Figure 5.1: Example of enhanced CO concentrations observed by satellite during the ASM 2005. **Left:** Horizontal Structure of carbon monoxide (CO) measured by the Microwave Limb Sounder (MLS) in the ASM anticyclone at 100 hPa in July-August 2005. Arrows show horizontal wind vectors. **Right:** Vertical Structure of the MLS CO measurements averaged from 20°-100°E. Solid lines denote isentropes (320, 340, 360, 380, 450 and 500 K) while the thick dashed line corresponds to the thermal tropopause derived from NCEP/NCAR reanalysis (Park et al., 2007).

The ASM is one of the largest atmospheric features on Earth and is not only characterized by convective clouds. There are many different aspects, but a major cause can be traced back to the regional topography which shields warm moist air over South Asia (sub-Himalayan countries) from the cold and dry extra-tropics. This

leads to very high equivalent potential temperatures at the south-western flank of the Himalayas, which drives the deep convective up-drafts during Northern Hemispheric Summer. A combination of the elevated surface heating over the Tibetan plateau and predominant northward surface winds orographically uplifted at the south-western slopes of the Himalayas lead to the overall climatological weather phenomenon which additionally drives an anticyclonic circulation centred at 200 to 100 hPa (Gottschaldt et al., 2018; Park et al., 2007) (cf. Figure 5.1). This Asian summer monsoon anticyclone (ASMA) generally extents from eastern Europe to eastern Asia, but the shape, strength and location of the centre can vary strongly over longer time-scales. The overall up-welling in the eastern ASM (Tibetan Mode) is accompanied with a subsidence in the western part (Iranian Mode) affecting mid-tropospheric air masses in the Mediterranean region at the end of the summer monsoon period and leading to enhanced O_3 levels (Lelieveld et al., 2001). During the ASM the anticyclone generally acts as a transport barrier for pollutants.

5.1.3 Flight mission

Following the test flights (#1 - #4) over Germany and southern Europe from 22 to 27 of January (OMO-EU), the main campaign (OMO-ASIA) took place during July and August 2015. After three additional test flights (#5 - #7) in July near Oberpfaffenhofen (Germany), the aircraft was transferred to Paphos (Cyprus). Measurement flights started there on 21 July and took place over the geographic region shown in Figure 5.2. The coloured lines indicate different flight tracks, which are shown in greater detail in Appendix A.1. An overview of all OMO-ASIA measurement flights (flight number, date, location, OH and HO_2 data coverage) is given in Table 5.1.

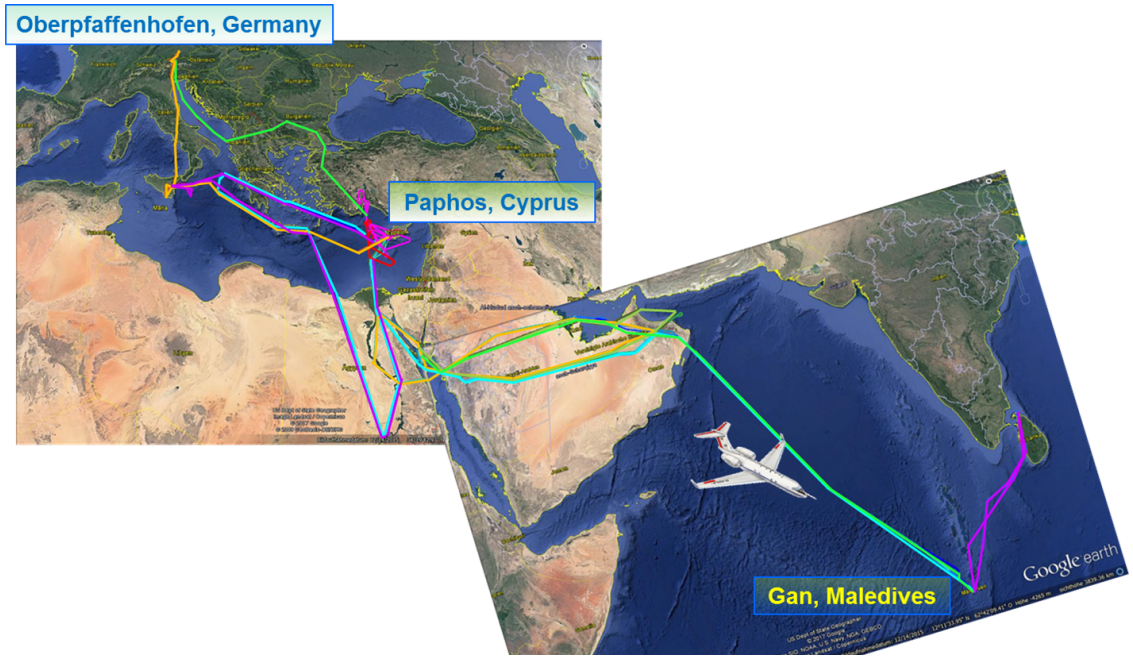

Figure 5.2: Flight tracks of HALO during OMO-ASIA. For individual tracks see Appendix A.1.

There were 14 days of flights in total during OMO. Three of them were performed before the transfer flight to Gan on the 01 August 2015 and they mainly circled over Cyprus and the Mediterranean. From Gan three flights took place, two of them over the Indian Ocean to Bahrain and the other into the Bay of Bengal. HALO returned to Paphos on 10 August 2015. The following three flights concentrated on the Arabian Peninsula. Flight #22 and #23 aimed for Egypt. The former bypassed southern Greece, while the latter visited Mount Etna on its way back to Paphos in hope to catch volcanic plumes. This target was repeated on the transfer flight #24 back to Oberpfaffenhofen where the campaign ended.

Table 5.1: OH and HO_2 data coverage for all the flights during the OMO campaign. **red:** not measured, **green:** measured, **red-green:** measured half-flight. Date format: dd.mm.yyyy, OP: Oberpfaffenhofen.

Flight #	Date	Flight base	Flight target	OH	HO_2
8	21.07.2015	OP	Paphos	●	●
9	25.07.2015	Paphos	Mediterranean	●	●
10	28.07.2015	Paphos	Mediterranean	●	●
11	01.08.2015	Paphos	Gan	●	●
12	06.08.2015	Gan	Bahrain	●	●
13	06.08.2015	Bahrain	Gan	●	●
14	08.08.2015	Gan	Sri Lanka	●	●
15	09.08.2015	Gan	Bahrain	●	●
16	09.08.2015	Bahrain	Gan	●	●
17	10.08.2015	Gan	Bahrain	●	●
18	10.08.2015	Bahrain	Paphos	●	●
19	13.08.2015	Paphos	Arab. Peninsula	●	●
20	15.08.2015	Paphos	Arab. Peninsula	●	●
21	18.08.2015	Paphos	Arab. Peninsula	●	●
22	23.08.2015	Paphos	Egypt - Greece	●	●
23	25.08.2015	Paphos	Egypt - Etna	●	●
24	27.08.2015	Paphos	Etna - OP	●	●

5.1.4 Instrumentation

Measurements of radicals were central for the investigation of the upper tropospheric chemistry during OMO. The radicals OH and HO_2 were measured by two new LIF instruments developed for HALO by FZJ (AirLIF instrument) and MPIC Mainz (HORUS). Furthermore, a chemical amplifier instrument (PERCEAS) was on board to measure RO_x (RO_2 + HO_2 + OH). Additional other instruments measured trace gases, solar actinic radiation, and meteorological parameters that are needed to interpret the radical observations and to constrain chemical box models. Table 5.2 provides a list of instruments for measured species, their position in the aircraft cabin and the institution operating the instrument (cf. Figure 5.3). Fig-

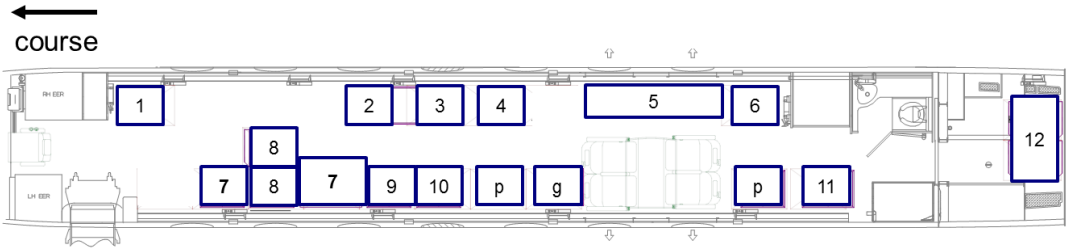

Figure 5.3: HALO cabin layout during OMO. See Table 5.2 for the numbers (Broch, 2011).

ure 5.4 shows the outer positions of the MPIC and FZJ instruments in the cabin of the aircraft. Our instrumental set-up was in the front next to HORUS. While our inlet was on top of the aircraft, theirs was directly underneath below the aircraft.

Technically, HORUS and AirLIF are similar. Both are FAGE (fluorescence assay with gas expansion) type instruments running at roughly 10 hPa and using an excitation wavelength of 308 nm. Each institution was using an identically constructed inlet system to decelerate and sample ambient air (cf. Figure 3.5). In the AirLIF instrument, only the OH cell is connected to the shrouded inlet, while HO_2 is sampled by a separate inlet without shroud (cf. Figure 3.10). HORUS in contrast runs both detection cells in series with OH as the first detection axis (Martinez et al., 2010). Additionally, their system was operated with an inlet pre-injector (IPI) developed

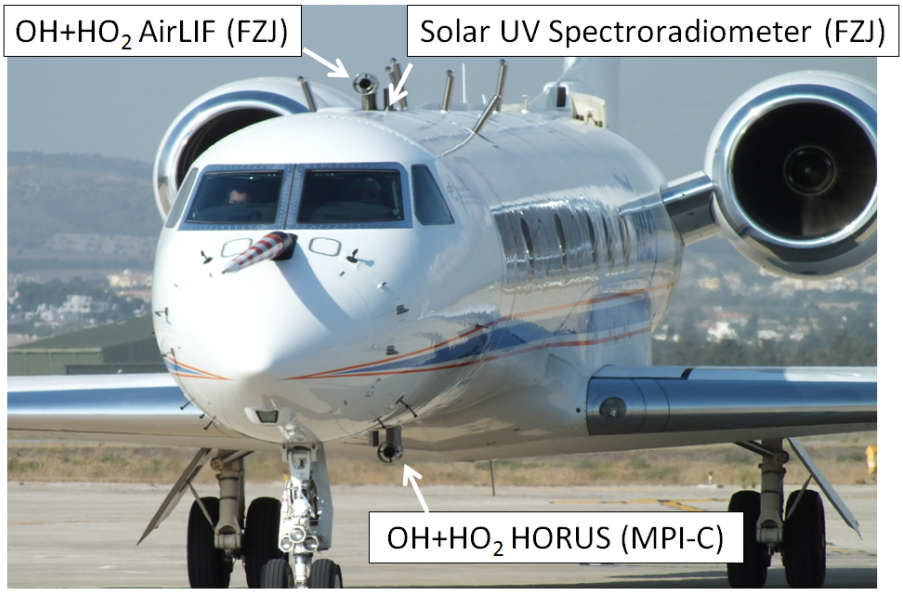

Figure 5.4: HALO on the air-field showing the FZJ OH and HO_2 inlet system on top and MPIC inlet system underneath the aircraft. Upward and downward-looking inlet optics of the FZJ spectral radiometer are mounted behind the OH inlets.

for application on HALO to keep track of possible interferences (D. Marno, personal communication). For that purpose a large flow from 50 to 230 $^{\mathrm{std\,l}}/_{\mathrm{min}}$ - depending on altitude - is drawn through the IPI using a 6.5 mm nozzle, where nitrogen or propane is alternatingly added. When propane is added, ambient OH is scavenged

and the remaining OH signal is then interpreted as background. The pressure in the IPI is only 6 hPa below static ambient from which only 4 to 16 $^{std\,l}/_{min}$ are collected through a critical orifice of 1.4 mm diameter into the actual detection cell.

While the AirLIF system is not running an IPI converter, similar numbers - 1 to 9 $^{std\,l}/_{min}$ - occur for the flow through the critical orifice whose diameter is 1 mm. Both AirLIF cells in addition add 1 $^{std\,l}/_{min}$ of nitrogen as purge flow - OH: tube purge + baffle purge, HO_2: cell purge + baffle purge.

Even though the excitation wavelength and wavelength modulation over a few on-resonant points is the same, there is a subtle difference in the laser usage. While the AirLIF directs an expanded 308 nm laser beam only once through the detection cell, the HORUS system is working at a relatively low laser light intensity and instead makes use of a White laser multipass cell design (Martinez et al., 2010).

5.2 HO_X measurements

The AirLIF instrument measured OH and HO_2 on HALO over a range up to 15 km and was mostly running automatic, but on-resonance laser wavelength adjustments temporarily had to be maintained manually after flight level changes. The time resolution was roughly 40 s (two off- and five on-line points). After the first flight from Gan to Bahrain the etalon motor broke, which could only be repaired back in Paphos after the return on 10 August and the flight east of India into the Bay of Bengal (#14-#19) was therefore missed. During flight #21 over Saudi Arabia on 18 August some HO_x data were lost due to a burn spot appearing on the SHG crystal behind the pump Laser converting to the 532 nm, but this problem was fixed until the next flight. Generally flight data were acquired on flight numbers #8-#13 and #20-#24.

Ground based calibrations were done consistently between each flight in the first and last period on Cyprus (Paphos, cf. Section 4.2.3). No calibrations were done on Gan. Nevertheless in-flight calibrations were done during almost all flights when the atmospheric water vapour concentration was sufficiently high. As explained in Chapter 4, interferences were subtracted first and then the signals were converted to concentrations using the OH and HO_2 sensitivities (cf. Figure 4.15 and 4.17). For OH, only the ozone-water interference had to be considered (cf. Figure 4.20). This interference was negligible on the HO_2 cell (cf. Figure 4.26), as was the background from the added NO (cf. Figure 4.27).

Final HO_x data measured by the AirLIF system were uploaded on the HALO database as data files #6193-#6203 (from 2018-11-23) and replace the previous data set from 2016-09-15. They contain the precision of each measurement point, which is determined by the instrumental Poisson noise. Accuracy and precision are strictly separated and the former is discussed in Section 4.7. For OH and HO_2 there are two contributions coming from the error of the calibration method and the un-

Table 5.2: HALO cabin layout and measured species during OMO (cf. Figure 5.3).

Instrument	Measured quantity	Technique*	Institution	HALO position
KMS FAIRO	OVOC O_3	PTRMS Fast CLD	KIT Karlsruhe	1
CPC	Particles	CPC	DLR-IPA	2
SOFIA	NMVOC	Fast GCMS	MPIC Mainz	3
AENEAS	NO/NO_y	CLD	DLR-IPA	4
SHARC BAHAMAS	H_2O met. parameter	DOAS BDAS	DLR DLR	5
TRIHOP	CO, CH_4, ROOH, H_2O_2, HCHO	QCS	MPIC Mainz	6
AirLIF	**OH, HO_2**	**LIF**	**FZ Jülich**	**7**
HORUS GANDALF	OH, HO_2 NO_2	LIF LIF	MPIC Mainz	8
PERCEAS	RO_x	CA	University Bremen	9
HALO-SR	**Spectral actinic flux density**	**CCD SR**	**FZ Jülich University Leipzig**	**10**
IPA-CIMS	SO_2, HNO_3	CIMS	DLR-IPA	11
MIRAH	NMVOC + isotopes	GCMS (canisters)	University Wuppertal	12
miniDOAS	HONO, BrO_2, CLO, CLO_2, IO, ...	DOAS	University Heidelberg	12
vacuum pumps				p
gas supply				g

* **LIF:** Laser Induced Fluorescence, **PTRMS:** Proton Transfer Reaction Mass Spectrometer, **CLD:** ChemiLuminescence Detector, **DOAS:** Differential Optical Absorption Spectrometer, **BDAS:** Basic Data Acquisition System, **CIMS:** Chemical Ionization Mass Spectrometer, **QCS:** Quantum Cascade Spectrometer, **GCMS:** Gas Chromatograph Mass Spectrometer, **CA:** Chemical Amplifier, **CCD SR:** Charged Coupled Device Spectral Radiometer, **CPC:** Condensation Particle Counter

certainty of the pressure ratio between inlet and detection cell. HO_2 has another error source due to the mass-flow correction factor. Combined an overall accuracy of 17 % (1σ) can be attributed to OH with increased uncertainty of 34 % between 10.5 and 13 km, while for HO_2 the total accuracy varies between 0 km and 13.5 km from 18 to 26 %, increasing further to 35 % above 13.5 km (cf. Figure 4.28).

As noted before, besides AirLIF there was HORUS measuring HO_x of which by the time of this writing only data of flight #12 and #20-#24 were available (HALO database: dataset #5067-#5078, 2017-06-14). They will be used for a measurement comparison in the following section. HORUS similarly provides precision values of about 10 % (1σ) for OH and HO_2. Accuracy is given by 21 % and 28 % (1σ) for OH and HO_2, respectively.

Final PerCEAS - RO_x measurements - data were not available as of yet and are not considered throughout the upcoming analysis.

5.2.1 Time-Series

During OMO-ASIA most OH and HO_2 data were measured in the upper troposphere (10-15 km). Lower altitudes (3-10 km) were - besides take-off and landing - only occasionally probed mainly over the Mediterranean Sea (flights #10, #22 - #24). On flights #23 and #24, the aircraft passed Mount Etna at low altitude (3 km). For an overview of all AirLIF HO_x measurements see Appendix A.2.

Figure 5.5 shows two flight examples. The OH and HO_2 data measured by AirLIF and HORUS show good precisions and demonstrate good instrumental agreement with respect to the observed temporal and spatial variability of the radicals and their absolute concentrations (for details cf. Section 5.2.2). Flight #20, crossing the Arabian Peninsula, almost stayed at constant flight level (11.5-13 km) and shows a large variability (0.2 to 0.7 ppt) in the OH. The transfer-flight #24 back to Oberpfaffenhofen which bypassed the mount Etna on Sicily between 11:00 and 12:30 covers many different flight levels (upper tropospheric flight levels range from 11.5 to 13.8 km and lower flight levels down to 3 km) and only shows little variation in the OH (0.3 ± 0.1 ppt). In contrast HO_2 exhibits pronounced variations with 1 to 5 ppt in the upper troposphere above 11 km (flight #20 and #24) and shows much higher values of 20-30 ppt at low altitudes (3 km, flight #24). When changing flight levels the NO mixing ratios vary between 0.1 and 0.4 ppb at high altitudes (> 11.5 km) and 0.05 ppb in the lower troposphere. HO_2 shows a general anti-correlation with NO similar to observations at ground (Holland et al., 2003). For OH a pronounced correlation with NO can be observed in the upper troposphere. These observations agree with the results obtained by Brune et al. (1998), who observed such correlations between OH and NO and anti-correlations between HO_2 and NO in the upper troposphere over California (USA) during the SUCCESS mission 1996. Such correlations are mainly the result of the conversion of HO_2 to OH by the reaction with NO (cf. Reaction R15). This will be corroborated by a box-model calculation later in this chapter which includes further interpretations (cf. Section 5.2.3 and 5.3.1).

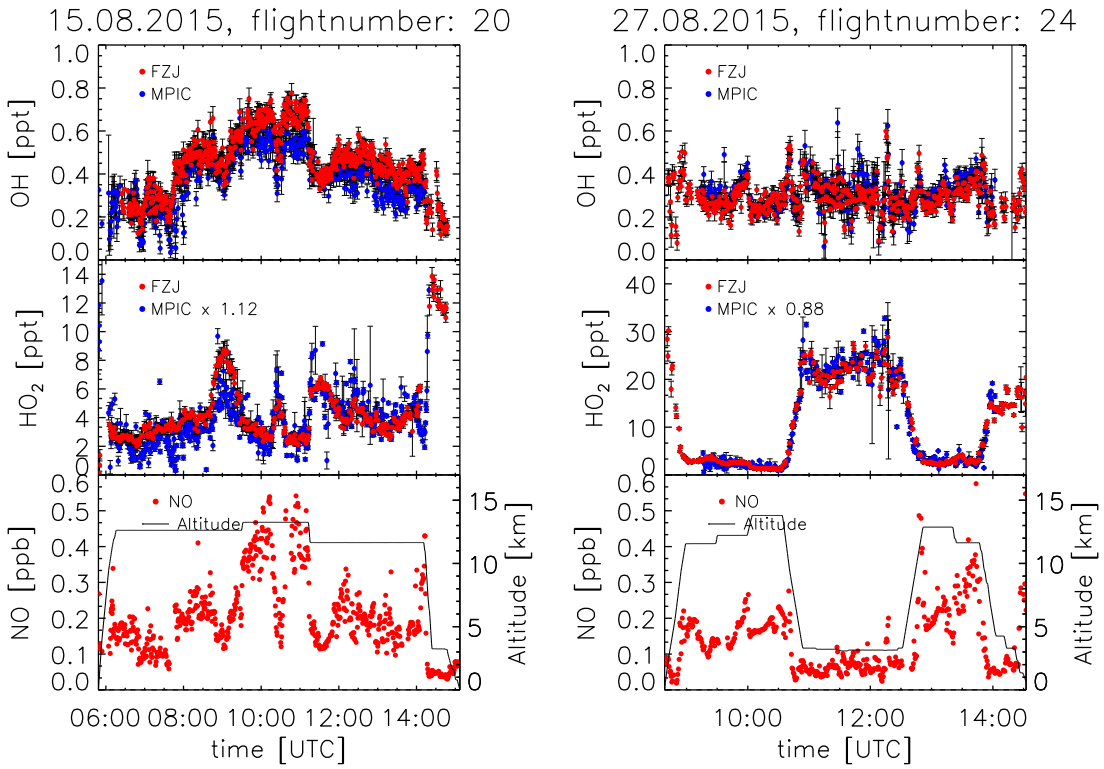

Figure 5.5: Left: Flight #20 crossing the Arabian Peninsula. The flight showed a large correlated variability of NO, OH, and HO_2 at almost constant altitude (11.5 - 13 km). Note the different HO_2 scales for flight #20 and #24. **Right:** Transfer Flight (#24) back to Oberpfaffenhofen at 11.5 - 13.5 km on the 27.08.2015. HALO bypassed mount Etna on Sicily at 3 km altitude between 10:45 and 12:30 UTC. The change of flight altitude had almost no influence on the OH mixing ratios, but resulted in a large change of the measured NO and HO_2 mixing ratios. This flight exhibits a distinct NO anti-correlation of HO_2.

5.2.2 HO_x measurement comparison

HO_x data measured by AirLIF and HORUS are compared in Figure 5.5 for flights #20 and #24. Other flights (#12, #13, #21, #22, #23) with simultaneous HO_x measurements by both instruments can be found in Appendix A.2. Within their measurement errors both datasets generally show a good agreement in comparison, but some few temporary differences occur. For example on flight #21 between 07:00 and 08:00 UTC HORUS shows some transient decrease in measured OH, whose reason is not clear, but which look like outliers. On flight #22 there are systematic deviations in the observed OH between AirLIF and HORUS. After a good agreement at flight altitudes of 5.5 - 13 km, both instruments start to diverge after 10:20 UTC until AirLIF OH is a factor of 1.4 higher than HORUS OH. This discrepancy is larger than the combined 1σ calibration errors (17 % for AirLIF, 21 % for HORUS) and it is not clear why it shows up only during this particular time period. However - looking at the altitude and Figure 4.15 and 4.28 - an influence due to the pressure jump in the AirLIF sensitivities can not be excluded, in particular the size of the discrepancy fits the magnitude of the OH sensitivity jump (factor 1.5).

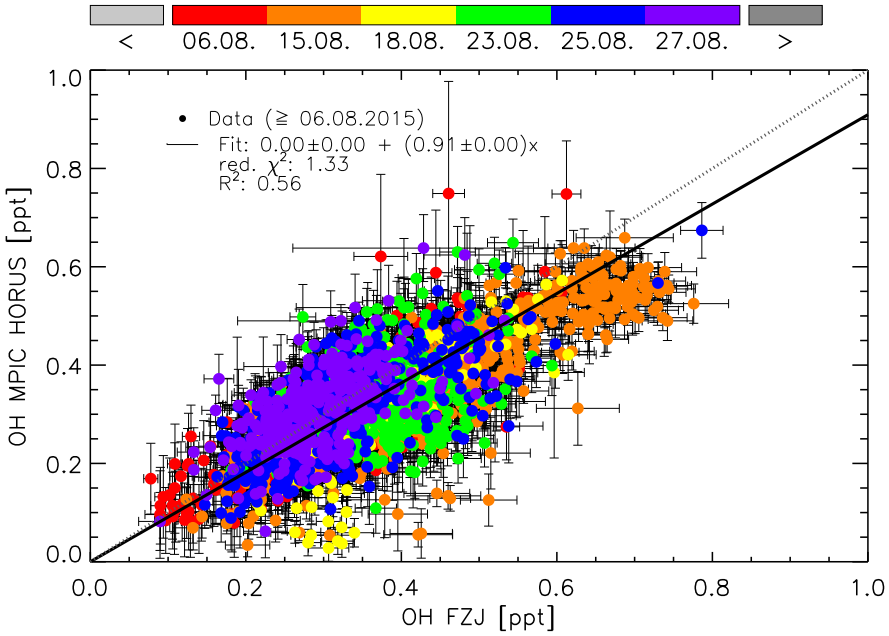

Figure 5.6: FZJ vs. MPIC correlation plot showing all the OH data from 06 August to 27 August. The dashed line represents the 1:1 line. Shown error bars represent measurement precision (1σ). The regression is forced through zero. Colour codes represent date of measurement (dd.mm.) in 2015.

In case of HO_2, major systematic deviations between AirLIF and HORUS are observed on two occasions for unknown reasons. On flight #22 between 06:40 and 7:30 UTC there is a factor of 2 discrepancy between HORUS and AirLIF (5.5 - 11.3 km altitude), while there is good agreement for the rest of the flight. The biggest discrepancy occurs on flight #12, where HORUS measures a factor of 3 higher HO_2 mixing ratios than AirLIF, which is in contrast to the good agreement of the OH measurements by the two instruments. This difference indicates a problem with the chemical HO_2 to OH conversion in one of the instruments during this flight. Nevertheless HORUS and AirLIF still show the same relative trend. In view of the other flights at about 12.5 km with only a few ppt, values of 20 ppt measured by HORUS do not seem plausible. A mean value of 6 ppt seen by AirLIF appears more reasonable. Ultimately the cause for the discrepancy between HORUS and AirLIF data on this flight is not known though.

Apart from the few discrepancies discussed above, the OH measurements by the two instruments agree very well considering the statistical precision and calibration uncertainties. Due to the large uncertainties for the HO_2 calibrations (up to 35 % for AirLIF, 28 % for HORUS), all data except the discrepancies on flight #12 and #22 can also be seen as a good agreement.

In Figure 5.6 and 5.7 all the HORUS data starting from the 06.08.2015 were plotted against FZJ measurements. The regression is a linear function and was done with

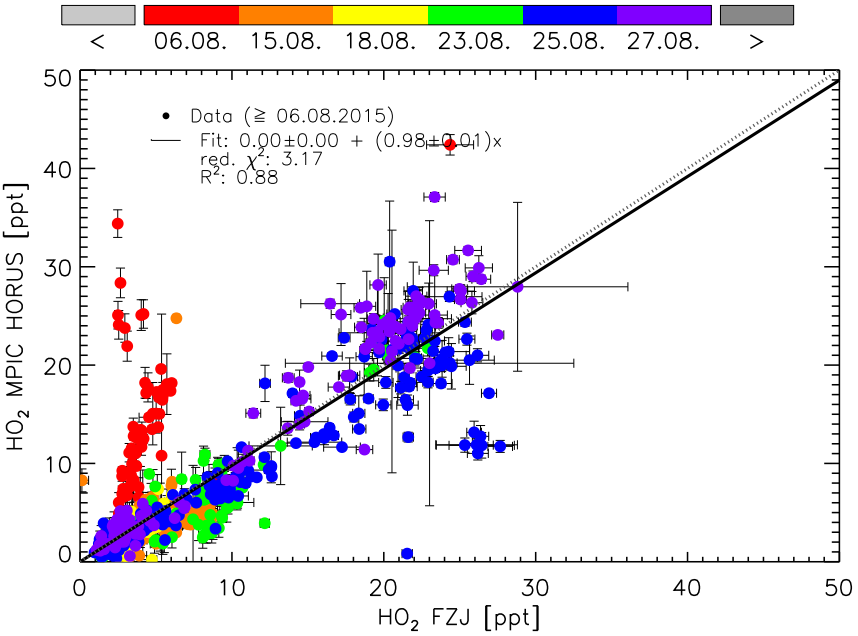

Figure 5.7: FZJ vs. MPIC HO_2 correlation plot showing data from 06 August to 27 August 2015. Shown error bars represent measurement precision (1σ). The regression is forced through zero and the red data points were not included in the linear regression. Colour codes represent date of measurement (dd.mm.) in 2015.

a self-written IDL procedure minimizing the expression

$$\chi^2 \sim \sum_k \left\{ p_{xk} \left(X_k - x_k \right)^2 + p_{yk} \left(Y_k - y_k \right)^2 \right\} \tag{5.1}$$

under the constraint $y_k = \beta_0 + \beta_1 x_k$ where β_0, β_1 (offset, slope) and x_k are sets of parameters and X_k, Y_k are the data. The weights p_{xk}, p_{yk} were set to a constant value. The minimization procedure follows an adjustment of the steepest gradient method known as Levenberg-Marquardt. The offset β_0 in the fitting process was generally forced to zero, because the dynamic range of measurements on some flights was small (e.g. OH during flight #24) and did not allow meaningful two-parameter linear regression.

For OH the good agreement between HORUS data already seen in the time-series manifests itself also throughout the campaign with a slope of the regression line close to one. The correlation coefficient ($R^2 = 0.56$) is lower than expected though, for mainly two reasons. Looking at Figure 5.5 shows that compared to HO_2 the relative variability of OH is small for some flights and will appear as a circular point cloud in the scatter plot, which by definition have little correlation. For example flight #24 has a low correlation factor of 0.35. The lowest R^2 occurs on 23 August (flight #22) and is as low as 0.05, but with a slope of 0.92 forced through zero. In contrast the highest correlation factor is 0.8 on flight #20 with a slope of 0.82. A second reason for the overall low correlation coefficient in Figure 5.6 is a varying agreement of AirLIF and HORUS from flight to flight. The slopes of regression lines for individual flights change between 0.82 (flight #20) and 1.06 (flight #24), which points to unaccounted variability in the calibrations of one or both instruments.

These variations collectively disperse the overall appearance contributing to the low correlation coefficient of 0.56. As such the slope of 0.91 is a satisfactory result which represents the overall good agreement of OH quite well in view of the OH time-series given in the Appendix A.2. The slopes for the different flights (0.82 - 1.06) lie well in the range expected from the instrumental calibration errors (17 % - 34 % for AirLIF, 21 % for HORUS).

HO_2 (cf. Figure 5.7) also shows a satisfactory picture in direct comparison to HORUS data with high correlation. Since data points from 06 August seem to be completely off the general trend, they were excluded from the fitting procedure. The dynamic range is much larger and leads to a correlation coefficient of $R^2 = 0.88$ and a slope very close to 1. It should be noted that without the mass-flow correction (cf. Figure 4.24) the slope is merely ≈ 0.3 and the data seemed highly uncorrelated with $R^2 \approx 0.27$. The significant improvement after the correction for the fluid-dynamical effect of decreased mass-flow indicates to have tackled the core of the initial major discrepancy.

5.2.3 Altitude profiles of HO_x

Figure 5.8 shows altitude profiles for important quantities to HO_x. The top left panel shows OH as measured during OMO (light-grey) and the median over all data points of the time-series in the Appendix A.2 (dark-grey) with 1σ calibration uncertainty bands (medium-grey). The panel for the HO_2/OH ratio shows in addition two theoretical curves: the green line is an approximation calculated using Equation 5.3; the blue line represents a full model simulation (cf. Section 5.3.1).

From 0 to 15 km the median of the OH mixing ratio is almost constant increasing slightly from 0.18 ppt near ground to 0.4 ppt at 15 km. In contrast HO_2 exhibits a strong altitude dependence with maximum values of 25 ppt at 1 km. At higher altitudes, HO_2 decreases steadily to 1 - 2 ppt at 15 km.

The vertical profiles and concentrations for OH and HO_2 observed during OMO-ASIA are in accordance with other aircraft measurements that were performed in other global regions (North America, Pacific, Atlantic) during daytime. The most recent study about *Atmospheric Oxidation in the Presence of Clouds during Deep Convective Clouds and Chemistry* (DC3) on the NASA DC-8 aircraft by Brune et al. (2018) shows HO_2 mixing ratios at 12 km around 5 ppt. The campaign concentrated over the regions Colorado, Texas/Oklahoma and Alabama where it sampled deep convections. Older studies show similar values: 4 ppt at 10 km which took place over the North Atlantic (Brune et al., 1999), 10 ppt at 12 km over North America and the western Atlantic Ocean (Ren et al., 2008) and 10 ppt at 8 km over the Suriname rainforest (Martinez et al., 2010). With decreasing altitude, observed HO_2 mixing ratios are generally found to increase reaching maximum values near 1 km. At this altitude the median is 22 ppt in the DC3 study and 25 ppt for the OMO campaign which is in astounding agreement considering the rather different locations of the campaigns. The other two studies from 2008 and 2010 observed similar daytime values around 25 ppt near ground, but Brune et al. (1999) did not measure near

ground, since low altitude flights were after sunset.

The mixing ratio of OH is generally found to change little between the lower and upper troposphere. Near ground typical median OH mixing ratios are in the range between 0.18 ppt (this work) and 0.25 ppt (Martinez et al., 2010) and at 12 km altitude typical values between 0.3 ppt (this work and DC3) and 0.6 ppt (Ren et al., 2008) have been reported. Lower values were measured by Brune et al. (1999) being 0.1 ppt at 8 km altitude. These findings suggest that HO_x mixing ratios at higher altitudes are globally not very susceptible to the location which is reasonable considering the constancy of various important precursors, long-lived reactants (e.g. CO, CH_4) and photolysis frequencies during clear sky at these levels. Most local emissions at ground likely only affect the lower part of the troposphere and lead to the observed variability in OH, but will be degraded by the time they reach the upper troposphere.

The median vertical profiles of CO, ozone and methane are relatively constant from 0 to 15 km. This is expected for methane as it is very long lived and thus should be well mixed. Below the planetary boundary layer median CO takes values up to 120 ppb and decreases to 70 ppb above 4 km. The enhanced values below 4 km are probably due to emissions at ground. Similar observations have been reported by Brune et al. (2018).

Although the observed median ozone mixing ratio is relatively constant over the height of the troposphere, considerable variability is observed in the upper troposphere at a given altitude, which may be partly due to transport from the stratosphere. Near ground ozone mixing ratios of 50 ppb are expected and are also found in Brune et al. (2018). At 12 km however DC3 observes a median of 100 ppb while during OMO slightly decreased values of only 70 ppb are found.

The vertical profile of NO during OMO (cf. Figure 5.8) shows a C-shape with 0.1 ppb at ground, decreasing to 0.04 ppb at 6 km in a pronounced minimum and then increasing again up to 0.2 ppb at 12 km. Such C-shape profiles of NO have been first reported from aircraft measurements over the Pacific by Ridley et al. (1987) and over the Western Atlantic by Drummond et al. (1988). In a model analysis by Ehhalt et al. (1992), the high NO values near ground were attributed to ground-based emissions, whereas the maximum values in the upper troposphere were explained by fast vertical transport (deep convection) from the boundary layer, with additional contributions from aircraft emissions, lightning and stratospheric transport. The role of these processes on the photochemical ozone production in the upper troposphere has been analysed, for example, by Cooper et al. (2006).

The sharp decrease in water vapour with increasing altitude is well predicted due to the exponential temperature dependence of the saturation vapour pressure in Clausius-Clapeyron equation. The photolysis frequency j_{O^1D} depends most strongly on the solar zenith angle, stratospheric ozone, tropospheric aerosols and clouds. Under cloud free conditions as in the case of OMO-ASIA, j_{O^1D} is expected to show only small variations with altitude in the troposphere (cf. Figure 2.3). The variability of

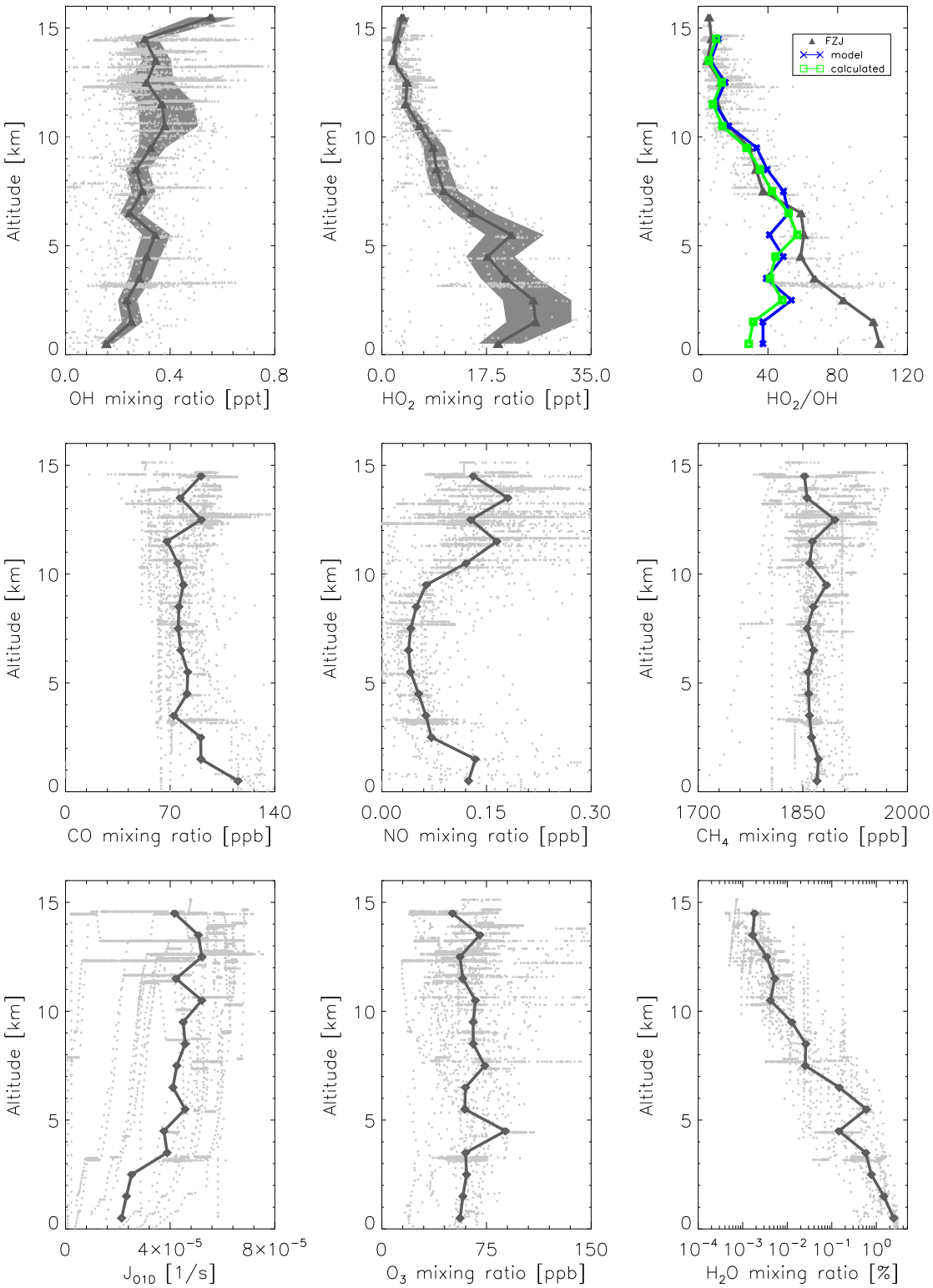

Figure 5.8: Altitude profiles of measured radicals (OH, HO_2) and controlling parameters. Only AirLIF radical data are shown. Median is taken over all data points of the time-series in the Appendix A.2. Dark-grey: median, light-grey: single measurement, medium-grey for OH and HO_2: 1σ calibration uncertainty bands.

the measurements shown in Figure 5.8 is mainly due to different solar zenith angles.

The observed HO_2/OH ratio (cf. Figure 5.8 upper right panel) shows values around 100 near ground and decreases linearly until 11 km with values of 10 and from where it only decreases marginally with increasing altitude. Other studies exhibit similar ratios as observed during OMO. For example Cantrell et al. (2003b), Ren et al. (2008), Stone et al. (2010) and Brune et al. (2018) show HO_2/OH ratios of 100-250, 140, 100 and 120 near ground respectively. Cantrell et al. (2003b) discusses this dependence with respect to NO and for different CO mixing ratios and also finds that model results under-predict these ratios near ground. Above 10 km Ren et al. (2008) and Brune et al. (2018) show 12 and 15 for the HO_2/OH ratio, while Stone et al. (2010) only measured up to 7 km with a ratio of 30 at this altitude.

Going back to HO_x, a simple expression for the HO_2/OH ratio can be derived by considering HO_2 in steady state

$$\frac{\mathrm{d}\,[\mathrm{HO_2}]}{\mathrm{d}t} = \sum_i k_{\mathrm{C}_i+\mathrm{OH}}\,[\mathrm{C}_i]\,[\mathrm{OH}] + P_{\mathrm{HO_2}} - k_{\mathrm{HO_2}}\,[\mathrm{HO_2}] = 0\,, \tag{5.2}$$

where the sum on the right hand side goes over all species which react with OH to form HO_2 such as CO, O_3, HCHO, H_2O_2 and CH_3OH (cf. Figure 2.4). P_{HO_2} are primary HO_2 sources as well as production via $RO_2 + NO$ (cf. Reaction R13 and R14) and k_{HO_2} is the HO_2 reactivity which will be dominated by the reaction with NO and ozone. Here it is assumed that the decay of HNO_4 of reaction R29 does not appear, as this reaction is assumed to be in thermal equilibrium with the production of HNO_4 from $HO_2 + NO_2$ (cf. Section 5.3.2). It is then just a matter of simple rearrangement to arrive at

$$\frac{[\mathrm{HO_2}]}{[\mathrm{OH}]} = \frac{\sum_i k_{\mathrm{C}_i+\mathrm{OH}}\,[\mathrm{C}_i]}{k_{\mathrm{HO_2}}} + \frac{P_{\mathrm{HO_2}}}{k_{\mathrm{HO_2}}\,[\mathrm{OH}]}\,. \tag{5.3}$$

As is confirmed by the model calculations in Section 5.3.1, it is a good approximation at high altitudes to neglect P_{HO_2} and only consider the first summand in Equation 5.3 where all the quantities are assumed to be accurately measured. Above 7 km this approximation already gives an astounding agreement with the measurements (Figure 5.8). In the lower troposphere (< 7 km), the estimated ratio calculated by Equation 5.3 starts to deviate from the measured ratio by up to a factor of three, which must therefore solely come from the second term alone. The calculated ratios at ground predict a value of ≈ 30 compared to ≈ 100 for the observation, which suggests that the production of HO_2 from RO_2 conversion (cf. Reaction R13 and R14) and photolysis of HCHO (cf. Reaction R22) become important in the lower troposphere, which is consistent with numerous ground-based field observations in clean (Stone et al., 2018) and polluted environments (Tan et al., 2018).

For a better understanding of the discrepancy, possible contributions to P_{HO_2} can be estimated. Two contributions ($\frac{j_{\mathrm{HCHO}}[\mathrm{HCHO}]}{[\mathrm{OH}]}$ and $\frac{j_{\mathrm{CH_3OOH}}[\mathrm{CH_3OOH}]}{[\mathrm{OH}]}$) due to the photolysis of HCHO and CH_3OOH turn out (cf. Section 5.3.2) to only account for a few percent which is by far not sufficient considering the gap which needs to be

filled. The production of HO_2 from the $RO_2 + NO$ reaction is difficult to calculate due to the lack of knowledge in the RO_2 mixing ratio, but a very rough estimate can be made by assuming $[RO_2] \approx [HO_2]$ in accordance to observations in the lower troposphere as it has been observed in many ground based field campaigns (Mihelcic et al., 2003; Tan et al., 2017). With this assumption, the calculated HO_2/OH ratio increases by about a factor of 2 at all altitudes. This leads to improved agreement for the observed HO_2/OH ratio below 4 km, but to a large over-prediction above 4 km. This indicates that the RO_2/HO_2 ratio must be much smaller than one in the upper troposphere.

The quantities k_{HO_2} and P_{HO_2} in Equation 5.3 both depend on RO_2. In k_{HO_2} there is an additional loss due to the reaction $RO_2 + HO_2$ (cf. Reaction R26), while in P_{HO_2} the main reaction is controlled by $RO_2 + NO$ (cf. Reaction R13). Writing Equation 5.3 as

$$\frac{[HO_2]}{[OH]} = \frac{\sum_i k_{C_i+OH}\,[C_i]}{k^0_{HO_2}} \frac{1 + \frac{k_{RO_2+NO}[RO_2][NO]}{\sum_i k_{C_i+OH}[C_i][OH]}}{1 + \frac{k_{RO_2+HO_2}[RO_2]}{k^0_{HO_2}}} \tag{5.4}$$

where the superscript 0 stands for the base case without RO_2, it can be seen that the HO_2/OH ratio increases with RO_2 relative to $RO_2 = 0$. For the base loss rate $k^0_{HO_2} \approx 0.05\,{}^1/_{s}$ is used (taken from flight data, it is governed by NO and O_3). Similarly the secondary production via OH gives $\sum_i k_{C_i+OH}\,[C_i]\,[OH] \approx 1 \times 10^7\,{}^1/_{cm^3\,s}$ at ground conditions (taken from flight data). As rate constant for RO_2 with NO $8.8 \times 10^{-12}\,{}^{cm^3}/_{s}$ is assumed, while for HO_2 they vary between $5 \times 10^{-12}\,{}^{cm^3}/_{s}$ and $2 \times 10^{-11}\,{}^{cm^3}/_{s}$ for different RO_2 species. To explain a factor of three at 1 - 2 km altitude, RO_2 mixing ratios must then lie in the range of 30 and 50 ppt, which is in comparison to HO_2 (21 - 32 ppt) a realistic range (Mihelcic et al., 2003; Tan et al., 2017). With increasing altitude (up to 7 km) the importance of RO_2 as HO_2-source decreases significantly. This hints that generally reactive non-methane VOCs are not transported much further up, which is in accordance with transport times of air-masses and the life-time of these more reactive VOCs.

Above 7 km, the HO_2 formation is dominated by the reaction OH + CO (cf. Reaction R8), whereas k_{HO_2} is mainly controlled by the reaction HO_2 + NO (cf. Reaction R15) forming OH. Apparently, Reactions R8 and R15 control the partitioning of HO_x in the upper troposphere, which also explains the observed positive correlation between NO and OH, and the anti-correlation between NO and HO_2 on flight #20 at high altitudes (Figure 5.5). Comparable results were obtained by (Wennberg et al., 1998), when they performed first measurements of OH and HO_2 in the upper troposphere over the Pacific Ocean near Hawaii. Reactions R8 and R15 do not only determine the HO_x partitioning, but also control the radical cycling that leads to photochemical ozone production in the upper troposphere (Wennberg et al., 1998). Similar results were obtained in airborne studies above North America and the North Atlantic (Brune et al., 1999; Jaegle et al., 1999; Ren et al., 2008).

5.3 HO_x model analysis

In this section atmospheric-chemical box-model calculations for OH and HO_2 will be presented and compared to the OMO-measurements. The investigative focus will lie on the upper troposphere where most of the measurements took place, and it will be analysed to what extent the radical chemistry is understood herein. Some limitations concern the incompleteness of various trace-gas measurements which are needed as input (constraint) for the box-model. However the results will still be used, to obtain insights in the most important production- and destruction processes for OH and HO_2, and to deduce an altitude profile.

5.3.1 Box model

A zero-dimensional box model was used to calculate steady-state radical concentrations for OH, HO_2 and RO_2 using an integration time of 10 000 s. RACM2 (Goliff et al., 2013) was used as a state-of-the-art gas-phase chemical mechanism. No heterogeneous chemistry (e.g., uptake of HO_2 on aerosol or water particles) was included, since no flights were done within clouds. The differential rate equation systems were solved by FACSIMILE (Malleson et al., 1990) using the compiler program EASY (Brauers and Rohrer, 1999) for easy handling of the program input (chemical equations and boundary conditions). Some minor modifications were done: a general dilution loss rate of 5 days was assumed for all substances and the OH + CO reaction rate constant was replaced by the recommended JPL version (Burkholder et al., 2015).

Table A.1 (Appendix A.3) shows the chemical species and photolysis frequencies which are important to the box model. O_3, H_2O, CO, CH_4, H_2O_2, ROOH, acetone, CH_3OH and NO were constrained by in-situ measurements. Experimental data gaps for CO and H_2O were filled with global atmospheric-chemistry model (EMAC), results made available by A. Pozzer (MPIC Mainz) on the HALO data archive for OMO (see footnotes in Table A.1). For CO, data gaps were filled on the first half flight of 6 August, and on 15, 23 and 27 August. After the transfer flight to Gan, water vapour measurements were only available restrictedly, as the SHARC hygrometer got damaged. Thereafter, only measurements at lower altitudes were available from the less sensitive VAISALLA humidity sensor. EMAC data were also used replacing missing measurements of HNO_3, HCHO and CH_3CHO. For H_2 a fixed value of 550 ppb was used. Non-methane hydrocarbons (NMHC) were set to zero in the model due to the lack of measured data. For benzene, toluene and isoprene only few measured data are available. These were not used because the available data were at the limit of detection (72 ppt for isoprene, 20 ppt for the aromatics). The potential role of missing VOC data is discussed later. Photolysis frequencies were constrained by measurements (cf. Table A.1). For the calculation of air number densities and reaction rate constants, static pressure and temperature supplied by BAHAMAS (cf. Table B.2) were used.

Generally EMAC model data and measured H_2O and CO show agreement within 20 % during temporal overlap giving trust in using EMAC data as replacement of

missing measurements. Variation of the input data for HNO_3 and CH_3CHO by a factor of 2 has negligible influence ($< 1\,\%$) on the modelled HO_x concentrations. A corresponding variation of the HCHO input changes the modelled OH and HO_2 by up to 20 % in the upper troposphere and up to 5 % below 5 km.

The base model was run into equilibrium assuming a steady state time of 10 000 s. Theoretically this should be at least twice as much as the longest occurring life-time which at present is the assumed dilution loss rate of 5 days (except for decomposition processes as in PAN and HNO_4 at very cold temperatures). This was tested in the model and only affected the result up to a few percent. However such long integration times are not sensible, since certain boundary conditions such as the constancy of photolysis frequencies are not fulfilled, but in essence this means that calculated species with a long lifetime only influence the HO_x chemistry very weakly in the present case.

Besides HO_x, also other trace gases (NO_2, HONO, PAN, HNO_4) were simulated by the box model. HONO and NO_2 are relatively short-lived due to photolysis at all altitudes. Therefore they reach photo-stationary state ($NO_2 \leftrightarrow NO + O_3$; $HONO \leftrightarrow OH + NO$) in the model within the chosen integration time. PAN and HNO_4 are expected to reach thermal equilibrium within the model integration time only in the lower troposphere (cf. Reaction R43, R30), while above 7 km the thermal dissociation is slow due to the cold temperatures and plays no role in the model ($\tau_{HNO_4,\Delta,7\,km} = 2500\,s$, $\tau_{HNO_4,\Delta,8\,km} = 10\,000\,s$, $\tau_{PAN,\Delta,7\,km} = 12\,d$, $\tau_{PAN,\Delta,8\,km} = 116\,d$). Assuming initial concentrations of zero, the formation of PAN and HNO_4 constitutes an effective radical sink in the model above 7 km. The relevance was tested by turning off the entire production of these reservoir species. A negligible effect of PAN was found, because at high altitudes the branching ratio with respect to the formation of PAN is small compared to the other reaction with NO to form CH_3O_2 (cf. Figure 2.4). On the other hand, for HNO_4 the maximum impact on the modelled HO_x is 10 %.

5.3.2 HO_x model measurement comparison

Figure 5.9 shows the OH and HO_2 vertical profile of measured (grey) and modelled (blue) mixing ratios from 0 to 15 km. Furthermore, observed-to-modelled ratios are used to evaluate how well the model agrees with observations. The evaluation considers the experimental 1σ uncertainty of OH and HO_2 (cf. Figure 4.28) and an estimated 1σ model error of 20 % representing errors of reaction kinetic data (Brune et al., 2018). Figure 5.9 also shows the modelled and measured HO_2/OH ratios and their ratio. The additional uncertainty caused by the model input parameters (Table A.1) will be discussed separately below.

From a qualitative perspective measurement and model altitude profiles of OH and HO_2 do agree reasonably well. Between 7 and 11.5 km altitude OH agrees within the combined uncertainty, while above the model results overestimate the measurements by up to a factor of 2. Similarly below 7 km the model predicts up to a factor of 2.5 of the observations. In contrast HO_2 measurements and model results agree within

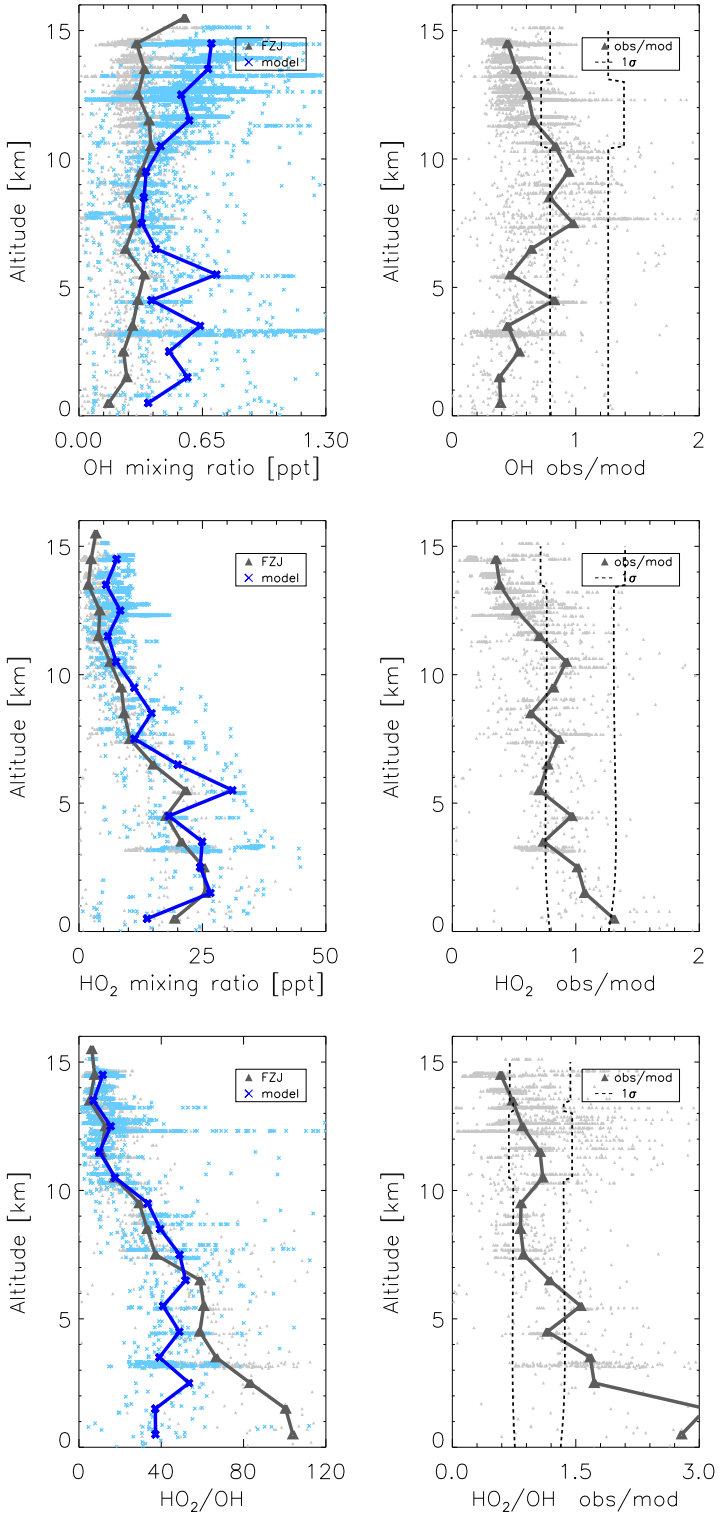

Figure 5.9: Vertical profile of modelled and measured OH, HO_2 and HO_2/OH during the OMO flights. Experimental data are the same as shown in Figure 5.8. **Left:** Shaded dots and crosses represent measured (grey) and modelled (blue) 1-minute data points. Big triangles and crosses denote median values over 1 km bins. **Right:** Observed-to-modelled ratios. Vertical dashed lines enclose the range of model-measurement agreement. The width is given by the combined uncertainty ($\pm 1\sigma$) calculated from the uncertainties of measurement and model.

their combined uncertainty up to 11.5 km and only above the model overpredicts by a factor of 2.5. This happens in the same way as for OH, resulting in a correct prediction of the HO_2/OH ratio between 7 and 15 km. Below 7 km the ratio starts to deviate up to a factor of 3 (cf. Figure 5.9). This was already encountered in the previous discussion at the end of Section 5.2.3.

In order to understand the altitude profiles, it helps to look at Figures 5.10 and 5.11 for the production and loss rates of OH and HO_2 respectively and consider the steady state equations for the mixing ratios

$$x_{\mathrm{OH}} = \frac{P_{\mathrm{OH}}}{k_{\mathrm{OH}}\,[\mathrm{M}]} \tag{5.5}$$

$$x_{\mathrm{HO_2}} = \frac{P_{\mathrm{HO_2}}}{k_{\mathrm{HO_2}}\,[\mathrm{M}]}\,. \tag{5.6}$$

P_{OH} decreases continuously over almost two orders of magnitude from 0 to 15 km, while k_{OH} decreases a bit more than one order of magnitude. As is well known, the number density will also be reduced according to the ideal gas law and the barometric formula by about a factor of 5 from 0 to 15 km. In effect the mixing ratio stays almost constant, slightly increasing. Generally all chemical reaction processes decrease in rate with increasing altitude, leading to elevated OH and HO_2 life-times. This is mainly due to the reduced collision rate of the molecules, but can be superimposed with changes in the kinetic reaction constants that are potentially pressure and temperature (with positive or negative activation energy) dependent.

The most important OH sources (cf. Figure 5.10, top right panel) are the recycling reactions of NO and O_3 with HO_2 which together make up for 86 % above 11 km and 67 % below 2 km (cf. Appendix Figure A.16). In the lower troposphere (up to 7 km) the primary production viz $O(^1D) + H_2O$ also contributes significantly (26 % below 2 km), but above 11 km this contribution makes up for only 1 % of the total OH production.

According to Figure 5.10 (bottom right panel) the major contribution to k_{OH} comes from the reaction with CO followed by methane and ozone ($>$ 11 km: 73 %, $<$ 2 km: 60 %). Their fraction is relatively constant over all altitudes as all these species are long-lived and well-mixed in the troposphere. Pronounced discrepancies in the smaller contributions are due to NO and NO_2 with a fraction of 4.4 % and 1 % above 11 km, respectively, while below 2 km this picture is reversed i.e. 1.7 % and 7.2 %, respectively. This change is most likely attributed to the NO_2/NO reversal between the upper and lower troposphere. Formaldehyde values should be viewed with caution as different EMAC models (FZJ vs. MPIC) seem to deviate up to over a factor of 2 (cf. Section 5.3.3). Above 11 km formaldehyde contributes only 2.4 % of the total reactivity, while below 2 km the value increases to 7.1 %. It should be kept in mind that HCHO only acts as a recycling agent, but not as an actual sink in this context. A similar argument is true for methanol, but the difference in the upper and lower troposphere is not very pronounced. Lastly molecular hydrogen with assumed constant mixing ratio, contributes four times more to OH reactivity in the very lower troposphere than above 11 km. A distinct contribution also arising stems

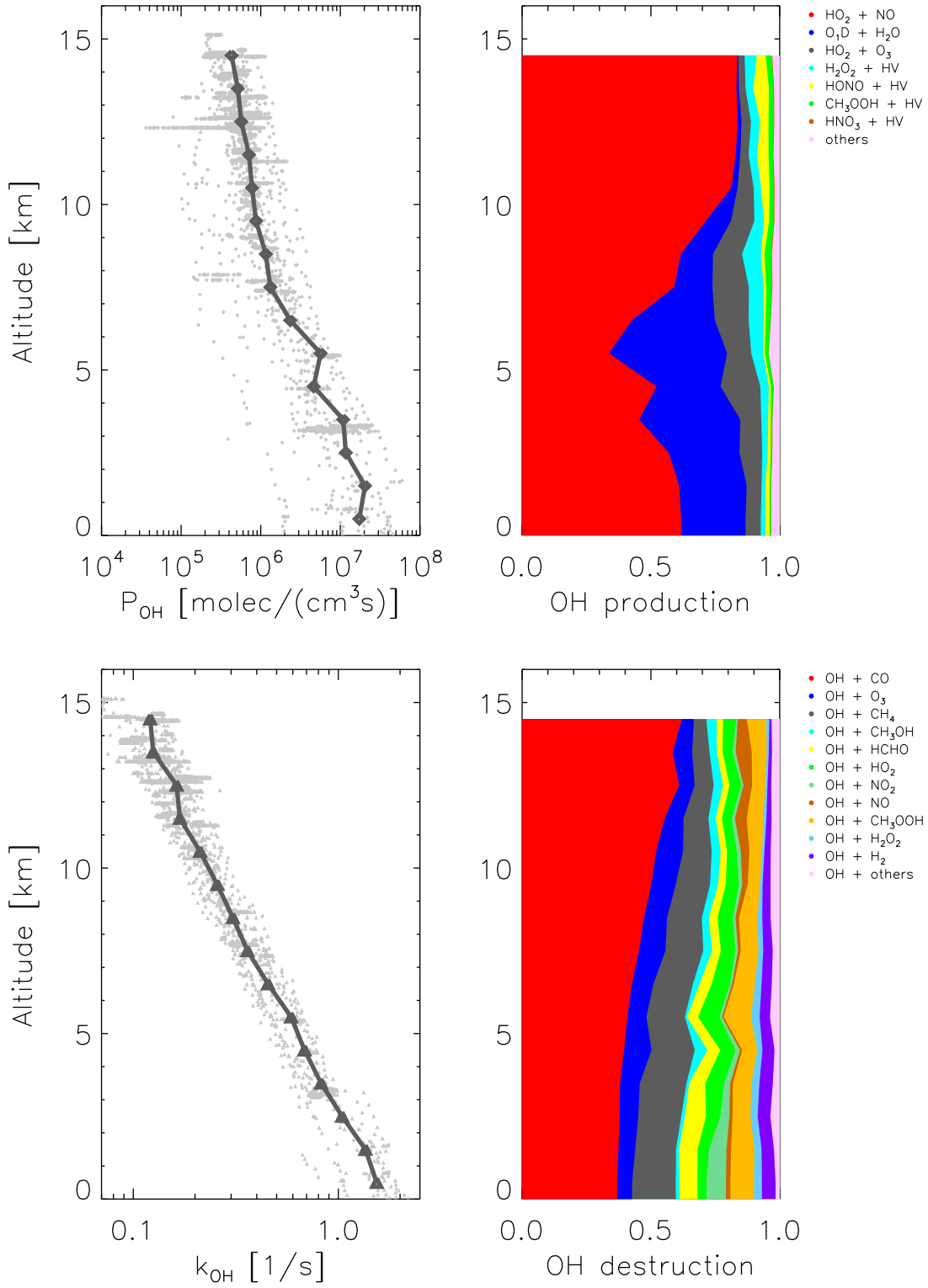

Figure 5.10: Left: Total OH production (top) and reactivity (bottom). **Right:** The most prominent contributions to the OH production (top) and reactivity (bottom).

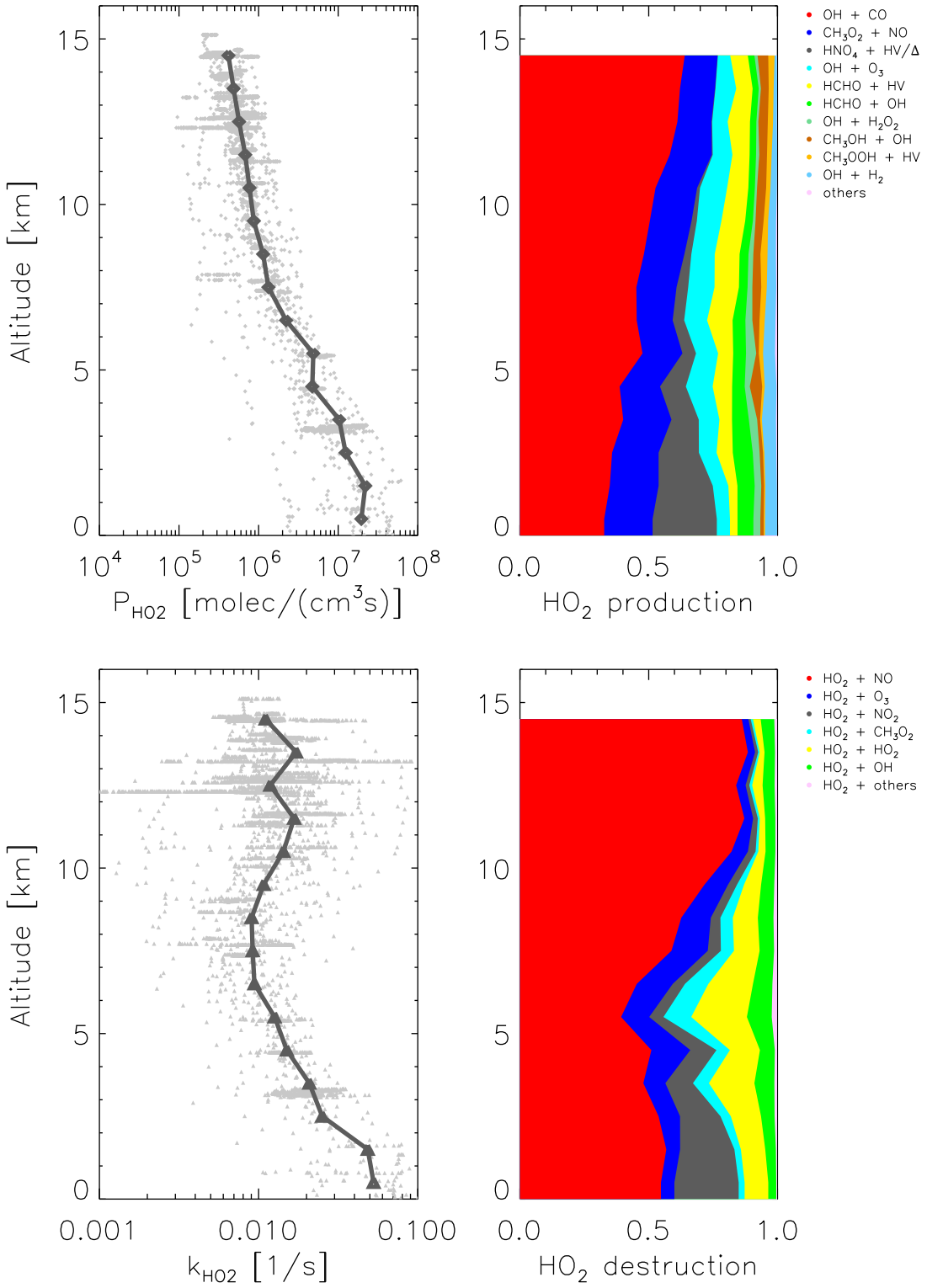

Figure 5.11: Left: Total HO_2 production (top) and reactivity (bottom). **Right:** The most prominent contributions to the HO_2 production (top) and reactivity (bottom).

from methyl-hydrogen-peroxide (> 11 km: 6.3 %, < 2 km: 9.2 %), but this reaction partly retains OH and the other part yields RO_x in the form of CH_3O_2 and will eventually recycle. The radical-radical termination reaction with HO_2 contributes in the same amount above 11 km and below 2 km. The reaction $OH + NO \leftrightarrow HONO$ as it appears in Figure 5.10 is in photo-stationary state and does therefore not contribute to the OH mixing ratio. It is remarkable that more than 95 % of OH reactivity is explained by only a few reactants with an overall rather basic chemistry. The total k_{OH} decreases roughly exponentially with altitude, since its major contributors (CO, ozone, methane) follow the ambient number density with their roughly constant mixing ratios.

The HO_2 reactivity is dominated by the reaction with NO, which has a C-shaped altitude profile (cf. Figure 5.8). At low altitudes, k_{HO_2} decreases with height. This changes at about 7 km when the NO mixing ratio has a minimum and starts to increase again with altitude. This effect is enhanced due to the further temperature decrease and the negative activation energy of $NO + HO_2$ and completely outweighs the decrease in number density, even leading to a slight increase in k_{HO_2}. Note that at the same time the loss rate is almost only driven by the reaction $HO_2 + NO$ (cf. Figure 5.11, bottom right panel). While the dominant reaction is always with NO, near ground there is also a higher contribution due to ozone and the HO_2 self-reaction (5.3 % and 9.3 %, respectively).

P_{HO_2} on the other hand steadily decreases with altitude, resulting in the strong decline in the HO_2 mixing ratios. HO_2 production is dominated by the reaction $OH + CO$ at all altitudes contributing 61 % above 11 km and only 34 % below 2 km (cf. Figure A.18). This is followed by the reaction $CH_3O_2 + NO$ which has a similar portion at all altitudes with roughly 16 %. All the other recycling reactions with OH (O_3, HCHO, H_2O_2, CH_3OH, H_2) together make up for about 15 % above 11 km and 21 % below 2 km. As was already seen in the OH reactivity discussion, HCHO and H_2 contributions are enhanced in the lower troposphere. In addition HCHO also constitutes a primary source for HO_2 due to photolysis. This behaviour is reversed with only 3.2 % of the total production below 2 km, but 7.1 % in the upper troposphere. Note that there is another major reactant near ground, namely NO_2 forming HNO_4. At typical mid-latitude temperatures this intermediate is however unstable and therefore decays back into its educts which can be seen by looking at Figure 5.11 (right panels) where the same portion arises as HO_2 production due to HNO_4 decay as in HO_2 reactivity with NO_2. Even though the effect is small - because of NO being that dominant - it can be also seen that at high altitudes a small reactivity with NO_2 remains, which however looking again at Figure 5.11 (top right panel) now does not any more appear as production. The reason has already been discussed in the introduction, as the cold stabilizes HNO_4.

5.3.3 Model uncertainties

The altitude profiles suggest that the discussion is split into three regimes:

- Altitude Range 0-7 km
  OH is overestimated by a factor up to 2.5, while HO_2 is predicted correctly

within the combined measurement uncertainties. The HO_2/OH ratio however is underestimated by up to a factor of 3.

- Altitude Range 7-11.5 km
  Both OH and HO_2 as well as the HO_2/OH ratio are all correctly modelled within the combined known uncertainties.

- Altitude Range 11.5-15 km
  OH is overestimated by up to a factor of 2 and also HO_2 model results overshoot by up to a factor of 2.5. Nevertheless the overestimation is cancelled in the HO_2/OH ratio, thus giving an excellent description of the measured ratio.

Altitude Range 0-7 km

The large over-prediction of OH in the model has two possible explanations. One option is a too large OH production rate. According to Figure 5.10 the main OH sources below 7 km are the photolysis of ozone ($\approx 26\,\%$) and the reaction of HO_2 with NO ($\approx 61\,\%$). The quantities O_3, H_2O, j_{O^1D} and NO used to constrain the OH production rate in the model have been measured with good accuracies and the modelled HO_2 agrees well with the measured HO_2. For these reasons, the OH production rate appears to be well determined and is not likely responsible for the over-prediction of OH. A more likely reason is an underestimation of the OH loss rate, because data for non-methane VOCs are missing as constraint (cf. Section 5.2.3). A sensitivity run with additional VOCs in the form of 50 ppt isoprene - leading up to 2 ppt of isoprene-peroxide radicals - for 0-7 km constitutes a major improvement of the predicted OH, while HO_2 remains in relative good agreement with the observations (Figure 5.12). The decrease in OH can be seen in two different ways.

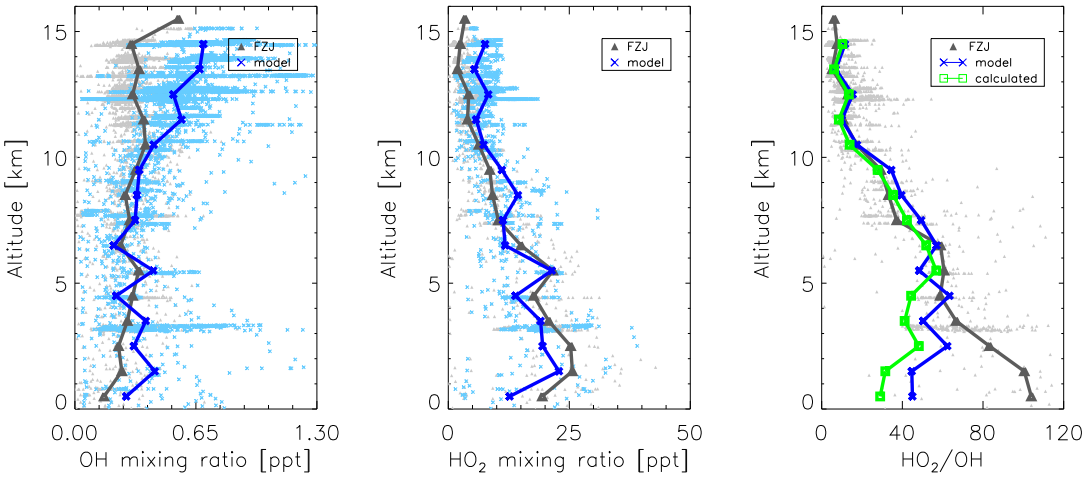

Figure 5.12: Addition of 50 ppt isoprene below 7 km.

On the one hand it is a direct effect of isoprene and its degradation products (e.g. MACR, MVK, Aldehyde) on the OH reactivity increasing it from 1.3 $^1/_s$ to 1.7 $^1/_s$ at e.g. 2 km. On the other hand, from Equation 5.4 it is seen that the HO_2/OH ratio

increases due to the presence of RO_2. Total HO_x then slightly decreases, as the total RO_x production and reactivity are essentially the same as for HO_x without isoprene present. In particular some lost HO_x self-reactivity ($OH + HO_2, HO_2 + HO_2$) will be compensated by the new reactions $OH + RO_2$ and $HO_2 + RO_2$. After all, RO_2 has to be subtracted from RO_x to yield the HO_x concentration. It then follows from the identity $[OH] = \frac{[HO_x]}{\frac{[HO_2]}{[OH]}+1}$ that OH decreases. A similar argument can be applied to HO_2 for which the lower secondary production via OH is partly compensated by the elevated direct production from $RO_2 + NO$. Since $\frac{[HO_2]}{[OH]} \gg 1$, the increased HO_2/OH ratio hardly changes the pre-factor of the similar identity $[HO_2] = \frac{\frac{[HO_2]}{[OH]}[HO_x]}{\frac{[HO_2]}{[OH]}+1}$. Therefore HO_2 primarily only changes due to the reduction in HO_x, which is much less pronounced. This qualitative analysis can be also made quantitative: Total HO_x before the introduction of isoprene can be taken from Figure 5.9 and is about 26 ppt for 2 to 5 km altitude. In the presence of isoprene, this will be in the form of RO_x which then gives $[HO_x] \approx 26\,\text{ppt} - 2\,\text{ppt} = 24\,\text{ppt}$. From Figure 5.12 (right panel) the HO_2/OH ratio can be read, giving $\frac{[HO_2]}{[OH]} \approx 60$ and hence $[HO_2] \approx 23.6\,\text{ppt}$ while $[OH] \approx 0.4\,\text{ppt}$ in accordance with Figure 5.12 (left panels).

Generally very little is known about non-methane VOCs from measurements during the OMO flights. Some halogenated VOCs (e.g. CH_3Cl) were measured by the SOFIA instrument (MPI-C) serving as tracers for anthropogenic pollution (Lelieveld et al., 2018), but did not play any role as OH reactants due to their small concentrations and reaction rate constants. Toluene and benzene were occasionally detected by KMS (PTR-MS, KIT) and SOFIA at very low concentrations in the low ten ppt range. Also these compounds did not play a role as OH reactants. In principle, KMS could have detected isoprene, but the measurements were below the limit-of-detection of 72 ppt at almost all times, though already a few tenth ppt would already have a significant impact on HO_x. Nevertheless, EMAC model results predict only very low mixing ratios ($< 0.001\,\text{ppt}$), which is not unreasonable for most flights over regions with little or no forests e.g. Arabian Peninsula, Arabian Sea and the Indian Ocean. As isoprene is very short-lived, it will be predominantly encountered in regions with high ground emissions (Apel et al., 2012). Evidently other VOCs than isoprene, with a similar reactivity as that of 50 ppt of the latter ($\approx 0.1\,^1/_s$) would qualify just as well in the discussion above. Ultimately however the role of VOCs during OMO - in particular in the lower troposphere - can not be fully clarified due to lack of data.

Altitude Range 11.5-15 km

Above 11.5 km both - OH and HO_2 - are progressively overestimated by the model, while the HO_2/OH ratio is predicted within the combined uncertainty. The latter is mainly governed by the HO_x recycling agents CO and NO (cf. Equation 5.3). The over-prediction of OH and HO_2 by a similar factor suggests that either not all HO_x termination reactions are accounted for, or the primary HO_x production is overestimated. From the point of HO_x destruction, the most significant contributions stem from the reaction $OH + CH_4$ and $OH + HO_2$ making up for 25 % each. However, only the latter is an actual sink since the former in the presence

of NO will recycle HO_2. Another 15 % each are due to the HO_2 self-reaction and $OH + CH_3OOH$ of which only the former is again an actual sink. The reaction of OH with CH_3OOH will partly retain OH (35 %), while the rest forms CH_3O_2 and will thus recycle to HO_x in the presence of NO. The remaining 20 % constitute an actual sink ($HO_2 + NO_2, HO_2 + CH_3O_2, OH + NO_2, OH + HNO_3, OH + HNO_4$ with similar magnitudes). Since HO_x is over-predicted by over a factor of 2, this also means that the contribution to k_{HO_x} from termination radical-radical reactions is over-estimated by roughly a factor of 2, which is substantial because the radical-radical HO_x loss rate is 40 % of the total HO_x loss rate at present. A potential

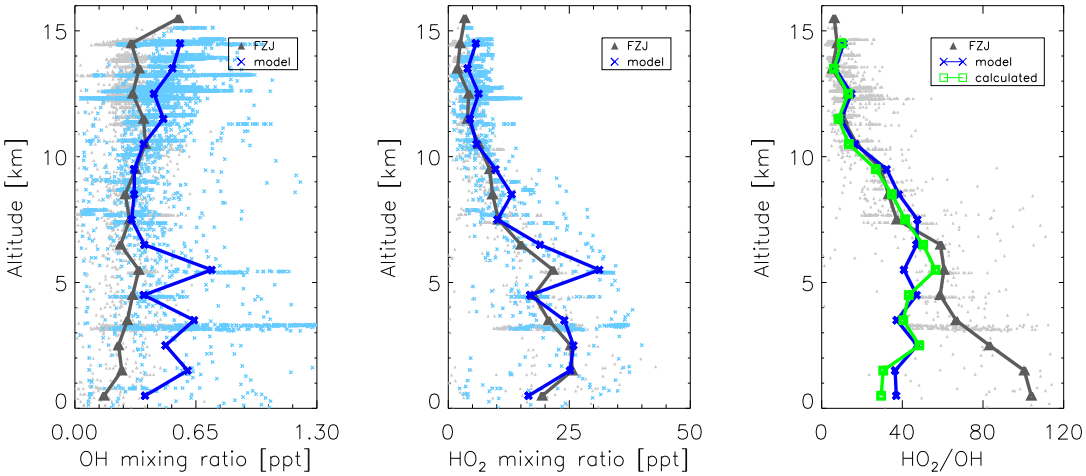

Figure 5.13: Reduction of precursors H_2O_2 and CH_3OOH by measurement uncertainties 25 % and 28 %, respectively. HCHO is taken from EMAC FZJ instead of EMAC MPIC and additionally includes the $HCHO + HO_2 \rightarrow HOCH_2O_2$ chemistry which is a major sink for HCHO and reduces HCHO by up to over a factor of 2 compared to EMAC MPIC.

missing sink would thus have to compensate this radical-radical sink, before it has an effect on the concentration. In terms of the reactants already present there is also not much room to account for this as methane can be assumed to be accurately measured. Also NO_2 can be expected to be calculated to decent accuracy, while CH_3O_2 would be smaller and not larger if HO_x is smaller. Sufficient uncertainties can also not stem from HNO_3 (EMAC) and HNO_4 (calculated), since together they contribute only about 6 % to the total HO_x loss rate. Other possible sinks that are not incorporated in RACM2 are the formation of methyl-peroxy-nitrate. Its effect is similar to that of HNO_4 (generally: alkyl-peroxy-nitrates), whose impact on HO_x was about 10 %. In view of findings during biomass burning events where several hundred ppt of different VOCs are measured in the upper troposphere - leading to C-shaped profiles similar to those of NO - that were transported by deep convection (Apel et al., 2012), it can not be fully excluded that unknown VOCs will partially contribute to an effective HO_x sink. This is because RO_2s formed by the reaction with OH do not necessarily recycle to HO_2, but can also form alkoxy-nitrates or alkyl-peroxy-nitrates which can be stable in particular under cold conditions. However as mentioned in the previous paragraph, given the lack of forestal coverage at the campaign site of OMO, it does seem more unlikely than overestimated primary sources.

The most important HO_x sources are the photolysis of HCHO (43.7 %), H_2O_2 (23.3 %), CH_3OOH (25.9 %) and O_3 (7.1 %). By reducing the precursors H_2O_2 and CH_3OOH by their measurement uncertainties (25 % and 28 % respectively at all altitudes) and replacing HCHO MPIC EMAC values by the corresponding HCHO FZJ EMAC model results (D. Taraborrelli, personal communication), the general tendency is improved by about 50 % (cf. Figure 5.13). The likely reason for the differences in the modelled formaldehyde is the inclusion of the reaction of HCHO with HO_2 in the FZJ EMAC model, which leads to the formation of hydroxy-alkyl-peroxy radicals, $HOCH_2O_2$

$$HCHO + HO_2 \quad \longleftrightarrow \quad HOCH_2O_2 \tag{R49}$$

This reaction is strongly temperature dependent. At low temperatures in the upper troposphere, $HOCH_2O_2$ is formed and can undergo various loss reactions for example with HO_2 or NO, which overall constitutes a loss mechanism for formaldehyde. This chemistry was first described in a theoretical study by Hermans et al. (2005), who proposed about 30 % loss of formaldehyde and, by a similar mechanism, also for acetone in the tropical tropopause region. The formation is relatively slow with a rate constant of only $2.2 \times 10^{-13}\,\mathrm{cm^3/s}$ at 200 K, decreasing as temperature increases being $7.8 \times 10^{-14}\,\mathrm{cm^3/s}$ at 300 K. Although reaction R49 has a significant impact on HCHO, it contributes only little to the total loss rate of HO_2. This also implies that the HO_2/OH ratio should not change by inspection of Equation 5.3, since H_2O_2 and HCHO are negligible in the secondary production of HO_2, because it is governed by CO and other species (cf. Figure A.17).

Evidently there is not only the concentration going into the HO_x production rate, but also the photolysis frequencies. The uncertainty for HCHO is relatively high with 15 %, because of the lack of data on the quantum yields (B. Bohn, personal communication). Errors for the photolysis frequencies of CH_3OOH and H_2O_2 are also 15 % (cf. Table A.1). More unlikely, but not impossible, these values could add up on the total uncertainty of the concentrations to reduce the HO_x production even further. This however is not done in further detail, but should emphasize that the reduction of the concentrations implemented as an estimate for the uncertainty in the production of HO_x as in Figure 5.13 is by no means an upper limit, but a reasonable overall deviation.

Chapter 6

Summary and Conclusions

The goal of this work was to investigate the chemistry of atmospheric OH and HO_2 radicals in the upper troposphere during the Asian summer monsoon period 2015 within the Oxidation Mechanism Observation (OMO) campaign. Concentrations of OH and HO_2 were measured by a laser-induced fluorescence instrument (AirLIF) on the German research aircraft HALO between the Mediterranean Sea and the Maldives in the Indian Ocean. The measured data are compared to theoretical model predictions in order to test the understanding of atmospheric oxidation processes. For this purpose the precedingly developed AirLIF instrument at Forschungszentrum Jülich was thoroughly characterized in the laboratory and different calibration concepts applied and compared. The radical measurements during OMO were then evaluated and a zero-dimensional chemical box-model calculation for the expected OH and HO2 radical concentrations was tested against the measurement results.

The OMO campaign took place from 21 July until 27 August 2015 and was divided in three phases. Till 01 August 2015 HALO was stationed on the airport of Paphos (Cyprus) and mainly flew over Cyprus and the Mediterranean Sea. During the second phase HALO was stationed on Gan (Maldives) aiming for the flight targets Bahrain and Sri Lanka, west and east of India respectively. From 10 August till the end of the campaign, HALO was again stationed on Cyprus and covered the Arabian Peninsula, Egypt and Greece as primary flight targets. At the end of the campaign for two flights Mount Etna was visited. In total OMO Asia comprised 17 flights up to 15 km of which AirLIF measured 2/3 of the time. Other institutes involved in OMO were the Karlsruhe Institute of Technology (KIT), the German Aerospace Center (DLR), the Max-Planck Institute for Chemistry (MPIC Mainz) and the universities Bremen, Wuppertal, Heidelberg and Leipzig. The MPIC Mainz provided a second LIF instrument measuring OH and HO2 radicals contemporaneously for the first time.

Throughout the campaign, the AirLIF instrument measured OH and HO_2 with good signal-to-noise ratios in both channels. Air was sampled from outside the aircraft through critical orifices and guided by inlet tubes into detection cells inside the aircraft. OH sampling took place inside of a shrouded inlet in order to minimize OH losses in the inlet tube. The HO_2 channel did not have such a shrouded inlet. The pressure in the inlet tubes and cells was reduced by a factor 30 to 100 compared to

ambient pressure. OH was directly detected by LIF in the OH cell, whereas HO_2 was first converted by reaction with NO to OH in the other cell. The conditions in the measurement channels changed with flight altitude, which is expected to cause considerable variations of the detection sensitivities.

Different calibration concepts have been applied and combined to determine the OH and HO_2 detection sensitivities as a function of flight altitude, ambient pressure and temperature. These include the well-established ground-based calibrations between flights to track the absolute sensitivities. The relative dependence with altitude was measured in the laboratory using a newly designed photochemical radical source which allows calibration at reduced pressure to simulate ambient air pressure at flight conditions. For the OH-channel as an additional option an in-flight calibration unit inside the shrouded inlet was used. It is however limited to below 10 km, because the radical production by the artificial photolysis of ambient water vapour becomes too small.

During the laboratory characterization of the HO_2 channel a fluid dynamical effect on the HO_2 nozzle was discovered which is due to the lacking shrouded inlet and lead to an overestimated HO_2 inlet pressure which was assumed to be static ambient pressure. It was possible to correct this by calculating the true mass flow through the nozzle using the computational fluid dynamics (CFD) software ANSYS Fluent.

When the in-flight calibrations and the laboratory pressure dependent calibrations were scaled to those done at ground conditions during OMO, the former two showed a convincing agreement in relative dependence giving trust in the characterization results. Over the altitude range up to 15 km the OH and HO_2 measurement sensitivities vary by factors up to 11 and 81, respectively. This strong altitude dependence is mainly driven by pressure dependent quenching of the OH fluorescence inside the measurement cell. For OH, wall losses inside the inlet tube also play an important role which are controlled by the mass flow through the inlet tube. For HO_2 wall losses are neglectable, but the conversion efficiency from HO_2 to OH will change with flight altitude. It crucially depends on the square of the volume flow through the measurement cell. Above 12 km there is an unexpected discontinuity in the pressure dependent calibration curve for OH and HO_2, which is presumably caused by abrupt changes in the flow conditions of the gas expansion that will influence the OH wall loss and HO_2 conversion efficiency. In the vicinity of this jump the measurement sensitivity changes abruptly by a factor of 1.5 for OH and 2.4 for HO_2, albeit in opposite direction.

To simulate the in-flight conditions, other research groups have confided in using different nozzle sizes to change the mass-flow through the system instead of varying ambient pressure. As part of a consistency check, both methods have been compared in detail and it is confirmed that they essentially agree. However, discontinuities in the pressure dependence of the OH calibration curve are presumably related to a change in conditions of the gas expansion and are thereby unique to a specific nozzle. The correct detection of this jump in sensitivity is therefore limited to the newly developed radical source.

In addition to the OH and HO_2 measurements it was originally planned to measure RO_2. During OMO the HO_2 cell cycled between the HO_x and RO_x mode every three scans by adding NO at the top of the inlet tube. This specific design without an intermediate nozzle - which would serve as a chemical reactor - lead to an abrupt signal break down at higher altitudes whose behaviour was not clear at first. In hindsight it is most likely due to the low mass flow and as such low volume flow rate through the tube caused by the fluid dynamical effect discussed above, which leads to premature conversion to OH with subsequent loss of OH at the walls. For future aircraft based campaigns these results suggest the use of a shrouded inlet also for the HO_2/RO_2 cell.

The ozone-water interference on the OH channel is at most 20 % at ground, but negligible above 3 km (< 3 %). On the HO_2 channel, both the ozone-water interference and the NO interference are negligible over all altitudes (< 1 %). From tests during OMO-EU it was known, that due to the lack of a shrouded inlet on the HO_2 cell, OH does not have to be subtracted prior to evaluation, since it is lost inside the inlet tube.

The OMO campaign offered for the first time the opportunity for an in-flight intercomparison of two HO_x measurement instruments over the full height of the troposphere. OH and HO_2 showed a good agreement between AirLIF and HORUS in the time-series plots, both in absolute numbers within the combined measurement uncertainties (OH: 13 % for AirLIF, 21 % for HORUS; HO_2: up to 35 % for AirLIF, 28 % for HORUS; 1σ), but also in relative correspondence. This excludes the flight on 06 August 2015 where HO_2 HORUS and AirLIF differ by over a factor of 3. A comparison of the mixing ratios on the other flights at these altitudes however indicates that the problem lies most likely on HORUS side. The general good agreement also manifests itself in the correlation plot (HORUS vs. FZJ) including all overlapping data throughout the campaign. OH shows a slope of 0.91 (forced through zero) with a correlation coefficient of $R^2 = 0.56$. The relatively small correlation coefficient can be explained by the low natural variability of the measured data, which in most cases were measured at constant flight levels. For HO_2 the slope is very close to 1 with 0.98 (forced through zero) while also the correlation coefficient is relatively high with $R^2 = 0.88$. Before the mass-flow correction due to the streamline curvature over the HO_2 nozzle both values were decreased by a factor 2 to 3 and the data appeared highly dispersed while with the correction the data appear very compact. This confirms the application of the correction besides its theoretical justification.

In a next step the altitude profiles were analysed. Important controlling parameters (CO, NO, methane, ozone and water) were adducted first and compared to other studies. It is found for example that the C-shaped NO profile has been observed before and can be explained by fast vertical transport (deep convection) from the boundary layer. Likewise CO, methane, ozone and water vapour profiles match those found in other studies (cf. Section 5.2.3). Finally, OH and HO_2 mixing ratios from previous campaigns over the Pacific, the Atlantic and North America show

similar vertical profiles and OH generally shows only little variation between the lower (0.25 ppt) and upper (0.4 ppt) troposphere. In contrast HO_2 mixing ratios vary greatly with 25 ppt at 1 km and only 1-2 ppt at 15 km. A simple analytical expression for the HO_2/OH ratio – derived from the recycling reactions between HO_2 and OH – was used assuming photo-stationary state (cf. Equation 5.3), which predicts the measured ratio down to 6 km while below the ratio is underestimated by up to a factor of 3. This gap in the lower troposphere can be closed if RO_2 mixing ratios are incorporated and assumed to be in the range of 30 to 50 ppt which is in comparison to HO_2 (21-32 ppt) a realistic range. Evidently the importance of RO_2 as an HO_2 source decreases significantly with altitude. Above 7 km the HO_2 formation is dominated by the reaction OH + CO, whereas the HO_2 reactivity is mainly controlled by the reaction HO_2 + NO forming OH. These two reactions control the partitioning of HO_x in the upper troposphere, which explains the observed positive correlation between NO and OH and the anti-correlation between NO and HO_2 for example on flight #20 at high altitudes.

Finally, measured OH and HO_2 concentrations were compared with steady-state box model calculations using RACM2 as a chemical mechanism. The model was constrained by measured trace gases and photolysis frequencies. The constrained parameters include CO, NO, methane, ozone, water vapour, H_2O_2, CH_3OOH, acetone, methanol and photolysis frequencies. Missing measurement data for formaldehyde, acetaldehyde and nitric acid were substituted by simulated data from the global atmospheric-chemistry model EMAC operated by MPIC (Mainz) and molecular hydrogen was set to a fixed value of 550 ppb. For all compounds a dilution loss rate of 5 days was assumed. The reaction rate constant for OH + CO was replaced by the recommended JPL version. Other than methane hydrocarbons were set to zero, because measurements were at limit of detection. Compounds as PAN or HNO_4 play no role on the HO_x budget in the lower troposphere while they can become a sink in the upper troposphere where they are stabilized by the cold. It was checked if these contributions remain small when the reactions are switched off. For PAN the impact is negligible and HNO_4 affects the HO_x budget no more than 10 %.

The model-measurement comparison shows good agreement between 7 km and 11.5 km in OH and HO_2. Below 7 km OH is overestimated by a factor of 2.5 while HO_2 is predicted correctly within the combined measurement uncertainties. This leads to an under prediction of the HO_2/OH ratio by up to a factor of 3. It was shown that the addition of a small amount of OH reactivity (0.1 $^1/_s$) due to unmeasured VOCs close the gap for OH, while HO_2 stays in agreement within the combined measurement and model uncertainties. Only below 2 km a discrepancy of the HO_2/OH ratio of 2.5 remains. Above 11.5 km the situation is different in that OH is over predicted by a factor of 2, but also HO_2 by a factor of 2.5. Therefore the HO_2/OH ratio is predicted correctly within the combined measurement and model uncertainties. This indicated that there either is a missing HO_x termination reaction or an overestimated HO_x primary source. No plausible missing HO_x sink could be identified. The over-prediction of HO_x by the model is more likely caused by an overestimation of the HO_x precursors which mainly include HCHO and peroxides (CH_3OOH and H_2O_2). In a sensitivity run, the HCHO values simulated by the EMAC model at

MPIC were replaced by simulated data from the EMAC model operated at FZJ, which includes an additional loss for HCHO by reaction with HO_2. The resulting reduction of HCHO by a factor of 2 and reducing the measured peroxides by their experimental uncertainties, improved the OH and HO_2 prediction by about 50 % while the ratio does not change. Because of these limitations on the correct prognosis of the model, it is advisable for future aircraft campaigns to lay more stress on VOC and HCHO measurements, as they seem to be key-players for a proper understanding of the atmospheric chemistry in the lower and upper troposphere respectively. In the same way it would be also beneficial to measure RO_2 on future campaigns, since they directly influence HO_x and could give further insights in possible missing RO_2 sources and their implications on the HO_x budget.

Appendix A

A.1 Individual Flight Tracks

The figures below show all OMO-ASIA flight tracks during which AirLIF was measuring. The figure captions give dates and flight numbers (#).

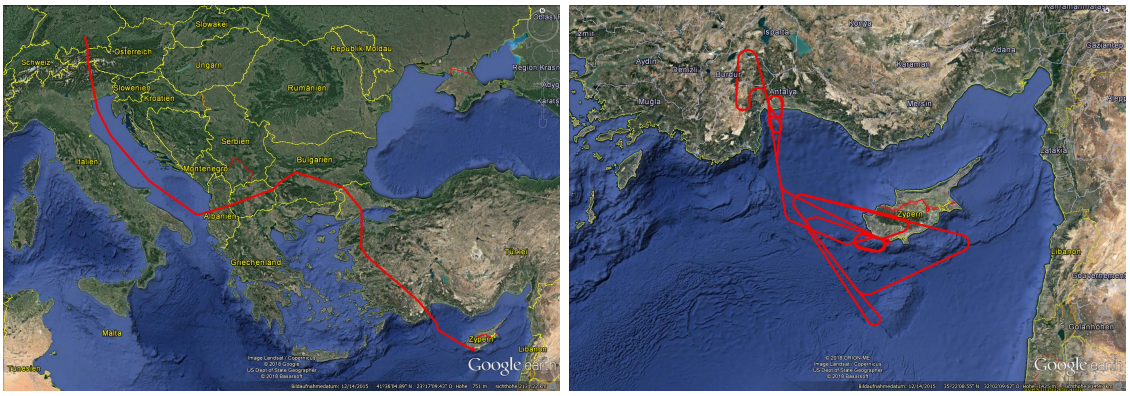

Figure A.1: Left: 21.07.2015 (# 08), **Right:** 25.07.2015 (# 09)

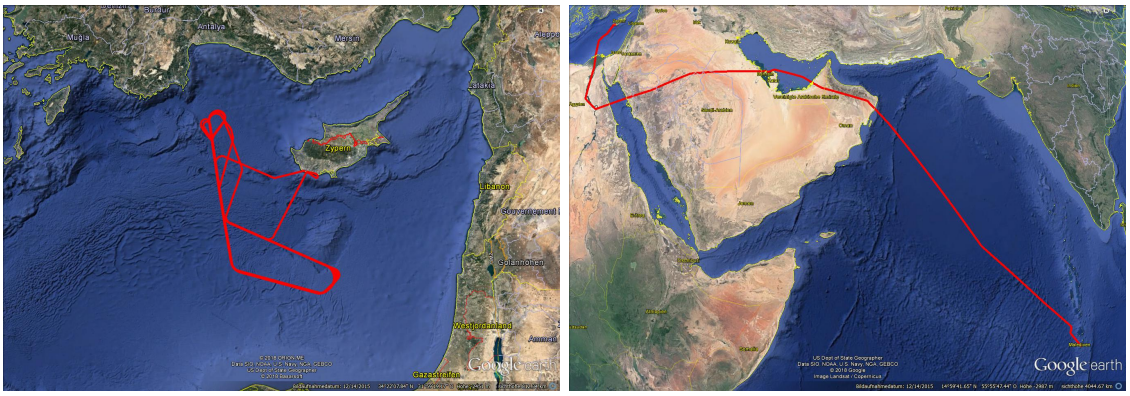

Figure A.2: Left: 28.07.2015 (# 10), **Right:** 01.08.2015 (# 11)

Figure A.3: Left: 06.08.2015 (# 12/13), **Right:** 15.08.2015 (# 20)

Figure A.4: Left: 18.08.2015 (# 21), **Right:** 23.08.2015 (# 22)

Figure A.5: Left: 25.08.2015 (# 23), **Right:** 27.08.2015 (# 24)

A.2 Measurement results for each flight

The figures below show OH, HO_2 and NO measurement results for each flight. From 6^{th} of August MPIC data is included for comparison. Error bars show 1σ precision.

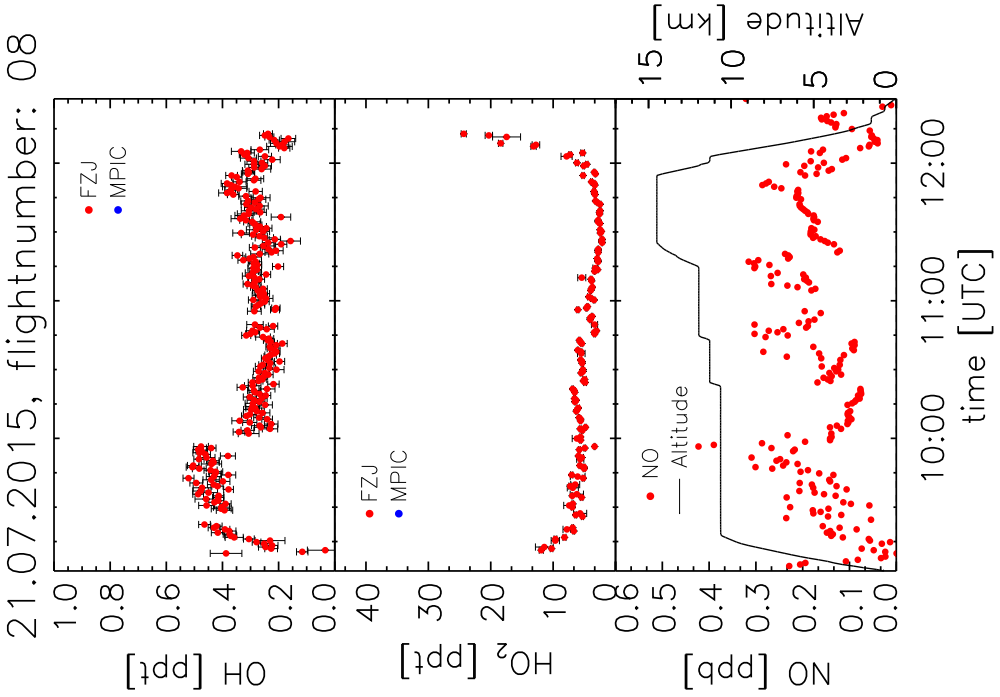

Figure A.6: Transfer flight from Oberpfaffenhofen to Paphos (Cyprus).

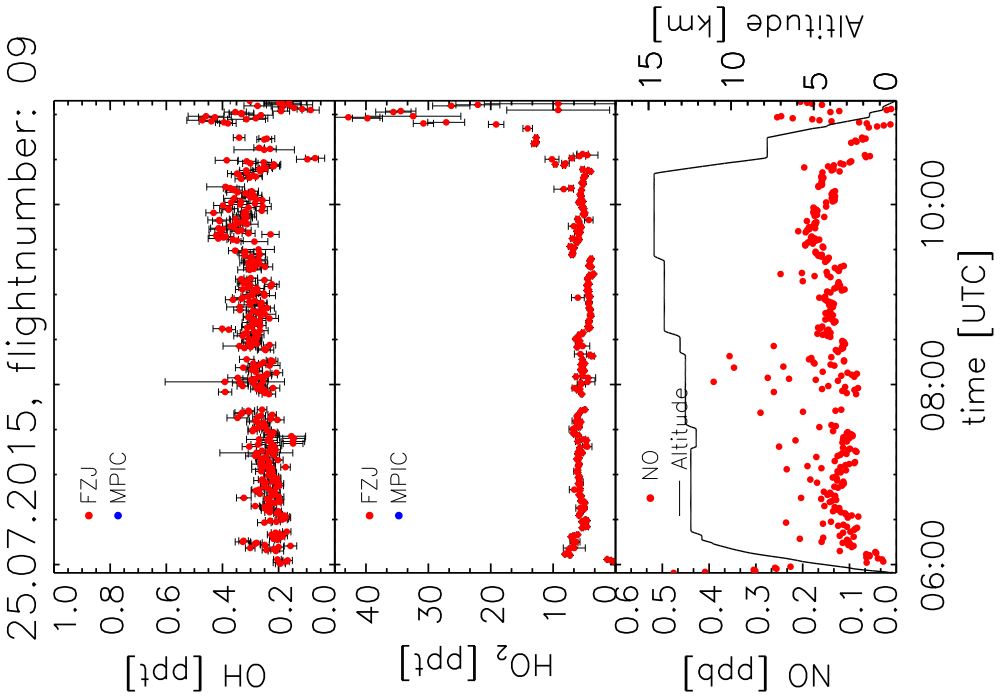

Figure A.7: Circling over Cyprus with a short excursion into Turkey.

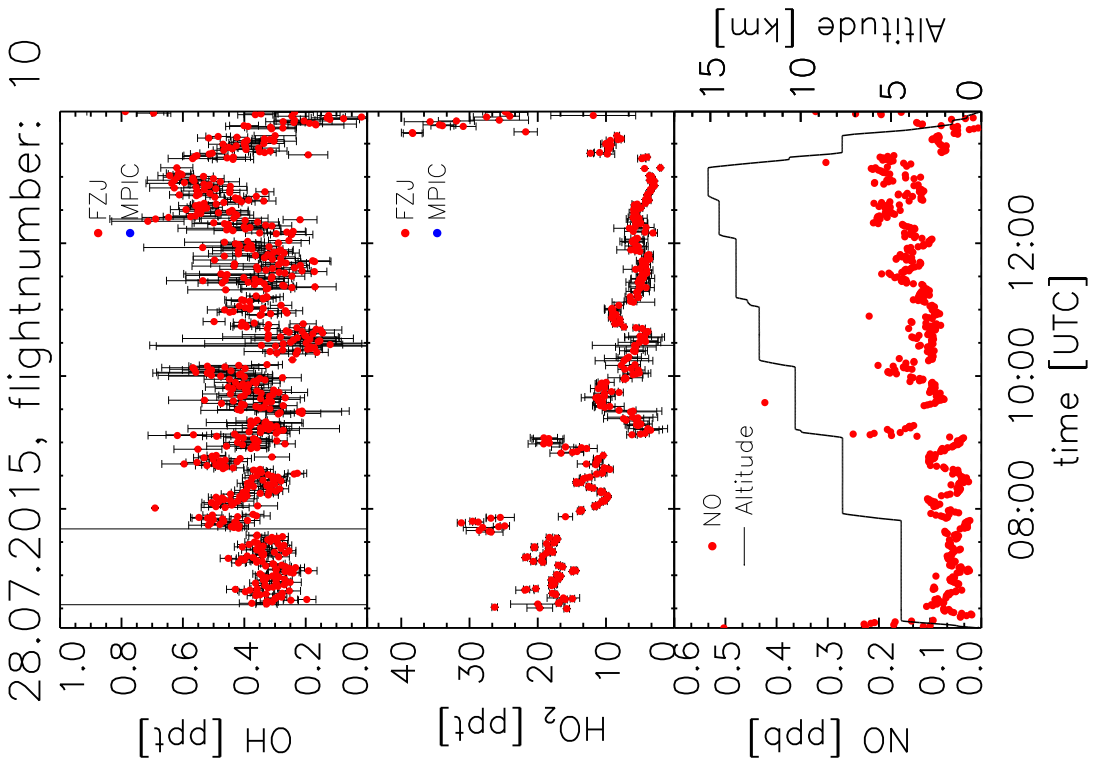

Figure A.8: Circling over the Mediterranean.

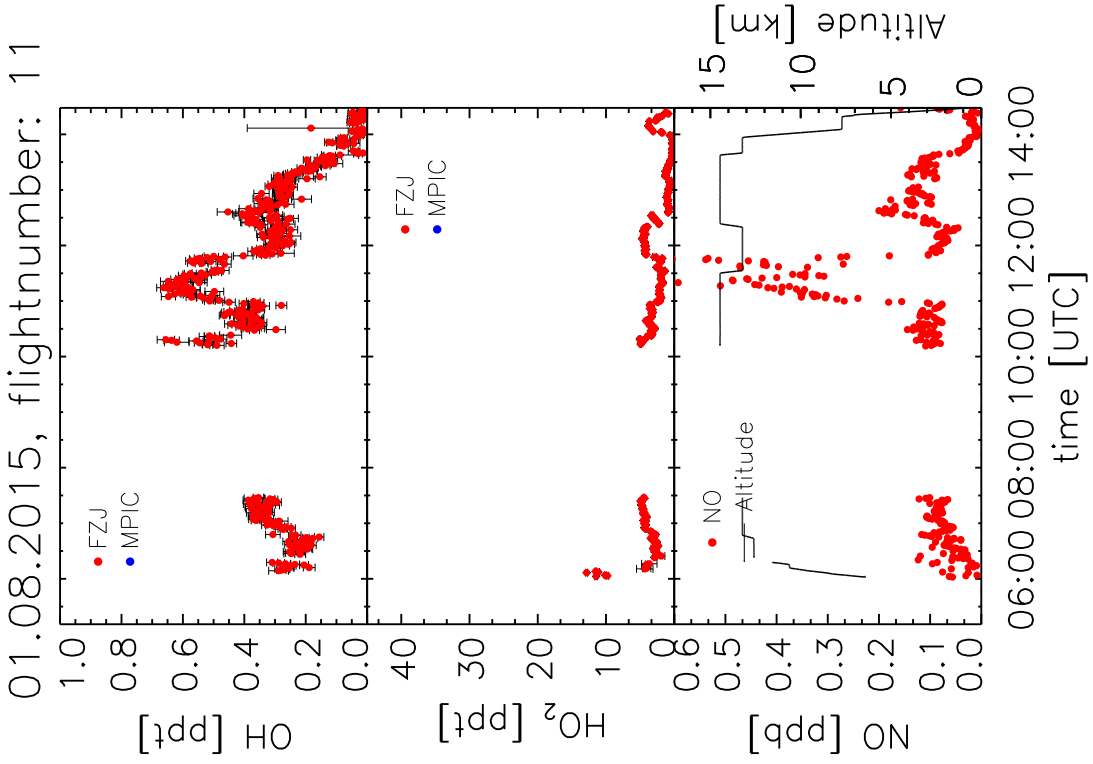

Figure A.9: Transfer flight from Paphos to Gan (Maldives) with stop in Bahrain.

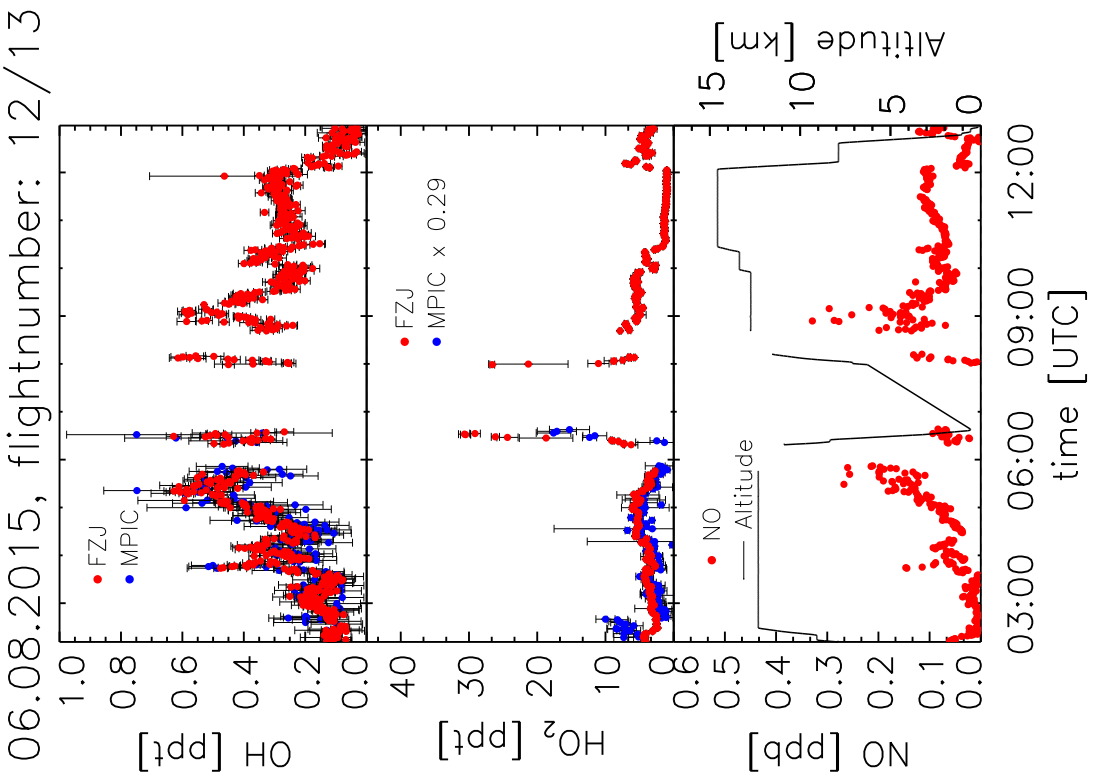

Figure A.10: Flight from Gan to Bahrain.

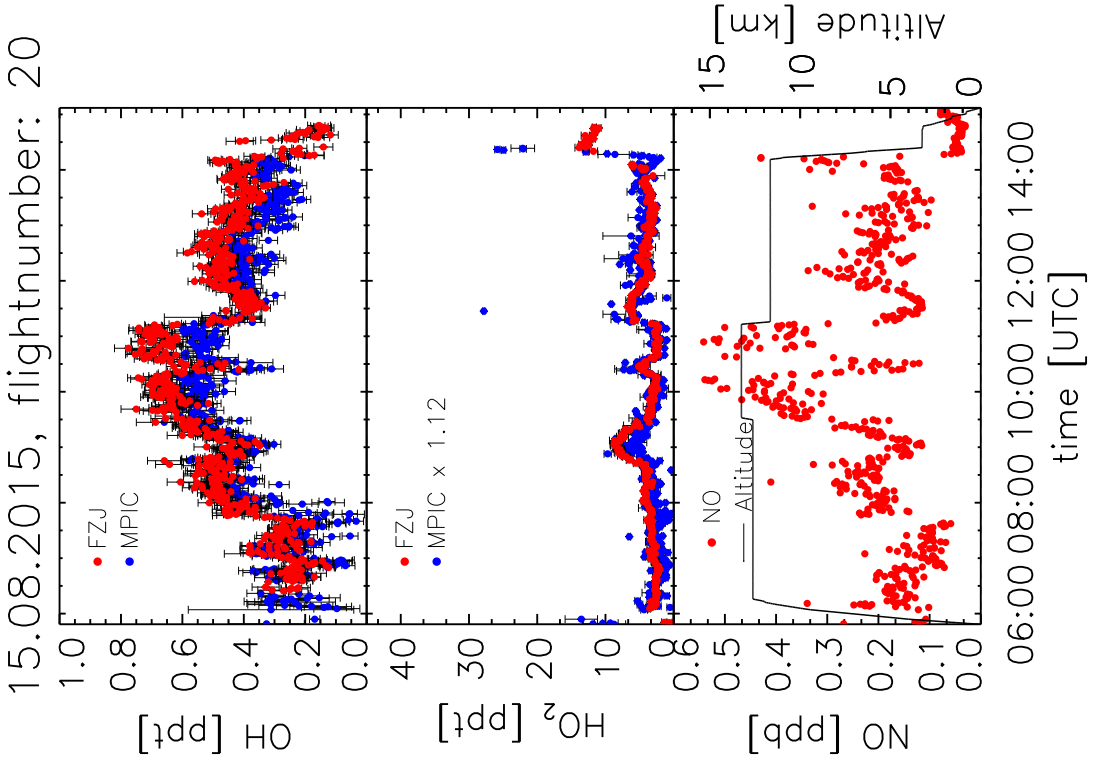

Figure A.11: Flight from Paphos over Saudi Arabia.

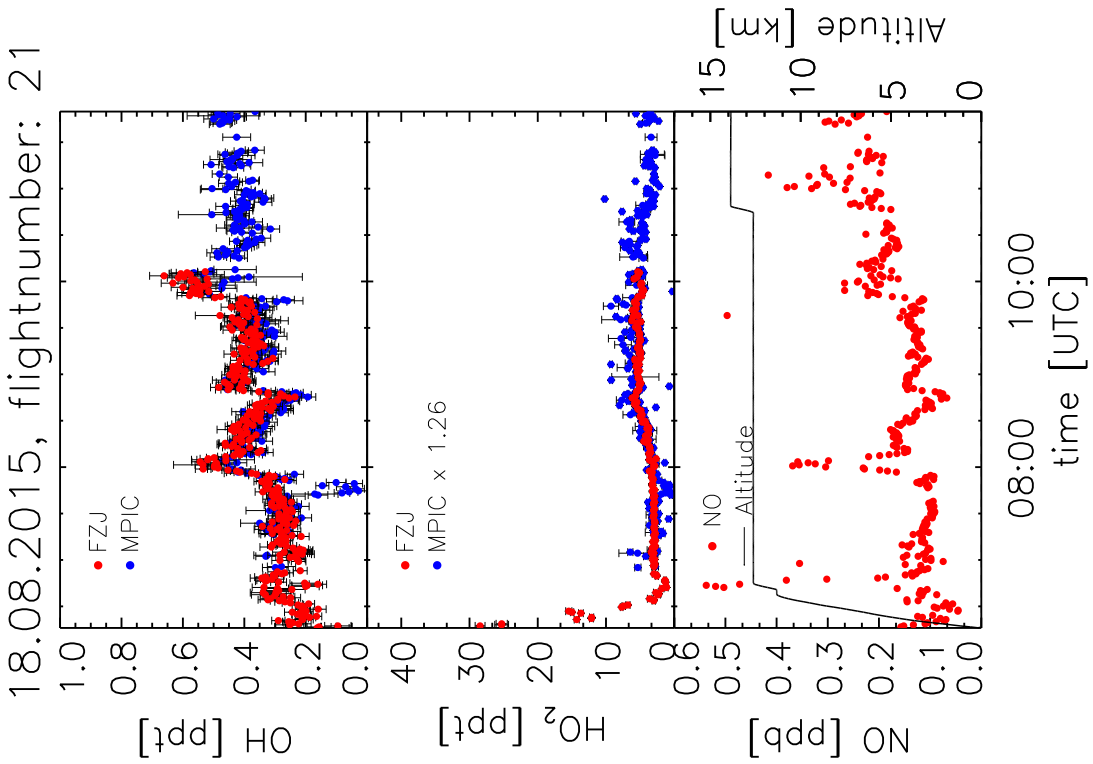

Figure A.12: Second flight over Saudi Arabia.

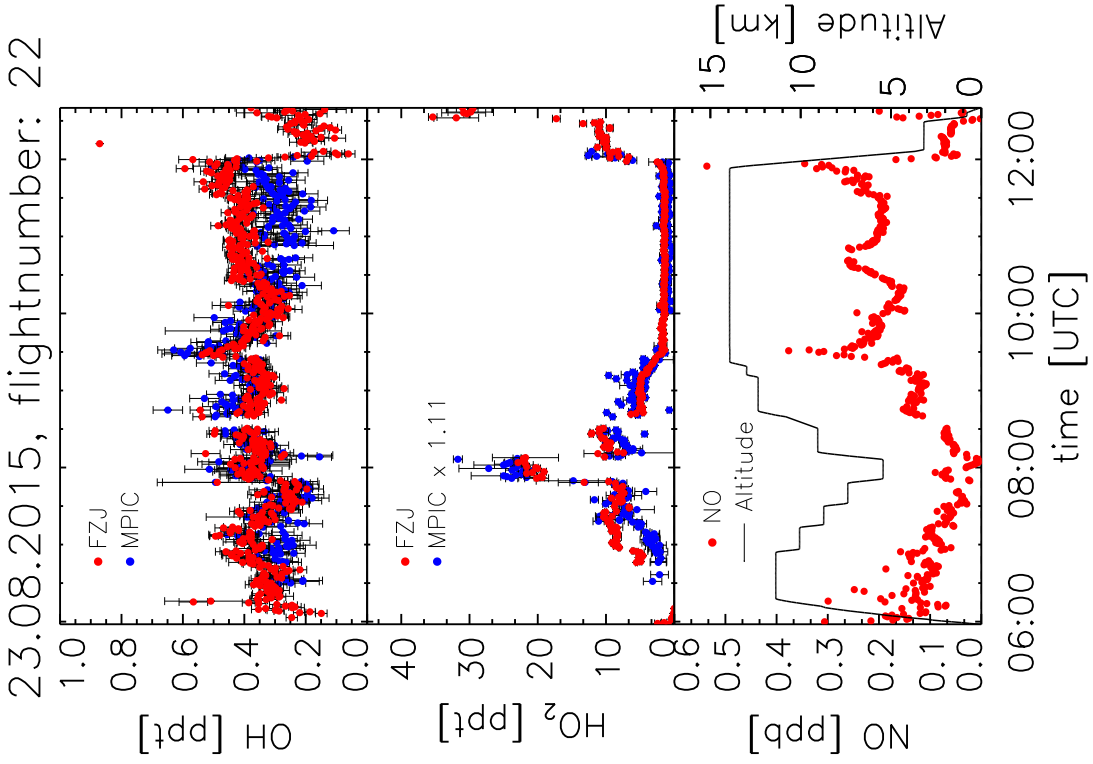

Figure A.13: Flight from Paphos to Egypt and back via south Greece.

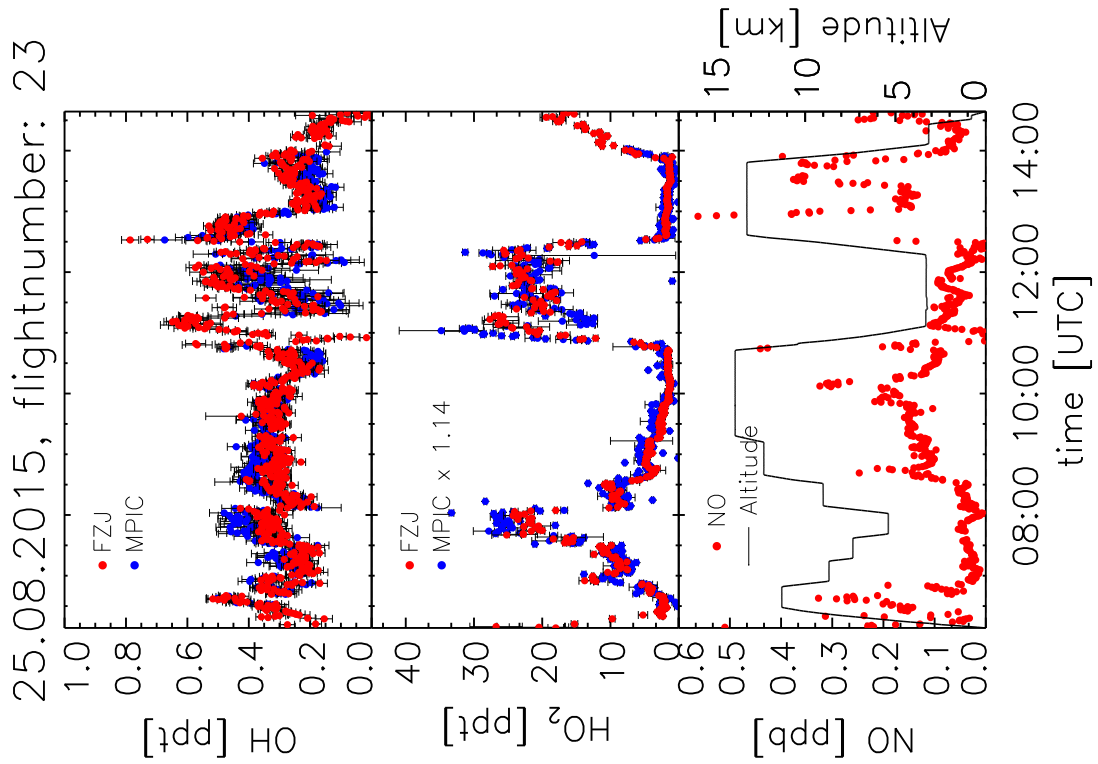

Figure A.14: Second flight over Egypt with excursion to Mount Etna and back to Paphos over south Greece.

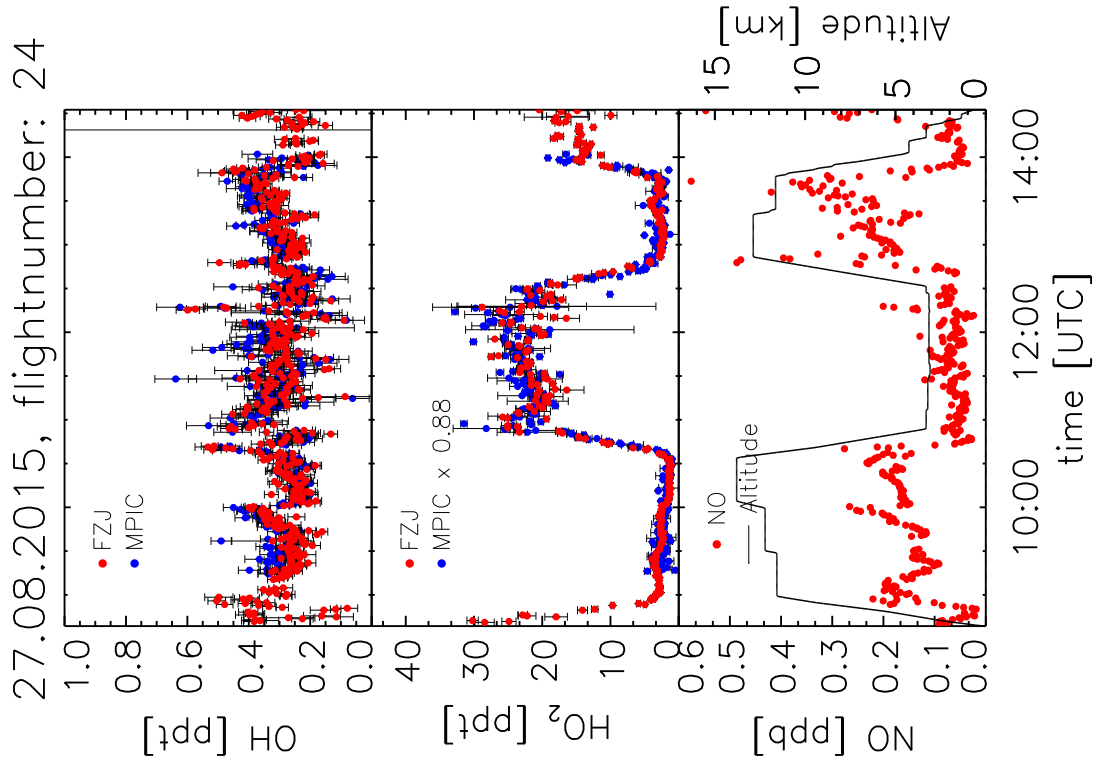

Figure A.15: Transfer flight back to Oberpfaffenhofen with another excursion to Mount Etna.

A.3 Available Data

Table A.1: List of chemical compounds that are simulated by the chemical box-model in this work, or are constrained by measurements on board of HALO. Missing input data for long-lived species are taken from a global simulation model (EMAC).

		Model			
	Compound	Output	Constraint	Uncertainty [%]	Data Source
Radicals	OH	●			
	HO_2	●			
	RO_2	●			
Radical Precursor	O_3		●	2	FAIRO[1]
	H_2O		●	5-20	SHARC[2]
	H_2O_2		●	25	TRIHOP[3]
	CH_3OOH		●	28	TRIHOP[3]
	HONO	●			
	HNO_3		●		EMAC[4]
	HCHO		●		EMAC[4]
	CH_3CHO		●		EMAC[4]
	HNO_4	●			
	Acetone		●	10	KMS[5]
OH Reactants	CO		●	3-20	TRIHOP[6]
	CH_4		●	<1	TRIHOP[6]
	Isoprene			10	KMS[5]
	Toluene			10	KMS[5]
	Benzene			10	KMS[5]

[1] FAIRO data from HALO database. Datasets #4025-#4042 from 2016-05-29.
[2] SHARC data from HALO database. Datasets #3946-#3949, #3951-#3953, #3674-#3691 until 2016-05-04. After 08-01, data from the Vaisala Sensor (BAHAMAS) was used for altitudes below 8 km. Generally, and in particular after 08-01, EMAC model results were used to fill data gaps.
[3] TRIHOP data from HALO database. Sum of organic peroxides and H_2O_2 datasets #4776-#4792 from 2016-11-24. Measured sum of organic peroxides used as a representative for CH_3OOH.
[4] Model output from the global transport chemistry model EMAC operated by MPIC Mainz. The data are taken from the HALO database. Datasets from 2016-09-22.
[5] KMS data from HALO database. Datasets #4370-#4387 from 2016-09-14. For Isoprene, Toluene, Benzene there are only few data available which are at LOD (72 ppt for Isoprene and 20 ppt for Benzene, Toluene). Except for Acetone: Data not used.
[6] TRIHOP data from HALO database. CO and CH_4 datasets #4043-#4071 until 2016-10-26. CO data gaps (first half of 08-06, 08-15, 08-23, 08-27) filled with EMAC model result.

		Model			
	Compound	Output	Constraint	Uncertainty [%]	Data Source
	Methanol		●	>10	KMS[7]
	NO_2	●			
	NO		●	9	AENEAS[8]
	PAN	●			
j-values	j_{O^1D}		●	10	HALO-SR[9]
	j_{NO_2}		●	10	HALO-SR
	j_{HCHOm}		●	15	HALO-SR
	j_{HCHOr}		●	15	HALO-SR
	j_{CH_3CHO}		●	25	HALO-SR
	j_{HONO}		●	15	HALO-SR
	j_{HNO_3}		●	15	HALO-SR
	j_{HNO_4}		●	30	HALO-SR
	$j_{H_2O_2}$		●	15	HALO-SR
	j_{CH_3OOH}		●	15	HALO-SR
	$j_{acetone}$		●	20	HALO-SR
	j_{PAN}		●	25	HALO-SR
	j_{gly}		●	30	HALO-SR

[7] KMS data from HALO database. Methanol datasets #4370-#4387 from 2016-09-14. Data gaps filled with EMAC model result.

[8] AENEAS data from HALO database. NO and NO_y datasets #3930-#3955 from 2016-04-12. NO_y data not used. In addition to the relative uncertainty there is an absolute error of 5 ppt.

[9] HALO-SR data from HALO database. Datasets #5087-#5104 from 2017-10-26. The dataset #5103 for 2015-08-25 was calculated by the radiative-transfer model LIBRADTRAN (B. Bohn).

Table A.2: Institutes responsible and persons in charge of various other OMO measurements or global modelling results used as box-model constraints as in Table A.1.

Data	Source
BAHAMAS	V. Dreiling and M. Zöger, Flight Department, DLR Oberpfaffenhofen
OH, HO_2	H. Harder, D. Marno and M. Martinez, Max-Planck Institute for Chemistry, Mainz
NO	H. Ziereis, G. Stratmann and P. Stock, Institute for Physics of the Atmosphere, DLR Oberpfaffenhofen
CO, CH_4	H. Fischer, L. Tomsche and U. Parchatka, Max-Planck Institute for Chemistry, Mainz
H_2O_2, ROOH	H. Fischer, B. Hottmann and S. Hafermann, Max-Planck Institute for Chemistry, Mainz
EMAC model	A. Pozzer and P. Joeckel, Max-Planck Institute for Chemistry, Mainz
O_3, OVOCs	A. Zahn, Institute for Meteorology and Climate Research, KIT Karlsruhe
Photolysis	B. Bohn, Institute for Energy- and Climate Research, Forschungszentrum Jülich

A.4 Pie Charts

The figures below show the contributions to the production and reactivity of OH and HO_2 above 11 km and below 2 km calculated by the box-model.

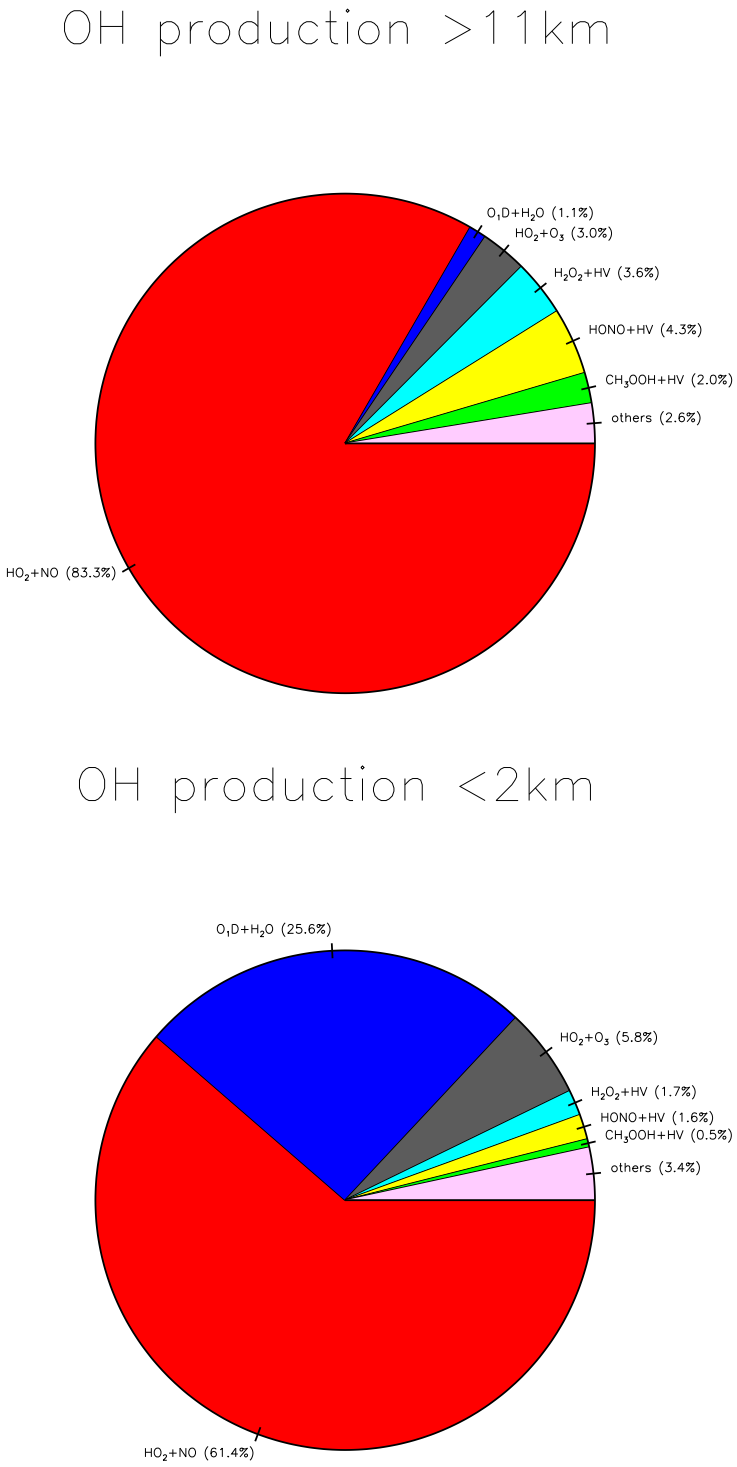

Figure A.16: Mean contributions to OH production rate in the upper (>11 km) and lower (<2 km) troposphere.

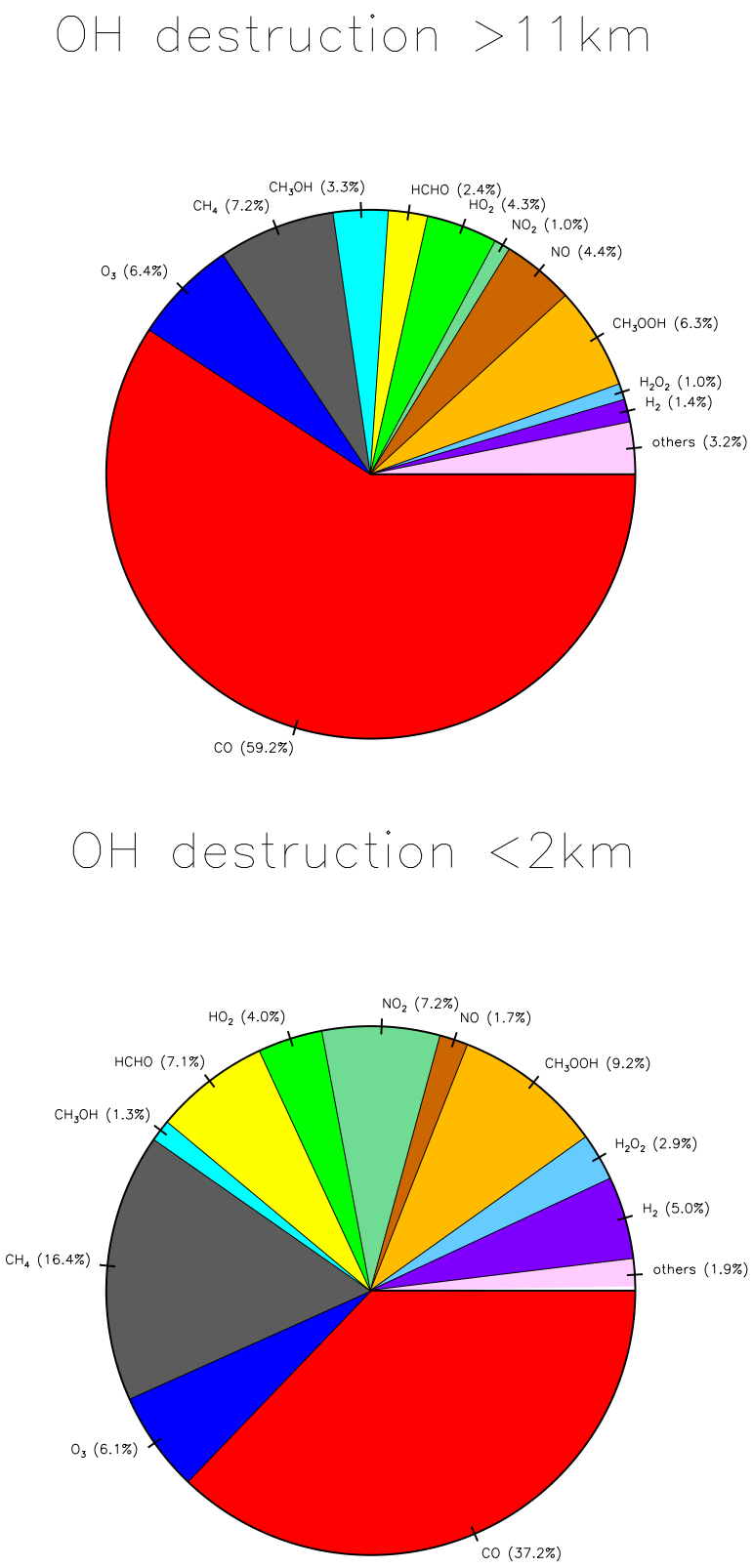

Figure A.17: Mean contributions to OH reactivity in the upper (>11 km) and lower (<2 km) troposphere.

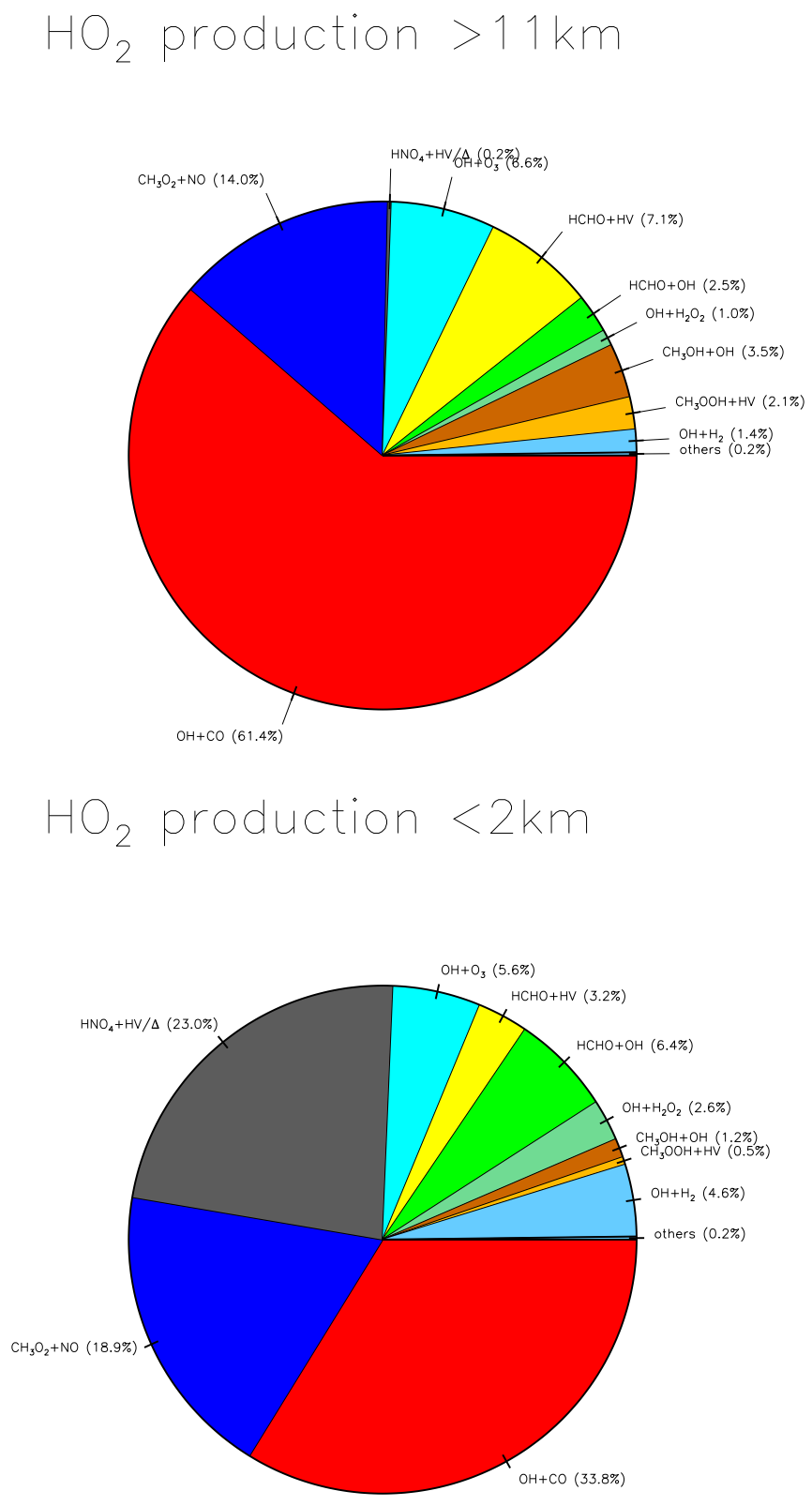

Figure A.18: Mean contributions to HO_2 production rate in the upper (>11 km) and lower (<2 km) troposphere.

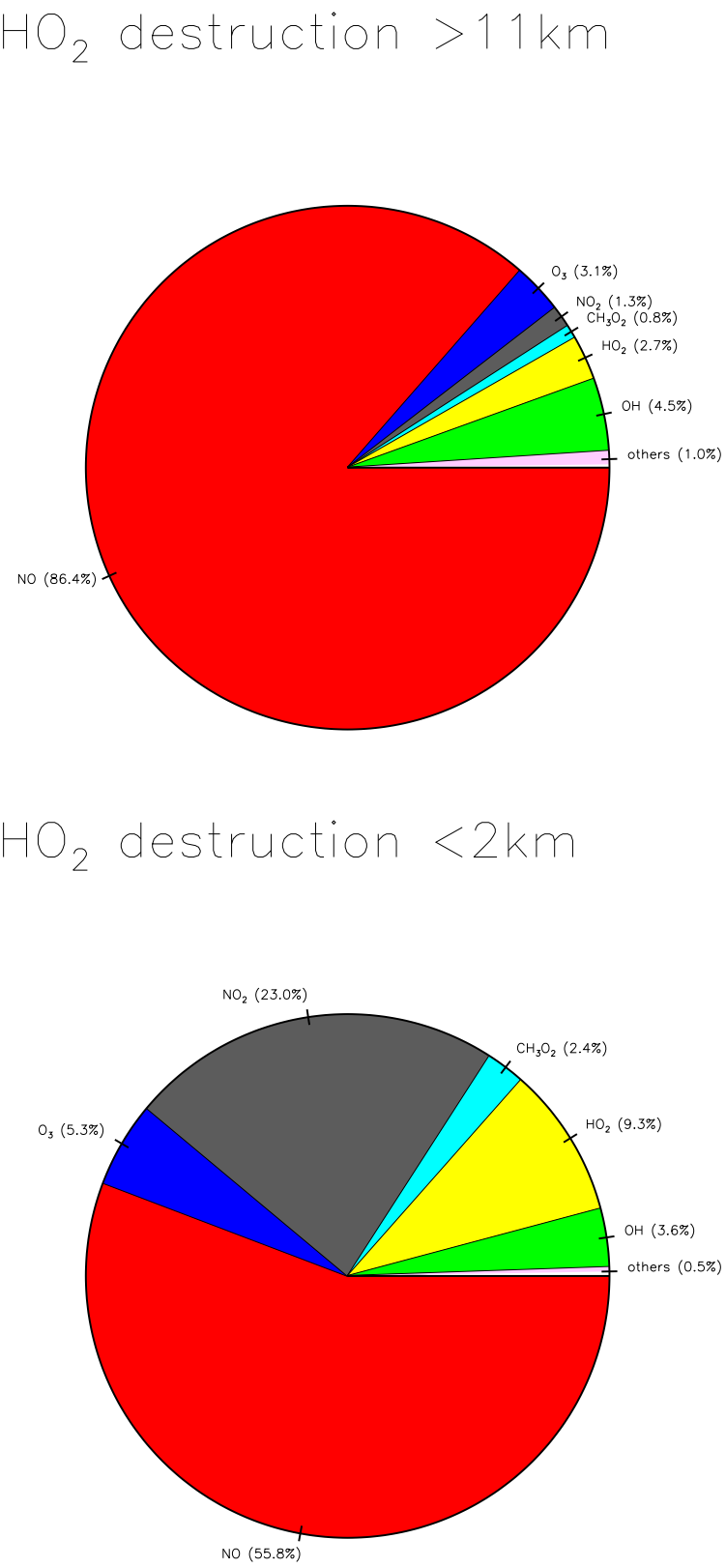

Figure A.19: Mean contributions to HO_2 reactivity in the upper (>11 km) and lower (<2 km) troposphere.

Appendix B

B.1 Technical Terms

Table B.1: Explanations for frequently used technical expressions.

Static air pressure/temperature	Ambient air pressure/temperature (outside of aircraft)
Total air pressure/temperature	Stagnation pressure/temperature, when ambient air is brought to rest
Inlet air pressure/temperature	Static air pressure/temperature in OH inlet
Mach number (Ma)	Ratio of air velocity v with respect to speed of sound c
Air velocity/speed True Airspeed (TAS)	Air velocity relative to aircraft
Inlet air velocity	Decelerated air speed in OH inlet
Altitude	Height above sea level

B.2 Basic meteorological and avionic data of HALO

Table B.2: Data supplied from BAHAMAS (HALO database, newest datasets between 2015-09-21 and 2016-05-04, #3946-#3953 and #3674-#3691) which were essential to the evaluation of OH and HO_2 concentrations. Note that water was present in four different units. For this work, the required *Volume Mixing Ratio*s were calculated from the more complete *Absolute Humidity* dataset.

1	Height above sea level (Altitude) [m]
2	Mach number
3	Calculated True Airspeed [$^{m}/_{s}$]
4	Static Pressure [hPa]
5	Static Air Temperature [K]
6	Total Air Temperature [K]
7	Volume Mixing Ratio [%]
8	Absolute Humidity (water) [$^{g}/_{m^3}$]
9	Mass Mixing Ratio (water) [$^{g}/_{kg}$]
10	Relative Humidity with respect to water [%]

Table B.3: Other parameters measured by the Pitot-tube in the back of the shrouded inlet.

Total (Ram) pressure	Pitot-tube*
Differential pressure	Pitot-tube*
Static temperature	Pt-100** (not exactly calibrated)

* Agrees within 1 % with the total pressure calculated from BAHAMAS data (static pressure, Mach-number) using Equation 3.9 and 3.10.

** Scales linearly (slope: 0.93, offset: +4 K) with the total air temperature from BAHAMAS. For the data evaluation in this work, the BAHAMAS temperature data were used.

B.3 In-Flight Measurement Conditions

Colour Codes represent the date during the OMO campaign in 2015.

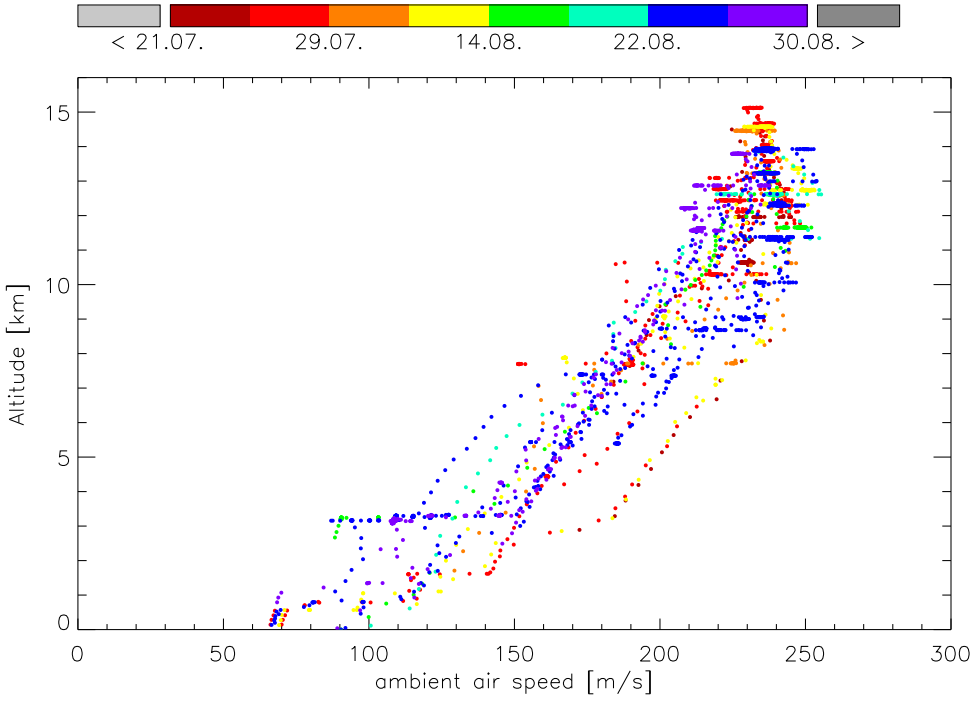

Figure B.1: Ambient air speed as provided by the Bahamas System.

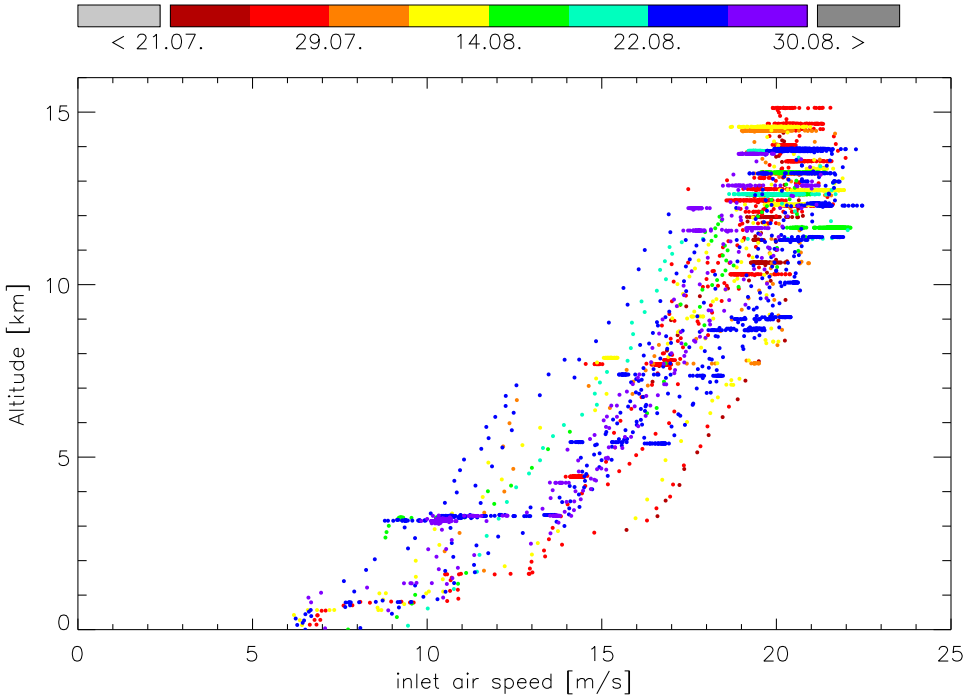

Figure B.2: Inlet airspeed determined by Pitot tube measurements in the shrouded inlet.

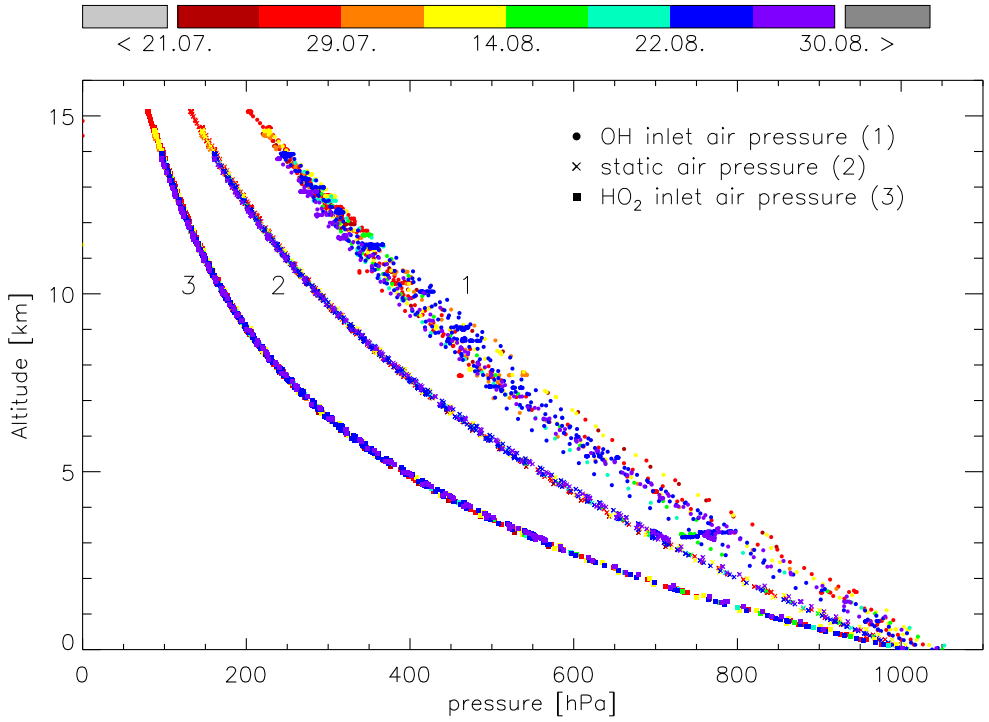

Figure B.3: Static air pressure is supplied by the BAHAMAS system and the pressure in the shrouded OH inlet is measured by a Pitot tube in the back of the shrouded inlet. The effective inlet pressure of the HO_2 cell is estimated by a CFD model calculation (cf. Figure 4.24).

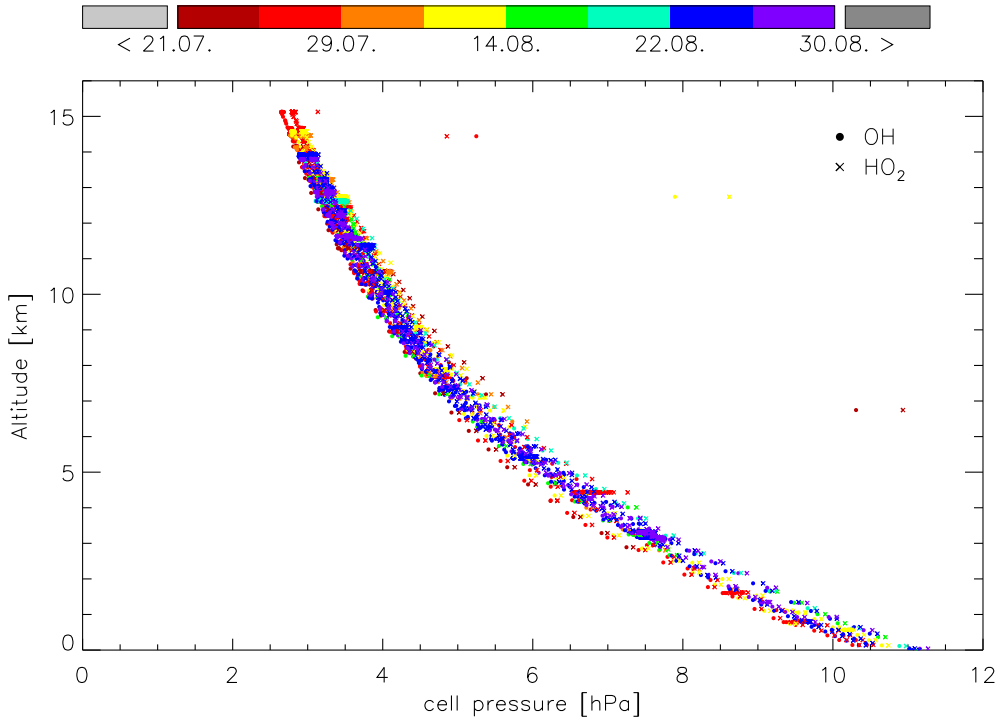

Figure B.4: OH and HO_2 cell pressures. Since OH and HO_2 are on the same exhaust/pump, pressures in the cells are essentially the same.

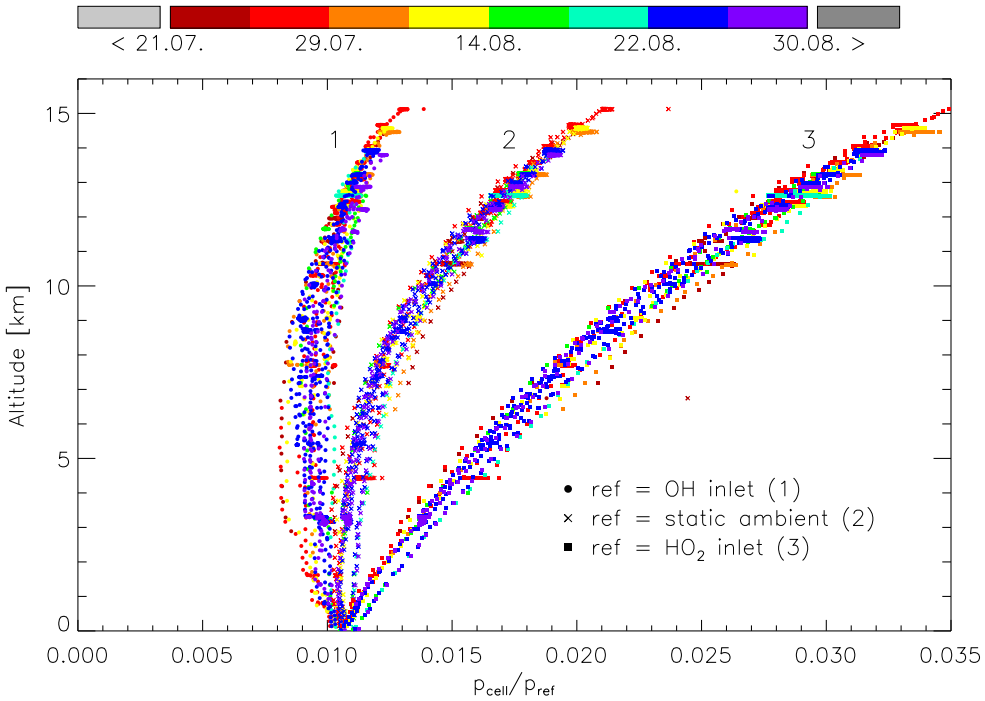

Figure B.5: (1): OH cell pressure ratio $\frac{p_{\mathrm{OH\ cell}}}{p_{\mathrm{ref}}}$. (2,3): HO_2 cell pressure ratio $\frac{p_{\mathrm{HO_2\ cell}}}{p_{\mathrm{ref}}}$.

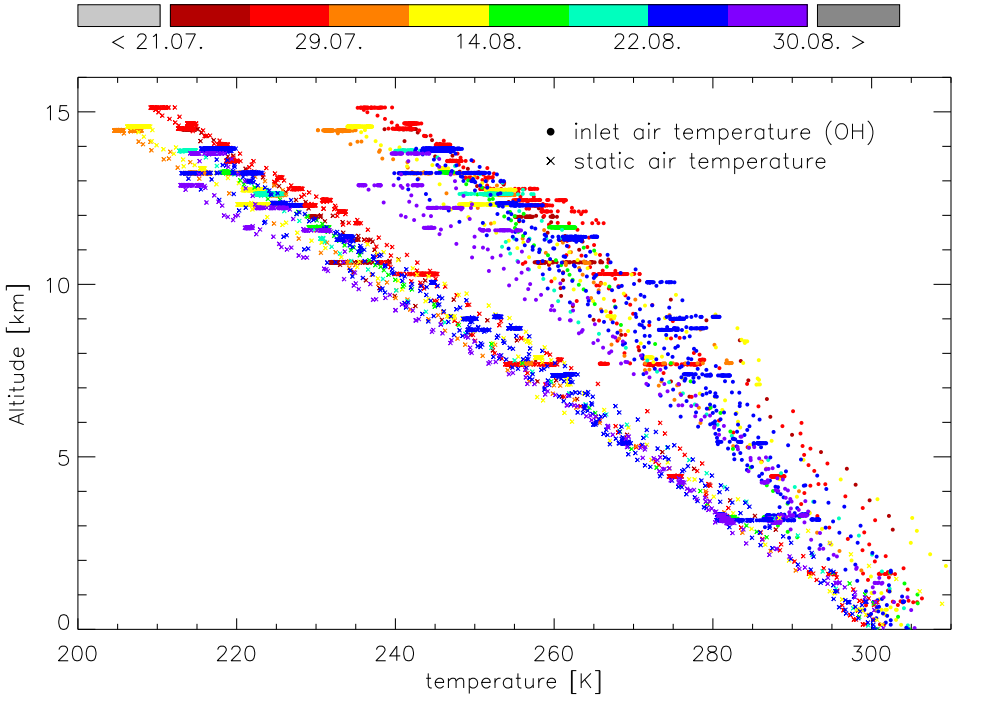

Figure B.6: Static ambient air temperature is supplied by the BAHAMAS system. The OH inlet temperature is calculated from the static ambient temperature, the Mach-number of the ambient air and the inlet air velocity using Bernoulli's principle.

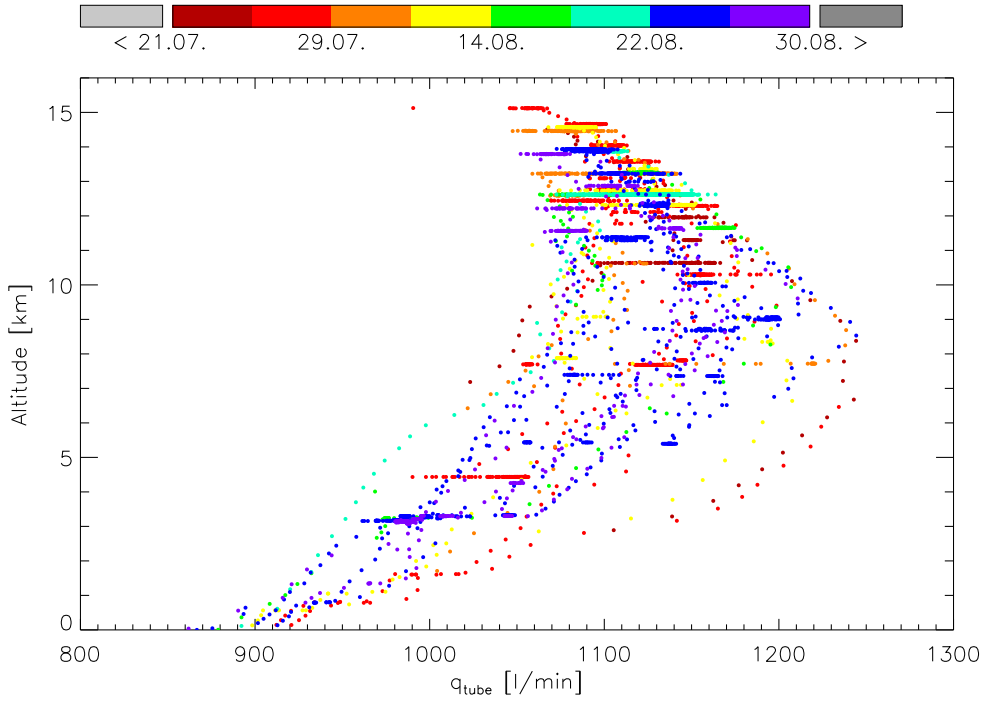

Figure B.7: Volume flow rate through the inlet tube of the OH cell. While OH and HO_2 cell pressure are the same at a given altitude, the ambient pressure the nozzle sees is higher for the OH cell than for the HO_2 cell, leading to an increased mass flow rate and consequently higher volume flow rate.

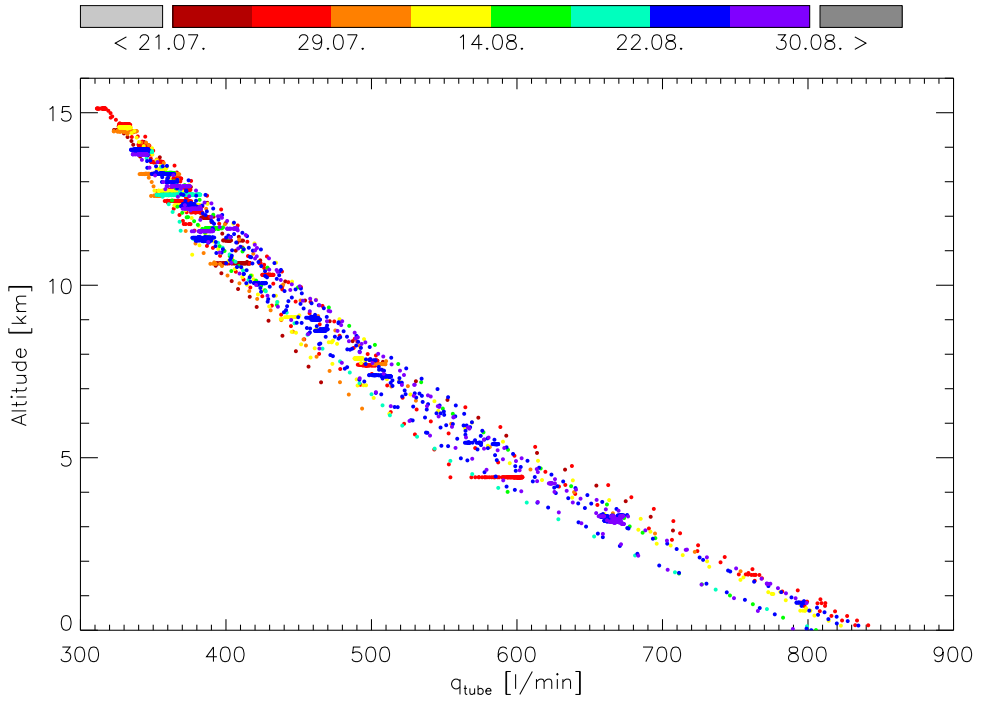

Figure B.8: Volume flow rate through the inlet tube of the HO_2 cell. It is lower than on the OH cell not only because the nozzle samples from the lower static ambient pressure, but also due to an additional reduction of the effective inlet pressure as a result of the air moving over the nozzle at velocities close to Mach 1 at high altitudes.

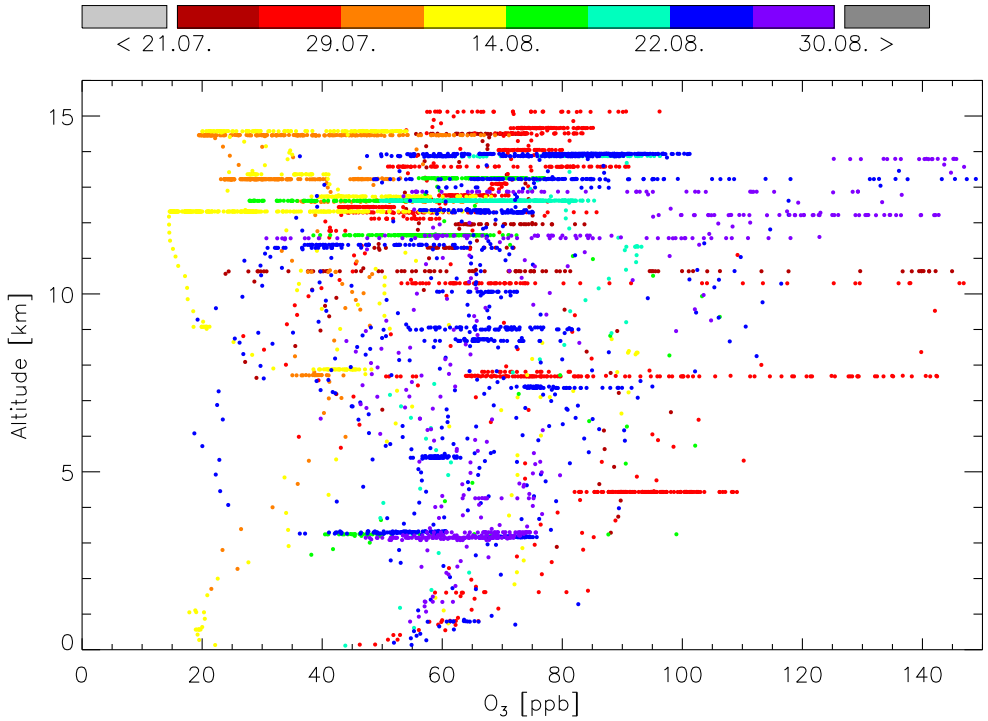

Figure B.9: Ozone mixing ratio measured by the on-board FAIRO.

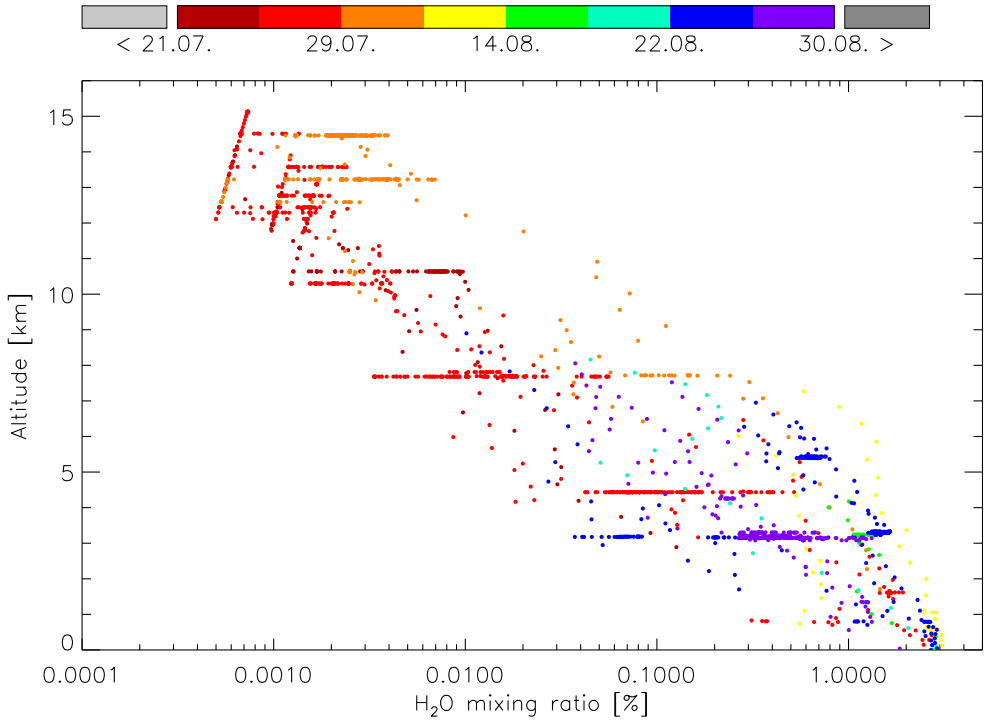

Figure B.10: Water vapour mixing ratio (logarithmic scale) measured by the on-board SHARC and additionally by a Vaisala sensor.

Appendix C

C.1 Pressure dependent calibration

Below you will find important pressure dependent factors of the sensitivity (ω and η, cf. Equation 4.17) calculated using OMO data. Colour Codes represent the date during the OMO campaign in 2015.

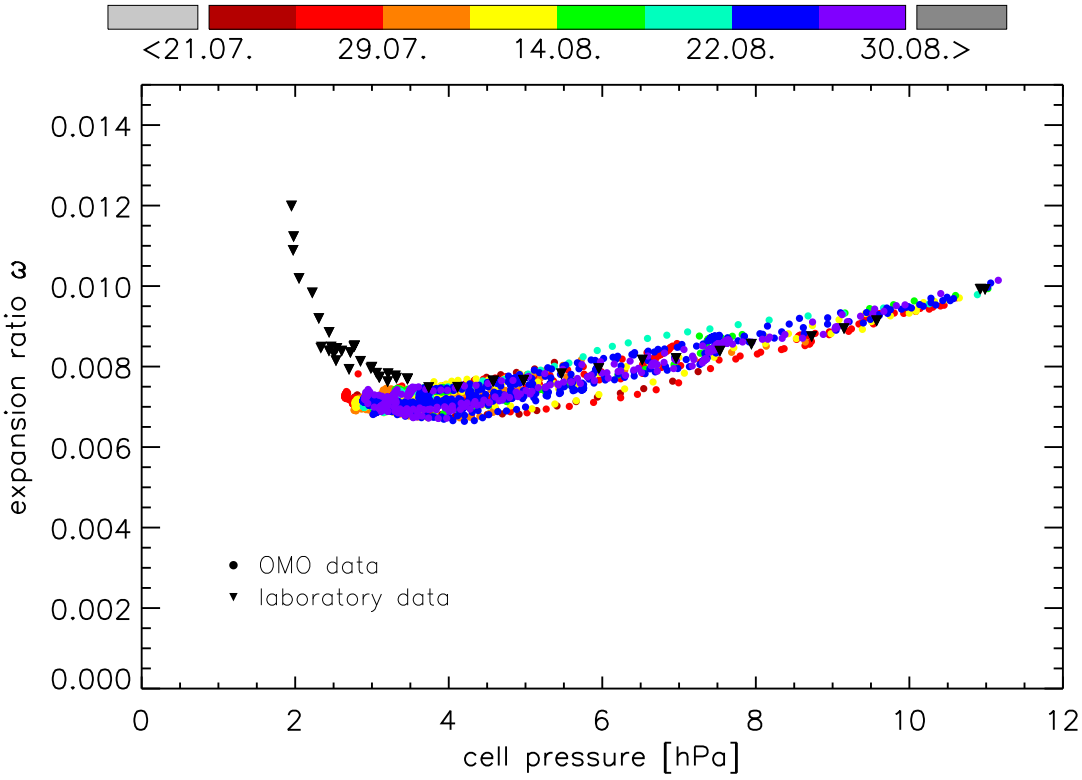

Figure C.1: Expansion ratio ω as calculated by equation (4.12) for the OH cell. The black triangles represent the expansion ratio for the laboratory measurements. For low pressures these deviate from OMO, because on the aircraft this corresponds to low temperatures. However, the major variability is due to q_{tube} (cf. Figure B.7), while the dependence on inlet temperature at the entrance of the nozzle is only weak ($\omega \propto T_{\text{inlet}}$).

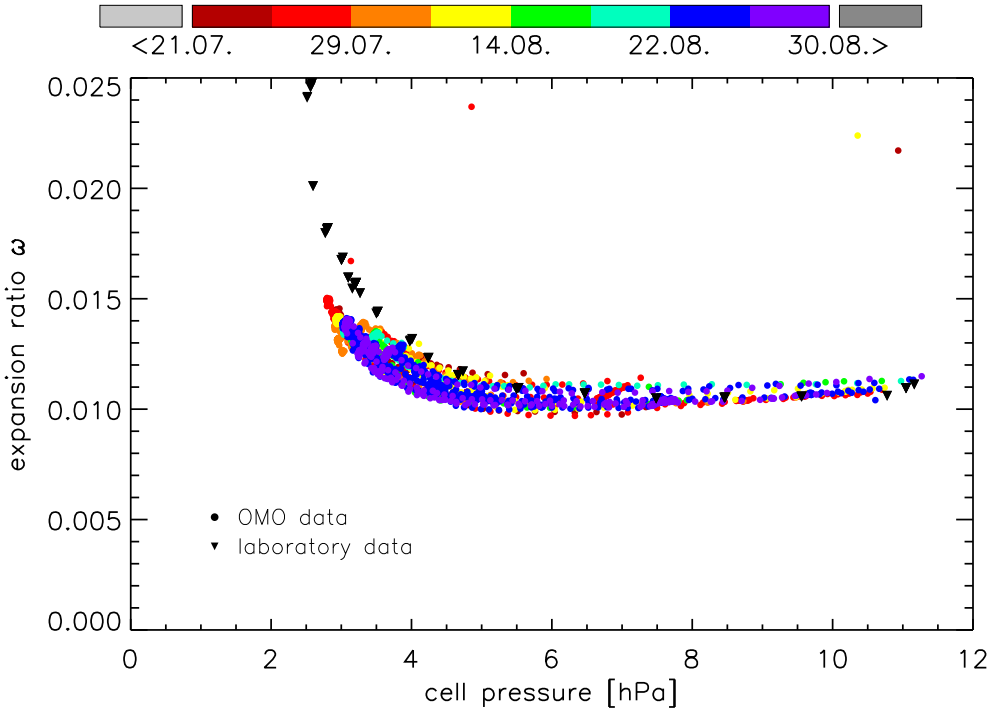

Figure C.2: Expansion ratio ω as calculated by equation (4.12) for the HO_2 cell. The black triangles represent the expansion ratio for the laboratory measurements. There is hardly any variability until very low cell pressures. The discrepancy of the laboratory data to the OMO data is due to the lower ambient temperature during flights ($\omega \propto T_{\mathrm{amb}}$).

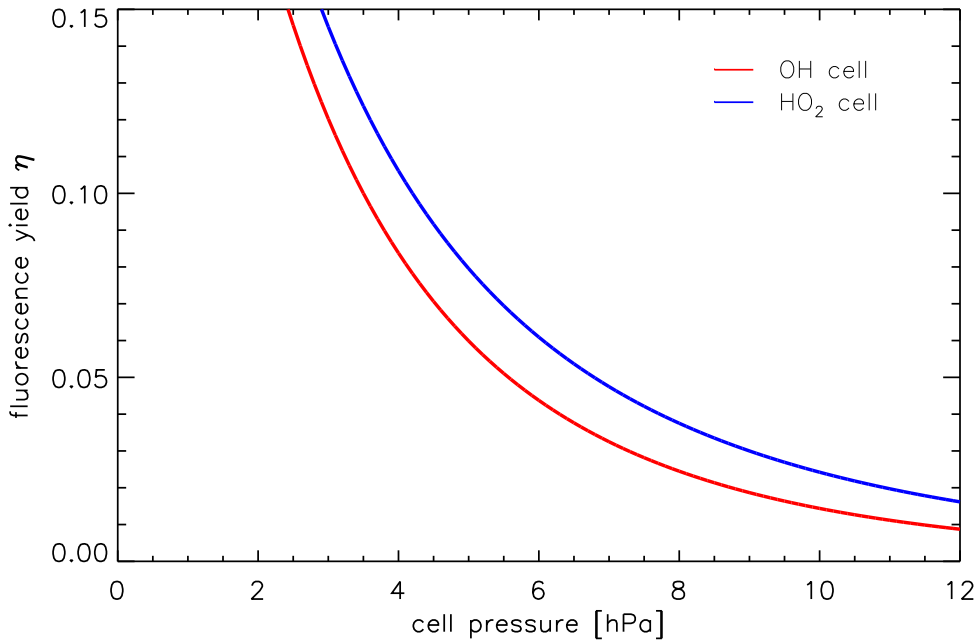

Figure C.3: Fluorescence yield η calculated by Equation 3.4 as a function of cell pressure for the OH channel (red) and the HO_2 channel (blue). The two curves differ due to unequal delay timings on the OH and HO_2 channel.

C.2 The apparent cross-section $\sigma_{O_2}^{app}$ for the in-flight calibration unit

Section 4.2.1 introduced the concept of in-flight calibration, alongside which the flight factor ff in Equation 4.24 relies on the knowledge of the apparent oxygen cross-section defined by Equation 4.23. It arises due to the fact that the oxygen absorption cross-section is finely structured (Schumann-Runge bands) over the narrow width of the 185 nm Hg-emission line and is determined by a separate experiment in the laboratory at constant temperature of 20 °C. The O_2 column density $x = [O_2]\, l$ in Equation 4.23 contains an unknown effective length l for the total path the light traverses through the absorber before it is detected. This quantity was determined in a first measurement using N_2O as an absorber. The cross-section of N_2O ($\sigma_{N_2O} = 1.43 \times 10^{-19}\,\mathrm{cm}^2$) is very well known and constant over the spectral width of the Hg-emission line. This therefore suggests to write

$$l = -\frac{1}{\sigma_{N_2O}\,[N_2O]} \ln \frac{I_{185}}{I_{185}^0}\,. \tag{C.1}$$

However, the above value will depend on the N_2O concentration, because the upper mirror is concave and the true length will vary with the exact position within the cross-section of the finitely extended light-ray, while the measured signal will average over this geometry dependence. Nevertheless, since the oxygen cross-section is roughly a factor of 10 smaller than the N_2O cross-section with $\sigma_{O_2} \cdot x \ll 1$, the value of interest will be the regime for very small N_2O concentrations. From Figure C.4 the length reads $l = 8.02 \pm 0.11$ cm and compares well with the geometrical length of twice the deceleration tube diameter 8.3 cm.

In the second part of the experiment, N_2O is replaced by O_2 and the measurement is repeated. The apparent O_2 cross-section is then calculated by Equation 4.23 and the result is depicted in Figure C.5 as a function of column density x.

During the experiment ambient pressure and temperature were recorded from which the ambient number density is obtained. The flows of absorber and carrier (N_2) gas were regulated by mass-flow controllers and the absorber mixing ratio x_i ($i = O_2, N_2O$) is calculated by the fraction to total standard flow

$$x_i = \frac{q_{0,i}}{q_{0,i} + q_{0,N_2}}\,. \tag{C.2}$$

The previously mentioned detector offset due to stray light was 0.925 ± 0.009V.

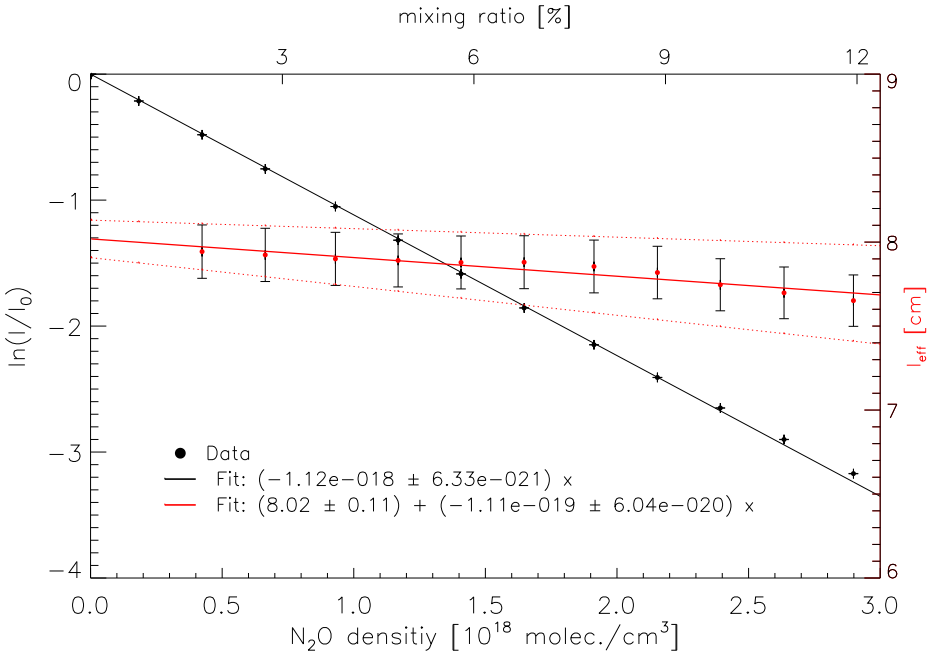

Figure C.4: The effective length is calculated from Equation C.1. It is a function of the N_2O concentration, because the measured signal is an average over the geometry which is not planar. The length of interest is for very low N_2O concentrations, since the O_2 cross-section is roughly a factor of 10 smaller than the N_2O cross-section. The upper and lower dotted lines are the 1σ error bands.

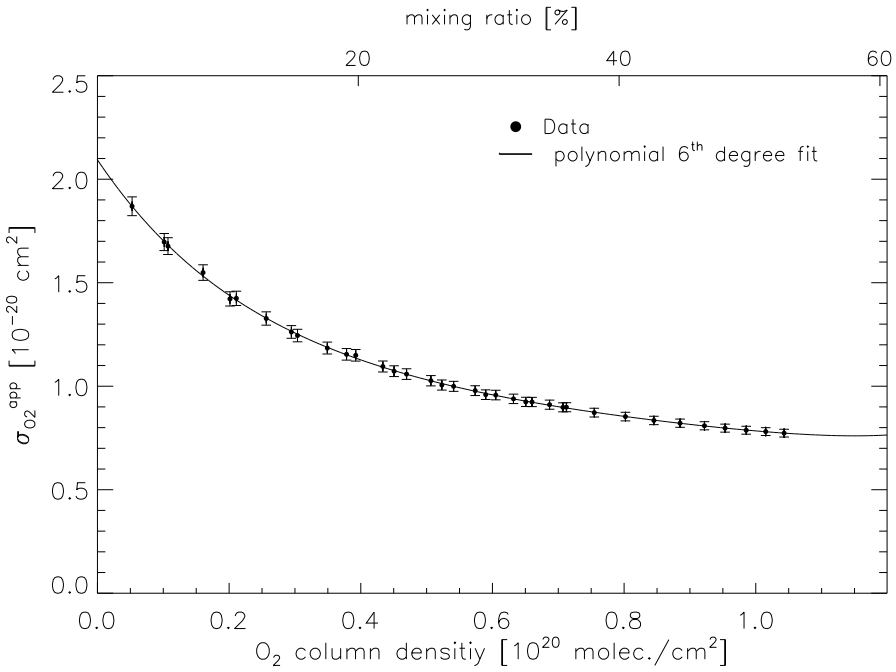

Figure C.5: The apparent cross-section $\sigma_{O_2}^{app}$ for oxygen as a function of column density x used to correct the light intensity measured within the in-flight calibration unit (cf. Equation 4.24). The error bars correspond to the 1σ precision of each averaged measurement point. Fit function: $2.09 - 4.73\,x + 9.54\,x^2 - 13.24\,x^3 + 12.09\,x^4 - 6.51\,x^5 + 1.55\,x^6$

C.3 The effective cross-section $\sigma_{O_2}^{\text{eff}}$ for the new radical source

The procedure goes along the lines the measurement for the apparent cross-section $\sigma_{O_2}^{\text{app}}$ of the in-flight calibration unit (cf. Appendix C.2). The effective cross-section (cf. Equation 4.26) can be written as (Sedlacek, 2001; Hofzumahaus et al., 1997)

$$\begin{aligned}\sigma_{O_2}^{\text{eff}}(x) &= \frac{\int_{\text{Hg-185 nm}} \sigma_{O_2}(\lambda) I_\lambda^0(\lambda)\, e^{-x\,\sigma_{O_2}(\lambda)}\, d\lambda}{\int_{\text{Hg-185 nm}} I_\lambda^0(\lambda)\, e^{-x\,\sigma_{O_2}(\lambda)}\, d\lambda} \\ &= -\frac{d}{dx} \ln \frac{I_{185}(x)}{I_{185}(0)} \\ &= \frac{d}{dx}\, x\, \sigma_{O_2}^{\text{app}}(x) \end{aligned} \tag{C.3}$$

where I_λ^0 is the spectral intensity of the lamp seen by the detector without absorber, $I_{185}(x)$ the total intensity of the Hg-emission line seen by the detector and $x = [O_2]\, l$ the oxygen column density. $\sigma_{O_2}^{\text{eff}}$ represents the effective absorption cross-section of O_2 in a thin layer of air after the lamp radiation has passed through the oxygen column density x. Since the tube is circular, l amounts to an unknown effective length and is determined with N_2O as an absorber for small concentrations (cf. Equation C.1). It is seen in Figure C.6 were a mean value of $l = 1.63 \pm 0.05$ cm is obtained with no visible dependence on the N_2O density. This result is then used when the experiment is repeated with oxygen as an absorber. The derivative of the logarithmic intensity drop with respect to column density x then yields the effective oxygen cross-section (Figure C.7).

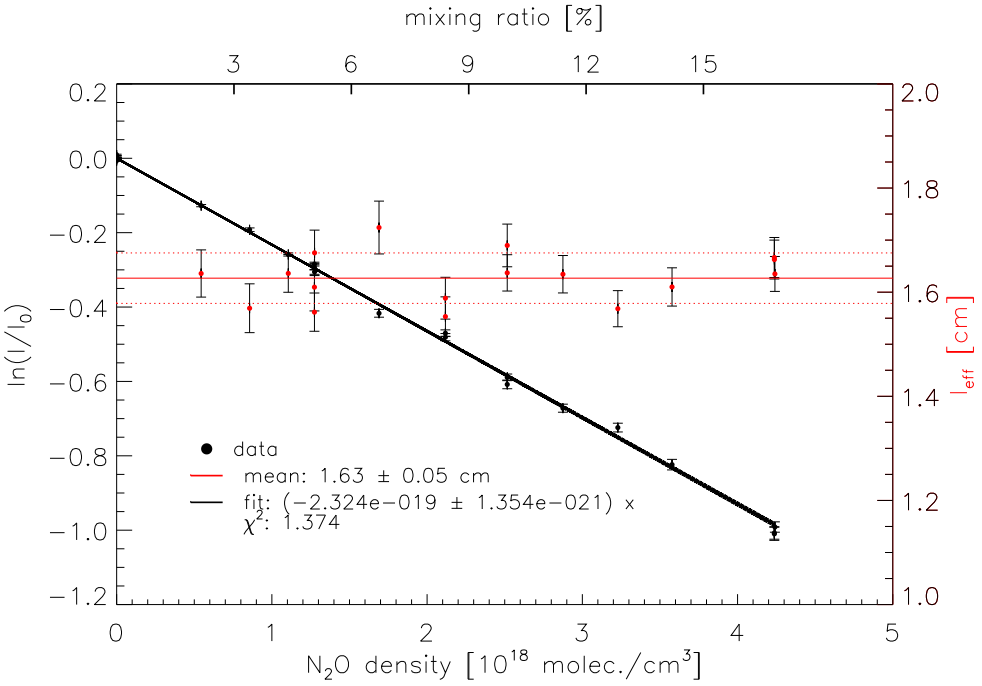

Figure C.6: Logarithmic plot of the intensity I_{185} from the 185 nm radiation against the N_2O density. The dashed lines show the 1σ errors on the regression line. The red points show the effective length (mean: $l = 1.63 \pm 0.05$ cm) as a function of the N_2O absorber density.

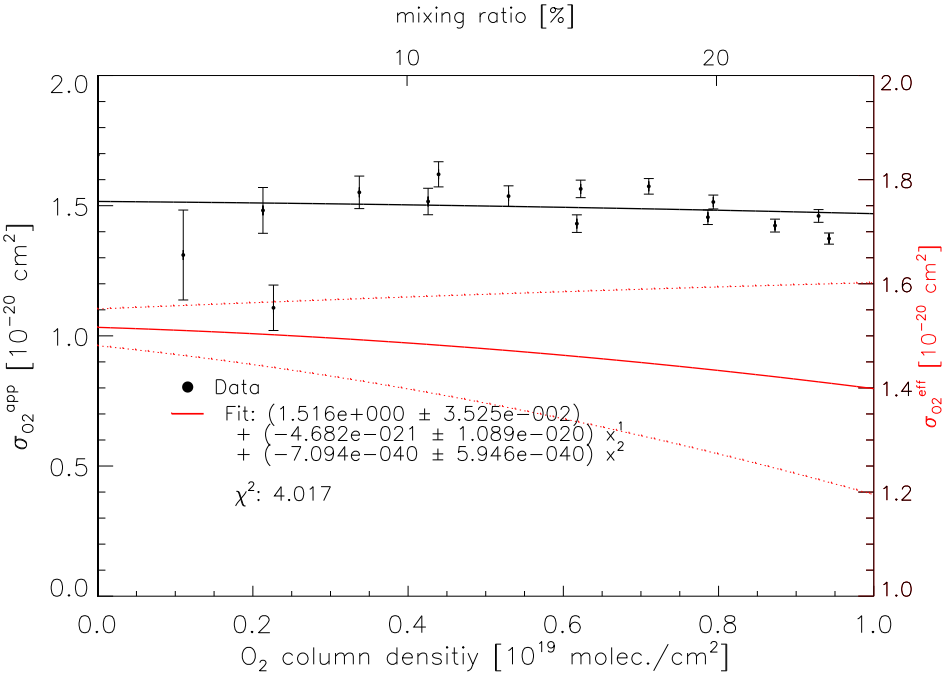

Figure C.7: Effective oxygen cross-section measured for the new radical source (red line). The black line shows the apparent cross-section defined by Equation 4.23. The red line follows from the black line by derivation of $x\,\sigma_{O_2}^{app}(x)$ with respect to column density x. The dashed red lines show the 1σ band.

C.4 The ozone production factor a

The ozone production factor a (cf. Equation 4.29) for the new radical source KQ5 is a pressure dependent quantity which is measured in a separate experiment. Since the amount of ozone generated by the lamp is relatively low (< 2 ppb), it is measured by a sensitive chemiluminescence detector (CLD, manufacturer: Eco Physics, type: CLD 770 AI ppt). The application of the CLD was originally intended for NO measurements, but it was modified to measure ozone by adding NO instead of O_3 to produce excited NO_2 radicals. The detection limit for the instrument is roughly 50 ppt. It samples from the flow after the gas expansion behind the nozzle and needs to be calibrated as well. This is done with ozone mixing ratios between 50 and 150 ppb created by an ANSYCO ozone calibrator (KI O341M) and implies linearity.

After the calibration of the CLD, the mean ozone mixing ratio sampled by the nozzle that is created in the photolysis region of the tube is measured for standard flows of synthetic air ranging from 15 to 25 $^{\mathrm{std\,l}}/_{\mathrm{min}}$. The value is multiplied with the volume flow q_v of the air through the tube (calculated from the standard flow at given conditions) and normalized to lamp intensity measured by the photo diode giving

$$a = \frac{x_{O_3}\, q_\mathrm{v}}{I_{185}^{\mathrm{meas}}} \tag{C.4}$$

in units $[^{\mathrm{ppb\,l}}/_{\mathrm{V\,min}}]$. This procedure is repeated for various pressures between 250 and 1000 hPa inside the calibration tube. Figure C.8 shows the ozone production factors a as a function of the pressure in the radical source at room temperature. The results are shown for a standard flow of 20 $^{\mathrm{std\,l}}/_{\mathrm{min}}$. Measurements were also performed at different flow rates (15-25 $^{\mathrm{std\,l}}/_{\mathrm{min}}$) and showed only a weak dependence of ± 1 $^{\mathrm{ppb\,l}}/_{\mathrm{V\,min}}$ between 18 and 22 $^{\mathrm{std\,l}}/_{\mathrm{min}}$. The linear regression in Figure C.8 is given by $83.4 - 6.25\,p$ where p is given in bar. The precision of the data corresponds to a 1σ error of 2 $^{\mathrm{ppb\,l}}/_{\mathrm{V\,min}}$.

Besides a few factors that do not change (tube geometry, O_2 mixing ratio), the quantity a/Φ_{O_3} only depends on the effective oxygen cross-section and the flow profile. For these two quantities no major pressure dependence is to be expected and indeed - under the assumption that Φ_{O_3} is constant - Figure C.8 shows only a weak dependence of a over the pressure range from 200 to 1000 hPa, where it changes linearly up to 6 %. In respect thereof, extrapolating the quantity a/Φ_{O_3} to even lower pressures with the purpose of applying it to Equation 4.29 at e.g. 50 hPa seems justified. However, in order for this argument to hold, it is crucial for Φ_{O_3} to be indeed constant over the pressure range considered in Figure C.8 (250-1000 hPa). This will be the case, if the lifetime τ_O of the O-atoms is much shorter than the transport time from the photolysis region to the inlet nozzle. Since at constant mass flow through the tube, the latter changes proportional to pressure inside the tube (volume flow $\propto 1/p$) and the former varies inversely proportional with the square of the pressure in the aforementioned pressure range ($\tau_\mathrm{O}^{-1} = k_{\mathrm{O+O_2}}\,[\mathrm{O_2}]$, $k_{\mathrm{O+O_2}} \propto [\mathrm{M}]$), it is sufficient to estimate for the one condition at 250 hPa. With a distance of 6 cm from the photolysis region to the inlet nozzle, a standard flow of 20 $^{\mathrm{std\,l}}/_{\mathrm{min}}$ and an inner tube diameter of 18.7 mm, the transport (reaction) time for the velocity field

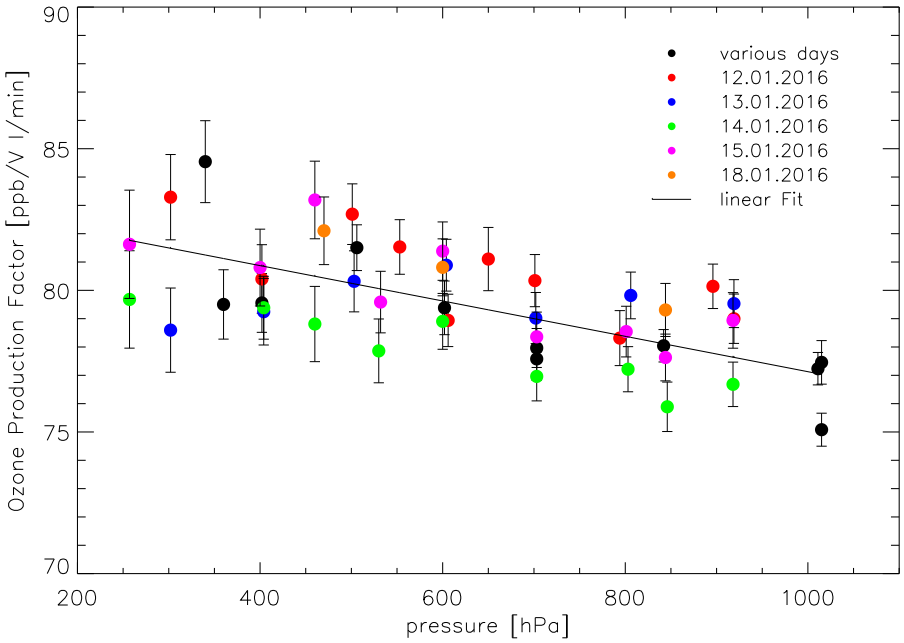

Figure C.8: Pressure dependence of the ozone production factor a for the calibration source KQ5 and a nozzle diameter of 1 mm. The air mass flow is kept constant at 20 $^{\mathrm{std\,l}}/_{\mathrm{min}}$. Measurements from one day were relatively stable, but for different days there is significant variability which constitutes the total uncertainty. The solid line is the fit used for the calculation of the OH concentration during laboratory pressure dependent calibrations.

(velocity $< 2 \times$ plug flow velocity) is larger than 5 ms. In contrast the lifetime of the O-atoms is calculated to 0.2 ms (Burkholder et al., 2015), which is more than an order of magnitude smaller than the transport time.

For much lower tube pressures it is expected that not all O-atoms produced within the photolysis region will be converted to ozone by the time the air reaches the inlet nozzle. Nevertheless, in this case both quantities a and Φ_{O_3} will be diminished by the same factor, which cancels in the ratio a/Φ_{O_3}.

A similar argument applies to the formation of HO_2 via the reaction $H + O_2$; the lifetime of the H-atoms is much shorter than the transport time to the inlet nozzle.

C.5 Nozzle vs. pressure variation

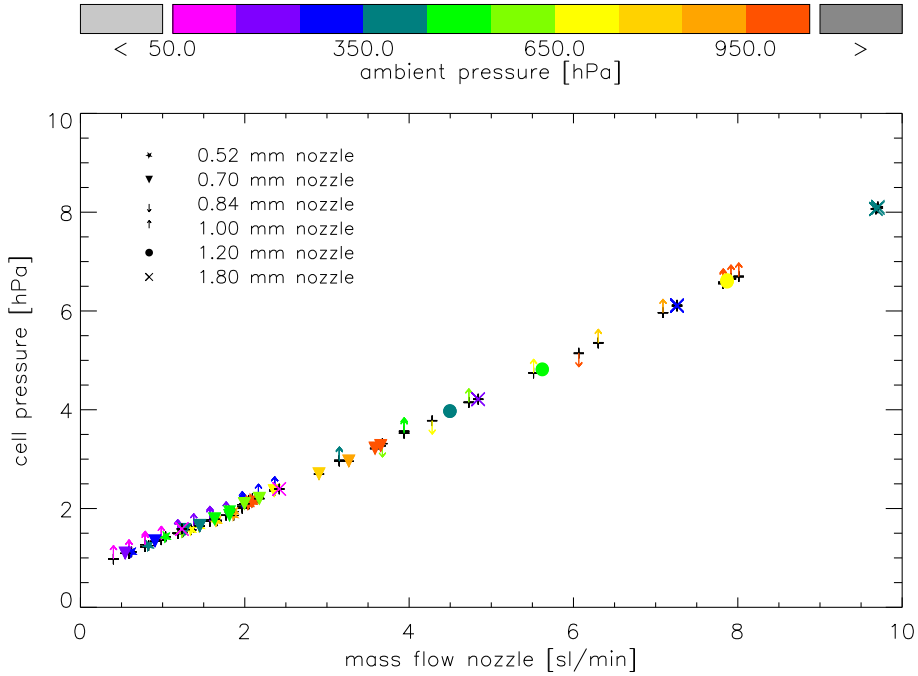

Figure C.9: Cell pressure as a function of the mass flow through the nozzle for various nozzle diameters. As the pump speed was assumed to be reproducibly the same at a given mass flow, the nozzle factors μ were calibrated such that all curves lie on top of each other.

Table C.1: Nozzle factors μ used in Equation 3.14 for the different nozzle sizes examined. Note that a value of $\mu = 1$ is the theoretically upper limit if the nozzle diameter would be exact. These are however only nominal values and the true diameter can deviate from this. This does not affect the determination of the mass flow as the nozzles are calibrated with respect to the mass flow of the 1 mm nozzle.

nozzle diameter [mm]	μ
0.52	0.93
0.70	0.89
0.84	1.05
1.00	0.95
1.20	0.95
1.80	0.90

C.6 HO_2 conversion efficiency

Figure 4.23 essentially shows the in-flight conversion efficiency from HO_2 to OH by the reaction with NO. Due to the dynamic effect of inlet pressure reduction, the mass-flow correction has been included into this diagram (going into both, the x- and y-coordinates). However, since it naturally obeys the inverse square relationship, this will automatically superimpose the measured dependence, of which an inverse square relationship is to be seen. Hence, Figure C.10 is included which only shows the measured laboratory data without mass-flow correction.

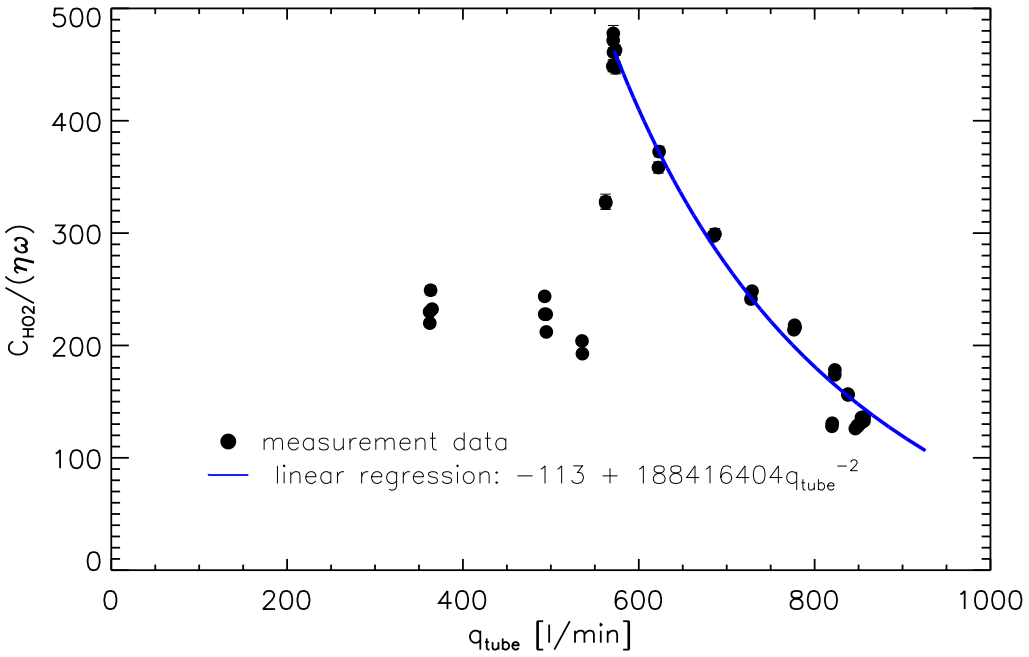

Figure C.10: Same graphic as in Figure 4.23 where the mass-flow correction has additionally been removed.

Bibliography

[AFGL 1986] AFGL, Air Force Geophysics L.: Atmospheric Constituent Profiles (0-120 km). In: *Environmental Research Papers* 954 (1986). – US Standard Atmosphere (1976)

[ANS 2018] ANSYS, Inc. (Ed.): *ANSYS Fluent User's Guide*. 16.1. Canonsburg: ANSYS, Inc., 2018

[Apel et al. 2012] Apel, E.C. ; Olson, J.R. ; Crawford, J.H. ; Hornbrook, R.S. ; Hills, A.J. ; Cantrell, C.A. ; Emmons, L.K. ; Knapp, D.J. ; Hall, S. ; III, R.L. M. ; Weinheimer, A.J. ; Fried, A. ; Blake, D.R. ; Crounse, J.D. ; Clair, J.M. S. ; Wennberg, P.O. ; Diskin, G.S. ; Fuelberg, H.E. ; Wisthaler, A. ; Mikoviny, T. ; Brune, W. ; Riemer, D.D.: Impact of the deep convection of isoprene and other reactive trace species on radicals and ozone in the upper troposphere. In: *Atmospheric Chemistry and Physics* 12 (2012), S. 1135–1150

[Atkinson et al. 2004] Atkinson, Roger ; Baulch, D.L. ; Cox, R.A. ; Crowley, J.N. ; Hampson, R.F. ; Hynes, R.G. ; Jenkin, M.E. ; Rossi, M.J. ; Troe, J.: Evaluated kinetic and photochemical data for atmospheric chemistry. In: *Atmospheric Chemistry and Physics 4* I (2004), Nr. 6, S. 1461–1738

[Baardsen and Terhune 1972] Baardsen, E.L. ; Terhune, R.W.: Detection of OH in the atmosphere using a dye laser. In: *Applied Physics Letters* 21 (1972), S. 209

[Becker et al. 1974] Becker, K.H. ; Haaks, D. ; Tatarczyk, T.: The Natural lifetime of OH (2Sigma+, v=0, N=2, J=32) and its quenching by atomic hydrogen. In: *Chemical Physics Letters* 25 (1974), Nr. 4, S. 564–567

[Bey et al. 2001] Bey, Isabelle ; Aumont, Bernard ; Toupance, Gerard: A modeling study of the nighttime radical chemistry in the lower continental troposphere. Origin and evolution oflows HOx. In: *Geophysical Research Letters* 106 (2001), Nr. D9, S. 9991–10001

[Brauers and Rohrer 1999] Brauers, Theo ; Rohrer, Franz: *Easy AtmoSpheric chemistrY*. Ver. 2. Juelich, Wilhelm-Johnen Str.: Forschungszentrum Juelich, 1999

[Broch 2011] Broch, Sebastian: *Ein neues LIF-Instrument fuer flugzeug- und bodengebundene Messungen von OH- und HO2-Radikalen in der Troposphaere*. Forschungszentrum Juelich GmbH; Grafische Medien, 2011

[Brune et al. 1998] Brune, W. ; Faloona, I.C. ; Tan, D. ; Weinheimer, A.J. ; Campos, T. ; Ridley, B.A. ; Vay, S.A. ; Collins, J.E. ; Sachse, G.W. ; Jaegle, L. ; Jacob, D.J.: Airborne in-situ OH and HO2 observations in the cloud-free troposphere and lower stratosphere during SUCCESS. In: *Geophysical Research Letters* 25 (1998), May, Nr. 10, S. 1701–1704

[Brune et al. 1999] Brune, W.H. ; Tan, D. ; Faloona, I.F. ; Jaegle, L. ; Jacob, D.J. ; Heikes, B.G. ; Snow, J. ; Kondo, Y. ; Shetter, R. ; Sachse, G.W. ; Anderson, B. ; Gregory, G.L. ; Vay, S. ; Singh, H.B. ; Davis, D.D. ; Crawford, J.H. ; Blake, D.R.: OH and HO2 chemistry in the North Atlantic free troposphere. In: *Journal of Geophysical Research* 26 (1999), Nr. D20

[Brune et al. 2018] Brune, William H. ; Ren, Xinrong ; Zhang, Li ; Mao, Jinqiu ; Miller, David O. ; Anderson, Bruce E. ; Blake, Donald R. ; Cohen, Ronald C. ; Diskin, Glenn S. ; Hall, Samuel R. ; Hanisco, Thomas F. ; Huey, L. G. ; Nault, Benjamin A. ; Peischl, Jeff ; Pollack, Ilana ; Ryerson, Thomas B. ; Shingler, Taylor ; Sorooshian, Armin ; Ullmann, Kirk ; Wisthaler, Armin ; Wooldridge, Paul J.: Atmospheric Oxidation in the Presence of Clouds during the Deep Convective Clouds and Chemistry (DC3) Study. In: *Atmospheric Chemistry and Physics* (2018)

[Burkholder et al. 2015] Burkholder, J.P. ; Sander, S.P. ; Abbatt, J.P.D. ; Barker, J.R. ; Huie, R.E. ; Kolb, C.E. ; Kurylo, M.J. ; Orkin, V.L. ; Wilmouth, D.M. ; Wine, P.H.: *Chemical Kinetics and Photochemical Data for Use in Atmospheric Studies*. NASA JPL, 2015

[Cantrell et al. 2003a] Cantrell, Christopher A. ; Edwards, G.D. ; Stephens, S. ; Mauldin, R.L. ; Zondlo, M.A. ; Kosciuch, E. ; Eisele, F.L. ; Shetter, R.E. ; Lefer, B.L. ; Hall, S. ; Flocke, F. ; Weinheimer, A. ; Fried, A. ; Apel, E. ; Kondo, Y. ; Blake, D.R. ; Blake, N.J. ; Simpson, I.J. ; Bandy, A.R. ; Thornton, D.C. ; Heikes, B.G. ; Singh, H.B. ; Brune, W.H. ; Harder, H. ; Martinez, M. ; Jacob, D.J. ; Avery, M.A. ; Barrick, J.D. ; Sachse, G.W. ; Olson, J.R. ; Crawford, J.H. ; Clarke, A.D.: Peroxy radical behavior during the Transport and Chemical Evolution over the Pacific (TRACE-P) campaign as measured aboard the NASA P-3B aircraft. In: *Journal of Geophysical Research* 108 (2003), Nr. D20, S. 8797

[Cantrell et al. 2003b] Cantrell, Christopher A. ; Mauldin, L. ; Zondlo, M. ; Eisele, F. ; Kosciuch, E. ; Shetter, R. ; Lefer, B. ; Hall, S. ; Campos, T. ; Ridley, B. ; Walega, J. ; Fried, A. ; Wert, B. ; Flocke, F. ; Weinheimer, A. ; Hannigan, J. ; Coffey, M. ; Atlas, E. ; Stephens, S. ; Heikes, B. ; Snow, J. ; Blake, D. ; Blake, N. ; Katzenstein, A. ; Lopez, J. ; Browell, E.V. ; Dibb, J. ; Scheuer, E. ; Seid, G. ; Talbot, R.: Steady state free radical budgets and ozone photochemistry during TOPSE. In: *Journal of Geophysical Research* 108 (2003), Nr. D48361

[Cantrell et al. 1997] Cantrell, Christopher A. ; Zimmer, Audrey ; Tyndall, Geoffrey S.: Absorption cross sections for water vapor from 183 to 193 nm. In: *Geophysical Research Letters* 24 (1997), Nr. 17, S. 2195–2198

[Carpenter et al. 1997] Carpenter, Lucy J. ; Monks, Paul S. ; Bandy, Brian J. ; Penkett, Stuart A. ; Galbally, Ian E. ; Meyer, (Mick) C.: A study of peroxy radicals and ozone photochemistry at coastal sites in the northern and southern hemispheres. In: *Journal of Geophysical Research* (1997)

[Chan and Yao 2008] Chan, Chak K. ; Yao, Xiaohong: Air pollution in mega cities in China. In: *Atmospheric Environment* 42 (2008)

[Commane et al. 2010] Commane, R. ; Floquet, C.F.A. ; Ingham, T. ; Stone, D. ; Evans, M.J. ; Heard, D.E.: Observations of OH and HO2 radicals over West Africa. In: *Atmospheric Chemistry and Physics* 10 (2010), S. 8783–8801

[Cooper et al. 2006] Cooper, O.R. ; Stohl, A. ; Trainer, M. ; Thompson, A.M. ; Witte, J.C. ; Oltmans, S.J. ; Morris, G. ; Pickering, K.E. ; Crawford, J.H. ; Chen, G. ; Cohen, R.C. ; Bertram, T.H. ; Wooldridge, P. ; Perring, A. ; Brune, W.H. ; Merrill, J. ; Moody, J.L. ; Tarasick, D. ; Nedelec, P. ; Forbes, G. ; Newchurch, M.J. ; Schmidlin, F.J. ; Johnson, B.J. ; Turquety, S. ; Baughcum, S.L. ; Ren, X. ; Fehsenfeld, F.C. ; Meagher, J.F. ; Spichtinger, N. ; Brown, C.C. ; McKeen, S.A. ; McDermid, I.S. ; Leblanc, T.: Large upper tropospheric ozone enhancements above midlatitude North America during summer: In situ evidence from the IONS and MOZAIC ozone measurement network. In: *Journal of Geophysical Research: Atmospheres* 111 (2006), Nr. D24

[Creasey et al. 1997] Creasey, David J. ; Heard, Dwayne E. ; Pilling, Michael J. ; Whitaker, Benjamin J. ; Berzins, Martin ; Fairlie, Roger: Visualisation of a supersonic free-jet expansion using laser-induced fluorescence spectroscopy: Application to the measurement of rate constants at ultralow temperatures. In: *Applied Physics B* 65 (1997), S. 375–391

[Crosley and Smith 1990] Crosley, David R. ; Smith, Gregory P.: A photochemical model of ozone interference effects in laser detection of tropospheric OH. In: *Journal of Geophysical Research* 95 (1990), Nr. D10, S. 16427–16442

[Davis et al. 1976] Davis, D.D. ; Heaps, W. ; McGee, T.: Direct measurements of natural tropospheric levels of OH via an aircraft borne tunable dye laser. In: *Geophysical Research Letters* 3 (1976), Nr. 6, S. 331–333

[Davis et al. 1981] Davis, D.D. ; Rodgers, M.O. ; Fischer, S.D. ; Heaps, W.S.: A theoretical assessment of the O3/H2O interference problem in the detection of natural levels of OH via laser induced fluorescence. In: *Geophysical Research Letters* 8 (1981), Nr. 1, S. 73–76

[Demtroeder 2011] Demtroeder, Wolfgang: *Laserspektroskopie 1.* Springer, 2011

[Dimpfl and Kinsey 1979] Dimpfl, William L. ; Kinsey, James L.: Radiative lifetimes of OH(A2-Sigma) and Einstein coefficients for the A-X system of OH and OD. In: *Journal of Quantitative Spectroscopy & Radiative Transfer* 21 (1979), S. 233–241

[DLR 2009] DLR: *HALO DLR.* http://www.halo.dlr.de/index.html, 2009

[Dorn et al. 1995] Dorn, H.P. ; Neuroth, R. ; Hofzumahaus, A.: Investigation of OH absorption cross seections of rotational transitions in the A2-Sigma+, v'=0 ¡- X2-Pi, v'=0 band under atmospheric conditions: Implications for tropospheric long-path absorption measurements. In: *Journal of Geophysical Research* 100 (1995), S. 7397–7409

[Drummond et al. 1988] Drummond, J.W. ; Ehhalt, D.H. ; Volz, A.: Measurements of nitric oxide between 0-12 km altitude and 67deg N to 60 deg S latitude obtained during STRATOZ III. In: *Journal of Geophysical Research: Atmospheres* 93 (1988), Nr. D12

[Ehhalt 1999] Ehhalt, D.H.: Photooxidation of trace gases in the troposphere Plenary Lecture. In: *Physical Chemistry Chemical Physics* 1 (1999), Nr. 24, S. 5401–5408

[Ehhalt et al. 1992] Ehhalt, D.H. ; Rohrer, F. ; Wahner, A.: Sources and Distribution of NOx in the Upper Troposphere at Northern Mid-Latitudes. In: *Journal of Geophysical Research* 97 (1992), March, Nr. D4, S. 3725–3738

[Eisele et al. 1997] Eisele, F.L. ; Mauldin, III ; Tanner, D.J. ; Fox, J.R. ; Mouch, T. ; Scully, T.: An inlet/sampling duct for airborne OH and sulfuric adic measurements. In: *Journal of Geophysical Research* 102 (1997), S. 27993–28001

[Engel et al. 1992] Engel, V. ; Staemmler, V. ; Wal, R.L. V. ; Crim, F.F. ; Sension, R.J. ; Hudson, B. ; Andresen, P. ; Hennig, S. ; Weide, K. ; Schinke, R.: Photodissociation of water in the frist absorption band: a prototype for dissociation on a repulsive potential energy surface. In: *Journal of Physical Chemistry* 96 (1992), Nr. 8, S. 3201–3213

[Faloona et al. 2000] Faloona, Ian ; Tan, David ; Brune, William H. ; Jaegle, Lyatt ; Jacob, Daniel J. ; Kondo, Y. ; Koike, M. ; Chatfield, Robert ; Pueschel, Rudolf ; Ferry, Guy ; Sachse, Glen ; Vay, Stephanie ; Andersons, Bruce ; Hannon, John ; Fuelberg, Henry: Observations of HOx and its relationship with NOx in the upper troposphere during SONEX. In: *Journal of Geophysical Research* 105 (2000), Nr. D3, S. 3771–3783

[Faloona et al. 2004] Faloona, Ian ; Tan, David ; Lesher, Robert L. ; Hazen, Nathan L.: A Laser-induced Fluorescence Instrument for Detecting Tropospheric OH and HO2: Characteristics and Calibration. In: *Journal of Atmospheric Chemistry* 47 (2004)

[Finlayson-Pitts and Jr. 2000] Finlayson-Pitts, Barbara J. ; Jr., James N. P.: *Chemistry of the Upper and Lower Atmosphere*. AP, 2000

[Fuchs et al. 2011] Fuchs, Hendrik ; Bohn, B. ; Hofzumahaus, A. ; Holland, F. ; Lu, K.D. ; Nehr, S. ; Rohrer, F. ; Wahner, A.: Detection of HO2 by laser-induced fluorescence: calibration and interferences from RO2 radicals. In: *Atmospheric Measurement Techniques* 4 (2011), S. 1209–1225

[Fuchs et al. 2008] Fuchs, Hendrik ; Holland, Frank ; Hofzumahaus, Andreas: Measurement of tropospheric RO2 and HO2 radicals by a laser-induced fluorescence instrument. In: *Review of Scientific Instruments* 79 (2008), Nr. 084104

[Fuchs et al. 2016] Fuchs, Hendrik ; Tan, Zhaofeng ; Hofzumahaus, Andreas ; Broch, Sebastian ; Dorn, Hans-Peter ; Holland, Frank ; Kuenstler, Christopher ; Gomm, Sebastian ; Rohrer, Franz ; Schrade, Stephanie ; Tillmann, Ralf ; Wahner, Andreas: Investigation of potential interferences in the detection of atmospheric ROx radicals by laser-induced fluorescence under dark conditions. In: *Atmospheric Measurement Techniques* 9 (2016), S. 1431–1447

[Fuller et al. 1966] Fuller, Edward N. ; Schettler, P.D. ; Giddings, J. C.: New method for prediction of binary gas-phase diffusion coefficients. In: *Industrial & Engineering Chemistry* (1966)

[German 1975] German, K.R.: Direct measurement of the radiative lifetimes of the A2-Sigma+, v'=0 states of OH and OD. In: *Journal of Chemical Physics* 62 (1975), Nr. 7, S. 2584–2587

[Goliff et al. 2013] Goliff, Wendy S. ; Stockwell, William R. ; Lawson, Charlene V.: The regional atmospheric chemistry mechanism, version 2. In: *Atmospheric Environment* 68 (2013), S. 174–185

[Gottschaldt et al. 2018] Gottschaldt, Klaus-Dirk ; Schlager, Hans ; Baumann, Robert ; Cai, Duy S. ; Eyring, Veronika ; Graf, Phoebe ; Grewe, Volker ; Joeckel, Patrick ; Jurkat-Witschas, Tina ; Voigt, Christiane ; Zahn, Andreas ; Ziereis, Helmut: Dynamics and composition of the Asian summer monsoon anticyclone. In: *Atmospheric Chemistry and Physics* 18 (2018), S. 5655–5675

[Hard et al. 1984] Hard, Thomas M. ; O'Brien, Robert J. ; Chan, Cornelius Y. ; Mehr-Abzadeh, Ahmad A.: Tropospheric free radical determination by fluorescence assay with gas expansion. In: *Environmental Science & Technology* 18 (1984), Nr. 10, S. 768–777

[Heard and Henderson 2000] Heard, Dwayne E. ; Henderson, David A.: Quenching of OH (A2 Sigma+, v'=0) by several collision partners between 200 and 344 K. Cross-section measurements and model comparisons. In: *Physical Chemistry Chemical Physics* 2 (2000), S. 67–72

[Heard and Pilling 2003] Heard, Dwayne E. ; Pilling, Michael J.: Measurement of OH and HO2 in the Troposphere. In: *Chemical Reviews* (2003)

[Hermans et al. 2005] Hermans, Ive ; Mueller, Jean-Francois ; Nguyen, Thanh L. ; Jacobs, Pierre A. ; Peeters, Jozef: Kinetics of alpha-Hydroxyalkylperoxyl Radicals in Oxidation Processes. HO2-Initiated Oxidation of Ketones/Aldehydes near the Tropopause. In: *Journal of Physical Chemistry* 109 (2005), S. 4303–4311

[Hofzumahaus et al. 1997] Hofzumahaus, A. ; Brauers, T. ; Aschmutat, U. ; Brandenburger, U. ; Dorn, H.P. ; Hausmann, M. ; Hegling, M. ; Holland, F. ; Plass-Dtilmer, C. ; Sedlacek, M. ; Weber, M. ; Ehhalt, D.H.: Reply to Brauers et al. In: *Geophysical Research Letters* 24 (1997), Nr. 23, S. 3039–3040

[Hofzumahaus et al. 2002] Hofzumahaus, Andreas ; Kraus, A. ; Kylling, A. ; Zerefos, C.S.: Solar actinic radiation (280-420 nm) in the cloud-free troposphere between ground and 12 km altitude: Measurements and model results. In: *Journal of Geophysical Research* 107 (2002), Nr. D18, 8139

[Hogan and Davis 1974] Hogan, P. ; Davis, D.D.: OH lifetime measurements of several K levels in the v'=1 manifold of the A2 Sigma+ electronic state: Excitation via tunable UV laser. In: *Chemical Physics Letters* 29 (1974), Nr. 4, S. 555–557

[Holland et al. 1995] Holland, Frank ; Hessling, M. ; Hofzumahaus, A.: In Situ Measurement of Tropospheric OH Radicals by Laser-Induced Fluorescence - A Description of the KFA Instrument. In: *Journal of the Atmospheric Sciences* 52 (1995), Nr. 19, S. 3393–3401

[Holland et al. 2003] Holland, Frank ; Hofzumahaus, Andreas ; Schaefer, Juergen ; Kraus, Alexander ; Paetz, H.W.: Measurements of OH and HO2 radical concentrations and photolysis frequencies during BERLIOZ. In: *Journal of Geophysical Research* 108 (2003), Nr. D4

[Ivanov et al. 2007] Ivanov, A.V. ; Trakhtenberg, S. ; Bertram, A.K. ; Gershenzon, Y.M. ; Molina, M.J.: OH, HO2, and Ozone Gaseous Diffusion Coefficients. In: *Journal of Physical Chemistry A* (2007)

[Jacob et al. 1997] Jacob, Daniel J. ; Prather, Michael J. ; Rasch, Philip J. ; Shia, Run-Lie ; Balkanski, Yves J. ; Beagley, Stephen R. ; Bergmann, Daniel J. ; Blackshear, W. T. ; Brown, Margaret ; Chiba, Masaru ; Chipperfield, Martyn P. ; Grandpre, J. de ; Dignon, Jane E. ; Feichter, Johann ; Genthon, Christopher ; Grose, W. L. ; Kasibhatla, Prasad S. ; Koehler, Ines ; Kritz, Mark A. ; Law, Kathy ; Penner, Joyce E. ; Ramonet, Michel ; Reeves, Claire E. ; Rotman, Douglas A. ; Stockwell, Deianeira Z. ; Velthoven, Peter F. J. V. ; Verver, Ge ; Wild, Oliver ; Yang, Hu ; Zimmermann, Peter: Evaluation and intercomparison of global atmospheric transport models using 222Rn and other short-lived tracers. In: *Journal of Geophysical Research* (1997)

[Jaegle et al. 1999] Jaegle, L. ; Jacob, D.J. ; Brune, W.H. ; Faloona, I.C. ; Tan, D. ; Kondo, Y. ; Sachse, G.W. ; Anderson, B. ; Gregory, G.L. ; Vay, S. ; Singh, H.B. ; Blake, D.R. ; Shetter, R.: Ozone production in the upper troposphere and the influence of aircraft during SONEX: approach of NOx-saturated conditions. In: *Journal of Geophysical Research* 26 (1999), Nr. D20

[Jaegle et al. 1997] Jaegle, L. ; Jacob, D.J. ; Wennberg, P.O. ; Spivakovsky, C.M. ; Hanisco, T.F. ; Lanzendorf, E.J. ; Hintsa, E.J. ; Fahey, D.W. ;

Keim, E.R. ; Proffitt, M.H. ; Atlas, E.L. ; Flocke, F. ; Schauffler, S. ; McElroy, C.T. ; Midwinter, C. ; Pfister, L. ; Wilson, J.C.: Observed OH and HO2 in the upper troposphere suggest a major source from convective injection of peroxides. In: *Geophysical Research Letters* (1997)

[Jaegle et al. 2001] Jaegle, Lyatt ; Jacob, Daniel J. ; Brune, William H. ; Wennberg, Paul O.: Chemistry of HOx radicals in the upper troposphere. In: *Atmospheric Environment* 35 (2001), S. 469–489

[Kanaya et al. 2001] Kanaya, Yugo ; Sadanaga, Y. ; Hirokawa, J. ; Kajii, Y. ; Akimoto, H.: Development of a Ground-Based LIF Instrument for Measuring HOx Radicals: Instrumentation and Calibrations. In: *Journal of Atmospheric Chemistry* 38 (2001), Nr. 1, S. 73–110

[Landau and Lifshitz 1987] Landau, L.D. ; Lifshitz, E.M. ; Sykes, J.B. (Ed.) ; Reid, W.H. (Ed.): *Course of Theoretical Physics*. Bd. 6: *Fluid Mechanics*. Second English Edition. Pergamon Press, 1987

[Lelieveld et al. 2001] Lelieveld, J. ; Crutzen, P.J. ; Ramanathan, V. ; Andreae, M.O. ; Brenninkmeijer, C.A.M. ; Campos, T. ; Cass, G.R. ; Dickerson, R.R. ; Fischer, H. ; Gouw, J.A. de ; Hansel, A. ; Jefferson, A. ; Kley, D. ; Laat, A.T.J. de ; Lal, S. ; Lawrence, M.G. ; Lobert, J.M. ; Mayol-Bracero, O.L. ; Mitra, A.P. ; Novakov, T. ; Oltmans, S.J. ; Prather, K.A. ; Reiner, T. ; Rodhe, H. ; Scheeren, H.A. ; Sikka, D. ; Williams, J.: The Indian Ocean Experiment: Widespread Air Pollution from South and Southeast Asia. In: *Science* 291 (2001), S. 1031–1036

[Lelieveld et al. 2018] Lelieveld, Jos ; Bourtsoukidis, E. ; Bruehl, C. ; Fischer, H. ; Fuchs, H. ; Harder, H. ; Hofzumahaus, A. ; Holland, F. ; Marno, D. ; Neumaier, M. ; Pozzer, A. ; Schlager, H. ; Williams, J. ; Zahn, A. ; Ziereis, H.: The South Asian monsoon - Pollution pump and purifier. In: *Science* (2018)

[Lengel and Crosley 1977] Lengel, Russell K. ; Crosley, David R.: Energy transfer in A2-Sigma+ OH. I. Rotational. In: *Journal of Chemical Physics* 67 (1977), S. 2085

[Lengel and Crosley 1978] Lengel, Russell K. ; Crosley, David R.: Energy transfer in A2-Sigma+ OH. II. Vibrational. In: *Journal of Chemical Physics* 68 (1978), S. 5309

[Levy 1972] Levy, Hiram: Photochemistry of the lower troposphere. In: *Planetary and Space Science* 20 (1972), Nr. 6, S. 919–935

[Li et al. 2014] Li, Xin ; Rohrer, Franz ; Hofzumahaus, Andreas ; Brauers, Theo ; Haeseler, Rolf ; Bohn, Birger ; Broch, Sebastian ; Fuchs, Hendrik ; Gomm, Sebastian ; Holland, Frank ; Jaeger, Julia ; Kaiser, Jennifer ; Keutsch, Frank N. ; Lohse, Insa ; Lu, Keding ; Tillmann, Ralf ; Wegener, Robert ; Wolfe, Glenn M. ; Mentel, Thomas F. ; Kiendler-Scharr, Astrid ; Wahner, Andreas: Missing Gas-Phase Source of HONO Inferred from Zeppelin Measurements in the Troposphere. In: *Science* 344 (2014), S. 292–296

[Lu et al. 2012] Lu, K.D. ; Rohrer, F. ; Holland, F. ; Fuchs, H. ; Bohn, B. ; Brauers, T. ; Chang, C.C. ; Haeseler, R. ; Hu, M. ; Kita, K. ; Kondo, Y. ; Li, X. ; Lou, S.R. ; Nehr, S. ; Shao, M. ; Zeng, L.M. ; Wahner, A. ; Zhang, Y.H. ; Hofzumahaus, A.: Observation and modelling of OH and HO2 concentrations in the Pearl River Delta 2006: a missing OH source in a VOC rich atmosphere. In: *Atmospheric Chemistry and Physics* 12 (2012), S. 1541–1569

[Malleson et al. 1990] Malleson, A.M. ; Kellett, H.M. ; Myhill, R.G. ; Sweetenham, W.P.: *FACSIMILE user guide*. 1. Oxfordshire: Harwell Lab, 1990

[Martinez et al. 2010] Martinez, Monica ; Harder, Hartwig ; Kubistin, D. ; Rudolf, M. ; Bozem, H. ; Eerdekens, G. ; Fischer, H. ; Kluepfel, T. ; Gurk, C. ; Koenigstedt, R. ; Parchatka, U. ; Schiller, C.L. ; Stickler, A. ; Williams, J. ; Lelieveld, Jos: Hydroxyl radicals in the tropical troposphere over the Suriname rainforest: airborne measurements. In: *Atmospheric Chemistry and Physics* 10 (2010), S. 3759–3773

[Matsumi et al. 2002] Matsumi, Y. ; Comes, F.J. ; Hancock, G. ; Hofzumahaus, A. ; Hynes, A. J. ; Kawasaki, M. ; Ravishankara, A.R.: Quantum yields for production of O(1D) in the ultraviolet photolysis of ozone: Recommendation based on evaluation of laboratory data. In: *Journal of Geophysical Research* (2002)

[Mauldin III et al. 1998] Mauldin III, R.L. ; Frost, G.J. ; Chen, G. ; Tanner, D.J. ; Prevot, A.S.H. ; Davis, D.D. ; Eisele, F.L.: OH measurements during the First Aerosol Characterization Experiment (ACE 1): Observations and model comparisons. In: *Journal of Geophysical Research* 103 (1998), Nr. D13, S. 16713–16729

[McDermid and Laudenslager 1982] McDermid, I. S. ; Laudenslager, James B.: Radiative lifetimes and quenching rate coefficients for directly excited rotational levels of OH (A2-Sigma+, v'=0). In: *Journal of Chemical Physics* 76 (1982), Nr. 4, S. 1824

[Mihelcic et al. 2003] Mihelcic, D. ; Holland, F. ; Hofzumahaus, A. ; Hoppe, L. ; Konrad, S. ; Muesgen, P. ; Paetz, H.W. ; Schaefer, H.J. ; Schmitz, T. ; Volz-Thomas, A. ; Baechmann, K. ; Schlomski, S. ; Platt, U. ; Geyer, A. ; Alicke, B. ; Moortgat, G.K.: Peroxy radicals during BERLIOZ at Pabstthum: Measurements, radical budgets and ozone production. In: *Journal of Geophysical Research* 108 (2003), Nr. D48254

[Olson et al. 2006] Olson, Jennifer R. ; Crawford, James H. ; Chen, Gao ; Brune, William H. ; Faloona, Ian C. ; Tan, David ; Harder, Hartwig ; Martinez, Monica: A reevaluation of airborne HOx observations from NASA field campaigns. In: *Journal of Geophysical Research* 111 (2006), Nr. D10301

[Park et al. 2007] Park, Mijeong ; Randel, William J. ; Gettelman, Andrew ; Massie, Steven T. ; Jiang, Jonathan H.: Transport above the Asian summer monsoon anticyclone inferred from Aura Microwave Limb Sounder tracers. In: *Journal of Geophysical Research* 112 (2007), Nr. D16309

[Park et al. 2009] Park, Mijeong ; Randel, William J. ; Gettelman, Andrew ; Massie, Steven T. ; Jiang, Jonathan H.: Transport above the Asian summer monsoon anticyclone inferred from Aura Microwave Limb Sounder tracers. In: *Journal of Geophysical Research* 112 (2009), Nr. D16309

[Rauthe-Schoech et al. 2016] Rauthe-Schoech, Armin ; Baker, Angela K. ; Schuck, Tanja J. ; Brenninkmeijer, Carl A. ; Zahn, Andreas ; Hermann, Markus ; Stratmann, Greta ; Ziereis, Helmut ; Velthoven, Peter F. ; Lelieveld, Jos: Trapping, chemistry, and export of trace gases in the South Asian summer monsoon observed during CARIBIC flights in 2008. In: *Atmospheric Chemistry and Physics* 16 (2016), S. 3609–3629

[Regelin et al. 2013] Regelin, E. ; Harder, H. ; Martinez, M. ; Kubistin, D. ; Ernest, C. T. ; Bozem, H. ; Klippel, T. ; Hosaynali-Beygi, Z. ; Fischer, H. ; Sander, R. ; Joeckel, P. ; Koenigstedt, R. ; Lelieveld, J.: HOx measurements in the summertime upper troposphere over Europe: a comparison of observations to a box model and a 3-D model. In: *Atmospheric Chemistry and Physics* 13 (2013), S. 10703–10720

[Ren et al. 2008] Ren, Xinrong ; Olson, Jennifer R. ; Crawford, James H. ; Brune, William H. ; Mao, Jingqiu ; Long, Robert B. ; Chen, Zhong ; Chen, Gao ; Avery, Melody A. ; Sachse, Glen W. ; Barrick, John D. ; Diskin, Glenn S. ; Huey, L. G. ; Fried, Alan ; Cohen, Ronald C. ; Heikes, Brian ; Wennberg, Paul O. ; Singh, Hanwant B. ; Blake, Donald R. ; Shetter, Richard E.: HOx chemistry during INTEX-A 2004: Observation, model calculation and comparison with previous studies. In: *Journal of Geophysical Research* 113 (2008), Nr. D05310

[Ridley et al. 1987] Ridley, B.A. ; Carroll, M.A. ; Gregory, G.L.: Measurements of nitric oxide in the boundary layer and free troposphere over the Pacific Ocean. In: *Journal of Geophysical Research: Atmospheres* 92 (1987), Nr. D2

[Rotta 1956] Rotta, Julius: Experimenteller Beitrag zur Entstehung turbulenter Stroemung im Rohr. In: *Archive of Applied Mechanics* 24 (1956), Nr. 4, S. 258–281

[Saunois et al. 2016] Saunois, Marielle ; Bousquet, Philippe ; Poulter, Ben ; Peregon, Anna ; Ciais, Philippe ; Canadell, Josep G. ; Dlugokencky, Edward J. ; Etiope, Giuseppe ; Bastviken, David ; Houweling, Sander ; Janssens-Maenhout, Greet ; Tubiello, Francesco N. ; Castaldi, Simona ; Jackson, Robert B. ; Alexe, Mihai ; Arora, Vivek K. ; Beerling, David J. ; Bergamaschi, Peter ; Blake, Donald R. ; Brailsford, Gordon ; Brovkin, Victor ; Bruhwiler, Lori ; Crevoisier, Cyril ; Crill, Patrick ; Covey, Kristofer ; Curry, Charles ; Frankenberg, Christian ; Gedney, Nicola ; Hoeglund-Isaksson, Lena ; Ishizawa, Misa ; Ito, Akihiko ; Joos, Fortunat ; Kim, Heon-Sook ; Kleinen, Thomas ; Krummel, Paul ; Lamarque, Jean-Francois ; Langenfelds, Ray ; Locatelli, Robin ; Machida, Toshinobu ; Maksyutov, Shamil ; McDonald, Kyle C. ; Marshall, Julia ; Melton, Joe R. ; Morino, Isamu ; Naik, Vaishali ; O'Doherty, Simon ; Parmentier, Frans-Jan W. ; Patra, Prabir K. ; Peng, Changhui ; Peng, Shushi ; Peters,

Glen P. ; Pison, Isabelle ; Prigent, Catherine ; Prinn, Ronald ; Ramonet, Michel ; Riley, William J. ; Saito, Makoto ; Santini, Monia ; Schroeder, Ronny ; Simpson, Isobel J. ; Spahni, Renato ; Steele, Paul ; Takizawa, Atsushi ; Thornton, Brett F. ; Tian, Hanqin ; Tohjima, Yasunori ; Viovy, Nicolas ; Voulgarakis, Apostolos ; Weele, Michiel van ; Werf, Guido R. d. ; Weiss, Ray ; Wiedinmyer, Christine ; Wilton, David J. ; Wiltshire, Andy ; Worthy, Doug ; Wunch, Debra ; Xu, Xiyan ; Yoshida, Yukio ; Zhang, Bowen ; Zhang, Zhen ; Zhu, Qiuan: The global methane budget 2000-2012. In: *Earth System Science Data* 8 (2016), S. 697–751

[Schaefer and Schmidt 1967] Schaefer, F.P. ; Schmidt, W.: Blitzlampengepumpte Farbstofflaser. In: *Z. Naturforschung* 22a (1967), S. 1563–1566

[Schlosser et al. 2009] Schlosser, E. ; Brauers, T. ; Dorn, H.-P. ; Fuchs, H. ; Haeseler, R. ; Hofzumahaus, A. ; Holland, F. ; Wahner, A. ; Kanaya, Y. ; Kajii, Y. ; Miyamoto, K. ; Nishida, S. ; Watanabe, K. ; Yoshino, A. ; Kubistin, D. ; Martinez, M. ; Rudolf, M. ; Harder, H. ; Berresheim, H. ; Elste, T. ; Plass-Duelmer, C. ; Stange, G. ; Schurath, U.: Formal blind intercomparison of OH measurements: results from the international campaign HOxComp. In: *Atmospheric Chemistry and Physics* 9 (2009), Nr. 20, S. 7923–7948

[Sedlacek 2001] Sedlacek, M.: *Messung der Hydroxylradikal-Konzentration in der marinen Troposphaere mittel laserinduzierter Fluoreszenz.* Universitaet Bonn, 2001

[Sorokin et al. 1967] Sorokin, P.P. ; Shiren, N.S. ; Lankard, J.R. ; Hammond, E.C. ; Kazyaka, T.G.: Stimulated Electronic Raman Scattering. In: *Applied Physics Letters* 10 (1967), S. 44

[Sparrow et al. 1964] Sparrow, E.M. ; Lin, S.H. ; Lundgren, T.S.: Flow Development in the Hydrodynamic Entrance Region of Tubes and Ducts. In: *The Physics of Fluids* 7 (1964), 3, Nr. 3, S. 338–347

[Stevens et al. 1994] Stevens, P.S. ; Mather, J.H. ; Brune, W.H.: Measurement of tropospheric OH and HO2 by laser-induced fluorescence at low pressure. In: *Journal of Geophysical Research* 99 (1994), Nr. D2, S. 3543–3557

[Stocker and Qin 2013] Stocker, Thomas (Ed.) ; Qin, Dahe (Ed.): *Climate Change 2013 - The Physical Science Basis (IPCC).* Cambridge University Press, 2013

[Stone et al. 2010] Stone, D. ; Evans, M.J. ; Commane, R. ; Ingham, T. ; Floquet, C.F.A. ; McQuaid, J.B. ; Brookes, D.M. ; Monks, P.S. ; Purvis, R. ; Hamilton, J.F. ; Hopkins, J. ; Lee, J. ; Lewis, A.C. ; Stewart, D. ; Murphy, J.G. ; Mills, G. ; Oram, D. ; Reeves, C.E. ; Heard, D.E.: HOx observations over West Africa during AMMA: impact of isoprene and NOx. In: *Atmospheric Chemistry and Physics* 10 (2010), October, S. 9415–9429

[Stone et al. 2018] Stone, Daniel ; Sherwen, Tomas ; Evans, Mathew J. ; Vaughan, Stewart ; Ingham, Trevor ; Whalley, Lisa K. ; Edwards, Peter M. ; Read, Katie A. ; Lee, James D. ; Moller, Sarah J. ; Carpenter,

Lucy J. ; Lewis, Alastair C. ; Heard, Dwayne E.: Impacts of bromine and iodine chemistry on tropospheric OH and HO2: comparing observations with box and global model perspectives. In: *Atmospheric Chemistry and Physics* 18 (2018)

[Takahashi et al. 2002] Takahashi, Kenshi ; Shinsuke, Hayashi ; Matsumi, Yutaka ; Taniguchi, N. ; Hayashida, Sachiko: Quantum yields of O(1D) formation in the photolysis of ozone between 230 and 308 nm. In: *Geophysical Research Letters* 107 (2002), Nr. D20, S. 4440

[Tan et al. 2017] Tan, Zhaofeng ; Fuchs, Hendrik ; Lu, Keding ; Hofzumahaus, Andreas ; Bohn, Birger ; Broch, Sebastian ; Dong, Huabin ; Gomm, Sebastian ; Haeseler, Rolf ; He, Lingyan ; Holland, Frank ; Li, Xin ; Liu, Ying ; Lu, Sihua ; Rohrer, Franz ; Shao, Min ; Wang, Baolin ; Wang, Ming ; Wu, Yusheng ; Zeng, Limin ; Zhang, Yinsong ; Wahner, Andreas ; Zhang, Yuanhang: Radical chemistry at a rural site (Wangdu) in the North China Plain: observation and model calculations of OH, HO2 and RO2 radicals. In: *Atmospheric Chemistry and Physics* (2017)

[Tan et al. 2018] Tan, Zhaofeng ; Lu, Keding ; Hofzumahaus, Andreas ; Fuchs, Hendrik ; Bohn, Birger ; Holland, Frank ; Liu, Yuhan ; Rohrer, Franz ; Shao, Min ; Sun, Kang ; Wu, Yusheng ; Zeng, Limin ; Zhang, Yinsong ; Zou, Qi ; Kiendler-Scharr, Astrid ; Wahner, Andreas ; Zhang, Yuanhang: Experimental budgets of OH, HO2 and RO2 radicals and implications for ozone formation in the Pearl River Delta in China 2014. In: *Atmospheric Chemistry and Physics* (2018)

[Tango et al. 1968] Tango, William J. ; Zare, Richard N. ; Link, John K.: Spectroscopy of K2 Using Laser-Induced Fluorescence. In: *Chemical Physics* 49 (1968), Nr. 10, S. 4264

[Vogel et al. 2016] Vogel, Baerbel ; Guenther, Gebhard ; Mueller, Rolf ; Grooss, Jens-Uwe ; Afchine, Armin ; Bozem, Heiko ; Hoor, Peter ; Kraemer, Martina ; Mueller, Stefan ; Riese, Martin ; Rolf, Christian ; Spelten, Nicole ; Stiller, Gabriele P. ; Ungermann, Joern ; Zahn, Andreas: Long-range transport pathways of tropospheric source gases originating in Asia into the northern lower stratosphere during the Asian monsoon season 2012. In: *Atmospheric Chemistry and Physics* 16 (2016), S. 15301–15325

[Wang and Davis 1974] Wang, Charles C. ; Davis, L.I.: Measurement of Hydroxyl Concentrations in Air Using a Tunable UV Laser Beam. In: *Physical Review Letters* 32 (1974), S. 349

[Wang et al. 1976] Wang, Charles C. ; Jr., L.I. D. ; Wu, C.H. ; Japar, S.: Laser-induced dissociation of ozone and resonance fluorescence of OH in ambient air. In: *Applied Physics Letters* 28 (1976), Nr. 1, S. 14

[Wennberg et al. 1994] Wennberg, P.O. ; Cohen, R.C. ; Stimpfle, R.M. ; Koplow, J.P. ; Anderson, J.G. ; Salawitch, R.J. ; Fahey, D.W. ; Woodbridge, E.L. ; Keim, E.R. ; Gao, R.S. ; Webster, C.R. ; May, R.D. ; Toohey, D.W. ; Avallone, L.M. ; Proffitt, M.H. ; Loewenstein, M. ; Podolske,

J.R. ; Chan, K.R. ; Wofsy, S.C.: Removal of Stratospheric O3 by Radicals: In Situ Measurements of OH, HO2, NO, NO2, ClO, and BrO. In: *Science* 266 (1994), Nr. 5184, S. 398–404

[Wennberg et al. 1998] Wennberg, P.O. ; Hanisco, T.F. ; Jaegle, L. ; Jacob, D.J. ; Hintsa, E.J. ; Lanzendorf, E.J. ; Anderson, J.G. ; Gao, R.S. ; Keim, E.R. ; Donnelly, S.G. ; Negro, L.A. D. ; Fahey, D.W. ; McKeen, S.A. ; Salawitch, R.J. ; Webster, C.R. ; May, R.D. ; Herman, R.L. ; Proffitt, M.H. ; Margitan, J.J. ; Atlas, E.L. ; Schauffler, S.M. ; Flocke, F. ; McElroy, C.T. ; Bui, T.P.: Hydrogen Radicals, Nitrogen Radicals and the Production of O3 in the Upper Troposphere. In: *Science 279* (1998)

[Secretariat of the World Meteorological Organization 1992] World Meteorological Organization, WMO92 Secretariat of t.: Definition. In: *International Meteorological Vocabulary* 2nd edition (1992), S. 636

Acknowledgements

At this point I initially want to thank Prof. Dr. Astrid Kiendler-Scharr, Prof. Dr. Andreas Wahner and PD Dr. Andreas Hofzumahaus for the opportunity to work on this topic at IEK-8 in the Forschungszentrum Jülich with the aim to graduate at the University of Cologne.

Special thanks goes to PD Dr. Andreas Hofzumahaus for the countless discussions and his support throughout for the almost four and a half years time I have been at the IEK-8. I would also like to special thank Dr. Sebastian Broch for his indispensable practical skills in introducing me to the new instrument and supporting me for the first two years of my Ph.D with whatever stupid question I could come up with.

I want to express my gratitude to the LIF-group, in particular to Dr. Anna Novelli for the many discussions and an open ear for anything. I'm also thankful to PD Dr. Hendrik Fuchs for the scientific discussions and help during the campaign, to Matthias Bachner for his technical support and to Dr. Frank Holland for the scientific discussions and his expertise in questions concerning IDL. Gratitude also goes to Kamil Kubik and Dominik Raak for their practical help.

Appreciation for the entire OMO-community in particular Dr. Hartwig Harder, Dr. Marcel Dorf, Prof. Dr. Jos Lelieveld and the DLR for making this campaign possible I also want to express. This includes the scientific discussions with Dr. Hartwig Harder and Daniel Marno within the HO_x inter-comparison workshop.

Gratitude I also want to convey to Dr. Domenico Taraborelli for several discussions and his offer to make available the FZJ EMAC model data, which helped to better understand the sensitivity and validity of the HO_x box-model results.

Finally I want to thank Saskia Weißen for her support throughout the time I have been at the Forschungszentrum in Jülich.

Ich versichere, dass ich die von mir vorgelegte Dissertation selbständig angefertigt, die benutzten Quellen und Hilfsmittel vollständig angegeben und die Stellen der Arbeit - einschließlich Tabellen, Karten und Abbildungen -, die anderen Werken im Wortlaut oder dem Sinn nach entnommen sind, in jedem Einzelfall als Entlehnung kenntlich gemacht habe; dass diese Dissertation noch keiner anderen Fakultät oder Universität zur Prüfung vorgelegen hat; dass sie - abgesehen von unten angegebenen Teilpublikationen - noch nicht veröffentlicht worden ist sowie, dass ich eine solche Veröffentlichung vor Abschluss des Promotionsverfahrens nicht vornehmen werde. Die Bestimmungen der Promotionsordnung sind mir bekannt. Die von mir vorgelegte Dissertation ist von Prof. Dr. Astrid Kiendler-Scharr betreut worden.

Date Christopher Künstler

Vita

Christopher Künstler

Contact

Address	Alte Dorfstr. 3 48317 Rinkerode
Mail	c.kuenstler@fz-juelich.de
Phone	01520 / 3 55 98 68
Born / In	22.03.1985 / Coesfeld
Citizenship	German
Family status	unmarried

Education / University

06/2019 – 02/2015	PHD candidate in Experimental Physics at the University of Cologne – execution of the work at and employed by the Institute of Energy and Climate Research (IEK8-Troposphere) in the Forschungszentrum Jülich • Title: Measurements of atmospheric OH and HO2 Radicals by Laser-Induced Fluorescence on the HALO aircraft during the OMO Asia 2015 campaign
03/2014	Diploma at the University of Münster • Title: Grundzustandsenergieaufspaltung im Razavy Potential in semi-klassischer Näherung
03/2014 – 10/2013	Group Exercise Instructor (Physics 1)
02/2011	Pre-Diploma Physics
10/2007	Start of Physics Studies at University of Münster

Education / School

05/2006	Abitur at Berufskolleg Borken
08/2002	Start of secondary school at Berufskolleg Borken
05/2001	Entrance Qualification

Rinkerode, 26.02.2020

CITY, DATE

SIGNATURE